DENSITY FUNCTIONAL THEORY STUDIES FOR SEPARATION OF ENANTIOMERS OF A CHIRAL SPECIES BY ENANTIOSPECIFIC ADSORPTION ON SOLID SURFACES

A Dissertation
Presented to
The Academic Faculty

by

Jeong Woo Han

In Partial Fulfillment
of the Requirements for the Degree
Doctor of Philosophy in the
School of Chemical and Biomolecular Engineering

Georgia Institute of Technology
May 2010

DENSITY FUNCTIONAL THEORY STUDIES FOR SEPARATION OF ENANTIOMERS OF A CHIRAL SPECIES BY ENANTIOSPECIFIC ADSORPTION ON SOLID SURFACES

Approved by:

Dr. David S. Sholl, Advisor
School of Chemical and Biomolecular Engineering
Georgia Institute of Technology

Dr. J. Carson Meredith
School of Chemical and Biomolecular Engineering
Georgia Institute of Technology

Dr. Pradeep K. Agrawal
School of Chemical and Biomolecular Engineering
Georgia Institute of Technology

Dr. Thomas M. Orlando
School of Chemistry and Biochemistry
Georgia Institute of Technology

Dr. Christopher W. Jones
School of Chemical and Biomolecular Engineering
Georgia Institute of Technology

Date Approved: March 30, 2010

To my parents, Hyun Suk Han and Ae Ja Kim, for always loving and praying for me…

ACKNOWLEDGEMENTS

Above all, I would like to thank my Lord, Jesus Christ, who has taken care of me during my PhD. He has comforted and encouraged me whenever I was knocked down. At every moment, I want to praise, worship, and glorify Him with the talents He gave me. He is the reason that I live and sing with all I am. I cannot live a day without Him.

I would like to express my deep and sincere gratitude to Dr. David S. Sholl, my advisor at the Georgia Institute of Technology as well as Carnegie Mellon University, who has taught, guided, and supported me with understanding, encouraging, and patience. A lot of his expertise and research insight have provided a good basis for the present thesis.

Along with my advisor, I am deeply grateful to my collaborators, Dr. E. Charles H. Sykes, Dr. John R. Kitchin, and Dr. Andrew J. Gellman who have been wonderful sources of advices and insights. I have been especially fortunate to have Dr. Pradeep K. Agrawal, Dr. Christopher W. Jones, Dr. J. Carson Meredith, and Dr. Thomas M. Orlando as my committee members.

I also would like to thank the previous and current Sholl group members, Dr. Taku Watanabe, Dr. Shiqiang Hao, Dr. Ji Zang, Dr. Thomas Manz, Dr. Sudhakar Alapati, Dr. Joanna N. James, Dr. Lymarie Semidey-Flecha, Dr. Chen Ling, Dr. Seda Keskin, Sang eun Jee, Ki Chul Kim, Sung Gu Kang, Emmanuel Haldoupis. Their kindness, encouraging, and support are greatly helpful to make this thesis possible.

I want to acknowledge the friendship of many people I met in Atlanta for making my stay memorable. I owe an enormous amount of gratitude to the members of Sugarloaf

Korean Baptist Church, especially to Hyo Jin Kweon, Younah Kang, and Giwan Choi who shared joy and grief with me as brothers and sisters in the name of Jesus Christ. I also want to acknowledge the friendship of the members of Korean ChBE Association including Hyea Kim, Hyewon Lee, and Nae Chul Shin. I am certainly grateful to Dr. Seung Soon Jang and Dr. Byung Cheol Kim for hosting and leading our Bible study.

I must extend my thanks and acknowledgement to Yongjin Park, Sungjun Yoon, Esak Lee, and Jonghye Woo for their prayers and supports in Jesus Christ. I would like to thank my many friends in Korea, Taehyung Kim, Hyun Lak Cho, Hongse Lee, Yudon Han, and Ho Sang Choi for their supports.

Finally, I would like to express my gratitude to my mother, Ae Ja Kim, and my father, Hyun Suk Han, who always love, support, and pray for me.

Jeong Woo Han

03.19.2010, Atlanta, USA

TABLE OF CONTENTS

LIST OF TABLES

LIST OF FIGURES

SUMMARY

The distinct response of biological systems to the two enantiomers of a chiral chemical has led to a large market for enantiopure pharmaceuticals and raised fundamental issues about the origin of biological homochirality. It is therefore important to understand the interactions of chiral molecules with chiral environments. Chiral environments associated with solid surfaces could potentially play a useful role in chirally specific chemical processing. There are a variety of routes for creating chiral solid surfaces. Surfaces of materials whose bulk crystal structure is enantiomorphic can be used as one type of chiral solid surfaces. Metal surfaces that are intrinsically chiral due to the presence of kinked surface steps provide another route for creating chiral solid surfaces. Alternatively, we can impart chirality onto surfaces by attaching irreversibly adsorbing chiral organic species on otherwise achiral surfaces. Understanding and ultimately controlling enantiospecific interactions of molecules on this kind of surfaces requires detailed insight into the adsorption geometries and energies of these complex interfaces. To tackle these issues, we performed density functional theory (DFT) calculations that have proved to be a useful tool for quantitative prediction of these effects. Besides our main topic above, we theoretically examine the effects of K atoms as a promoter coadsorbed with small molecules on Mo_2C surfaces, a promising catalyst for a range of chemicals applications. Our results in this thesis provide fundamental information about these systems and demonstrate that using DFT for this purpose can be a useful means of identifying the phenomena that control chiral surface chemistry.

CHAPTER 1

INTRODUCTION

1.1. Chirality

Any object that cannot be superimposed upon its mirror image is called to be chiral. Specifically, if any atom in a molecule is tetrahedrally bonded to four different functional groups, we can say that the molecule is chiral. A simple example of a chiral molecule is an amino acid, which has a central C atom that is bonded to H, NH_2, COOH, and a side chain that varies among different amino acids. For more complicated chiral molecules, multiple chiral centers may exist. The two mirror image forms of a chiral species are called enantiomers. Enantiomers of a molecule have the identical bulk physical properties such as boiling point and density.

Chirality is a crucial property of most biomolecules such as proteins and DNA which are the basis of life on earth. Each biomolecule in life tends to take exclusively one chiral form. As a consequence, two enantiomers of a chiral species often exhibit extremely different bioactivities. For example, *S*-penicillaminum gives good efficacy as an anti-arthritic but *R*-penicillaminum is extremely toxic[1]. Enantiomerically pure chiral compounds must, therefore, be produced for human dosage. This has led to an enormous market in pharmaceutical industry. In 2005, worldwide sales of enantiopure drugs were more than $US225 billion[2].

The existence of biological homochirality also raises profound questions about the origins of life[3-4]. Living organisms have exclusively selected one enantiomeric form of a chiral species. For instance, proteins are composed of almost entirely left handed amino acids while nucleic acids, starch, glycogen, and so on contain sugars that are all right handed. Even though various hypotheses have been proposed for the emergence of biological homochirality, our understanding of this phenomenon is far from complete.

These kinds of issues described above give us strong motivation to understand environments which can differentiate two enantiomers of a chiral molecule.

1.2. Creating chirality on solid surfaces

Solid surfaces as enantioselective heterogeneous catalysis can potentially be used for creating chiral environments that are applicable to chiral processing. There are several different routes to impart chirality onto this kind of surfaces[4-8]. These include using the surfaces of materials whose bulk crystal structure is chiral[9], utilizing intrinsically chiral metal surfaces, which are crystal planes with a surface structure lacking mirror symmetry[10-16], and attaching irreversibly adsorbing chiral modifiers on otherwise achiral surfaces[17-21].

1.2.1. Chiral mineral surfaces

Crystals that lack a center of symmetry provide the most obvious chiral surfaces for experimental study. The molecular crystals of enantiopure chiral species such as amino acids are chiral objects and the surfaces of these crystals are chiral. The crystals of many inorganic materials are also chiral. A good example of this is the common mineral quartz, one of the most abundant natural minerals in the earth's crust[22-24]. Quartz (SiO_2) has a structure that features a helical arrangement of corner-linked SiO_4 tetrahedra. The sense of that helix defines chirality into the entire crystal. Most early work for chiral minerals has therefore focused on adsorption of chiral species on quartz. More recently, Soai et al. have reported enantioselective chemical syntheses with the addition of powdered quartz as a chiral promoter[25]. Natural mineral samples of quartz are commonly twinned. That is, natural specimens of quartz include domains of both enantiomorphs of the crystal, implying that powdered samples of natural quartz have a mixture of the mineral's two enantiomers[4]. This complicates efforts to identify structural mechanisms and quantitative information of adsorption on the specific surfaces of quartz. Many other

common minerals are also chiral[9]. Hazen *et al.* have performed experiments to examine the enantiospecific adsorption of amino acids on specific crystal faces of the mineral calcite, a mineral whose bulk crystal structure is chiral, using large untwinned natural crystals[3]. These experiments demonstrated that the adsorption properties of some amino acids can be discriminated on these mineral surfaces. Since it is not experimentally easy to study structural mechanisms and energetics of adsorption on the specific surfaces of this kind of materials, theoretical descriptions at quantum level may play an important role for predicting which chiral species would show strong enantiospecific interactions with crystalline surfaces of quartz and other chiral minerals[26-27].

1.2.2. Chiral metal surfaces

The metals whose bulk crystals are highly symmetric can have surfaces that are chiral once a metal surface is created by cutting a single crystal along a plane that is not coincident with the crystal's symmetry directions, that is, certain high Miller index directions. The (*hkl*) Miller index surfaces of any fcc metal are chiral, provided that $h \neq k \neq l$ and $h \times k \times l \neq 0$ [14]. These surfaces (in their ideal, bulk-terminated structure) have regions of the low Miller index planes separated by steps that are a single atom high that do not point along a high symmetry direction on the surface. The chirality of these surfaces originates from the repeated intersections of unlike step edges on the surface[10, 14, 16]. One example is the naturally chiral (643) and $(\overline{643})$ surfaces as shown in Fig. 1.1. These surfaces are nonsuperimposable mirror image of one another and thus chiral. The straight steps and the kinks at every two lattice spacings which are formed by (100) and (111) microfacets are separated by (111) terraces. The handedness created by the arrangement of the microfacets forming the kinks on the surface implies that each one would interact differently with each enantiomer of a chiral species. The ideal structures of all chiral metal surfaces have this kind of structural frameworks; they only choose

different low Miller index microfacets forming the terrace, step and kink and the widths of the terrace, and the lengths of the step edge.

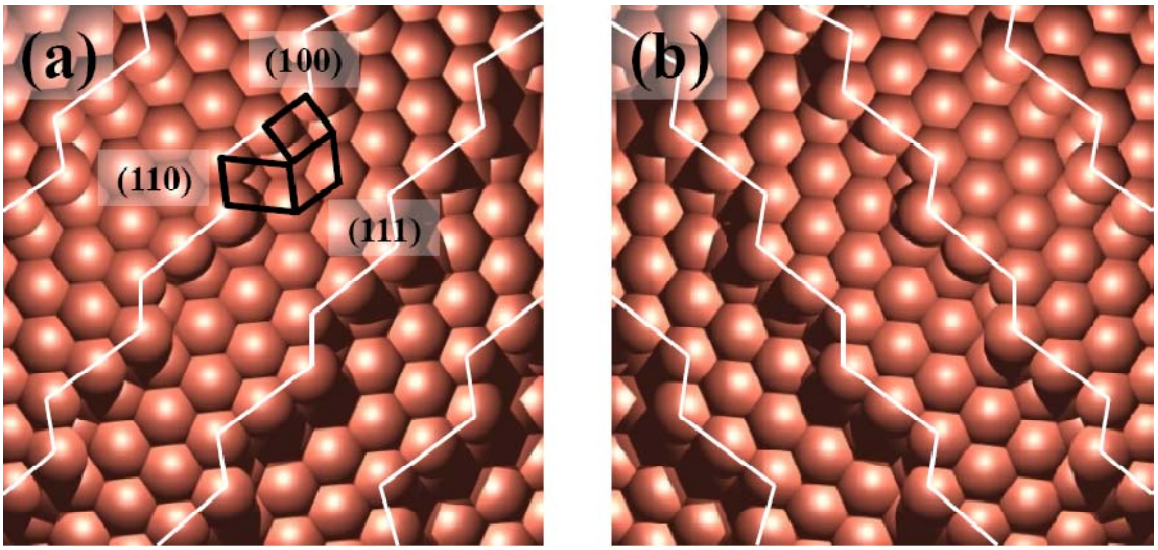

Figure 1.1: An example of chiral metal surface: a top view of an ideal fcc (a) (643) and (b) $(\overline{6}\overline{4}3)$ surfaces, with step edges highlighted with white solid lines. The three low Miller index microfacets that compose these surfaces are marked in (a).

In reality, the thermally activated diffusion of surface atoms along step edges on metal surfaces held at moderate temperatures causes coalescence of kinks, and formation of nonideal kink structures at the intersections of long step edges. This phenomena were observed on Cu(643) by a low-temperature scanning tunneling microscope (STM)[28] and on Cu(5 8 90) by a room temperature STM[29], leading to creation of longer step edges, wider terraces, and the coalescence of kink sites with the periodicity disrupted by thermal fluctuations. Both experimental[28] and theoretical[13] reports have, however, demonstrated that although thermal diffusion can cause significant local disorder, the net chirality of the surface is maintained since the kinks still occur at the intersections of three different low Miller index microfacets.

Enantiospecific adsorption on intrinsically chiral metal surfaces described above has been demonstrated in electrochemical[15, 30] and vacuum[12, 31] experiments and

examined using theoretical models[4, 11, 14]. The largest experimentally measured enantiospecific differences in adsorption energies for molecules physisorbed on metal surfaces are of order 1 kJ/mol[12, 32-33], while theoretical studies have reported much larger differences in adsorption energy which are ~13.5 kJ/mol for the chemisorption of cysteine on Au(17 11 9)[34] and ~12.5 kJ/mol for the adsorption of amino-(fluoro)methoxy on Cu(874)[35].

1.2.3. Chirally modified surfaces

Chirally modified surfaces can be created by irreversibly attaching the single enantiomer form of some chiral organic molecule as chiral templates to an otherwise achiral surface. The chirality of the template molecule causes the resulting functionalized catalyst to be chiral. This class of surfaces has been developed for only a limited number of effective chiral heterogeneous catalysts. The best known examples are hydrogenation of α-ketoesters on cinchona-modified Pt[36] and β-ketoesters on tartrate-modified Ni[37]. Even though these chirally modified surfaces showed very efficient enantioselectivity as the heterogeneous catalysts under optimized conditions, the fundamental mechanisms underlying their effectiveness for generalizing their properties to other classes of reactions or chirally modified surfaces are not well understood due to the complexity of these materials.

Density functional theory (DFT) calculations can be a useful tool to provide mechanistic insights for this kind of systems. It has been used to study the conformations of cinchonidine on Pt(111)[38-39], H-bonding interactions between α-hydroxyketones and protonated cinchonidine on Pt(111)[40], cinchonidine adsorbed on Au-containing surfaces[41], Pd-catalyzed hydrosilylation of styrene[42-43], asymmetric oxidative coupling of 2-naphthol using a SiO_2-supported vanadyl complex combined with experimental methods[44], and pyroglutamic acid as a chiral auxiliary in hydrogenation reactions on Rh(111)[45]. Combining these successful predictions with DFT, the efforts to probe the

mechanisms that determine the enantioselectivity of these catalysts are being continued using surface science and spectroscopic methods.

1.3. Mo_2C as a promising catalyst

Besides the main topic about chirality on solid surfaces, the adsorption of small species with K promoter on Mo_2C surfaces will also be discussed in this thesis. Molybdenum carbides are known to be potentially promising substitutes for expensive noble metals due to their similar catalytic properties[46] as well as resistance to sulfur poisoning[46-47], extreme hardness[48], high melting point[49], and excellent electric and thermal conductivities[50]. Previous reports demonstrated that doping with K can significantly changes the catalytic properties of Mo_2C[47, 51]. It would be therefore interesting to provide fundamental information about the properties of K atoms on Mo_2C surfaces, which will be useful for understanding the mechanistic influence of K promoters in complex catalytic reactions.

1.4. Thesis summary

In Chapter 2, we provide a simple overview of density functional theory (DFT) which will be our primary method throughout the entire thesis for predicting the physical and chemical properties of the systems we have interest in.

In Chapter 3 and 4, we examine enantiospecific adsorption of amino acids on hydroxylated α-quartz (0001) and $(10\bar{1}0)$, which are chiral mineral surfaces. In Chapter 3, we perform DFT calculations to study the adsorption of glycine, alanine, serine, and cysteine on the hydroxylated (0001) surface of α-quartz. Using DFT, the adsorption of glycine, alanine, serine, cysteine, aspartic acid and asparagine on the hydroxylated α-quartz $(10\bar{1}0)$ is also investigated in Chapter 4. Our results in these two Chapters provide initial information on how amino acids can exhibit enantiospecific adsorption on hydroxylated quartz surfaces.

In Chapter 5, we describe step decoration of chiral metal surfaces. The decoration of steps on these surfaces with additional metal atoms is one potential avenue for improving the enantiospecificity of those surfaces. For successful step decoration, the additional metal atoms should ideally remain at the kinked step sites on the surface. We identify pairs of metal adatoms and metal surfaces where this kind of step decoration could be thermodynamically stable. Using our DFT results that identify multiple stable examples of step decoration, we develop a model to predict surface segregation on a wide range of stepped metal surfaces. With this model, we estimate the stability of step decoration without further DFT calculations for surface segregation for all combinations of the 3d, 4d, and 5d metals. In order to create experimentally relevant step decorated surfaces such as Ag or Pd decorated Cu, it is also important to understand surface diffusion mechanisms including Ehrlich-Schwoebel (ES) barrier[52-53]. Comparing our DFT results with low-temperature scanning tunneling microscopy (STM), gives an example of how work of this kind can allow us to understand complicated surface alloying mechanisms.

We move on to study of the adsorption of amino acid that can be used as one potential class of chiral modifiers on metal surfaces in Chapter 6. There has been disagreement between experimental and theoretical reports for chemical speciation of glycine on metal surfaces. Using DFT combined with Monte Carlo simulations, three hypotheses we propose are tested to provide to reconcile this discrepancy.

Besides our main topic, we examine H and CO adsorption with K promoter on Mo_2C surfaces in Chapter 7. Using K as a promoter is known to strongly influence the selectivity of catalytic reactions on Mo_2C catalysts. To provide fundamental information about this observation, we perform DFT calculations to study K adsorption of seven low-index β–Mo_2C surfaces. K is found to bind most strongly on Mo_2C (001). This surface is also shown to favor a reconstruction in the absence of adsorbates. A small number of

calculations of H/K and CO/K coadsorption on the surface were also performed to probe the effect of K promoters on these adsorbed species.

Finally, we outline and discuss the main challenges and opportunities with regard to surface chemistry of chiral adsorption in Chapter 8.

References

(1) Lee, S., *Encyclopedia of Chemical Processing*. 2nd ed.; CRC Press: New York, 2005.
(2) Erb, S., *Pharmaceutical Technology* **2006**, Oct 3.
(3) Hazen, R. M.; Filley, T. R.; Goodfriend, G. A., *Proc. Nat. Acad. Sci.* **2001**, 98, 5487-5490.
(4) Hazen, R. M.; Sholl, D. S., *Nat. Mater.* **2003**, 2, 367-374.
(5) Barlow, S. M.; Raval, R., *Surf. Sci. Rep.* **2003**, 50, 201-341.
(6) James, J. N.; Sholl, D. S., *Curr. Opin. Colloid Interface Sci.* **2008**, 13, 60-64.
(7) Berg, A. M.; Patrick, D. L., *Angew. Chem. Int. Ed.* **2005**, 44, 1821-1823.
(8) Ernst, K.-H., *Top. Curr. Chem.* **2006**, 265, 209-252.
(9) Hazen, R. M., *Am. Mineral.* **2006**, 91, 1715-1729.
(10) McFadden, C. F.; Cremer, P. S.; Gellman, A. J., *Langmuir* **1996**, 12, 2483-2487.
(11) Sholl, D. S., *Langmuir* **1998**, 14, 862-867.
(12) Horvath, J. D.; Koritnik, A.; Kamakoti, P.; Sholl, D. S.; Gellman, A. J., *J. Am. Chem. Soc.* **2004**, 126, 14988-14994.
(13) Power, T. D.; Asthagiri, A.; Sholl, D. S., *Langmuir* **2002**, 18, 3737-3748.
(14) Sholl, D. S.; Asthagiri, A.; Power, T. D., *J. Phys. Chem. B* **2001**, 105, 4771-4782.
(15) Ahmadi, A.; Attard, G.; Feliu, J.; Rodes, A., *Langmuir* **1999**, 15, 2420-2424.
(16) Attard, G. A.; Ahmadi, A.; Feliu, J.; Rodes, A.; Herrero, E.; Blais, S.; Jerkiewicz, G., *J. Phys. Chem. B* **1999**, 103, 1381-1385.
(17) Humblot, V.; Haq, S.; Muryn, C.; Hofer, W. A.; Raval, R., *J. Am. Chem. Soc.* **2002**, 124, 503-510.
(18) Stacchiola, D.; Burkholder, L.; Zheng, T.; Weinert, M.; Tysoe, W. T., *J. Phys. Chem. B* **2005**, 109, 851-856.
(19) Baiker, A., *J. Mol. Catal. A.* **1997**, 115, 473-493.
(20) Lorenzo, M. O.; Baddeley, C. J.; Muryn, C.; Raval, R., *Nature* **2000**, 404, 376 - 379.
(21) Lee, I.; Ma, Z.; Kaneko, S.; Zaera, F., *J. Am. Chem. Soc.* **2008**, 130, 14597-14604.
(22) Bonner, W. A.; Kavasmaneck, P. R.; Martin, F. S.; Flores, J. J., *Science* **1974**, 186, 143-144.
(23) Karagounis, G.; Coumonlos, G., *Nature* **1938**, 142, 162-163.
(24) Tsuchida, R.; Kobayashi, M.; Nakamura, A., *J. Chem. Soc. Jpn* **1935**, 56, 1339.
(25) Soai, K.; Osanai, S.; Kadowaki, K.; Yonekubo, S.; Shibata, T.; Sato, I., *J. Am. Chem. Soc.* **1999**, 121, 11235-11236.
(26) Han, J. W.; Sholl, D. S., *Langmuir* **2009**, 25, 10737-10745.
(27) Asthagiri, A.; Hazen, R. M., *Mol. Simulat.* **2007**, 33, 343-351.

(28) Baber, A. E.; Gellman, A. J.; Sholl, D. S.; Sykes, E. C. H., *J. Phys. Chem. C* **2008**, 112, 11086-11089.
(29) Dieluweit, S.; Ibach, H.; Giesen, M.; Einstein, T. L., *Phys. Rev. B* **2003**, 67, -.
(30) Attard, G. A., *J. Phys. Chem. B* **2001**, 105, 3158-3167.
(31) Horvath, J. D.; Gellman, A. J., *J. Am. Chem. Soc.* **2001**, 123, 7953-7954.
(32) Gellman, A. J.; Horvath, J. D.; Buelow, M. T., *J. Mol. Catal. A* **2001**, 167, 3-11.
(33) Horvath, J. D.; Gellman, A. J., *J. Am. Chem. Soc.* **2002**, 124, 2384-2392.
(34) Greber, T.; Šljivancanin, Ž.; Schillinger, R.; Wider, J.; Hammer, B., *Phys. Rev. Lett.* **2006**, 96, 056103.
(35) Bhatia, B.; Sholl, D. S., *Angew. Chem. Int. Ed.* **2005**, 44, 7761-7764.
(36) Jacoby, M., *Chem. Eng. News* **2004**, 82, 37-41.
(37) Keane, M. A., *Langmuir* **1997**, 13, 41-50.
(38) Vargas, A.; Baiker, A., *J. Catal.* **2006**, 239, 220-226.
(39) Vargas, A.; Hoxha, F.; Bonalumi, N.; Mallat, T.; Baiker, A., *J. Catal.* **2006**, 240, 203-212.
(40) Nieminen, V.; Taskinen, A.; Toukonitty, E.; Hotokka, M.; Murzin, D. Y., *J. Catal.* **2006**, 237, 131-142.
(41) Behzadi, B.; Vargas, A.; Ferri, D.; Ernst, K. H.; Baiker, A., *J. Phys. Chem. B* **2006**, 110, 17082-17089.
(42) Magistrato, A.; Togni, A.; Rothlisberger, U., *Organometallics* **2006**, 25, 1151-1157.
(43) Magistrato, A.; Woo, T. K.; Togni, A.; Rothlisberger, U., *Organometallics* **2004**, 23, 3218-3227.
(44) Tada, M.; Kojima, N.; Izumi, Y.; Taniike, T.; Iwasawa, Y., *J. Phys. Chem. B* **2005**, 109, 9905-9916.
(45) Barbosa, L. A. M. M.; Sautet, P., *J. Catal.* **2003**, 217, 23-29.
(46) Oyama, S. T., *Catal. Today* **1992**, 15, 179-200.
(47) Woo, H. C.; Park, K. Y.; Kim, Y. G.; Nam, I. S.; Chung, J. S.; Lee, J. S., *Appl. Catal.* **1991**, 75, 267-280.
(48) Liao, J. J.; Wilcox, R. C.; Zee, R. H., *Scripta. Metall. Mater.* **1990**, 24, 1647-1652.
(49) Hwu, H. H.; Chen, J. G., *Chem. Rev.* **2005**, 105, 185-212.
(50) Nelson, J. A.; Wagner, M. J., *Chem. Mater.* **2002**, 14, 4460-4463.
(51) Xiang, M. L.; Li, D. B.; Li, W. H.; Zhong, B.; Sun, Y. H., *Fuel* **2006**, 85, 2662-2665.
(52) Ehrlich, G.; Hudda, F. G., *J. Chem. Phys.* **1966**, 44, 1039.
(53) Schwoebel, R. L.; Shipsey, E. J., *J. Appl. Phys.* **1966**, 37, 3682.

CHAPTER 2

COMPUTATIONAL METHODS

Density functional theory (DFT) is one of the most popularly used computational tools to investigate the electronic structure of many-body systems such as atoms, molecules, and condensed phases. In this Chapter, we present a brief overview of DFT, which will be our primary method to study the topics discussed in this thesis. A detailed introduction of DFT is beyond the scope of this Chapter, as excellent review articles and books are readily available[1-9]. Although in 1926, Schrödinger published the first account of his wave equation, there to date have been no exact analytic solutions to the Schrödinger equation for systems of many atoms. With the dramatic advance of modern computing ability, remarkable numerical methods have, however, been developed to accurately predict the quantum mechanical structure of a system of atoms.

The ideas of DFT are based on two fundamental mathematical theorems proved by Hohenberg and Kohn[10]. They firstly showed that the ground state total energy of a system of interacting electrons is a unique functional of the electron density. This theorem states that there exists a unique mapping between the ground state electron density of the system and the ground state wave function of the system. They further identified that the electron density that minimizes the energy of the overall functional is the true electron density corresponding to the full solution of the Schrödinger equation. In 1965, Kohn and Sham showed that the problem of many interacting electrons in an external potential can be mapped exactly to a set of noninteracting electrons in an effective external potential[11], leading to a set of self-consistent, single particle equations known as the Kohn-Sham equations:

$$\left[-\frac{\hbar^2}{2m}\nabla^2 + V\left(\vec{r}\right) + V_H\left(\vec{r}\right) + V_{XC}\left(\vec{r}\right) \right] \psi_i\left(\vec{r}\right) = \varepsilon_i \psi_i\left(\vec{r}\right) \qquad (2.1)$$

In this equation, the energy of the system is decomposed into principal components including the kinetic energy, the nuclei-electron static attraction, the electron-electron static repulsions, and the non-classical electron-electron interactions. While we can use exact methods to calculate the Columbic interactions and other classical components in the system's energy, the exact form of the non-classical energies, that is, the exchange-correlation energy functional is not known. An approximation for this functional must therefore be made. DFT calculations have typically employed either the local density approximation (LDA) or the generalized gradient approximation (GGA) to describe the exchange-correlation energy functional. The LDA assumes that the energy of each electron can be related to the energy of that electron in a uniform electron gas with the same (global) density as the local electron density in the actual system. The GGA includes corrections for local gradients in the electron density and is often implemented as a corrective function of the LDA.

Since the 1970s, DFT has been very popular for solving the problems in solid state physics. It can be used to efficiently model isolated molecules, bulk solids, and material interfaces including surfaces. DFT calculations, however, do not accurately account for dispersive interactions, so the improvement of functional to describe the van der Waals forces is an actively ongoing research topic today. Throughout the entire thesis, we have employed plane wave DFT calculations using the Vienna *ab initio* Simulation Package (VASP) [3, 12-14]. These calculations have used the ultrasoft pseudopotentials[14-15] or the projector augmented wave (PAW) method[16-17] to describe ionic cores. Our calculations have used the generalized gradient approximation (GGA) with the Perdew-Wang 91[18] functional or the revised Perdew-Burke-Ernzerhof (rPBE) functional[19-20] to describe the exchange-correlation contributions to the total energy. All of our calculations have used plane wave basis functions using periodic boundary conditions to model solid surfaces. The interaction between molecules and surfaces are represented via a periodic system in which the material extends to infinity in the plane of

the surface, but is separated from its periodic images in the direction normal to the surface by a vacuum region. More details for DFT calculations on each topic are presented completely in the corresponding Chapter.

References

(1) Hammer, B.; Norskov, J. K., *Adv. Catal.* **2000**, 45, 71-129.
(2) Greeley, J.; Norskov, J. K.; Mavrikakis, M., *Annu. Rev. Phys. Chem.* **2002**, 53, 319-348.
(3) Sholl, D. S.; Steckel, J. A., *Density functional theory : a practical introduction*. John Wiley & Sons, Inc.: Hoboken, NJ, 2009.
(4) Payne, M. C.; Teter, M. P.; Allan, D. C.; Arias, T. A.; Joannopoulos, J. D., *Rev. Mod. Phys.* **1992**, 64, 1045-1097.
(5) Parr, R. G.; Weitao, Y., *Density-Functional Theory of Atoms and Molecules*. Oxford University Press: Oxford, 1994.
(6) Koch, W.; Holthausen, M. C., *A Chemist's Guide to Density Functional Theory*. Wiley-VCH: Berlin, 2001.
(7) Martin, R. M., *Electronic Structure: Basic Theory and Practical Methods*. Cambridge University Press: Cambridge, 2004.
(8) Seminario, J. M.; Politzer, P. P., *Modern Density Functional Theory - A Tool for Chemistry, Theoretical and Computational Chemistry*. Elsevier: Amsterdam, 1995.
(9) Fiolhais, C.; Noguera, F.; Marques, M. A. L., *A Primer in Density-Functional Theory*. Springer-Verlag: Berlin, 2003.
(10) Hohenberg, P.; Kohn, W., *Phys. Rev.* **1964**, 136, B864-&.
(11) Kohn, W.; Sham, L. J., *Phys. Rev.* **1965**, 140, 1133-1137.
(12) Kresse, G.; Furthmuller, J., *Phys. Rev. B* **1996**, 54, 11169-11186.
(13) Kresse, G.; Hafner, J., *Phys. Rev. B* **1993**, 47, 558-561.
(14) Kresse, G.; Hafner, J., *J. Phys.: Condens. Matter* **1994**, 6, 8245-8257.
(15) Vanderbilt, D., *Phys. Rev. B* **1990**, 41, 7892-7895.
(16) Blöchl, P. E., *Phys. Rev. B* **1994**, 50, 17953.
(17) Kresse, G.; Joubert, D., *Phys. Rev. B* **1999**, 59, 1758-1775.
(18) Perdew, J. P.; Chevary, J. A.; Vosko, S. H.; Jackson, K. A.; Pederson, M. R.; Singh, D. J.; Fiolhais, C., *Phys. Rev. B* **1992**, 46, 6671-6687.
(19) Perdew, J. P.; Burke, K.; Ernzerhof, M., *Phys. Rev. Lett.* **1996**, 77, 3865-3868.
(20) Perdew, J. P.; Burke, K.; Ernzerhof, M., *Phys. Rev. Lett.* **1997**, 78, 1396-1396.

CHAPTER 3

ENANTIOSPECIFIC ADSORPTION OF AMINO ACIDS ON HYDROXYLATED QUARTZ (0001)

3.1. Introduction*

Quartz, one of the most abundant natural minerals in the earth's crust[1-5], can potentially provide an enantiospecific environment for chiral molecules. Its bulk crystal structure is intrinsically chiral; that is, mirror images of the crystals cannot be superimposed upon one another[6-7]. Natural specimens of quartz are frequently twinned and include domains of both enantiomorphs of the crystal. Experiments exploring chiral interactions with quartz were performed as early as the 1930s[8-10]. More recently, experiments that used powdered quartz as a promoter in chirally specific syntheses were performed[11]. Among the various surfaces of quartz, a number of previous studies have concentrated on α-quartz (0001), which is one of the principal faces found in experiment[12], and carefully addressed what the structure of the surface will be under experimentally relevant conditions[1, 3, 5, 13-15]. A primary conclusion from these studies was that the hydroxylated form of this surface is much more stable under essentially all circumstances than the surface created simply by cleaving the bulk material.

Understanding and ultimately controlling enantiospecific interactions of molecules on surfaces requires detailed insight into the adsorption geometries and energies of these complex interfaces. Density functional theory (DFT) has proved to be a

---

* The results described in this chapter have been published in Han, J. W.; Sholl, D. S., *Langmuir* **2009,** 25, 10737-10745.

useful tool for quantitative prediction of these effects that cannot be achieved by using less computationally demanding methods such as classical force fields[16]. DFT calculations have been used to examine chiral adsorption on both flat metal surfaces[17-21] and on stepped metal surfaces that are intrinsically chiral[22-27]. DFT was also used for examining the adsorption of alanine on a chiral face of the mineral calcite[28].

Goumans *et al.* recently reported a careful series of DFT calculations that reexamined the structure and energies of the cleaved, reconstructed, and hydroxylated (0001) α-quartz surfaces[13]. Using the structural information from these calculations, we used DFT to examine the adsorption of methylamine and methanol on hydroxylated α-quartz (0001)[29]. These small molecules are not chiral, but they include amine and hydroxyl groups, two of the important functional groups in amino acids. Our results showed how these small molecules bind to the surface primarily through hydrogen bonds, and provide a useful basis for considering adsorption of multifunctional species such as amino acids on the surface.

In this Chapter, we investigate the adsorption of the amino acids glycine, alanine, serine, and cysteine on the hydroxylated α-quartz (0001) surface using DFT calculations. Aside from their central importance in biochemistry, amino acids can be considered as prototypical multifunctional molecules. The four species we have chosen are among the simplest of all amino acids, which makes a systematic study of their adsorption properties with DFT feasible. Glycine is not chiral, but as the simplest amino acid it is the natural starting point for understanding the adsorption configurations available on the quartz (0001) surface. Alanine is the simplest chiral amino acid, and we show below that adsorption of alanine is strongly analogous to glycine. Serine and cysteine were chosen because they are the simplest amino acids in which the side chain has the potential of hydrogen bonding to the surface. Each of these species, with the exception of glycine, is

chiral, so a focus of our calculations is to explore whether the adsorption of these amino acids on the surface can be enantiospecific. No quantitative information is currently available regarding enantiospecific adsorption of these species on single crystal quartz surfaces, so the aim of our calculations was to determine the strength of these effects among the particular amino acids we examined. In the long run, knowledge of the phenomena that control enantiospecific adsorption on this and other mineral surfaces may provide insights into applications of these surfaces in sensing or separations applications or possible roles of surfaces of this kind in the origins of homochirality in biology.

3.2. Calculation methods

Our plane wave DFT calculations were performed with the Vienna *ab initio* simulation package (VASP) with the ultrasoft pseudopotentials available in this package[30-32]. The results below used the generalized gradient approximation (GGA) with the Perdew-Wang 91[33] functional. All calculations used a plane wave expansion with a cutoff of 396 eV. Geometries were relaxed using a conjugate gradient algorithm until the forces on all unconstrained atoms were less than 0.03 eV/Å.

The previously reported structure[13, 29] was used for construction of the hydroxylated α-quartz (0001) surface. Bulk quartz, which has a hexagonal structure with space group $P3_121$, was constructed using a unit cell with DFT-optimized hexagonal lattice constants, $a = b = 5.056$ Å, $c = 5.561$ Å, in good agreement with the experimental values of $a = b = 4.916$ Å, $c = 5.405$ Å[34]. All surface calculations used supercells defined using the DFT-optimized bulk lattice constants. The surface was represented by a slab ~11 Å thick six O-Si-O layers thick with the bottom three O-Si-O layers constrained in their bulk positions. A vacuum spacing of ~15 Å was used in the direction of the surface normal for all calculations. It is important to note that our calculations correspond to the adsorbed molecules interacting with the hydroxylated surface in a vacuum, not in the presence of a solvent.

In order to avoid the interactions between adsorbates, all our calculations were performed for a coverage corresponding to one molecule per supercell, that is, with an area of 88.6 $Å^2$/molecule for a (2×2) surface unit cell[29]. Our results were computed using a 2×2×1 Monkhorst-Pack *k*-point mesh. Numerical tests confirmed that this sampling of *k* space was sufficient to give well converged results. The geometries of gas phase amino acids were optimized in the supercell of the same size as the surface calculations. When examining adsorption, molecules were placed on only one side of the slab. Dipole corrections were applied in computing all of the energies reported below[35-36].

The adsorption energy, E_{ads}, of a molecule was defined by

$$E_{ads} = \left(E_{surf} + E_{molecule}\right) - E_{total}, \tag{3.1}$$

where E_{total} is the total energy of the system containing the adsorbed amino acid, E_{surf} the total energy for the optimized bare hydroxylated surface, and $E_{molecule}$ the total energy for the amino acid in the gas phase. With this definition, positive adsorption energies correspond to energetically favored states.

The zero point energies associated with H in amino acids and hydroxylated quartz surfaces may not be negligible[29]. To assess the role of zero point energies in Eq. (3.1), the normal modes and vibrational frequencies were calculated within the harmonic approximation using finite difference displacement of 0.03 Å. All atoms in each amino acid and the atoms in the surface hydroxyl groups were the degrees of freedom included in these calculations. Once the normal mode frequencies, v_i, were computed, the zero point energy is defined by $\sum_i \frac{hv_i}{2}$. The adsorption energy including the zero point energies, E_{ads}^{ZP}, is then calculated by

$$E_{ads}^{ZP} = \left(E_{surf} + E_{surf}^{ZP} + E_{molecule} + E_{molecule}^{ZP}\right) - \left(E_{total} + E_{total}^{ZP}\right), \tag{3.2}$$

where E_{total}^{ZP} is the zero point energy of the system containing the adsorbed amino acid, E_{surf}^{ZP} the zero point energy for the optimized bare hydroxylated surface, and $E_{molecule}^{ZP}$ the zero point energy for the amino acid in the gas phase.

In order to characterize the enantiospecificity of adsorption in each example, we used the enantiospecific difference in adsorption energies, defined as the total energy of the most stable structure of the adsorbed *S* enantiomer minus the total energy of the most stable structure of the adsorbed *R* enantiomer[27]. With this definition, a positive value indicates that the *R* enantiomer is more strongly adsorbed to the surface than the *S* enantiomer.

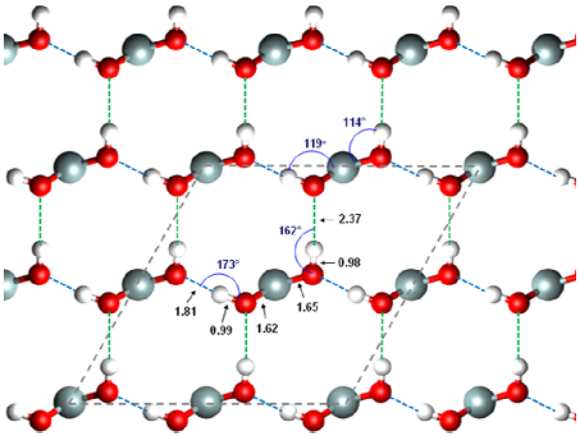

Figure 3.1: Top view of the DFT optimized geometry of the hydroxylated α-quartz (0001) surface, using a (2×2) surface unit cell. For clarity, only surface atoms are shown. Selected bond lengths (in Å) and angles (in degrees) are indicated. Silicon atoms are shown as light gray spheres, oxygen atoms as red spheres and hydrogen atoms as white spheres, respectively. The two distinct types of hydrogen bonds are shown with as green and blue dashed lines. The gray dashed lines indicate the surface unit cell.

The optimized surface structure of hydroxylated α-quartz (0001) found using Goumans *et al.*'s results[13] as initial geometries is shown in Fig. 3.1. This surface structure is in good agreement with previous theoretical observations[5, 13, 15, 29], providing a herringbone structure of Si-$(OH)_2$. For each surface hydroxyl group, two kinds of hydrogen bonds are formed with two nearest hydroxyls on the surface. The bond lengths

of these two hydrogen bonds are quite different; 1.81 and 2.37 Å, respectively. The two distinct hydrogen bonds make the hydroxylated α-quartz (0001) surface nonsuperimposable on its mirror image, imparting chirality into this surface. Several key pieces of structural information for this surface are summarized in Table 3.A.1 of the Appendix 3.A.

3.3. Structures of amino acids adsorption on hydroxylated α-quartz (0001)

3.3.1. Glycine

Glycine, H_2NCH_2COOH, is the simplest amino acid. Unlike all other amino acids, glycine is achiral. It is, however, worthwhile to study the adsorption of glycine on the hydroxylated α-quartz (0001) surface because it will illustrate crucial characteristics of other amino acids on the surface. When amino acids are adsorbed in their globally neutral form, they may exist either as uncharged molecules ($H_2NCHRCOOH$) or as zwitterions ($^{+}H_3NCHRCOO^{-}$)[37]. In the gas phase, most amino acids exist in their uncharged form, whereas in their molecular crystals or in aqueous solutions, they are usually zwitterionic[37-38]. In order to clarify which chemical speciation is more relevant for adsorption on hydroxylated α-quartz (0001), we investigated the adsorption of both uncharged and zwitterionic glycine. We did not examine the configurations available to deprotonated glycine on the surface, a state that is common on metal surfaces where the surface can easily bind individual H atoms[16, 19-20, 24-25, 38-42] but that is unlikely to be relevant on the fully hydroxylated quartz surface. We note in this context that experimental studies of amino acid adsorption on pristine TiO_2 surfaces have shown that a deprotonated molecular state is favored on these surfaces due to the possibility of the H atom from the molecule binding to a surface O atom while the carboxyl groups in the molecule bind with surface Ti atoms in a bidentate fashion[43].

In our previous study[29], we examined the adsorption of methylamine and methanol on hydroxylated α-quartz (0001). These calculations identified three possible sites capable of forming hydrogen bonds with adsorbing molecules; above the longer (weaker) surface hydrogen bond, above the shorter (stronger) surface hydrogen bond, and above the surface disilanols[29]. The resulting hydrogen bonds can potentially form in a tridentate fashion between binding sites on the surface and the N and O atoms of glycine, so the N and O atoms of glycine would face the surface. A challenging aspect of computationally examining molecular adsorption for species such as glycine is that large numbers of adsorption configurations must be examined to have confidence that a global minimum can be identified[22, 26-27]. To address this challenge, we examined configurations for both uncharged and zwitterionic glycine in a systematic way. Specifically, the N atom of glycine was first placed on each possible binding site of the surface and configurations were generated by rotating glycine about this point by increments of 30 degrees. We also examined the adsorption configurations of the mirror images of the glycine states just described without changing the underlying surface. This generates a new set of initial configurations because of the chirality of the surface. In total, therefore, we considered 72 initial configurations for each form of glycine. Each configuration was fully relaxed to find a local energy minimum for the adsorbed molecule.

After calculations from all initial structures, we have found three distinct energy states for zwitterionic glycine. For all the other states, one hydrogen atom in NH_3 group was internally transferred to an oxygen atom in COO group, changing zwitterionic glycine into its uncharged form. The lowest energy structure we observed for zwitterionic glycine on hydroxylated quartz (0001) is shown in Fig. 3.2. In this structure, the three N-H distances are 1.02, 1.05, and 1.07 Å, while the two C-O distances are 1.25 and 1.28 Å, indicating that it is reasonable to describe the adsorbed species as zwitterionic. For uncharged glycine, 24 distinct stable energy states were observed. The total energy difference between the most and least stable configurations was ~0.5 eV. Among these

states, the two most stable structures for neutral glycine are shown in Fig. 3.3. In the most stable of these two structures, the two C-O distances are 1.23 and 1.33 Å, and the N-H distances are 1.02 and 1.03 Å, confirming that it is reasonable to describe the adsorbed molecule as H_2NCH_2COOH.

In their lowest energy states, the total energy of the system with adsorbed uncharged glycine (Fig. 3.3a) is 0.05 eV less than that of the zwitterionic form (Fig. 3.2). Although this energy difference is not large, our previous calculations for methanol and methylamine adsorption on this surface[29] suggest that the zwitterionic species will be slightly further destabilized if zero point energies are taken into account. In fact, when we calculated zero point energies for both uncharged and zwitterionic glycine adsorption, the total energy difference between them was increased to 0.07 eV. We therefore decided to focus the rest of our calculations on the uncharged adsorbed species, and we have not considered adsorption of zwitterionic amino acids in the calculations described in the remainder of this Chapter.

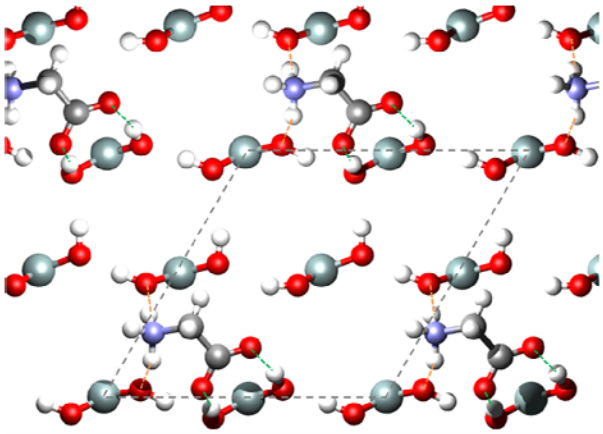

Figure 3.2: Top view of the most stable DFT optimized geometry of absorbed zwitterionic glycine on the hydroxylated α-quartz (0001) surface. For clarity, only surface atoms and adsorbed zwitterionic glycine are shown. In addition to the atoms clarified in Fig. 3.1, carbon atoms are shown as gray spheres and nitrogen atoms as blue spheres, respectively. Several hydrogen bonds are also depicted as green and orange dashed lines. The gray dashed lines indicate the surface unit cell.

The preferred binding site of glycine (Fig. 3.3a) is above the longer hydrogen bond on the bare surface, which is depicted with green dashed lines in Fig. 3.1. This adsorption site is consistent with previous theoretical results for the adsorption of CO[13], H_2O[5], CH_3NH_2[29] and CH_3OH[29] on this surface. During adsorption, two long hydrogen bonds of the bare surface are broken and replaced by four new hydrogen bonds with the carboxyl and amine groups of glycine, respectively. This process causes significant structural deformation of the surface where hydrogen bonds between surface hydroxyls are broken as new hydrogen bonds with the adsorbing molecule are formed. We return to this point in section 3.5. The most stable configuration (Fig. 3.3a) has an adsorption energy of 0.77 eV, while the adsorption energy of the configuration shown in Fig. 3.3b is 0.76 eV. The less stable configuration shown in Fig. 3.3b came from optimization of the initial configuration defined by the mirror image of glycine in Fig. 3.3a. If the zero point energy of each species is included, the adsorption energy defined by Eq. (3.2) decreases to 0.71 eV for the most stable configuration and 0.68 eV for the less stable one, respectively.

In the most stable structure for glycine on the surface, the lengths of two hydrogen bonds involved in the amine group (yellow dashed lines in Fig. 3.3a) are 1.58 Å for $H_{surf}\ldots N_{mole}$ and 2.14 Å for $O_{surf}\ldots H_{mole}$ and those involved in the carboxyl group (green dashed lines in Fig. 3.3a) are 1.85 Å for $H_{surf}\ldots O_{mole}$ and 1.77 Å for $O_{surf}\ldots H_{mole}$, respectively. In case of the less stable structure, the lengths of two hydrogen bonds associated in the amine group (yellow dashed lines in Fig. 3.3b) are 1.56 Å for $H_{surf}\ldots N_{mole}$ and 2.06 Å for $O_{surf}\ldots H_{mole}$ and those involved in the carboxyl group (green dashed lines in Fig. 3.3b) are 1.78 Å for $H_{surf}\ldots O_{mole}$ and 1.92 Å for $O_{surf}\ldots H_{mole}$, respectively. For both states, the lengths of $H_{surf}\ldots N_{mole}$ are very similar to those seen in methylamine adsorption (1.57 Å)[29]. However, the length of $H_{surf}\ldots O_{mole}$ is much longer than that in methanol adsorption (1.53 Å)[29] because both oxygen atoms in carboxyl groups are involved in hydrogen bonding, which makes each oxygen atom less free to

approach to the surface than in the case of methanol. More information about the surface structures of Si-$(OH)_2$ upon glycine adsorption in these two states is available in Table 3.A.1 of the Appendix 3.A. There are 4 different Si-$(OH)_2$ groups in a (2×2) surface unit cell. Each number in Table 3.A.1 corresponds to each Si-$(OH)_2$ group that is also marked in Fig. 3.3.

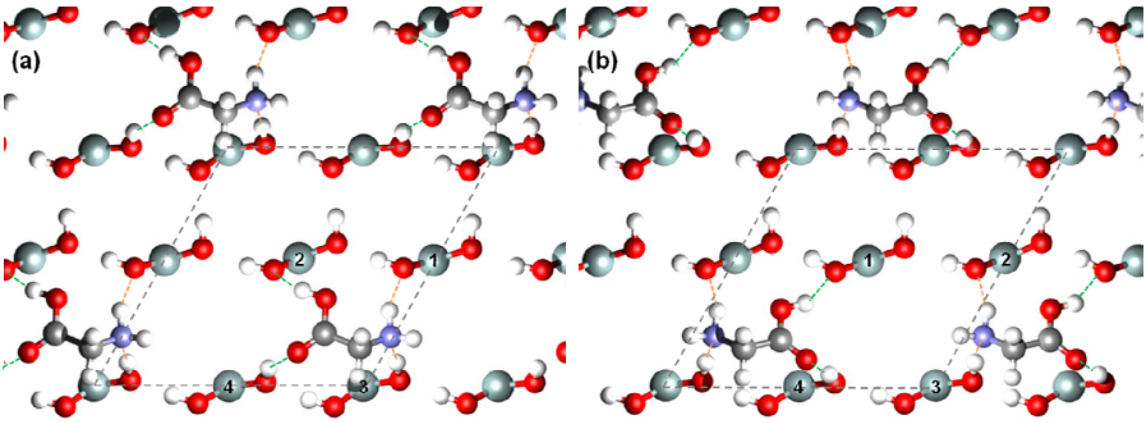

Figure 3.3: Top views of (a) the most stable and (b) a less stable DFT optimized geometry of absorbed uncharged glycine on the hydroxylated α-quartz(0001). The energy difference between two states is 0.01 eV. For clarity, only surface atoms and adsorbed uncharged glycine are shown. Several hydrogen bonds are also depicted as green and orange dashed lines. The gray dashed lines indicate the surface unit cell. The number on each Si-$(OH)_2$ in a surface unit cell corresponds to one in Table 3.A.1 of the Appendix 3.A.

3.3.2. Alanine

Alanine, H_2NCHCH_3COOH, has a methyl group as a substituent group attached to the α-carbon, which makes this molecule chiral. Previous reports demonstrated that when alanine adsorbs onto metal surfaces in its deprotonated form, it has the same tridentate footprint as glycine[21, 39, 44-45]. It is, therefore, reasonable to expect that alanine will bind on hydroxylated α-quartz (0001) in a similar way to glycine, and that any enantiospecificity associated with this binding will be weak.

Initial configurations for finding the most stable configurations of alanine adsorption are constructed based on the ten most stable structures of glycine adsorption. The other 14 less stable structures of glycine adsorption are > 0.3 eV less favored than the most stable one, so we have not used them to make the initial configurations of

alanine adsorption. In the ten configurations, each hydrogen atom attached to the α-carbon in glycine is substituted with methyl group. In total, therefore, 20 initial configurations were examined. After calculations from all initial structures, 20 stable states have been observed; that is, each initial configuration is associated with a distinct stable state. These local minima are direct analogs of the glycine adsorption configurations, with very similar adsorption geometries and energies to those of glycine (see Fig. 3.7 and Table 3.A.1 of the Appendix 3.A).

The most stable structure of *R*-alanine adsorbed on the surface (Fig. 3.4a) is the analog of the most stable configuration for glycine adsorption (Fig. 3.3a), while the most stable structure for *S*-alanine (Fig. 3.4b) is the analog of the slightly less stable glycine configuration shown in Fig. 3.3b. In the most stable *R*-alanine structure, the lengths of two hydrogen bonds involved in the amine group (yellow dashed lines in Fig. 3.4a) are 1.59 Å for $H_{surf}…N_{mole}$ and 2.17 Å for $O_{surf}…H_{mole}$ and those involved in the carboxyl group (green dashed lines in Fig. 3.4a) are 1.87 Å for $H_{surf}…O_{mole}$ and 1.78 Å for $O_{surf}…H_{mole}$, respectively. Here, the length of $H_{surf}…N_{mole}$ is close to the result in methylamine adsorption (1.57 Å)[29], as it is for glycine. In the most stable *S*-alanine structure, the lengths of two hydrogen bonds associated in the amine group (yellow dashed lines in Fig. 3.4b) are 1.61 Å for $H_{surf}…N_{mole}$ and 2.16 Å for $O_{surf}…H_{mole}$ and those involved in the carboxyl group (green dashed lines in Fig. 3.4b) are 1.74 Å for $H_{surf}…O_{mole}$ and 1.86 Å for $O_{surf}…H_{mole}$, respectively. More information about the surface structures of Si-$(OH)_2$ upon the adsorption of the two alanine enantiomers in the most stable configurations is also listed in Table 3.A.1 of the Appendix 3.A.

The adsorption energies of *R*- and *S*-alanine are identical to the energies for glycine in the analogous structures; 0.77 eV (0.76 eV) for *R*-alanine (*S*-alanine). The geometric and energetic similarities between alanine and glycine adsorption indicate that the methyl group of alanine does not have a distinct effect on its adsorption to the surface. If zero point energies are included, the adsorption energies are changed to 0.71

eV (0.69 eV) for *R*-alanine (*S*-alanine). These results show that adsorption of alanine on this surface exhibits very weak, if any, enantiospecificity.

3.3.3. Serine

Serine, $H_2NCHCH_2OHCOOH$, has a CH_2OH group as a side chain attached to the α-carbon. This OH group can potentially offer one more opportunity for hydrogen bonding with the surface than in alanine. Initial configurations were constructed using the nine most stable adsorbed structures of glycine, with an H atom on the α-carbon replaced with a CH_2OH group for each configuration. Three distinct OH positions in the CH_2OH were considered for each structure in case this group is not able to rotate freely. In addition, initial configurations defined by the mirror images of the serine configurations just described were examined. This gave 54 initial configurations of serine on the surface. Our calculations from these initial structures showed that there are 18 distinct energy states that are each associated with the most stable OH position among three initial positions in the CH_2OH.

The most stable structures for *R*- and *S*-serine observed from these calculations are shown in Fig. 3.5a and b, respectively. For both enantiomers, the hydroxyl group in a side chain forms a hydrogen bond with the surface, but the molecule's amine group does not participate in the hydrogen bond with the surface. In the most stable structure of *R*-serine adsorption, the lengths of the two hydrogen bonds involved in the carboxyl group (green dashed lines in Fig. 3.5a) are 1.68 Å for $H_{surf}\ldots O_{mole}$ and 1.87 Å for $O_{surf}\ldots H_{mole}$ and those involved in the hydroxyl group (yellow dashed lines in Fig. 3.5a) are 1.66 Å for $H_{surf}\ldots O_{mole}$ and 1.69 Å for $O_{surf}\ldots H_{mole}$, respectively. In the most stable configuration of *S*-serine adsorption, the lengths of the two hydrogen bonds involved in the carboxyl group (green dashed lines in Fig. 3.5b) are 1.72 Å for both $H_{surf}\ldots O_{mole}$ and $O_{surf}\ldots H_{mole}$ and those involved in the hydroxyl group (yellow dashed lines in Fig. 3.5b) are 1.64 Å for $H_{surf}\ldots O_{mole}$ and 1.73 Å for $O_{surf}\ldots H_{mole}$, respectively. For both configurations, the

bond lengths of $H_{surf}\ldots O_{mole}$ involved in the hydroxyl groups are shorter than those associated with the carboxyl groups observed in glycine, alanine, and serine adsorption, indicating that the bonding fashion of the serine's hydroxyl group in this configuration is similar to that of methanol[29]. More information about the surface hydroxyl structures upon the adsorption of the two serine enantiomers in their most stable states is also available in Table 3.A.1 of the Appendix 3.A.

The adsorption energy of *R*-serine in its most preferred configuration (Fig. 3.5a) is 0.89 eV, while the adsorption energy of *S*-serine in its most stable structure (Fig. 3.5b) is 0.94 eV. These are the highest adsorption energies among the amino acids we have examined on this surface. If the definition of the enantiospecificity mentioned above is applied here, the enantiospecific energy difference between enantiomers of serine is -0.05 eV. When we consider the effect of the zero point energies, the adsorption energies are reduced to 0.79 eV (0.87 eV) for *R*-serine (*S*-serine), increasing the enantiospecific energy different to -0.08 eV.

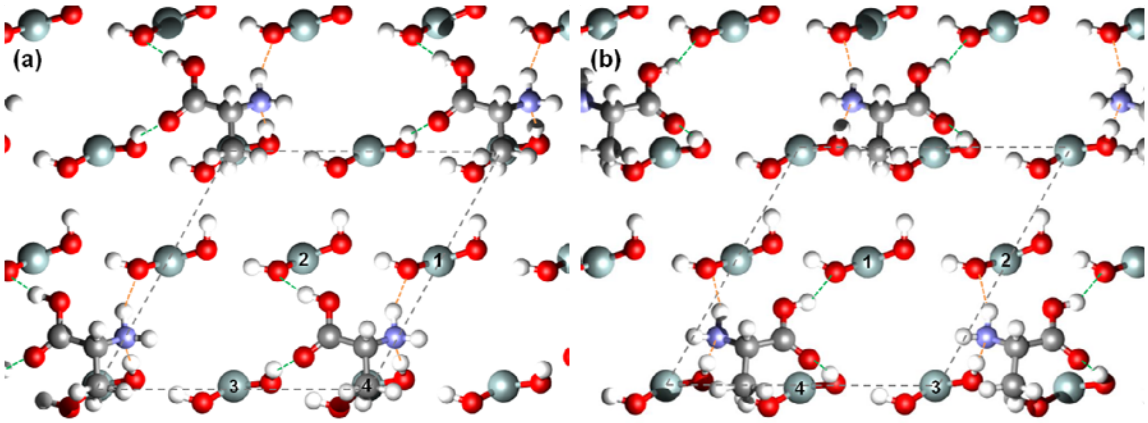

Figure 3.4: Top views of the most stable DFT optimized geometry of absorbed (a) *R*- and (b) *S*-alanine on the hydroxylated α-quartz (0001) surface, which provide similar configurations as Fig. 1 (a) and (b) except CH_3 group attached to α-carbon instead of H, respectively. For clarity, only surface atoms and adsorbed alanine are shown. Several hydrogen bonds are also depicted as green and orange dashed lines. The gray dashed lines indicate the surface unit cell. The number on each Si-$(OH)_2$ in a surface unit cell corresponds to one in Table 3.A.1 of the Appendix 3.A.

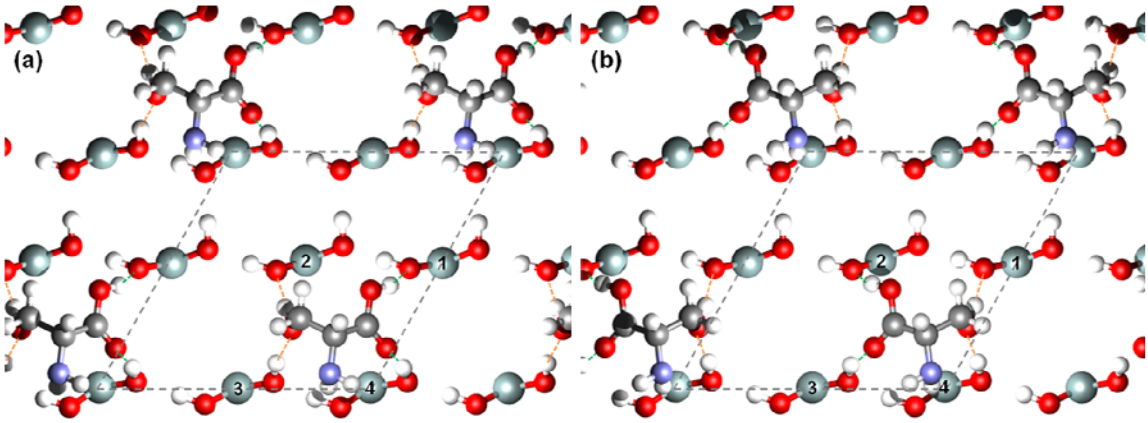

Figure 3.5: Top views of the DFT optimized geometry of absorbed (a) *R*- and (b) *S*-serine on the hydroxylated α-quartz (0001) surface. For clarity, only surface atoms and adsorbed serine are shown. Several hydrogen bonds are also depicted as green and orange dashed lines. The gray dashed lines indicate the surface unit cell. Note that N attached to α-carbon of serine does not participate in hydrogen bonding with the surface. The number on each Si-$(OH)_2$ in a surface unit cell corresponds to one in Table 3.A.1 of the Appendix 3.A.

The second most stable configuration of each enantiomer of serine is similar to the most favored structures except that the N atom in amine group attached to α-carbon of serine does take part in hydrogen bonding with an H of the surface hydroxyl beneath the amine group. In a simplistic description of surface bonding, it might be expected that the adsorption energy is correlated to the number of bonds with the surface; this is not correct in this case. Even though there are more hydrogen bonds to the surface in the less stable configurations than in the most stable ones, the adsorption energies are decreased to 0.67 eV (0.70 eV) for *R*-serine (*S*-serine).

3.3.4. Cysteine

Cysteine, $H_2NCHCH_2SHCOOH$, has a CH_2SH group attached to its α-carbon. Cysteine adsorption has been studied on Au, Ag, Cu, and Pd and is driven on these surfaces by the strong affinity of a thiol group for metal atoms.[46-52] As we will show, the situation is quite different on a surface like quartz where binding is driven by the formation of hydrogen bonds. Similarly to serine, a SH group may have some

contribution to the adsorption on the surface via hydrogen bonding. We constructed the initial configurations of cysteine adsorption using the structures from 14 local minima of serine adsorption in Sec. 3.3.3, in each case replacing the hydroxyl group in the serine side chain with a thiol group. We have not used the other less stable 4 local minimum structures as the initial configurations because those are much less favored than the most stable one (> ~0.4 eV). These 14 initial configurations gave 14 distinct local minima for cysteine after optimization.

The most stable structures for each enantiomer on the surface are shown in Fig. 3.6. Interestingly, each enantiomer has two distinct adsorption configurations with essentially identical energy. Both states for each cysteine enantiomer are shown in Fig. 3.6. It is noteworthy that for these structures the sulfur atom is quite distant from the surface, so the thiol group cannot participate in the hydrogen bond with the surface. This occurs due to the large size of a sulfur atom, which does not allow a thiol group to fit on the binding site. Because adsorption occurs via hydrogen bonds of the amine and the carboxyl groups with the surface, cysteine adsorption can be regarded as analogous to glycine or alanine adsorption. In one (the other) of the structures of *S*-cysteine shown in Fig. 3.6, the lengths of the two hydrogen bonds involved in the amine group (yellow dashed lines in Fig. 3.6a (3.6c)) are 1.54 Å (1.60 Å) for $H_{surf}\ldots N_{mole}$ and 2.06 Å (2.16 Å) for $O_{surf}\ldots H_{mole}$ and those involved in the carboxyl group (green dashed lines in Fig. 3.6a (3.6c)) are 1.75 Å (1.87 Å) for $H_{surf}\ldots O_{mole}$ and 1.82 Å (1.76 Å) for $O_{surf}\ldots H_{mole}$, respectively. For the two structures of *R*-cysteine in Fig. 3.6, the lengths of the two hydrogen bonds associated in amine group (yellow dashed lines in Fig. 3.6b (3.6d) are 1.59 Å (1.63 Å) for $H_{surf}\ldots N_{mole}$ and 2.28 Å (2.14 Å) for $O_{surf}\ldots H_{mole}$ and those involved in the carboxyl group (green dashed lines in Fig. 3.6b (3.6d)) are 1.82 Å (1.75 Å) for $H_{surf}\ldots O_{mole}$ and 1.72 Å (1.85 Å) for $O_{surf}\ldots H_{mole}$, respectively. Similarly to glycine or alanine adsorption, for all of these states, the lengths of $H_{surf}\ldots N_{mole}$ also show good agreement with that in methylamine adsorption (1.57 Å)[29]. Table 3.A.1 of the Appendix

3.A lists the structural information for the surface hydroxyls upon the adsorption of these two pairs of cysteine enantiomers.

The adsorption energies of *S*-cysteine (*R*-cysteine) in the two most stable structures are 0.862 and 0.860 eV (0.821 and 0.816 eV), respectively. The enantiospecific energy difference for cysteine adsorption is, therefore, -0.04 eV. If the zero point energy of each species is included, the adsorption energies are decreased to 0.777 and 0.782 eV (0.742 and 0.735 eV) for *S*-cysteine (*R*-cysteine) in the two most stable structures, respectively. In this case, their enantiospecificities are slightly split into -0.035 eV (between Figs. 3.6a and b) and -0.047 eV (between Figs. 3.6c and d), respectively.

3.4. Enantiospecific adsorption of amino acids on hydroxylated α-quartz (0001)

In this section, we further discuss the enantiospecificity of amino acid adsorption on hydroxylated α-quartz (0001). Because glycine is not chiral, there is no enantiospecific adsorption of glycine on the surface. As we discussed above, the difference between adsorption energies of *R*- and *S*-alanine in their lowest energy states is less than 0.01 eV. For serine adsorption, however, there is a significant energy difference between the lowest energy states of the two enantiomers, as the binding of *S*-serine to the surface (neglecting zero point energies) is 0.05 eV stronger than the binding of *R*-serine. Cysteine adsorption is also enantiospecific by 0.04 eV by this definition, with *S*-cysteine adsorbing more strongly than *R*-cysteine. These differences are the meaningful enantiospecific adsorption energy differences when compared to the previous theoretical and experimental studies in related systems[22-23, 26-28, 53-56]. For example, Gellman *et al.* identified differences in the adsorption energies of ~0.010 eV for *R*-3-methyl cyclohexanone on Cu(643)$^{R\&S}$ using temperature programmed desorption experiments performed in ultra-high vacuum[57]. Attard *et al.* used electro-oxidation of D- and L-glucose on Pt{643}^{S} to obtain the enantiospecificity of ~0.015 eV[53]. The largest

enantiospecific energy difference that has been reported to date is 0.14 eV for the adsorption of cysteine on Au(17 11 9), a result obtained using DFT calculations[23].

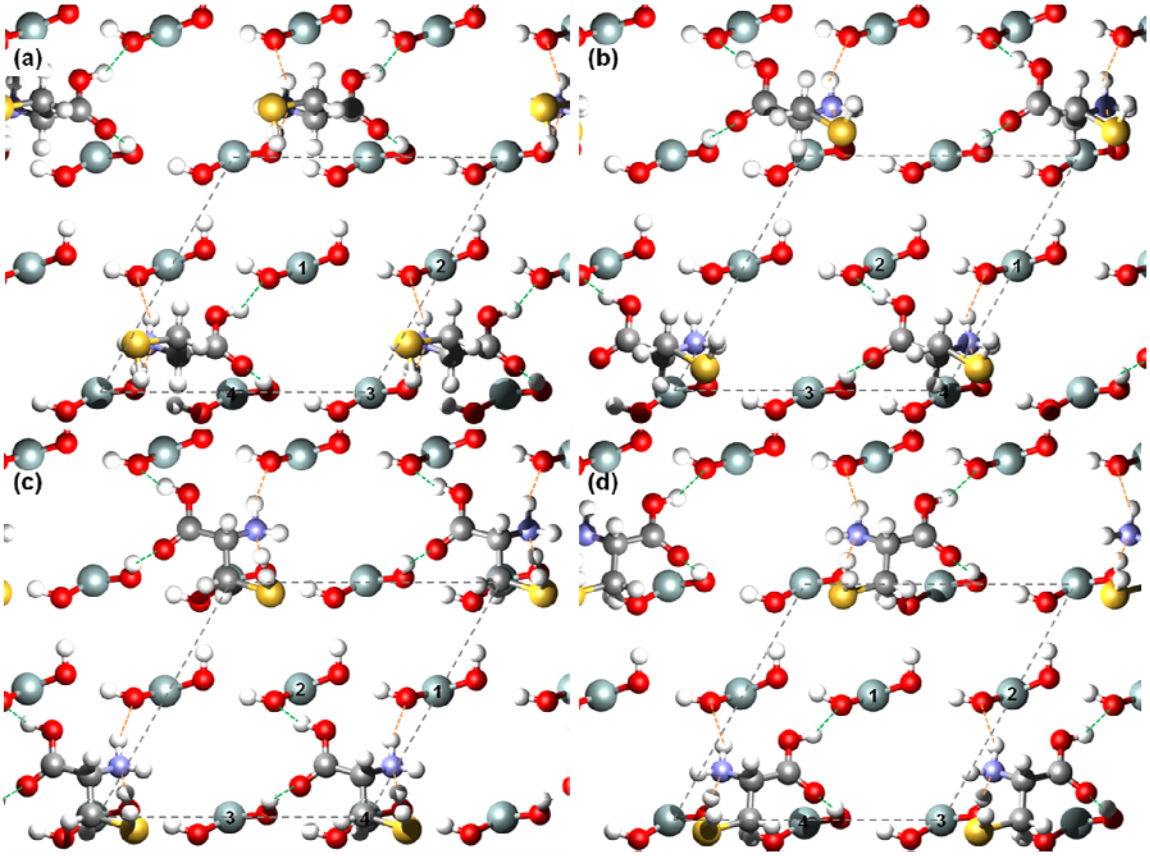

Figure 3.6: Top views of the DFT optimized geometries of absorbed (a), (c) *S*- and (b), (d) *R*-cysteine on the hydroxylated α-quartz (0001) surface. *S*-cysteine in (a) and (c) and *R*-cysteine in (b) and (d) are in the almost same lowest energy states, respectively. For clarity, only surface atoms and adsorbed serine are shown. In addition to the atoms clarified in previous figures, sulfur atoms are shown as yellow spheres. Several hydrogen bonds are also depicted as green and orange dashed lines. The gray dashed lines indicate the surface unit cell. Note that in all cases, S in a side chain tends to be far from the surface due to the steric effects. The number on each Si-$(OH)_2$ in a surface unit cell corresponds to one in Table 3.A.1 of the Appendix 3.A.

The origin of the enantiospecific binding of serine can be explained as follows. Both enantiomers bind to the surface in the same fashion; they break two hydrogen bonds of the bare surface and form four new hydrogen bonds. When we concentrate on the carboxyl and CH_2OH group of serine, each group approaches a binding site to make two new hydrogen bonds in the opposite direction relative to the long hydrogen bond of bare

surface. For the two enantiomers, the adsorption structure of *R*-serine is equivalent to the structure for *S*-serine for which the carboxyl group in *S*-serine exchanges its position with the CH_2OH group, and vice versa. In this process, the constraints of the molecule and the surface do not allow the functional groups in *R*-serine to bind as strongly as in *S*-serine. The enantiospecificity of cysteine adsorption cannot be explained in such a simplistic way; as we show in the next section there are multiple contributions to the overall adsorption energy that combine to create the energy differences that exist between the adsorbed enantiomers of this molecule.

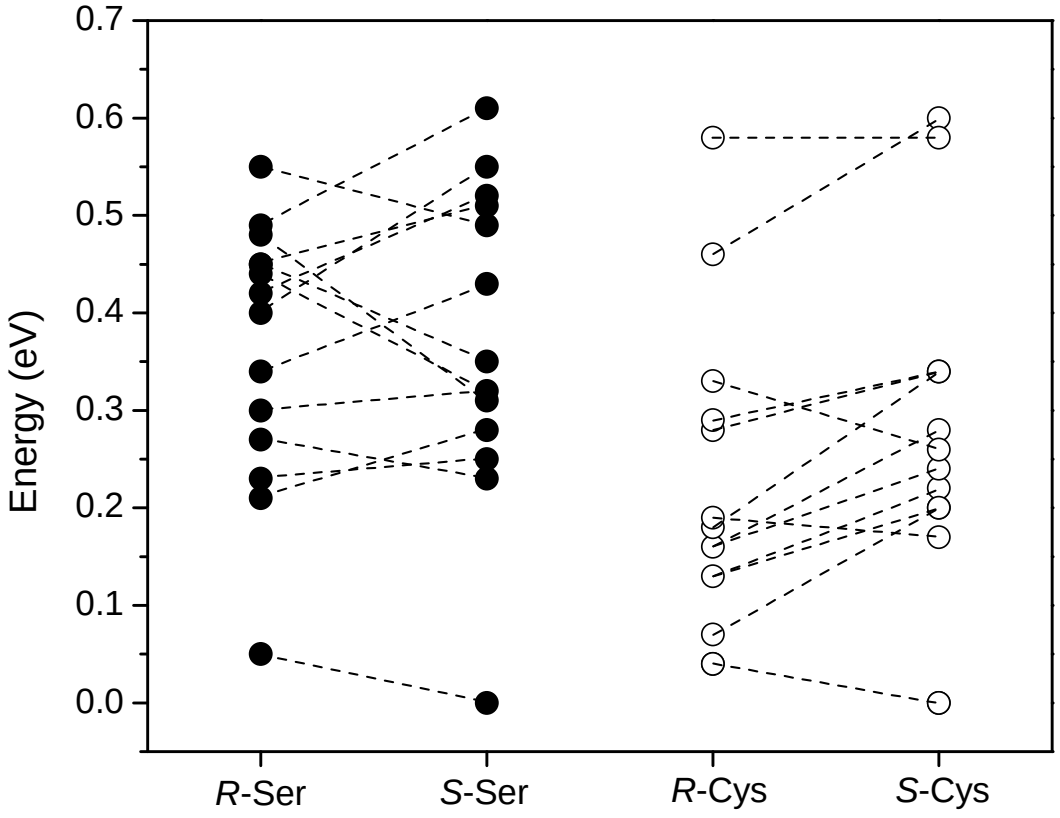

Figure 3.7: Energies of the distinct local minima observed for serine and cysteine adsorbed on the hydroxylated α-quartz (0001) surface measured relative to the energy of the most favorably bound configuration of either enantiomer of the species of interest.

The discussion above has focused on the energy differences between the lowest energy states of the adsorbed enantiomers. As we have shown, however, multiple local minima exist on the surface for the two enantiomers of both serine and cysteine. Figure 3.7 shows the energies of 14 energy minima for each adsorbed enantiomer of serine and cysteine. Zero point energies were not included in this figure. An important feature of this figure is that we can directly associate each configuration for the *R*-enantiomer with a configuration that has the same structure on the surface but exists for the molecule's *S*-enantiomer. These associations are shown with dashed lines in Fig. 3.7, and provide evidence that we have not missed local minima of one of the adsorbed enantiomers in our examination of the complicated potential energy surface defined by these adsorbed molecules.

Experimental measurements of the molecular binding energy typically probe a thermal average of the available minima. Thus, it would be more experimentally relevant to include these effects when we consider the enantiospecificity of adsorption. Fortunately, it is possible to consider these effects in a straightforward way once the set of local minima are available for each enantiomer. We will denote the energy states in Fig. 3.7 for the two enantiomers of a molecule as $E_i^{R(S)}$ $\left(i = 1,2,3,\cdots\right)$. Using ideas from statistical perturbation theory[58-60], the difference in free energy between the adsorbed *R*- and *S*-enantiomer on the surface is rigorously given by[58, 61]

$$A^R - A^S = \Delta A^{R/S} = -kT \ln \left\langle e^{-\left(E^R - E^S\right)/kT} \right\rangle_S , \tag{3.3}$$

where $\left\langle \cdots \right\rangle_S$ represents a canonical average over states of enantiomer *S*. If we treat each enantiomer as having only a series of discrete energy states on the surface, Eq. (3.3) can be rewritten after some algebra as

$$\Delta A^{R/S} = \left(E_{\min}^R - E_{\min}^S\right) - kT \ln \left(\frac{\sum_i e^{-\Delta E_i^R/kT}}{\sum_i e^{-\Delta E_i^S/kT}} \right), \tag{3.4}$$

where $E_{\min}^{R(S)}$ is the minimum energy of each enantiomer and $\Delta E_i^{R(S)}$ is defined for each state as $\Delta E_i^{R(S)} = E_i^{R(S)} - E_{\min}^{R(S)}$. In the limit of low temperatures, this free energy difference is exactly the energy difference between the minimum energy states of the two enantiomers, as would be expected.

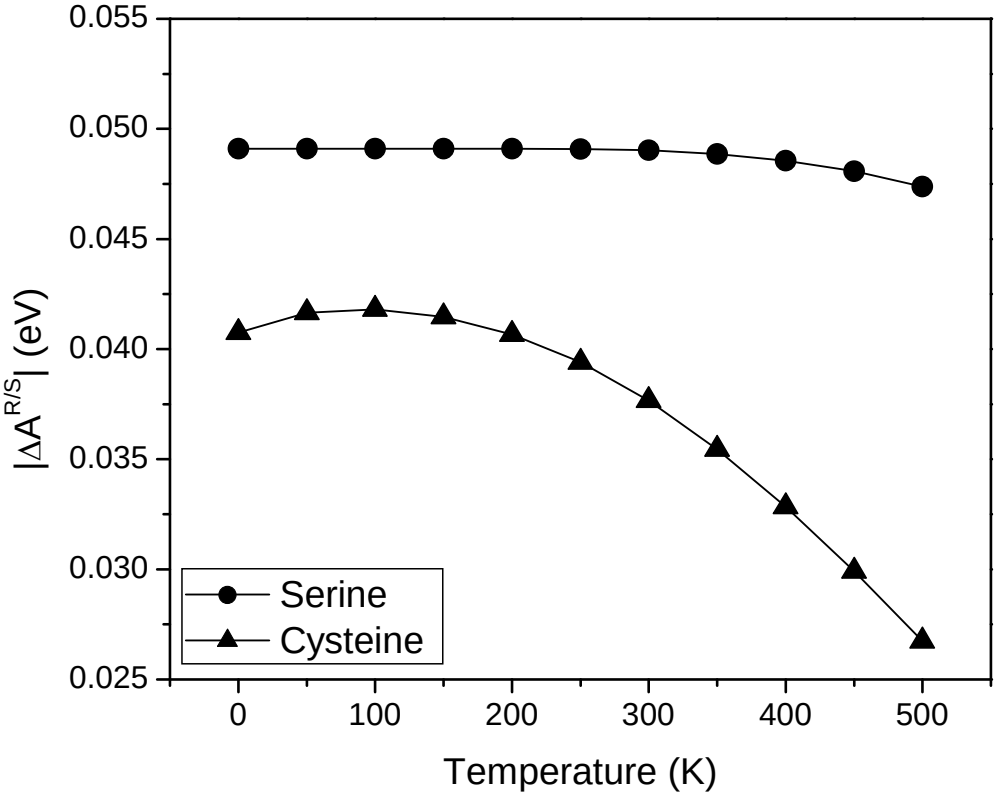

Figure 3.8: The absolute values of enantiospecificity including thermal average of the available minima as a function of temperature.

Figure 3.8 shows the results of Eq. (3.4) for cysteine and serine on quartz (0001) in terms of the absolute values of the free energy difference between adsorbed enantiomers, $\left|\Delta A^{R/S}\right|$. For both molecules, the energy difference between the minimum energy states is a very good approximation to the full free energy difference at all temperatures below room temperature. The enantiospecificity of binding for each amino

acid decreases as the temperature increases in the range of 0 to 500 K. This is not an inevitable consequence of Eq. (3.4); other systems may exist where the enantiospecificity increases with increasing temperature. The temperature effects for serine are weak, with the free energy difference only changing by 0.002 eV between 0 and 500 K. The temperature dependence for cysteine is stronger with the free energy difference changing by more than 0.014 eV as the temperature is increased from 0 to 500 K. This outcome can be understood be examining the distribution of energy states available to each enantiomer of cysteine. As can be seen in Fig. 3.7, the several lowest energy levels available for *R*-cysteine are lower than *S*-cysteine except for the minimum energy state of the *S*-enantiomer. As temperature increases, therefore, the thermal average over these minima reduces the enantiospecificity seen at 0 K favoring *S*-cysteine.

3.5. Contributions to the adsorption energy

Using Eq. (3.1) in Sec. 3.2, we calculated the adsorption energies of amino acids on the hydroxylated α-quartz (0001). Here, we describe a decomposition of the adsorption energy to examine how different physical aspects of the adsorption process contribute to the adsorption energy[17, 19, 29]. We computed the energy required for surface deformation by calculating the difference between the total energy of the optimized structure of the bare surface and the surface in the same geometry as the adsorbed structure but with no amino acid present. The deformation energy of amino acids upon the adsorption was similarly computed from the energy difference between amino acids with the structure defined by the adsorbed state and the minimum energy structure of a gas phase. The strength of the surface binding was then defined as the difference between the net adsorption energy and the net deformation energy[17, 19, 29]. The surface binding energy defined in this way is larger in magnitude that the net adsorption energy because of the unfavorable nature of the deformation energies. It is important to note that it is the adsorption energy that would be experimentally accessible via Temperature Programmed

Desorption or similar methods. The absolute values of the adsorption energies and the contributions to these energies of amino acids we have studied are summarized in Fig. 3.9. All configurations shown in Fig. 3.3-3.6 are represented in Fig. 3.9.

The adsorption energies for glycine and alanine are similar to each other, as stated above. For both species, the surface deformation energies are ~0.5 eV, while the molecular deformation energies are ~0.3 eV. For the adsorption of amino acids on this quartz surface, the surface hydroxyls deform substantially to form hydrogen bonds with the adsorbing molecule. Because of this, the surface deformation energies play an important role in the overall adsorption energy, unlike the adsorption of amino acids on metal surfaces such as Cu(110) and Cu(100), where surface deformation plays only a minor role[19-21]. For the most stable serine structures, the observed adsorption energies are increased compared to glycine and alanine.

Serine has the largest net adsorption energies of all the amino acids we have examined. The deformation energies for the surface and molecule are both ~0.35 eV for serine. This situation is different to the outcome for alanine and glycine, where the surface deformation energy is markedly larger than the molecule's deformation energy. It is clear from the results in Fig. 3.9 that the enantiospecificity in adsorption of serine on this surface is associated with the formation of hydrogen bonds with the surface, as mentioned in the previous section. In Section 3.3.3, we discussed the adsorption of serine in the second most stable configurations that formed a larger number of hydrogen bonds with the surface than the molecule adsorbed in its lowest energy state. The surface deformation energies for these configurations are much larger than these energies for the most stable configurations, so the energetic cost of this deformation is larger than the benefit of forming the additional hydrogen bonds.

In the case of the most stable cysteine configurations, the decomposition of the adsorption energy is reasonably similar to alanine and glycine, with the surface deformation playing a larger role than deformation of the adsorbate. It is interesting to

note that the contributions to the total adsorption energy of the two configurations of *R*-cysteine shown in Fig. 3.9 are quite different, even though the net adsorption energy of these configurations is essentially identical. The same observation also holds for the two *S*-cysteine configurations shown in Fig. 3.9. The results in Fig. 3.9 illustrate our statement in the previous section that it is not possible to attribute the enantiospecificity of adsorption for cysteine to a single contribution to the overall adsorption energy.

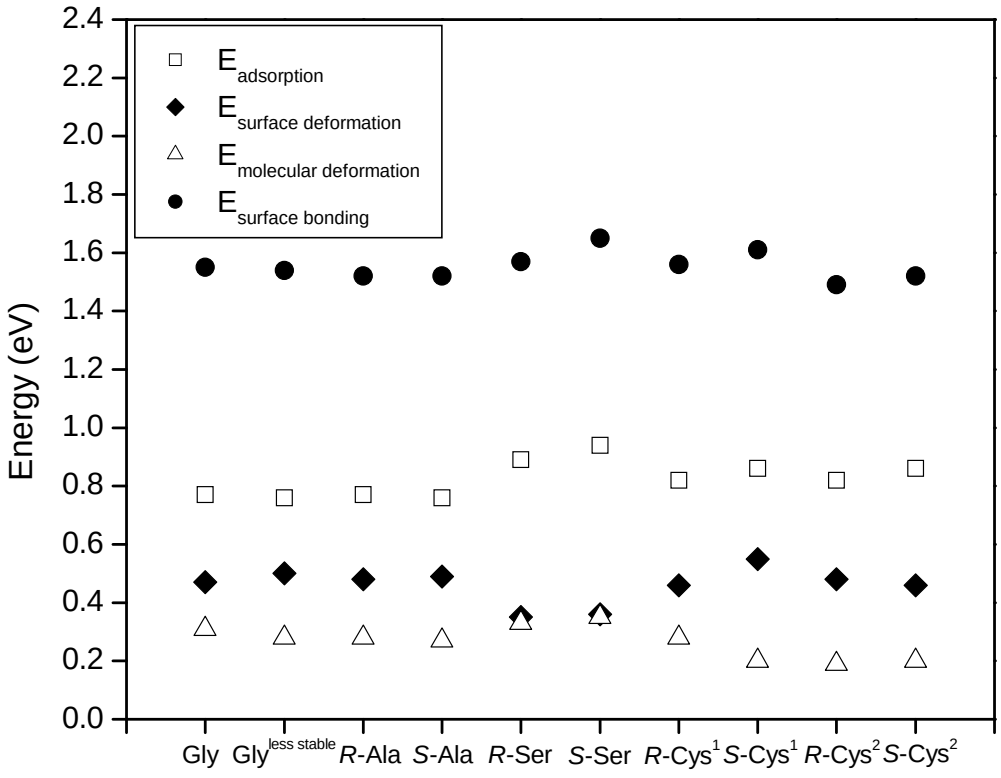

Figure 3.9: The adsorption energies of amino acids and their decomposed energies into surface deformation, molecular deformation, and surface bonding in their absolute values. Two different configurations with equal adsorption energy for each *R*- and *S*-cysteine are marked as superscript 1 and 2.

3.6. Conclusion

We have examined the adsorption of glycine, alanine, serine, and cysteine on hydroxylated α-quartz (0001) using DFT calculations. In order to find the most favorable

configurations of amino acids upon the adsorption, a large number of local minima have been investigated for each molecule. These results give the first information from DFT calculations regarding the adsorption of amino acids on this surface. Our calculations are suitable for considering the configurations of these molecules in experiments under vacuum conditions, since no solvent is present in the calculations. Our initial calculations with glycine indicated this amino acid binds with slightly higher adsorption energies in its neutral state than in a zwitterionic state. We therefore restricted our attention to the neutral states of the other amino acids on the surface. As for glycine, local minima for alanine, serine, and cysteine in a zwitterionic form can also be defined on the surface, and the methods that we have used could be extended to characterize these states.

Adsorption of glycine in its most energetically preferred sites occurs by breaking two of the hydrogen bonds that exists on the bare surface and creating four hydrogen bonds between the surface and the adsorbed molecule. The adsorption of alanine is strongly analogous to glycine, and we found negligible differences in adsorption energies between the two enantiomers of alanine. By contrast, we computed meaningful differences in adsorption energy between the enantiomers of serine and cysteine on the surface. In the adsorption of serine, the molecule binds to the surface via hydrogen bonding involving the CH_3OH side chain but not the molecule's amine group in its most favored adsorption configuration. When cysteine adsorbs on the surface, the sulfur atom tends to be distant from the surface due to its steric effects. We found that in the most stable states**,** *S*-serine binds to the surface stronger than the *R*-serine by 0.05 eV while *S*-cysteine adsorbs stronger than the *R*-cysteine by 0.04 eV. These energy differences are smaller than the largest enantiospecific energy differences that have been reported in previous DFT studies on other chiral surfaces: 0.14 eV for the adsorption of cysteine on Au(17 11 9)[23] and 0.13 eV for the adsorption of amino-(fluoro)methoxy on Cu(874)[26].

When we consider enantiospecific energy differences at finite temperature, a thermal average over multiple states should be considered. We have introduced a simple

method to define this average that has a well defined meaning in terms of adsorption free energies. Our results, however, showed that the enantiospecificity at 0 K is a useful value for characterizing this phenomenon because the effects of other energy minima at experimentally relevant temperatures are small.

Our results suggest that the other amino acids which have the side chains accessible to hydrogen bonding, such as aspartic acid and threonine, may have some enantiospecificity on this surface. For the future study, it would also be interesting to examine the adsorption of amino acids on other α-quartz surfaces, such as $(10\bar{1}0)$ and $(11\bar{2}0)$, in order to understand the potential for these surfaces to exhibit enantiospecific adsorption.

References

(1) de Leeuw, N. H.; Higgins, F. M.; Parker, S. C., *J. Phys. Chem. B* **1999,** 103, 1270-1277.
(2) Du, M.-H.; Kolchin, A.; Cheng, H.-P., *J. Chem. Phys.* **2004,** 120, 1044-1054.
(3) Du, Z.; de Leeuw, N. H., *Dalton Trans.* **2006**, 2623-2634.
(4) Li, I.; Bandara, J.; Shultz, M. J., *Langmuir* **2004,** 20, 10474-10480.
(5) Yang, J.; Wang, E. G., *Phys. Rev. B* **2006,** 73, 035406.
(6) Hazen, R. M., *Am. Mineral.* **2006,** 91, 1715-1729.
(7) Hazen, R. M.; Sholl, D. S., *Nat. Mater.* **2003,** 2, 367-374.
(8) Bonner, W. A.; Kavasmaneck, P. R.; Martin, F. S.; Flores, J. J., *Science* **1974,** 186, 143-144.
(9) Karagounis, G.; Coumonlos, G., *Nature* **1938,** 142, 162-163.
(10) Tsuchida, R.; Kobayashi, M.; Nakamura, A., *J. Chem. Soc. Jpn* **1935,** 56, 1339.
(11) Soai, K.; Osanai, S.; Kadowaki, K.; Yonekubo, S.; Shibata, T.; Sato, I., *J. Am. Chem. Soc.* **1999,** 121, 11235-11236.
(12) Dana, E. S., *Manual of Mineralogy*. John Wiley & Sons: London, 1941.
(13) Goumans, T. P. M.; Wander, A.; Brown, W. A.; Catlow, C. R. A., *Phys. Chem. Chem. Phys.* **2007,** 9, 2146-2152.
(14) Murashov, V. V., *J. Phys. Chem. B* **2005,** 109, 4144-4151.
(15) Rignanese, G.-M.; Charlier, J.-C.; Gonze, X., *Phys. Chem. Chem. Phys.* **2004,** 6, 1920-1925.
(16) James, J. N.; Sholl, D. S., *Curr. Opin. Colloid Interface Sci.* **2008,** 13, 60-64.
(17) Barbosa, L. A. M. M.; Sautet, P., *J. Am. Chem. Soc.* **2001,** 123, 6639-6648.
(18) Jones, G.; Jenkins, S. J.; King, D. A., *Surf. Sci.* **2006,** 600, L224-L228.
(19) Rankin, R. B.; Sholl, D. S., *Surf. Sci.* **2004,** 548, 301-308.
(20) Rankin, R. B.; Sholl, D. S., *J. Phys. Chem. B* **2005,** 109, 16764-16773.
(21) Rankin, R. B.; Sholl, D. S., *Surf. Sci.* **2005,** 574, L1-L8.
(22) Šljivancanin, Ž.; Gothelf, K. V.; Hammer, B., *J. Am. Chem. Soc.* **2002,** 124, 14789-14794.
(23) Greber, T.; Šljivancanin, Ž.; Schillinger, R.; Wider, J.; Hammer, B., *Phys. Rev. Lett.* **2006,** 96, 056103.
(24) Rankin, R. B.; Sholl, D. S., *Langmuir* **2006,** 22, 8096-8103.
(25) Rankin, R. B.; Sholl, D. S., *J. Chem. Phys.* **2006,** 124, 074703.
(26) Bhatia, B.; Sholl, D. S., *Angew. Chem. Int. Ed.* **2005,** 44, 7761-7764.
(27) Bhatia, B.; Sholl, D. S., *J. Chem. Phys.* **2008,** 128, 144709-1~144709-9.
(28) Asthagiri, A.; Hazen, R. M., *Mol. Simulat.* **2007,** 33, 343-351.
(29) Han, J. W.; James, J. N.; Sholl, D. S., *Surf. Sci.* **2008,** 602, 2478-2485.
(30) Kresse, G.; Furthmuller, J., *Phys. Rev. B* **1996,** 54, 11169-11186.
(31) Kresse, G.; Hafner, J., *Phys. Rev. B* **1993,** 47, 558-561.
(32) Kresse, G.; Hafner, J., *J. Phys.: Condens. Matter* **1994,** 6, 8245-8257.
(33) Perdew, J. P.; Chevary, J. A.; Vosko, S. H.; Jackson, K. A.; Pederson, M. R.; Singh, D. J.; Fiolhais, C., *Phys. Rev. B* **1992,** 46, 6671-6687.
(34) Levien, L.; Prewitt, C. T.; Weidner, D. J., *Am. Mineral.* **1980,** 65, 920.
(35) Neugebauer, J.; Scheffler, M., *Phys. Rev. B* **1992,** 46, 16067.
(36) Bengtsson, L., *Phys. Rev. B* **1999,** 59, 12301.

(37) Lambert, J.-F., *Orig. Life Evol. Biosph.* **2008,** 38, 211-242.
(38) Barlow, S. M.; Raval, R., *Surf. Sci. Rep.* **2003,** 50, 201-341.
(39) Barlow, S. M.; Raval, R., *Curr. Opin. Colloid Interface Sci.* **2008,** 13, 65-73.
(40) Nyberg, M.; Hasselstrom, J.; Karis, O.; Wassdahl, N.; Weinelt, M.; Nilsson, A.; Pettersson, L. G. M., *J. Chem. Phys.* **2000,** 112, 5420-5427.
(41) Nyberg, M.; Odelius, M.; Nilsson, A.; Pettersson, L. G. M., *J. Chem. Phys.* **2003,** 119, 12577-12585.
(42) James, J. N.; Sholl, D. S., *J. Mol. Catal. A: Chem.* **2008,** 281, 44-48.
(43) Fleming, G. J.; Adib, K.; Rodriguez, J. A.; Barteau, M. A.; Idriss, H., *Surf. Sci.* **2007,** 601, 5726-5731.
(44) Barlow, S. M.; Louafi, S.; Le Roux, D.; Williams, J.; Muryn, C.; Haq, S.; Raval, R., *Surf. Sci.* **2005,** 590, 243.
(45) Haq, S.; Massey, A.; Moslemzadeh, N.; Robin, A.; Barlow, S. M.; Raval, R., *Langmuir* **2007,** 23, 10694-10700.
(46) Ihs, A.; Lieberg, B., *J. Colloid Interface Sci.* **1991,** 144, 282.
(47) Kuhnle, A.; Linderoth, T. R.; Hammer, B.; Besenbacher, F., *Nature* **2002,** 415, 891-893.
(48) Kuhnle, A.; Linderoth, T. R.; Schunack, M.; Besenbacher, F., *Langmuir* **2006,** 22, 2156.
(49) Kuhnle, A.; Molina, L. M.; Linderoth, T. R.; Hammer, B.; Besenbacher, F., *Phys. Rev. Lett.* **2004,** 93, 086101.
(50) Lopez-Lozano, X.; Perez, L. A.; Garzon, I. L., *Phys. Rev. Lett.* **2006,** 97, -.
(51) Marti, E. M.; Methivier, C.; Pradier, C. M., *Langmuir* **2004,** 20, 10223.
(52) Santos, E.; Avalle, L. B.; Scurtu, R.; Jones, H., *Chem. Phys.* **2007,** 342, 236.
(53) Attard, G. A.; Ahmadi, A.; Feliu, J.; Rodes, A.; Herrero, E.; Blais, S.; Jerkiewicz, G., *J. Phys. Chem. B* **1999,** 103, 1381-1385.
(54) Sholl, D. S., *Langmuir* **1998,** 14, 862-867.
(55) Horvath, J. D.; Gellman, A. J., *J. Am. Chem. Soc.* **2001,** 123, 7953-7954.
(56) McFadden, C. F.; Cremer, P. S.; Gellman, A. J., *Langmuir* **1996,** 12, 2483-2487.
(57) Horvath, J. D.; Koritnik, A.; Kamakoti, P.; Sholl, D. S.; Gellman, A. J., *J. Am. Chem. Soc.* **2004,** 126, 14988-14994.
(58) Jorgensen, W. L.; Ravimohan, C., *J. Chem. Phys.* **1985,** 83, 3050-3054.
(59) Jorgensen, W. L., *Adv. Chem. Phys.* **1988,** 70, 469.
(60) Jorgensen, W. L., *Acc. Chem. Res.* **1989,** 22, 184-189.
(61) Power, T. D.; Sholl, D. S., *J. Vac. Sci. Technol. A* **1999,** 17, 1700-1704.

Appendix 3.A: Structural information for amino acid adsorption in their most stable states on hydroxylated α-quartz (0001)

Table 3.A.1 lists key structural information for hydroxylated α-quartz (0001) surface upon the adsorption of the amino acids we studied. Structural information for the bare surface is also included.

Table 3.A.1: Selected bond lengths or angles of the DFT-optimized geometries of adsorbed amino acids on hydroxylated α-quartz (0001). Structural information for the bare surface is also included. Two different configurations with almost equal energies for each *R*- and *S*-cysteine are marked as superscript 1 and 2.

	$Si(OH)_2$	*d*(O-H) /Å	*d*(H…O) /Å	*d*(Si-O) /Å	∠(O-H…O) /°	∠(Si-O-H) /°	carboxyl group $d(H_{surf}…O_{mole})$/Å $d(O_{surf}…H_{mole})$/Å	amine group $d(H_{surf}…N_{mole})$/Å $d(O_{surf}…H_{mole})$/Å	hydroxyl group $d(H_{surf}…O_{mole})$/Å $d(O_{surf}…H_{mole})$/Å
Bare surface		0.99, 0.98	1.81, 2.37	1.62, 1.65	173, 162	119, 114	-	-	-
Gly	**1**	1.00, 0.99	1.85, 1.93	1.62, 1.65	166, 167	118, 112	1.85	1.58	-
	2	0.99, 1.00	1.74, 1.85	1.64, 1.64	175, 171	118, 113			
	3	1.01, 0.99	1.68	1.63, 1.63	175	120, 125	1.77	2.14	-
	4	0.99, 1.06	1.74	1.64, 1.63	175	119, 113			
Gly (less stable)	**1**	1.01, 0.99	1.82, 1.94	1.63, 1.65	175, 172	117, 112	1.78	1.56	-
	2	0.99, 1.00	1.63, 1.81	1.63, 1.65	172, 172	121, 113			
	3	1.00, 1.06	1.73	1.64, 1.62	177	121, 123	1.92	2.06	-
	4	1.01, 0.99	1.62	1.63, 1.65	175	121, 114			
***R*-Ala**	**1**	0.99, 0.99	1.86, 1.91	1.62, 1.65	165, 167	119, 112	1.87	1.59	-
	2	0.99, 1.00	1.75, 1.89	1.64, 1.64	176, 171	118, 113			
	3	1.00, 0.99	1.69	1.63, 1.64	176	121, 126	1.78	2.17	-
	4	1.00, 1.05	1.73	1.64, 1.63	178	119, 113			
***S*-Ala**	**1**	1.01, 0.99	1.82, 1.93	1.63, 1.65	173, 169	116, 112	1.74	1.61	-
	2	0.99, 1.00	1.61, 1.82	1.62, 1.65	173, 172	122, 114			
	3	1.00, 1.05	1.73	1.64, 1.62	176	120, 127	1.86	2.16	-
	4	1.01, 1.00	1.64	1.63, 1.64	174	121, 114			
***R*-Ser**	**1**	1.00, 1.00	1.71, 1.89	1.63, 1.65	176, 169	120, 112	1.68	-	1.66
	2	1.00, 1.00	1.66, 1.87	1.63, 1.64	171, 171	121, 113			
	3	1.00, 1.01	1.71	1.63, 1.63	176	123, 125	1.87	-	1.69
	4	1.00, 1.00	1.67	1.64, 1.64	177	120, 113			
***S*-Ser**	**1**	1.00, 1.00	1.76, 1.89	1.63, 1.65	173, 169	122, 113	1.72	-	1.64
	2	1.00, 1.00	1.65, 1.87	1.64, 1.65	175, 170	120, 113			
	3	1.00, 0.99	1.71	1.63, 1.63	178	124, 127	1.72	-	1.73
	4	1.00, 1.01	1.68	1.64, 1.64	178	120, 114			
***R*-Cys[1]**	**1**	0.99, 0.99	1.83, 1.93	1.62, 1.65	167, 166	119, 111	1.82	1.59	-
	2	0.99, 1.00	1.74, 1.84	1.65, 1.64	176, 170	118, 112			
	3	1.00, 0.99	1.68	1.63, 1.63	178	123, 125	1.72	2.28	-
	4	1.00, 1,05	1.72	1.64, 1.63	174	120, 113			
***S*-Cys[1]**	**1**	1.01, 0.99	1.82, 1.93	1.64, 1.65	175, 172	116, 112	1.75	1.54	-
	2	0.99, 1.00	1.62, 1.80	1.62, 1.65	171, 172	121, 113			
	3	1.00, 1.07	1.71	1.64, 1.62	177	121, 125	1.82	2.06	-
	4	1.01, 0.99	1.62	1.63, 1.65	174	121, 114			
***R*-Cys[2]**	**1**	1.01, 0.99	1.81, 1.92	1.63, 1.65	173, 168	116, 112	1.75	1.63	-
	2	0.99, 1.00	1.61, 1.81	1.62, 1.65	173, 172	121, 113			
	3	1.00, 1.04	1.72	1.64, 1.62	178	121, 127	1.85	2.14	-
	4	1.01, 0.99	1.65	1.63, 1.64	174	120, 115			
***S*-Cys[2]**	**1**	0.99, 0.99	1.82, 1.92	1.62, 1.65	166, 167	119, 111	1.87	1.60	-
	2	0.99, 1.00	1.74, 1.88	1.64, 1.64	176, 170	118, 113			
	3	1.00, 0.99	1.70	1.63, 1.64	177	121, 126	1.76	2.16	-
	4	1.00, 1.05	1.73	1.64, 1.63	175	119, 113			

Appendix 3.B: Coordinates for glycine adsorption adsorbed on hydroxylated α-quartz (0001)

This appendix lists the coordinates for the most stable structures of uncharged and zwitterionic glycine discussed in this Chapter. The coordinates for each molecule are defined for a single supercell of a (2×2) surface unit cell with all coordinates in Å. The shaded sections of the table give the coordinates of the adsorbate; all other coordinates define the portion of the surface atoms. A table defining unit cell vectors for supercell is also listed in Å.

Table 3.B.1: Unit cell vectors of supercell used for calculations in this Chapter. (in Å)

	x	y	z
a	10.112	0.000	0.000
b	-5.056	8.758	0.000
c	0.000	0.000	22.000

Table 3.B.2: Coordinates for the most stable uncharged glycine adsorbed on hydroxylated α-quartz (0001). This configuration is shown in Fig. 3.3(a).

Atom	x	y	z	Atom	x	y	z	Atom	x	y	z
C	1.053	3.571	8.289	O	0.954	3.589	-1.841	O	-1.044	3.449	2.010
C	-0.272	4.074	7.745	O	1.508	0.960	-1.855	O	4.033	3.433	2.026
H	1.128	3.964	9.317	O	-1.082	5.317	-2.039	O	1.568	7.746	1.832
H	3.072	3.892	8.029	O	3.944	5.310	-2.044	O	1.000	5.140	1.877
H	0.985	2.480	8.348	O	-3.576	7.479	23.703	O	6.008	5.212	1.880
H	2.164	4.914	7.111	O	1.439	7.517	23.683	O	-3.535	7.812	1.740
H	-1.087	5.667	6.978	O	4.030	3.109	23.439	O	3.484	0.845	1.596
N	2.220	3.950	7.468	O	-1.026	3.127	23.435	O	8.505	0.864	1.593
O	-1.284	3.378	7.691	O	8.274	0.614	23.151	O	5.336	2.043	0.221
O	-0.218	5.356	7.386	O	3.235	0.592	23.141	O	2.808	6.067	0.219
				O	0.642	5.086	22.944	O	-2.259	6.073	0.212
				O	5.676	5.082	22.941	O	0.274	2.038	0.206
H	4.211	7.005	21.476	O	2.602	6.268	21.600	Si	-1.167	6.494	-0.905
H	-0.845	6.976	21.442	O	0.090	1.498	21.595	Si	3.872	6.496	-0.917
H	0.136	0.524	21.412	O	-2.469	6.236	21.588	Si	6.431	2.321	-0.917
H	5.196	0.536	21.376	O	5.153	1.503	21.587	Si	1.381	2.300	-0.932
H	1.696	2.183	21.352	O	-4.951	7.302	21.437	Si	2.432	-0.127	24.358
H	6.756	2.198	21.347	O	0.106	7.269	21.389	Si	7.459	-0.109	24.356
H	-2.403	5.324	21.234	O	7.702	2.497	21.260	Si	4.914	4.274	24.143
H	2.672	5.367	21.221	O	2.644	2.475	21.258	Si	-0.125	4.277	24.140
H	2.472	2.983	6.226	O	2.740	6.499	5.745	Si	-3.884	6.527	22.420
H	-2.328	2.769	6.302	O	-2.130	6.427	5.823	Si	1.169	6.537	22.410
H	-3.110	6.569	5.747	O	0.146	1.356	5.510	Si	-1.323	1.944	22.345
H	0.283	-0.569	5.548	O	5.136	1.472	5.537	Si	3.737	1.932	22.341
H	1.809	6.792	5.550	O	2.596	2.335	5.406	Si	3.887	6.785	4.632
H	5.264	-0.367	5.396	O	0.238	7.421	5.165	Si	-1.177	6.863	4.555

H	-0.815	1.610	5.450	O	7.690	2.254	5.466	Si	1.227	2.125	4.550
H	4.182	1.776	5.450	O	-4.808	7.214	5.361	Si	6.309	2.117	4.600
O	0.283	6.690	-0.193	O	0.664	3.560	4.026	Si	-0.070	4.423	2.872
O	-2.246	2.677	-0.222	O	5.883	3.535	3.942	Si	5.014	4.408	2.886
O	2.810	2.652	-0.228	O	3.458	8.006	3.656	Si	7.568	0.037	2.622
O	5.336	6.700	-0.238	O	3.202	-0.700	3.726	Si	2.425	0.097	2.565
O	-1.588	7.915	-1.599	O	-0.928	5.581	3.608	Si	1.400	6.405	0.942
O	3.433	7.910	-1.611	O	4.141	5.458	3.739	Si	3.897	2.254	0.913
O	5.998	3.605	-1.831	O	1.488	1.215	3.238	Si	-3.677	6.434	0.909
O	6.550	0.977	-1.839	O	6.626	1.077	3.409	Si	-1.163	2.258	0.909

Table 3.B.3: Coordinates for the most stable zwitterionic glycine adsorbed on hydroxylated α-quartz (0001). This configuration is shown in Fig. 3.2.

Atom	x	y	z	Atom	x	y	z	Atom	x	y	z
C	4.196	4.805	8.348	O	1.545	0.894	20.123	O	-0.986	3.506	1.894
C	5.154	3.723	7.812	O	6.601	0.894	20.123	O	4.104	3.524	1.858
H	2.074	4.716	8.394	O	-0.983	5.273	20.123	O	-3.526	7.939	1.801
H	2.809	3.591	7.374	O	4.073	5.273	20.123	O	1.566	7.854	1.877
H	2.695	5.227	6.905	O	-1.012	3.105	18.593	O	3.518	0.933	1.818
H	4.119	4.702	9.436	O	4.044	3.105	18.593	O	8.582	0.896	1.742
H	4.541	5.809	8.094	O	-3.540	7.484	18.593	O	0.989	5.258	1.794
N	2.843	4.574	7.733	O	1.516	7.484	18.593	O	6.042	5.336	1.860
O	6.331	4.055	7.538	O	3.180	0.663	18.079	O	0.318	1.901	0.219
O	4.597	2.581	7.682	O	8.236	0.663	18.079	O	5.367	1.880	0.214
				O	0.652	5.041	18.079	O	-2.221	6.254	0.215
				O	5.708	5.041	18.079	O	2.837	6.250	0.210
H	1.682	2.407	16.444	O	0.046	1.661	16.626	Si	1.422	2.195	-0.919
H	6.738	2.407	16.444	O	5.102	1.661	16.626	Si	6.478	2.195	-0.919
H	-0.846	6.786	16.444	O	-2.482	6.040	16.626	Si	-1.106	6.574	-0.919
H	4.210	6.786	16.444	O	2.574	6.040	16.626	Si	3.950	6.574	-0.919
H	0.104	0.719	16.361	O	2.620	2.729	16.430	Si	-0.085	4.236	19.268
H	5.161	0.719	16.361	O	7.676	2.729	16.430	Si	4.971	4.236	19.268
H	-2.424	5.097	16.361	O	0.092	7.108	16.430	Si	2.443	-0.143	19.268
H	2.632	5.097	16.361	O	5.148	7.108	16.430	Si	7.499	-0.143	19.268
H	3.266	2.115	5.362	O	-0.083	1.679	5.554	Si	3.706	2.044	17.422
H	7.198	3.117	6.449	O	5.007	1.542	5.443	Si	-1.350	2.044	17.422
H	5.260	-0.422	5.339	O	-2.091	6.283	5.842	Si	1.178	6.423	17.422
H	-4.851	7.998	5.693	O	2.599	6.331	5.666	Si	-3.878	6.423	17.422
H	-1.016	2.032	5.580	O	2.396	2.539	5.565	Si	1.088	2.295	4.625
H	4.925	1.860	6.433	O	7.485	2.560	5.650	Si	6.257	2.232	4.625
H	-3.069	6.253	5.813	O	0.219	7.360	5.160	Si	-1.241	6.821	4.587
H	1.670	6.678	5.476	O	5.164	7.051	5.460	Si	3.797	6.720	4.612
O	2.844	2.494	-0.218	O	0.666	3.718	3.953	Si	2.397	0.183	2.724
O	-2.212	2.494	-0.218	O	5.845	3.599	3.855	Si	7.575	0.100	2.712
O	0.316	6.873	-0.218	O	3.121	-0.659	3.884	Si	-0.084	4.529	2.779
O	-4.740	6.873	-0.218	O	3.394	8.022	3.769	Si	5.021	4.480	2.788
O	0.997	3.505	20.228	O	1.423	1.271	3.401	Si	-1.101	2.213	0.922
O	6.054	3.505	20.228	O	6.675	1.161	3.506	Si	3.952	2.208	0.926
O	-1.531	7.883	20.228	O	-1.001	5.667	3.469	Si	-3.637	6.588	0.927
O	3.526	7.883	20.228	O	4.059	5.476	3.624	Si	1.419	6.552	0.924

Appendix 3.C: Coordinates for alanine adsorption in the most stable states on hydroxylated α-quartz (0001)

Similar to Appendix 3.B but for alanine.

Table 3.C.1: Coordinates for the most stable *R*-alanine adsorbed on hydroxylated α-quartz (0001). This configuration is shown in Fig. 3.4(a).

Atom	x	y	z	Atom	x	y	z	Atom	x	y	z
C	-0.200	3.984	7.783	O	5.998	3.605	-1.831	O	6.624	1.073	3.411
C	1.214	2.141	8.796	O	6.550	0.977	-1.839	O	-1.053	3.463	1.998
C	1.148	3.608	8.403	O	0.954	3.589	-1.841	O	4.038	3.433	2.026
H	1.214	4.235	9.311	O	1.508	0.960	-1.855	O	1.572	7.748	1.826
H	0.444	1.905	9.538	O	-1.082	5.317	-2.039	O	0.999	5.144	1.879
H	1.060	1.499	7.923	O	3.944	5.310	-2.044	O	6.011	5.218	1.876
H	2.194	1.917	9.236	O	-3.576	7.479	23.703	O	-3.532	7.816	1.744
H	3.144	3.889	7.989	O	1.439	7.517	23.683	O	3.493	0.842	1.591
H	2.195	4.902	7.104	O	4.030	3.109	23.439	O	8.507	0.870	1.597
H	-1.087	5.526	6.959	O	-1.026	3.127	23.435	O	5.342	2.044	0.227
N	2.260	3.945	7.478	O	8.274	0.614	23.151	O	2.808	6.064	0.218
O	-1.158	3.218	7.706	O	3.235	0.592	23.141	O	-2.260	6.076	0.212
O	-0.217	5.257	7.383	O	0.642	5.086	22.944	O	0.274	2.038	0.207
				O	5.676	5.082	22.941	Si	-1.167	6.494	-0.905
				O	2.602	6.268	21.600	Si	3.872	6.496	-0.917
H	4.211	7.005	21.476	O	0.090	1.498	21.595	Si	6.431	2.321	-0.917
H	-0.845	6.976	21.442	O	-2.469	6.236	21.588	Si	1.381	2.300	-0.932
H	0.136	0.524	21.412	O	5.153	1.503	21.587	Si	2.432	-0.127	24.358
H	5.196	0.536	21.376	O	-4.951	7.302	21.437	Si	7.459	-0.109	24.356
H	1.696	2.183	21.352	O	0.106	7.269	21.389	Si	4.914	4.274	24.143
H	6.756	2.198	21.347	O	7.702	2.497	21.260	Si	-0.125	4.277	24.140
H	-2.403	5.324	21.234	O	2.644	2.475	21.258	Si	-3.884	6.527	22.420
H	2.672	5.367	21.221	O	2.741	6.494	5.740	Si	1.169	6.537	22.410
H	-3.114	6.558	5.743	O	-2.135	6.417	5.824	Si	-1.323	1.944	22.345
H	0.294	-0.564	5.522	O	0.159	1.336	5.463	Si	3.737	1.932	22.341
H	1.810	6.789	5.550	O	5.148	1.513	5.545	Si	3.889	6.782	4.629
H	5.260	-0.366	5.402	O	2.599	2.375	5.375	Si	-1.192	6.873	4.558
H	-0.802	1.591	5.416	O	0.227	7.425	5.169	Si	1.230	2.148	4.526
H	4.195	1.811	5.438	O	7.713	2.254	5.451	Si	6.325	2.126	4.595
H	2.469	2.987	6.221	O	-4.807	7.214	5.359	Si	-0.087	4.440	2.867
H	-2.291	2.742	6.301	O	0.629	3.579	4.032	Si	5.023	4.409	2.882
O	0.283	6.690	-0.193	O	5.909	3.539	3.923	Si	7.569	0.038	2.621
O	-2.246	2.677	-0.222	O	3.455	8.001	3.653	Si	2.427	0.110	2.564
O	2.810	2.652	-0.228	O	3.183	-0.675	3.748	Si	1.401	6.406	0.941
O	5.336	6.700	-0.238	O	-0.948	5.606	3.587	Si	3.899	2.254	0.913
O	-1.588	7.915	-1.599	O	4.151	5.453	3.743	Si	-3.675	6.440	0.910
O	3.433	7.910	-1.611	O	1.505	1.262	3.202	Si	-1.163	2.263	0.908

Table 3.C.2: Coordinates for the most stable *S*-alanine adsorbed on hydroxylated α-quartz (0001). This configuration is shown in Fig. 3.4(b).

Atom	x	y	z	Atom	x	y	z	Atom	x	y	z
C	4.175	2.158	8.884	O	5.998	3.605	-1.831	O	6.630	1.081	3.329
C	4.297	3.595	8.401	O	6.550	0.977	-1.839	O	-1.032	3.388	2.044
C	5.650	3.863	7.746	O	0.954	3.589	-1.841	O	4.009	3.496	2.012
H	4.957	1.929	9.614	O	1.508	0.960	-1.855	O	1.553	7.737	1.804
H	4.271	1.457	8.049	O	-1.082	5.317	-2.039	O	0.949	5.148	1.881
H	3.200	2.006	9.363	O	3.944	5.310	-2.044	O	6.020	5.222	1.883
H	4.292	4.268	9.280	O	-3.576	7.479	23.703	O	-3.512	7.824	1.752
H	2.312	3.972	8.044	O	1.439	7.517	23.683	O	3.466	0.907	1.661
H	3.283	4.886	7.084	O	4.030	3.109	23.439	O	8.513	0.822	1.534
H	6.560	5.237	6.687	O	-1.026	3.127	23.435	O	5.331	2.056	0.230
N	3.175	3.948	7.495	O	8.274	0.614	23.151	O	2.806	6.052	0.219
O	6.625	3.121	7.865	O	3.235	0.592	23.141	O	-2.259	6.074	0.211
O	5.665	5.017	7.081	O	0.642	5.086	22.944	O	0.279	2.035	0.205
				O	5.676	5.082	22.941	Si	-1.167	6.494	-0.905
				O	2.602	6.268	21.600	Si	3.872	6.496	-0.917
H	4.211	7.005	21.476	O	0.090	1.498	21.595	Si	6.431	2.321	-0.917
H	-0.845	6.976	21.442	O	-2.469	6.236	21.588	Si	1.381	2.300	-0.932
H	0.136	0.524	21.412	O	5.153	1.503	21.587	Si	2.432	-0.127	24.358
H	5.196	0.536	21.376	O	-4.951	7.302	21.437	Si	7.459	-0.109	24.356
H	1.696	2.183	21.352	O	0.106	7.269	21.389	Si	4.914	4.274	24.143
H	6.756	2.198	21.347	O	7.702	2.497	21.260	Si	-0.125	4.277	24.140
H	-2.403	5.324	21.234	O	2.644	2.475	21.258	Si	-3.884	6.527	22.420
H	2.672	5.367	21.221	O	2.768	6.507	5.751	Si	1.169	6.537	22.410
H	2.797	2.973	6.264	O	-2.493	6.363	5.660	Si	-1.323	1.944	22.345
H	7.411	2.555	6.424	O	0.109	1.459	5.593	Si	3.737	1.932	22.341
H	-3.376	6.827	5.508	O	5.098	1.374	5.448	Si	3.889	6.834	4.627
H	0.166	-0.359	5.525	O	2.637	2.323	5.461	Si	-1.287	6.740	4.624
H	1.805	6.690	5.600	O	0.074	7.221	5.422	Si	1.257	2.132	4.632
H	5.160	-0.553	5.555	O	7.605	2.221	5.507	Si	6.276	2.058	4.552
H	-0.844	1.745	5.513	O	-4.862	7.415	5.352	Si	-0.067	4.382	2.897
H	4.144	1.684	5.368	O	0.761	3.539	3.999	Si	5.026	4.422	2.890
O	0.283	6.690	-0.193	O	5.857	3.489	3.918	Si	7.562	0.026	2.567
O	-2.246	2.677	-0.222	O	3.430	8.000	3.615	Si	2.466	0.070	2.623
O	2.810	2.652	-0.228	O	-1.722	7.979	3.679	Si	1.391	6.388	0.936
O	5.336	6.700	-0.238	O	-0.956	5.454	3.708	Si	3.890	2.284	0.929
O	-1.588	7.915	-1.599	O	4.222	5.492	3.789	Si	-3.671	6.449	0.914
O	3.433	7.910	-1.611	O	1.518	1.103	3.410	Si	-1.160	2.240	0.901

Appendix 3.D: Coordinates for serine adsorption in the most stable states on hydroxylated α-quartz (0001)

Similar to Appendix 3.B but for serine.

Table 3.D.1: Coordinates for the most stable *R*-serine adsorbed on hydroxylated α-quartz (0001). This configuration is shown in Fig. 3.5(a).

Atom	x	y	z	Atom	x	y	z	Atom	x	y	z
C	-1.417	4.674	8.517	O	5.998	3.605	-1.831	O	6.754	0.934	3.558
C	-0.120	4.036	9.026	O	6.550	0.977	-1.839	O	-1.035	3.445	2.012
C	1.076	4.403	8.134	O	0.954	3.589	-1.841	O	4.027	3.406	2.051
H	0.072	4.505	10.005	O	1.508	0.960	-1.855	O	1.575	7.750	1.819
H	0.510	2.212	9.717	O	-1.082	5.317	-2.039	O	0.990	5.151	1.886
H	-0.343	2.128	8.324	O	3.944	5.310	-2.044	O	5.977	5.192	1.873
H	1.955	5.893	7.283	O	-3.576	7.479	23.703	O	-3.537	7.772	1.777
H	-1.328	5.767	8.536	O	1.439	7.517	23.683	O	3.450	0.840	1.576
H	-2.224	4.359	9.192	O	4.030	3.109	23.439	O	8.507	0.868	1.597
H	-1.964	5.069	6.645	O	-1.026	3.127	23.435	O	5.341	2.044	0.232
N	-0.289	2.610	9.224	O	8.274	0.614	23.151	O	2.807	6.059	0.218
O	1.227	5.715	7.945	O	3.235	0.592	23.141	O	-2.262	6.069	0.213
O	1.831	3.555	7.659	O	0.642	5.086	22.944	O	0.276	2.034	0.208
O	-1.720	4.258	7.172	O	5.676	5.082	22.941	Si	-1.167	6.494	-0.905
				O	2.602	6.268	21.600	Si	3.872	6.496	-0.917
H	4.211	7.005	21.476	O	0.090	1.498	21.595	Si	6.431	2.321	-0.917
H	-0.845	6.976	21.442	O	-2.469	6.236	21.588	Si	1.381	2.300	-0.932
H	0.136	0.524	21.412	O	5.153	1.503	21.587	Si	2.432	-0.127	24.358
H	5.196	0.536	21.376	O	-4.951	7.302	21.437	Si	7.459	-0.109	24.356
H	1.696	2.183	21.352	O	0.106	7.269	21.389	Si	4.914	4.274	24.143
H	6.756	2.198	21.347	O	7.702	2.497	21.260	Si	-0.125	4.277	24.140
H	-2.403	5.324	21.234	O	2.644	2.475	21.258	Si	-3.884	6.527	22.420
H	2.672	5.367	21.221	O	2.681	6.528	5.683	Si	1.169	6.537	22.410
H	2.451	2.808	6.294	O	-2.282	6.451	5.736	Si	-1.323	1.944	22.345
H	-2.299	2.987	6.274	O	0.101	1.352	5.533	Si	3.737	1.932	22.341
H	-3.245	6.699	5.626	O	5.159	1.454	5.545	Si	3.915	6.729	4.635
H	0.200	-0.533	5.604	O	2.591	2.297	5.448	Si	-1.192	6.824	4.578
H	1.758	6.824	5.430	O	0.192	7.367	5.275	Si	1.216	2.086	4.586
H	5.230	-0.414	5.475	O	7.710	2.279	5.566	Si	6.378	2.061	4.648
H	-0.851	1.665	5.509	O	-4.855	7.241	5.447	Si	-0.051	4.398	2.886
H	4.218	1.778	5.468	O	0.721	3.513	3.994	Si	5.054	4.341	2.907
O	0.283	6.690	-0.193	O	5.978	3.422	3.864	Si	7.632	-0.023	2.622
O	-2.246	2.677	-0.222	O	3.581	7.854	3.521	Si	2.450	0.057	2.574
O	2.810	2.652	-0.228	O	-1.729	8.017	3.653	Si	1.399	6.404	0.940
O	5.336	6.700	-0.238	O	-0.904	5.508	3.692	Si	3.891	2.248	0.914
O	-1.588	7.915	-1.599	O	4.240	5.338	3.881	Si	-3.684	6.416	0.915
O	3.433	7.910	-1.611	O	1.519	1.120	3.330	Si	-1.162	2.259	0.909

Table 3.D.2: Coordinates for the most stable *S*-serine adsorbed on hydroxylated α-quartz (0001). This configuration is shown in Fig. 3.5(b).

Atom	x	y	z	Atom	x	y	z	Atom	x	y	z
C	1.808	4.687	8.505	O	5.998	3.605	-1.831	O	6.731	0.920	3.553
C	0.520	4.029	9.020	O	6.550	0.977	-1.839	O	-1.030	3.444	2.016
C	-0.676	4.397	8.127	O	0.954	3.589	-1.841	O	4.025	3.413	2.039
H	0.328	4.499	9.998	O	1.508	0.960	-1.855	O	1.573	7.744	1.817
H	-0.084	2.208	9.741	O	-1.082	5.317	-2.039	O	0.993	5.147	1.890
H	0.746	2.110	8.334	O	3.944	5.310	-2.044	O	5.987	5.190	1.866
H	-1.513	5.925	7.271	O	-3.576	7.479	23.703	O	-3.533	7.775	1.783
H	1.708	5.778	8.551	O	1.439	7.517	23.683	O	3.452	0.841	1.589
H	2.629	4.365	9.160	O	4.030	3.109	23.439	O	8.494	0.874	1.597
H	2.357	5.107	6.622	O	-1.026	3.127	23.435	O	5.339	2.040	0.231
N	0.703	2.606	9.227	O	8.274	0.614	23.151	O	2.807	6.057	0.217
O	-0.817	5.712	7.968	O	3.235	0.592	23.141	O	-2.262	6.072	0.213
O	-1.422	3.555	7.628	O	0.642	5.086	22.944	O	0.276	2.033	0.209
O	2.096	4.303	7.147	O	5.676	5.082	22.941	Si	-1.167	6.494	-0.905
				O	2.602	6.268	21.600	Si	3.872	6.496	-0.917
H	4.211	7.005	21.476	O	0.090	1.498	21.595	Si	6.431	2.321	-0.917
H	-0.845	6.976	21.442	O	-2.469	6.236	21.588	Si	1.381	2.300	-0.932
H	0.136	0.524	21.412	O	5.153	1.503	21.587	Si	2.432	-0.127	24.358
H	5.196	0.536	21.376	O	-4.951	7.302	21.437	Si	7.459	-0.109	24.356
H	1.696	2.183	21.352	O	0.106	7.269	21.389	Si	4.914	4.274	24.143
H	6.756	2.198	21.347	O	7.702	2.497	21.260	Si	-0.125	4.277	24.140
H	-2.403	5.324	21.234	O	2.644	2.475	21.258	Si	-3.884	6.527	22.420
H	2.672	5.367	21.221	O	2.689	6.494	5.650	Si	1.169	6.537	22.410
H	2.472	2.990	6.245	O	-2.234	6.453	5.796	Si	-1.323	1.944	22.345
H	-2.303	2.882	6.308	O	0.105	1.343	5.543	Si	3.737	1.932	22.341
H	-3.203	6.659	5.687	O	5.153	1.456	5.549	Si	3.927	6.730	4.616
H	0.206	-0.539	5.600	O	2.583	2.310	5.506	Si	-1.175	6.813	4.600
H	1.762	6.830	5.463	O	0.216	7.368	5.284	Si	1.228	2.087	4.614
H	5.245	-0.414	5.486	O	7.708	2.269	5.535	Si	6.364	2.055	4.637
H	-0.846	1.654	5.522	O	-4.852	7.235	5.442	Si	-0.045	4.392	2.896
H	4.211	1.788	5.505	O	0.732	3.505	3.999	Si	5.058	4.339	2.892
O	0.283	6.690	-0.193	O	5.972	3.412	3.847	Si	7.624	-0.023	2.619
O	-2.246	2.677	-0.222	O	3.581	7.860	3.516	Si	2.459	0.051	2.592
O	2.810	2.652	-0.228	O	-1.728	7.995	3.668	Si	1.398	6.398	0.940
O	5.336	6.700	-0.238	O	-0.895	5.498	3.711	Si	3.890	2.244	0.914
O	-1.588	7.915	-1.599	O	4.249	5.338	3.867	Si	-3.682	6.421	0.914
O	3.433	7.910	-1.611	O	1.544	1.115	3.365	Si	-1.163	2.261	0.910

Appendix 3.E: Coordinates for cysteine adsorption in the most stable states on hydroxylated α-quartz (0001)

Similar to Appendix 3.B but for cysteine. Note that there are the two distinct sets of the most stable structures for each enantiomer of cysteine as discussed in this Chapter.

Table 3.E.1: Coordinates for the most stable *S*-cysteine adsorbed on hydroxylated α-quartz (0001). This configuration is shown in Fig. 3.6(a).

Atom	x	y	z	Atom	x	y	z	Atom	x	y	z
C	4.164	4.193	9.635	O	5.998	3.605	-1.831	O	6.547	1.182	3.264
C	4.188	3.538	8.233	O	6.550	0.977	-1.839	O	-1.030	3.444	2.010
C	5.549	3.842	7.622	O	0.954	3.589	-1.841	O	3.997	3.526	1.988
H	2.782	2.607	10.760	O	1.508	0.960	-1.855	O	1.540	7.794	1.777
H	2.219	3.955	7.981	O	-1.082	5.317	-2.039	O	0.952	5.209	1.922
H	4.161	2.448	8.359	O	3.944	5.310	-2.044	O	6.020	5.227	1.888
H	3.164	4.883	6.983	O	-3.576	7.479	23.703	O	-3.511	7.826	1.742
H	6.473	5.203	6.551	O	1.439	7.517	23.683	O	3.446	0.933	1.682
H	4.248	5.283	9.533	O	4.030	3.109	23.439	O	8.528	0.859	1.586
H	5.009	3.839	10.235	O	-1.026	3.127	23.435	O	5.328	2.057	0.231
N	3.058	3.940	7.386	O	8.274	0.614	23.151	O	2.803	6.069	0.226
O	6.534	3.133	7.838	O	3.235	0.592	23.141	O	-2.259	6.074	0.211
O	5.565	4.961	6.906	O	0.642	5.086	22.944	O	0.278	2.037	0.206
S	2.603	3.924	10.533	O	5.676	5.082	22.941	Si	-1.167	6.494	-0.905
				O	2.602	6.268	21.600	Si	3.872	6.496	-0.917
H	4.211	7.005	21.476	O	0.090	1.498	21.595	Si	6.431	2.321	-0.917
H	-0.845	6.976	21.442	O	-2.469	6.236	21.588	Si	1.381	2.300	-0.932
H	0.136	0.524	21.412	O	5.153	1.503	21.587	Si	2.432	-0.127	24.358
H	5.196	0.536	21.376	O	-4.951	7.302	21.437	Si	7.459	-0.109	24.356
H	1.696	2.183	21.352	O	0.106	7.269	21.389	Si	4.914	4.274	24.143
H	6.756	2.198	21.347	O	7.702	2.497	21.260	Si	-0.125	4.277	24.140
H	-2.403	5.324	21.234	O	2.644	2.475	21.258	Si	-3.884	6.527	22.420
H	2.672	5.367	21.221	O	2.685	6.453	5.741	Si	1.169	6.537	22.410
H	2.713	2.979	6.237	O	-2.572	6.365	5.638	Si	-1.323	1.944	22.345
H	7.347	2.546	6.405	O	0.014	1.460	5.547	Si	3.737	1.932	22.341
H	-3.446	6.849	5.495	O	5.022	1.385	5.431	Si	3.795	6.860	4.626
H	0.079	-0.341	5.510	O	2.556	2.273	5.455	Si	-1.347	6.762	4.628
H	1.726	6.673	5.615	O	0.004	7.235	5.449	Si	1.183	2.128	4.609
H	5.093	-0.538	5.577	O	7.528	2.228	5.481	Si	6.187	2.096	4.538
H	-0.937	1.753	5.464	O	-4.954	7.429	5.356	Si	-0.087	4.425	2.900
H	4.058	1.674	5.355	O	0.714	3.560	4.004	Si	4.979	4.468	2.882
O	0.283	6.690	-0.193	O	5.757	3.555	3.971	Si	7.506	0.093	2.577
O	-2.246	2.677	-0.222	O	8.339	-0.677	3.708	Si	2.430	0.094	2.621
O	2.810	2.652	-0.228	O	-1.774	8.023	3.708	Si	1.391	6.422	0.943
O	5.336	6.700	-0.238	O	-1.000	5.485	3.704	Si	3.888	2.294	0.929
O	-1.588	7.915	-1.599	O	4.142	5.571	3.711	Si	-3.671	6.448	0.913
O	3.433	7.910	-1.611	O	1.438	1.116	3.367	Si	-1.157	2.261	0.906

Table 3.E.2: Coordinates for the most stable *R*-cysteine adsorbed on hydroxylated α-quartz (0001). This configuration is shown in Fig. 3.6(b).

Atom	x	y	z	Atom	x	y	z	Atom	x	y	z
C	1.005	3.845	9.792	O	5.998	3.605	-1.831	O	1.472	1.219	3.250
C	0.911	3.483	8.294	O	6.550	0.977	-1.839	O	4.028	3.448	2.017
C	-0.404	4.041	7.756	O	0.954	3.589	-1.841	O	-1.056	3.466	1.995
H	2.880	4.020	11.291	O	1.508	0.960	-1.855	O	6.010	5.221	1.883
H	0.091	3.534	10.312	O	-1.082	5.317	-2.039	O	0.984	5.155	1.884
H	1.137	4.925	9.912	O	3.944	5.310	-2.044	O	1.574	7.753	1.823
H	0.820	2.392	8.204	O	-3.576	7.479	23.703	O	-3.534	7.821	1.735
H	2.912	3.833	8.110	O	1.439	7.517	23.683	O	8.510	0.871	1.597
H	2.018	4.889	7.192	O	4.030	3.109	23.439	O	3.480	0.858	1.611
H	-1.166	5.659	6.973	O	-1.026	3.127	23.435	O	5.340	2.042	0.227
N	2.081	3.916	7.513	O	8.274	0.614	23.151	O	2.807	6.062	0.219
O	-1.440	3.380	7.733	O	3.235	0.592	23.141	O	-2.260	6.074	0.212
O	-0.307	5.313	7.379	O	0.642	5.086	22.944	O	0.275	2.039	0.208
S	2.450	2.992	10.538	O	5.676	5.082	22.941	Si	-1.167	6.494	-0.905
				O	2.602	6.268	21.600	Si	3.872	6.496	-0.917
H	4.211	7.005	21.476	O	0.090	1.498	21.595	Si	6.431	2.321	-0.917
H	-0.845	6.976	21.442	O	-2.469	6.236	21.588	Si	1.381	2.300	-0.932
H	0.136	0.524	21.412	O	5.153	1.503	21.587	Si	2.432	-0.127	24.358
H	5.196	0.536	21.376	O	-4.951	7.302	21.437	Si	7.459	-0.109	24.356
H	1.696	2.183	21.352	O	0.106	7.269	21.389	Si	4.914	4.274	24.143
H	6.756	2.198	21.347	O	7.702	2.497	21.260	Si	-0.125	4.277	24.140
H	-2.403	5.324	21.234	O	2.644	2.475	21.258	Si	-3.884	6.527	22.420
H	2.672	5.367	21.221	O	-2.171	6.448	5.825	Si	1.169	6.537	22.410
H	7.697	2.745	6.337	O	2.720	6.502	5.742	Si	-1.323	1.944	22.345
H	2.389	2.979	6.262	O	5.069	1.466	5.486	Si	3.737	1.932	22.341
H	-3.151	6.596	5.739	O	0.080	1.362	5.495	Si	3.871	6.788	4.637
H	1.790	6.795	5.545	O	7.626	2.237	5.494	Si	6.269	2.113	4.591
H	0.252	-0.557	5.560	O	2.533	2.337	5.440	Si	-1.206	6.865	4.560
H	4.119	1.788	5.428	O	-4.832	7.224	5.382	Si	1.182	2.130	4.557
H	-0.882	1.612	5.433	O	0.210	7.415	5.173	Si	5.009	4.419	2.884
H	5.231	-0.369	5.387	O	0.633	3.567	4.025	Si	-0.093	4.436	2.871
O	0.283	6.690	-0.193	O	5.876	3.541	3.935	Si	7.568	0.043	2.621
O	-2.246	2.677	-0.222	O	4.133	5.463	3.742	Si	2.415	0.109	2.573
O	2.810	2.652	-0.228	O	3.189	-0.689	3.732	Si	1.400	6.409	0.943
O	5.336	6.700	-0.238	O	3.455	8.009	3.654	Si	3.897	2.260	0.916
O	-1.588	7.915	-1.599	O	-0.964	5.580	3.614	Si	-3.676	6.440	0.910
O	3.433	7.910	-1.611	O	6.620	1.078	3.405	Si	-1.163	2.263	0.908

Table 3.E.3: Coordinates for the most stable *S*-cysteine adsorbed on hydroxylated α-quartz (0001). This configuration is shown in Fig. 3.6(c).

Atom	x	y	z	Atom	x	y	z	Atom	x	y	z
C	1.139	2.194	8.778	O	5.998	3.605	-1.831	O	6.623	1.077	3.418
C	1.096	3.673	8.398	O	6.550	0.977	-1.839	O	-1.057	3.471	1.988
C	-0.263	4.051	7.796	O	0.954	3.589	-1.841	O	4.035	3.436	2.024
H	0.333	1.952	9.474	O	1.508	0.960	-1.855	O	1.571	7.751	1.829
H	0.995	1.578	7.883	O	-1.082	5.317	-2.039	O	0.999	5.146	1.878
H	2.593	2.257	10.684	O	3.944	5.310	-2.044	O	6.006	5.221	1.884
H	3.080	3.882	7.977	O	-3.576	7.479	23.703	O	-3.536	7.819	1.743
H	1.179	4.280	9.319	O	1.439	7.517	23.683	O	3.484	0.849	1.596
H	2.160	4.962	7.117	O	4.030	3.109	23.439	O	8.499	0.878	1.597
H	-1.154	5.594	6.980	O	-1.026	3.127	23.435	O	5.341	2.043	0.227
N	2.197	3.997	7.468	O	8.274	0.614	23.151	O	2.808	6.067	0.219
O	-1.215	3.278	7.710	O	3.235	0.592	23.141	O	-2.261	6.077	0.213
O	-0.288	5.328	7.419	O	0.642	5.086	22.944	O	0.275	2.037	0.208
S	2.740	1.668	9.480	O	5.676	5.082	22.941	Si	-1.167	6.494	-0.905
				O	2.602	6.268	21.600	Si	3.872	6.496	-0.917
H	4.211	7.005	21.476	O	0.090	1.498	21.595	Si	6.431	2.321	-0.917
H	-0.845	6.976	21.442	O	-2.469	6.236	21.588	Si	1.381	2.300	-0.932
H	0.136	0.524	21.412	O	5.153	1.503	21.587	Si	2.432	-0.127	24.358
H	5.196	0.536	21.376	O	-4.951	7.302	21.437	Si	7.459	-0.109	24.356
H	1.696	2.183	21.352	O	0.106	7.269	21.389	Si	4.914	4.274	24.143
H	6.756	2.198	21.347	O	7.702	2.497	21.260	Si	-0.125	4.277	24.140
H	-2.403	5.324	21.234	O	2.644	2.475	21.258	Si	-3.884	6.527	22.420
H	2.672	5.367	21.221	O	2.730	6.530	5.740	Si	1.169	6.537	22.410
H	2.417	3.025	6.217	O	-2.168	6.422	5.800	Si	-1.323	1.944	22.345
H	-2.351	2.750	6.326	O	0.123	1.351	5.481	Si	3.737	1.932	22.341
H	-3.147	6.575	5.715	O	5.101	1.493	5.531	Si	3.881	6.791	4.626
H	0.282	-0.566	5.532	O	2.557	2.386	5.393	Si	-1.206	6.875	4.549
H	1.797	6.811	5.540	O	0.212	7.418	5.169	Si	1.197	2.152	4.535
H	5.237	-0.373	5.407	O	7.663	2.243	5.486	Si	6.290	2.120	4.606
H	-0.839	1.603	5.438	O	-4.812	7.214	5.357	Si	-0.096	4.446	2.860
H	4.152	1.809	5.447	O	0.609	3.582	4.029	Si	5.012	4.413	2.888
O	0.283	6.690	-0.193	O	5.884	3.541	3.940	Si	7.566	0.045	2.623
O	-2.246	2.677	-0.222	O	3.464	8.011	3.645	Si	2.414	0.117	2.566
O	2.810	2.652	-0.228	O	3.183	-0.668	3.740	Si	1.401	6.409	0.942
O	5.336	6.700	-0.238	O	-0.957	5.613	3.575	Si	3.898	2.257	0.913
O	-1.588	7.915	-1.599	O	4.129	5.456	3.743	Si	-3.677	6.441	0.912
O	3.433	7.910	-1.611	O	1.478	1.250	3.220	Si	-1.164	2.265	0.906

Table 3.E.4: Coordinates for the most stable *R*-cysteine adsorbed on hydroxylated α-quartz (0001). This configuration is shown in Fig. 3.6(d).

Atom	x	y	z	Atom	x	y	z	Atom	x	y	z
C	4.227	2.175	8.844	O	5.998	3.605	-1.831	O	6.631	1.082	3.330
C	4.306	3.632	8.390	O	6.550	0.977	-1.839	O	-1.032	3.392	2.042
C	5.668	3.923	7.759	O	0.954	3.589	-1.841	O	4.010	3.491	2.013
H	5.056	1.939	9.517	O	1.508	0.960	-1.855	O	1.560	7.740	1.796
H	4.316	1.514	7.974	O	-1.082	5.317	-2.039	O	0.945	5.156	1.881
H	2.896	2.313	10.828	O	3.944	5.310	-2.044	O	6.018	5.221	1.882
H	2.325	3.912	8.030	O	-3.576	7.479	23.703	O	-3.517	7.826	1.754
H	4.275	4.281	9.286	O	1.439	7.517	23.683	O	3.472	0.898	1.648
H	3.260	4.914	7.098	O	4.030	3.109	23.439	O	8.514	0.827	1.537
H	6.595	5.316	6.747	O	-1.026	3.127	23.435	O	5.333	2.058	0.230
N	3.189	3.961	7.480	O	8.274	0.614	23.151	O	2.806	6.049	0.217
O	6.634	3.167	7.856	O	3.235	0.592	23.141	O	-2.259	6.078	0.213
O	5.699	5.100	7.142	O	0.642	5.086	22.944	O	0.279	2.037	0.205
S	2.642	1.738	9.634	O	5.676	5.082	22.941	Si	-1.167	6.494	-0.905
				O	2.602	6.268	21.600	Si	3.872	6.496	-0.917
H	4.211	7.005	21.476	O	0.090	1.498	21.595	Si	6.431	2.321	-0.917
H	-0.845	6.976	21.442	O	-2.469	6.236	21.588	Si	1.381	2.300	-0.932
H	0.136	0.524	21.412	O	5.153	1.503	21.587	Si	2.432	-0.127	24.358
H	5.196	0.536	21.376	O	-4.951	7.302	21.437	Si	7.459	-0.109	24.356
H	1.696	2.183	21.352	O	0.106	7.269	21.389	Si	4.914	4.274	24.143
H	6.756	2.198	21.347	O	7.702	2.497	21.260	Si	-0.125	4.277	24.140
H	-2.403	5.324	21.234	O	2.644	2.475	21.258	Si	-3.884	6.527	22.420
H	2.672	5.367	21.221	O	2.772	6.509	5.752	Si	1.169	6.537	22.410
H	2.807	2.987	6.232	O	-2.464	6.411	5.686	Si	-1.323	1.944	22.345
H	7.421	2.576	6.413	O	0.105	1.458	5.556	Si	3.737	1.932	22.341
H	-3.355	6.854	5.518	O	5.099	1.376	5.451	Si	3.894	6.836	4.627
H	0.170	-0.354	5.513	O	2.634	2.328	5.442	Si	-1.285	6.767	4.611
H	1.811	6.689	5.590	O	0.105	7.238	5.360	Si	1.250	2.154	4.611
H	5.186	-0.540	5.517	O	7.607	2.224	5.502	Si	6.277	2.060	4.551
H	-0.847	1.750	5.495	O	-4.857	7.418	5.349	Si	-0.080	4.400	2.893
H	4.145	1.679	5.355	O	0.743	3.572	4.010	Si	5.024	4.422	2.889
O	0.283	6.690	-0.193	O	5.852	3.489	3.920	Si	7.565	0.027	2.567
O	-2.246	2.677	-0.222	O	3.429	7.999	3.614	Si	2.453	0.089	2.612
O	2.810	2.652	-0.228	O	-1.760	8.016	3.700	Si	1.392	6.390	0.934
O	5.336	6.700	-0.238	O	-0.983	5.482	3.680	Si	3.892	2.282	0.926
O	-1.588	7.915	-1.599	O	4.224	5.493	3.789	Si	-3.672	6.450	0.915
O	3.433	7.910	-1.611	O	1.511	1.153	3.362	Si	-1.160	2.243	0.901

CHAPTER 4

ENANTIOSPECIFIC ADSORPTION OF AMINO ACIDS ON HYDROXYLATED QUARTZ $(10\bar{1}0)$

4.1 Introduction

In Chapter 3, we examined the enantiospecific adsorption of several amino acids on hydroxylated α-quartz (0001). We found negligible differences in adsorption energies for the most stable minima of enantiomers of alanine on this surface, while there are measureable energy differences between the two enantiomers of both serine and cysteine in their most stable states. The main source of this enantiospecificity is the difference in the strength of hydrogen bonds between the surface and the two enantiomers.

Downs and Hazen proposed chiral indices of crystalline surfaces as a measure of enantioselective potential based on atomic displacements from ideal mirror or glide plane symmetry[1]. When this chiral index is applied to the most common quartz surfaces ($\{10\bar{1}0\}$, $\{10\bar{1}1\}$, and $\{11\bar{2}0\}$), the $(10\bar{1}0)$ surface shows the largest chirality index. Although the concept of a chiral index is at best a heuristic guide, this result makes it interesting to consider enantiospecific adsorption on quartz $(10\bar{1}0)$. Recently, Kahr et al. have examined the adsorption of carminic acid on this surface using interatomic potentials, but found negligible energy difference between the two enantiomers[2].

In this Chapter, we examine the adsorption of glycine, alanine, serine, cysteine, aspartic acid and asparagine on hydroxylated α-quartz $(10\bar{1}0)$ using DFT calculations. Aspartic acid and asparagine were not investigated in our earlier work on quartz (0001). Although the calculations for these molecules with DFT are computationally demanding, they are interesting because these amino acids have more potential for forming hydrogen bonds with the surface than simpler amino acids.

4.2. Calculation methods

We performed plane wave DFT calculations using the Vienna *ab initio* simulation package (VASP) with the ultrasoft pseudopotentials available in this package[3-6]. For the exchange-correlation functional, the generalized gradient approximation (GGA) with the Perdew-Wang 91[7] functional was adopted. All calculations used a plane wave expansion with a cutoff of 396 eV. Geometries were relaxed using a conjugate gradient algorithm until the forces on all unconstrained atoms were less than 0.03 eV/Å.

The previously reported structure[8-9] was used for bulk α-quartz that has a hexagonal structure with space group $P3_121$. The DFT-optimized hexagonal lattice constants for bulk quartz ($a = b = 5.056$ Å, $c = 5.561$ Å) are in good agreement with experimental values ($a = b = 4.916$ Å, $c = 5.405$ Å)[10]. This structure was cleaved along the $(10\bar{1}0)$ plane to construct a surface that is represented by a slab ~12.1 Å thick containing eight O-Si-O layers with the bottom four O-Si-O layers constrained in their bulk positions. For all calculations, a vacuum spacing of ~14.8 Å was placed in the direction of surface normal. It is important to note that our calculations consider the adsorbed molecules interacting with the hydroxylated surface in the absence of a solvent, a situation relevant for experiments in ultra-high vacuum.

Calculations for adsorbed amino acids were performed with one molecule adsorbed in a (2×2) surface unit cell. This gives an area of 112.5 $Å^2$/molecule. This coverage was chosen to minimize the interactions between adsorbates. A 2×2×1 Monkhorst-Pack *k*-point mesh was used, which was sufficient to give well converged results. The geometries of gas phase amino acids were optimized in a supercell of the same size as the surface calculations. When examining adsorption, molecules were placed on only one side of the slab. Dipole corrections were therefore applied in computing all of the energies reported below[11-12].

The adsorption energy, E_{ads}, of a molecule was defined in a same way as in Eq. (3.1). The zero point energies associated with H in amino acids and hydroxylated quartz surfaces are also calculated using the same method as in Chapter 3 and appropriately incorporated into the adsorption energy calculations using Eq. (3.2). To characterize the enantiospecificity of adsorption in each example, we used the enantiospecific difference in adsorption energies, defined as in Chapter 3.

For the $(10\bar{1}0)$ plane of quartz, two terminations can potentially be exposed[13-15]. When the surface is hydroxylated, one termination can be covered with single silanol groups while the other is composed of geminal silanediol groups. Schlegel et al. showed from an X-ray reflectivity and atomic force microscopy study of $(10\bar{1}0)$–water interfaces that most of the surface silanol groups are single even though only some geminal silanediol groups were found[13]. DFT calculations performed by Murashov and Demchuk showed that after surface reconstruction, a quartz surface covered with single silanol groups has a lower surface energy than one with geminal silanediol groups[14-15]. In this Chapter, we therefore only consider the hydroxylated surface with single silanol groups. The optimized bare surface structure of hydroxylated α-quartz $(10\bar{1}0)$ is shown in Fig. 4.1. For each surface hydroxyl group, there are two types of hydrogen bonds formed with two nearest hydroxyls on the surface. The bond lengths of these two hydrogen bonds are 1.72 and 2.52 Å, good agreement with Murashov's previous theoretical report of 1.74 and 2.48 Å, respectively[14]. The hydroxylated α-quartz $(10\bar{1}0)$ surface is nonsuperimposable on its mirror image due to these two distinct hydrogen bonds.

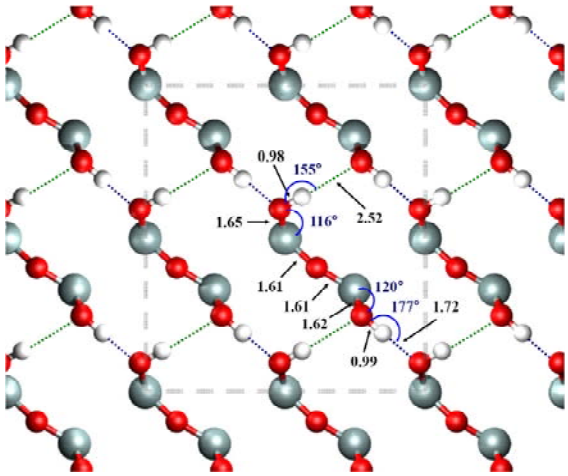

Figure 4.1: Top view of the DFT optimized geometry of the hydroxylated α-quartz $(10\bar{1}0)$ surface, using a (2×2) surface unit cell. For clarity, only surface silanol groups are shown. Selected bond lengths (in Å) and angles (in degrees) are indicated. Silicon atoms are shown as light gray spheres, oxygen atoms as red spheres and hydrogen atoms as white spheres, respectively. The two distinct types of hydrogen bonds are shown with as green and blue dashed lines. The gray dashed lines indicate the surface unit cell.

4.3. Structures of amino acids adsorption on hydroxylated α-quartz $(10\bar{1}0)$

4.3.1. Glycine and Alanine

Glycine, H_2NCH_2COOH, is the simplest amino acid. Glycine is achiral, so it cannot adsorb in an enantiospecific way. It is nevertheless worthwhile to examine the adsorption of glycine before considering more complex amino acids. Our results in Chapter 3 on hydroxylated α-quartz (0001) demonstrated that neutral glycine is the most stable chemical speciation for the adsorption on the surface. Here, we also consider only the adsorption of neutral amino acids on hydroxylated α-quartz $(10\bar{1}0)$. To identify possible binding sites, we first examined NH_3 adsorption on this surface. For these calculations, we divided a (1×1) surface unit cell into a 4×4 grid. NH_3 was then positioned 2 Å above each grid point as initial configuration for geometry optimization. After optimization, all initial structures were converged to two distinct energy states. The most stable binding site is above the longer hydrogen bond of the bare surface (green dashed lines in Fig. 1). During adsorption, the longer hydrogen bond in the surface is

broken and replaced by two new hydrogen bonds ($H_{surf}\ldots N_{mole}$ and $O_{surf}\ldots H_{mole}$) with NH_3. The less stable binding site is above the shorter hydrogen bond of the bare surface (blue dashed lines in Fig. 1). In this case the longer hydrogen bond is still broken and the surface hydroxyl that once made the longer hydrogen bond on the bare surface is lifted up to form the hydrogen bond with NH_3.

A challenging aspect of computationally examining molecular adsorption for species such as glycine is that large numbers of adsorption configurations must be examined to have confidence that a global minimum can be identified[16-18]. To address this challenge, we examined a variety of initial configurations in a systematic way. Specifically, the N atom of glycine was first placed on each binding site identified in our calculations with NH_3 and configurations were generated by rotating glycine about this point by increments of 30°. We also examined the adsorption configurations of the mirror images of the glycine states just described without changing the underlying surface. This generates a new set of initial configurations because of the chirality of the surface. In total, therefore, we considered 48 initial configurations. Each configuration was relaxed to find a local energy minimum for the adsorbed molecule.

From these calculations, multiple distinct energy states were found. Among them, we focus on only the ten most stable energy states because the other less stable structures are > 0.2 eV less favored than the most stable one. The most stable binding site of glycine (Fig. 4.2) has the molecule's NH_2 group above the longer hydrogen bond on the bare surface. As in the case of NH_3, during the adsorption, one long hydrogen bond of the bare surface is broken and the surface –OH is lifted up to form a new hydrogen bond with the adsorbing molecule (light blue dashed lines in Fig. 4.2). This process causes significant structural deformation of the surface. We return to this point in Sec. 4.5. The carboxyl group of glycine also forms two additional hydrogen bonds with the surface, acting as a hydrogen bond donor and receptor (green and purple dashed lines in Fig. 4.2). The most stable configuration shown in Fig. 4.2 has an adsorption energy of 0.71 eV. This

adsorption energy is 0.05 eV smaller than the result on the (0001) surface[9]. If zero point energy is included, the adsorption energy defined by Eq. (4.2) decreases to 0.67 eV. Information about the surface structures of HOSi-O-SiOH upon glycine adsorption in this state is available in Table 4.A.1 of the Appendix 4.A. There are four different HOSi-O-SiOH groups in a (2×2) surface unit cell. The numbers in Table 4.A.1 correspond to the groups as marked in Fig. 4.2.

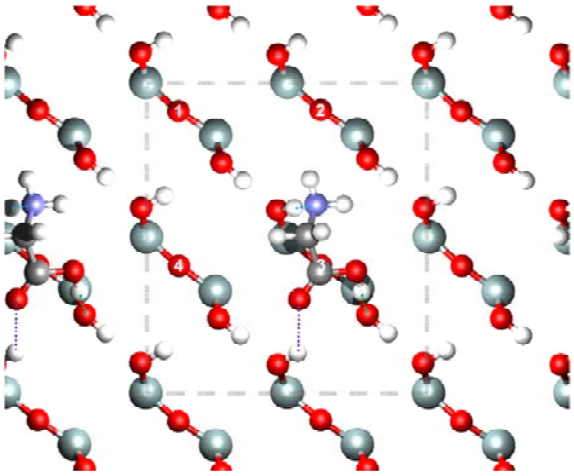

Figure 4.2: Top view of the most stable DFT optimized geometry of glycine on the hydroxylated α-quartz $(10\bar{1}0)$. For clarity, only glycine and the surface silanol groups and their connecting O are shown. In addition to the atoms described in Fig. 4.1, C atoms are shown in gray and N atoms in blue, respectively. Three kinds of hydrogen bonds are also depicted as light blue, green and purple dashed lines. The gray dashed lines indicate the surface unit cell. The distinct HOSi-O-SiOHs in a surface unit cell are numbered.

Alanine, H_2NCHCH_3COOH, is the simplest chiral amino acid. Previous reports demonstrated that when alanine adsorbs onto metal surfaces in its deprotonated form, it has the same tridentate footprint as glycine[19-22]. Our previous study on hydroxylated α-quartz (0001) also showed that the adsorption structure for each enantiomer of alanine in the most stable state is an analogue of adsorbed glycine[9]. This implies that the methyl group as a side chain in an alanine molecule does not play an important role in the adsorption. It is therefore reasonable to expect that alanine will bind on hydroxylated α-

quartz $(10\bar{1}0)$ in a similar way to glycine, and that any enantiospecificity associated with this binding will be weak.

Initial configurations for alanine adsorption were constructed from the ten most stable structures of glycine adsorption. In each configuration, each hydrogen atom attached to the α-carbon in glycine was substituted with a methyl group. The two configurations generated in this way from a single glycine configuration are different enantiomers of alanine. After calculations from these initial structures, 20 stable states were observed; that is, each initial configuration is associated with a distinct stable state. These local minima have very similar adsorption geometries and energies to those of glycine.

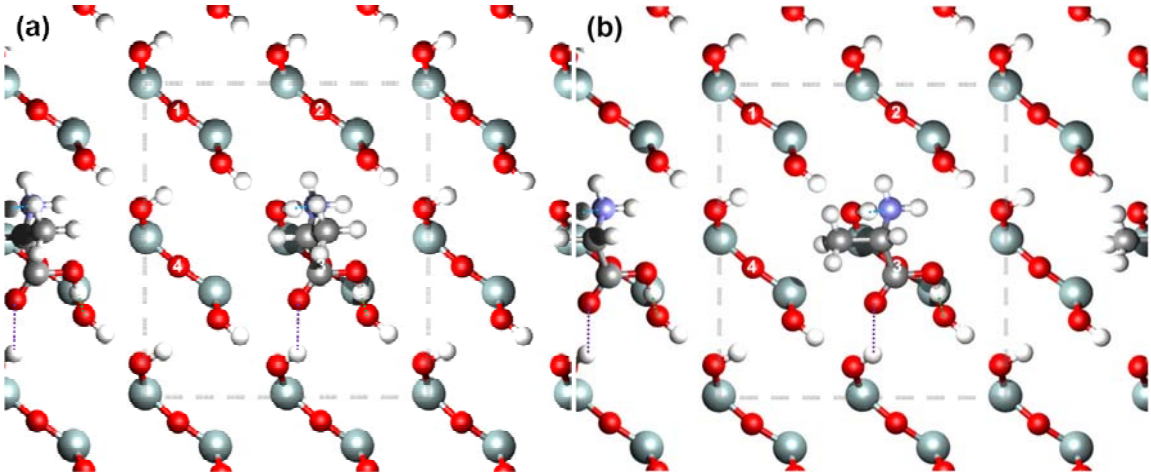

Figure 4.3: Top views of the most stable DFT optimized geometry of absorbed (a) *R*- and (b) *S*-alanine on hydroxylated α-quartz $(10\bar{1}0)$. Hydrogen bonds and atoms are shown in the way as in Fig. 4.2.

The most stable structures of both enantiomers of alanine on the surface (Fig. 4.3a and b) are analogues of the most stable configuration for glycine (Fig. 4.2). Structural information about the surface structures of HOSi-O-SiOH upon the adsorption of the two alanine enantiomers in the most stable configurations is given in Table 4.A.1 of the Appendix 4.A. The adsorption energy of *R*-alanine in the most stable configuration (Fig. 4.3a) is 0.73 eV while that of *S*-alanine (Fig. 4.3b) is 0.75 eV. If zero point energies

are included, the adsorption energies are changed to 0.72 eV (0.75 eV) for *R*-alanine (*S*-alanine). When the definition of the enantiospecificity mentioned in Chapter 3 is applied here, the enantiospecific energy difference between enantiomers of alanine is -0.02 eV (-0.03 eV) without (with) ZPEs. These results show that, as expected, adsorption of alanine on this surface does not exhibit strong enantiospecificity.

4.3.2. Serine and Cysteine

Serine, $H_2NCHCH_2OHCOOH$, is the simplest amino acid in which the side chain, a CH_2OH group, has the potential of H-bonding to the surface. We have reported that serine has appreciable enantiospecificity on hydroxylated α-quartz (0001); -0.05 eV (-0.08 eV) without (with) ZPE corrections[9]. It is therefore interesting to examine serine adsorption on quartz $(10\bar{1}0)$.

Initial configurations were constructed using the ten most stable adsorbed structures of glycine, with an H atom on the α-carbon replaced with a CH_2OH group for each configuration. Three distinct OH positions in the CH_2OH were considered for each structure in case this group is not able to rotate freely. In addition, initial configurations defined by the mirror images of the serine configurations just described were examined. This gave 60 initial configurations of serine on the surface. Our calculations from these initial structures showed that for each enantiomer, there are 30 distinct energy minima that are associated with each initial configuration.

The most stable structures for *R*- and *S*-serine observed from these calculations are shown in Fig. 4.4. Interestingly, *R*-serine adsorbs onto the surface via four bonds, indicating that the OH group in a side chain plays an important role. The *S*-serine adsorption configuration is, however, just the analogue of *S*-alanine adsorption structure, where three hydrogen bonds are formed during adsorption. For *S*-serine adsorption structure, one local minimum structure is found to adsorb to the surface via four bonds including CH_2OH binding, but it is 0.32 eV less stable than the most stable one. More

information about the surface hydroxyl structures upon the adsorption of serine in their most stable states is given in Table 4.A.1 of the Appendix 4.A.

The adsorption energy of *R*-serine in its most preferred configuration (Fig. 4.4a) is 0.76 eV, while the adsorption energy of *S*-serine in its most stable structure (Fig. 4.4b) is 0.72 eV. If the definition of the enantiospecificity mentioned above is applied here, the enantiospecific energy difference between enantiomers of serine is 0.04 eV. This enantiospecificity has a different sign from that of serine adsorption on the (0001) surface[9], suggesting that enantiospecificity of a chiral species could be varied depending on the surface planes even though they are terminated from the same bulk crystal. This is consistent with the reports that different crystallographic planes of quartz possess dramatically different adsorption characteristics[23-24]. Bhatia and Sholl also showed similar observations for molecular adsorption on intrinsically chiral Cu surfaces.[18] When we consider the effect of the zero point energies, the adsorption energies are reduced to 0.73 eV (0.70 eV) for *R*-serine (*S*-serine), decreasing the enantiospecific energy difference to 0.03 eV.

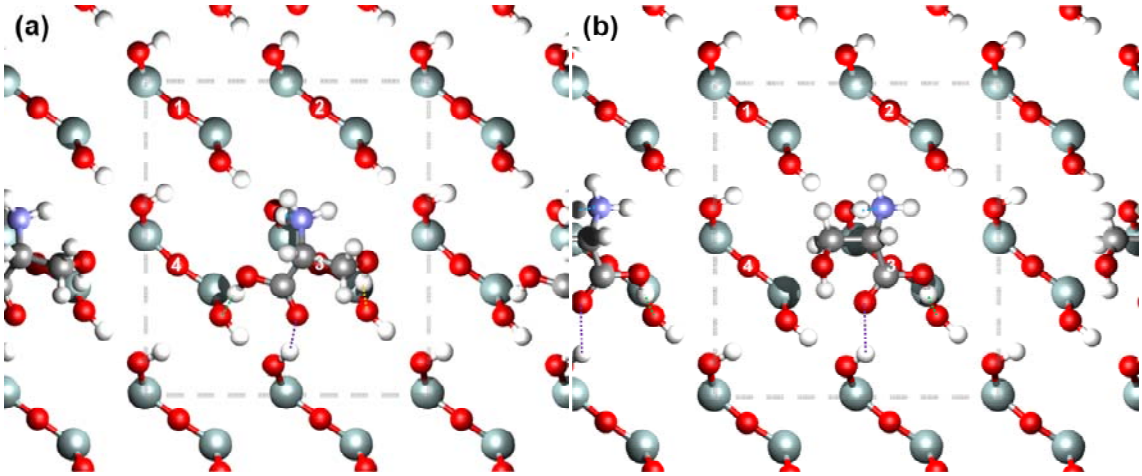

Figure 4.4: Top views of the most stable DFT optimized geometry of absorbed (a) *R*- and (b) *S*-serine on the hydroxylated α-quartz $(10\bar{1}0)$. Hydrogen bonds and atoms are shown in the way as in Fig. 4.2. In addition to the hydrogen bonds described in Fig. 4.2, one more kind of hydrogen bond is depicted as orange dashed lines.

Cysteine, $H_2NCHCH_2SHCOOH$, has a CH_2SH group attached to its α-carbon. Cysteine adsorption has been studied on Au, Ag, Cu, and Pd and is driven on these surfaces by the strong affinity of a thiol group for metal atoms[25-31]. Our previous report on hydroxylated α-quartz (0001), however, showed that due to the large size of a sulfur atom, the thiol group cannot participate in the hydrogen bond with the surface[9]. This situation might also be expected on the other surfaces where binding is driven by the formation of hydrogen bonds.

Initial configurations for cysteine adsorption were constructed using the structures from 10 local minima of serine adsorption for each enantiomer, in each case replacing the OH group in the serine side chain with a SH group. These 10 initial configurations for each enantiomer of cysteine gave 10 distinct local minima for each enantiomer after optimization.

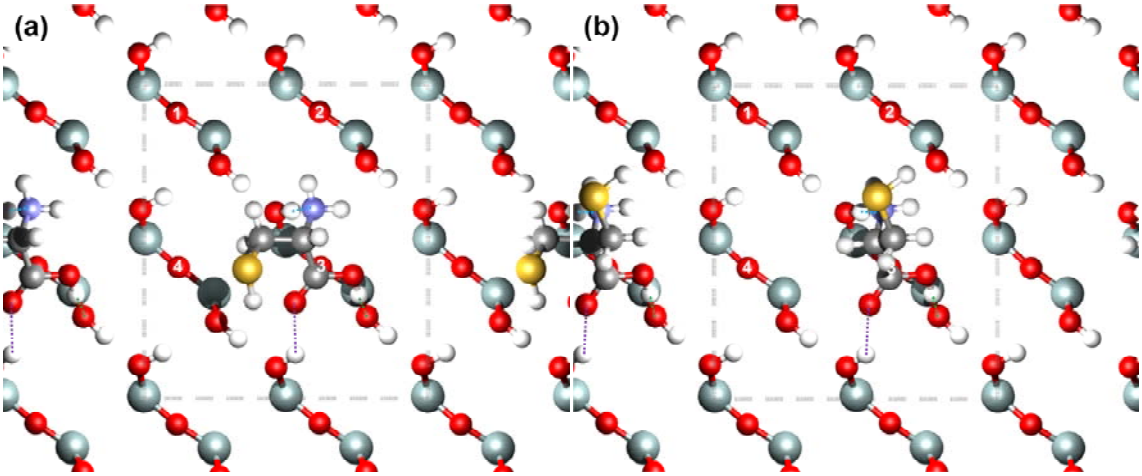

Figure 4.5: Top views of the most stable DFT optimized geometry of absorbed (a) *R*- and (b) *S*-cysteine on the hydroxylated α-quartz $(10\bar{1}0)$. Hydrogen bonds and atoms are shown in the way as in Fig. 4.2. In addition to the atoms described in Fig. 4.2, S atoms are shown in yellow.

The most stable structure for each cysteine enantiomer on the surface is shown in Fig. 4.5. As expected, the sulfur atom prefers to stay away from the surface because its large size does not allow a thiol group to fit on a binding site. Each enantiomer binds to the surface in an analogous way to corresponding enantiomer of the adsorbed alanine

structures shown in Fig. 4.3. Table 4.A.1 of the Appendix 4.A lists the structural information for the surface hydroxyls upon the adsorption of the two cysteine enantiomers.

The adsorption energies of two enantiomers of cysteine in the most stable states are essentially identical; 0.81 eV. The enantiospecific energy difference for cysteine adsorption is therefore negligible. If zero point energy is included, the adsorption energies of both enantiomers decrease to 0.78 eV. This can be understood by noting that the most stable structures of both cysteine enantiomers adsorbed on the surface (Fig. 4.5) are the analogues of the two alanine enantiomers in their most stable states (Fig. 4.3), so as for the methyl side group in alanine, the side chain of cysteine does not play a critical role upon its adsorption process. This result is different from on quartz (0001) which showed the enantiospecific adsorption of cysteine[9]. It may be considered as one reason for the difference that the hydroxylated α-quartz (0001) has a higher density of surface hydroxyl groups (0.090 $Å^{-2}$) than $(10\bar{1}0)$ (0.071 $Å^{-2}$), indicating that the large sulfur atom in cysteine on quartz (0001) is more sterically influenced by the surface atoms than on quartz $(10\bar{1}0)$.

4.3.3. Aspartic acid and Asparagine

Aspartic acid, $H_2NCHCH_2COOHCOOH$, has a CH_2COOH group attached to its α-carbon. Apart from serine, cysteine, and threonine, it is the simplest amino acid in which the side chain has the potential of H-bonding to the surface. It has been shown that aspartic acid has enantiospecific binding at the steps of calcite $(10\bar{1}1)$[32] and on the six faces of the $\{12\bar{3}1\}$ chiral trigonal scalenohedral calcite surface in solution[33]. Initial configurations for aspartic acid adsorption were constructed from the 10 most stable structures of each enantiomer of adsorbed serine. Three distinct COOH positions in the CH_2COOH were considered for each structure because this group might not be able to

rotate freely. Additionally, in case O and OH cannot rotate by 180° with respect to the C atom in the COOH group of the side chain without an energy barrier, two H positions were also considered for each structure. Among these 120 structures, we optimized 51 structures after excluding physically inaccessible initial structures. After optimization of these 51 structures, we further calculated the additional 24 initial structures of *R*-enantiomers that were generated by rotating the mirror images of the two most stable *S*-enantiomers about a binding site by increments of 30°.

The most stable structures for *R*- and *S*-aspartic acid are shown in Fig. 4.6. Other than the most stable configurations, we observed 16 (13) distinct energy states for the *R*-(*S*-) enantiomer. For each enantiomer in the most preferred structure, the COOH group in a side chain participates in two hydrogen bonds, acting as the donor (black dashed lines in Fig. 4.6) and the accepter (orange dashed lines in Fig. 4.6) of the hydrogen bonds, respectively. In Fig. 4.6, *S*-aspartic acid binds via five hydrogen bonds while *R*-aspartic acid adsorbs via four hydrogen bonds since the *R*-enantiomer's carboxyl group attached to its α-carbon forms only one hydrogen bond with the surface upon the adsorption (Fig. 4.6b). In the less stable configurations, aspartic acid binds to the surface via hydrogen bonds ranging from three to five (three or four) hydrogen bonds for the *R*- (*S*-) enantiomer. *R*-aspartic acid can exist in a local energy minimum that has five hydrogen bonds with the surface, but the energy of this configuration is 0.11 eV less stable than its most stable one. More information about the surface hydroxyl structures upon the adsorption of the two aspartic acid enantiomers in their most stable states is also available in Table 4.A.1 of the Appendix 4.A.

The adsorption energy of *R*-aspartic acid in its most preferred configuration (Fig. 4.6a) is 0.78 eV, while the adsorption energy of *S*-aspartic acid in its most stable structure (Fig. 4.6b) is 0.88 eV, giving an enantiospecific energy difference of -0.10 eV. This is the largest enantiospecificity among the amino acids we have examined on the $(10\bar{1}0)$ surface or on the (0001) surface[9]. When we include zero point energies, the adsorption

energies are reduced to 0.76 eV (0.84 eV) for *R*-aspartic acid (*S*-aspartic acid), decreasing the enantiospecific energy difference to -0.08 eV.

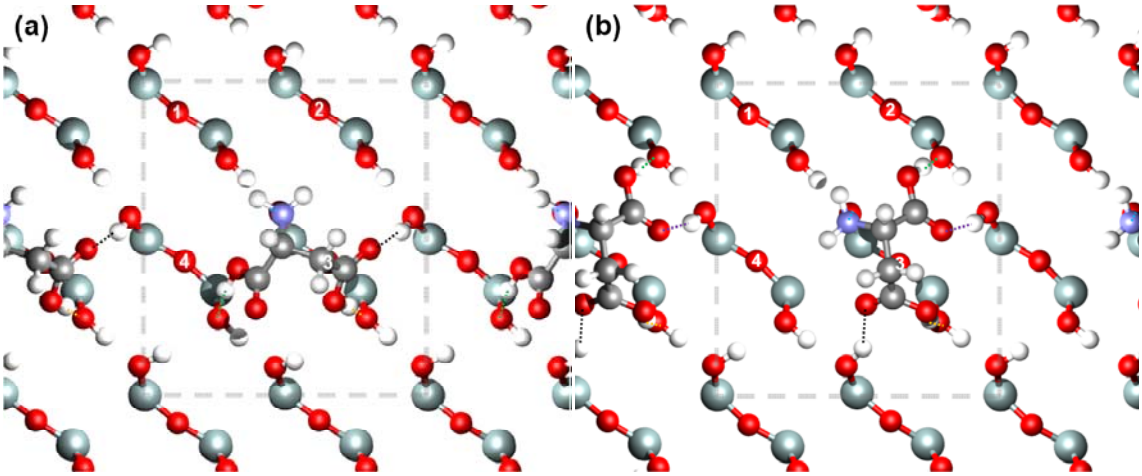

Figure 4.6: Top views of the most stable DFT optimized geometry of absorbed (a) *R*- and (b) *S*-aspartic acid on the hydroxylated α-quartz $(10\bar{1}0)$. Hydrogen bonds and atoms are shown in the way as in Fig. 4.4. In addition to the hydrogen bonds described in Fig. 4.4, one more kind of hydrogen bond is depicted as black dashed lines.

It is natural to move forward by studying asparagine, $H_2NCHCH_2CONH_2COOH$, which has a CH_2CONH_2 as a side chain, because structures can be easily optimized by substituting the OH in the aspartic acid side chain with NH_2. Initial configurations for asparagine adsorption were constructed using the 32 structures in the above-mentioned distinct states of adsorbed aspartic acid. In each case, we considered two NH_2 positions in the side chain because the amine group and the O atom with respect to C atom of the $CONH_2$ might not be able to freely rotate. In total, therefore, the calculations for 64 initial configurations were performed.

The most stable structures for *R*- and *S*-asparagine are shown in Fig. 4.7. We obtained 18 distinct energy states for each enantiomer. As for aspartic acid, in the most stable state, *R*- (*S*-) asparagine adsorbs onto the surface via four (five) hydrogen bonds. As can be seen in Fig. 4.7(b), *S*-enantiomer is the analogue of the most stable *S*-aspartic acid adsorption structure (Fig. 4.6b), replacing OH in the side chain with NH_2 while *R*-

enantiomer is the analogue of the second most stable *R*-aspartic acid adsorption structure. Table 4.A.1 of the Appendix 4.A also lists the structural information for the surface hydroxyls upon the adsorption of two asparagine enantiomers.

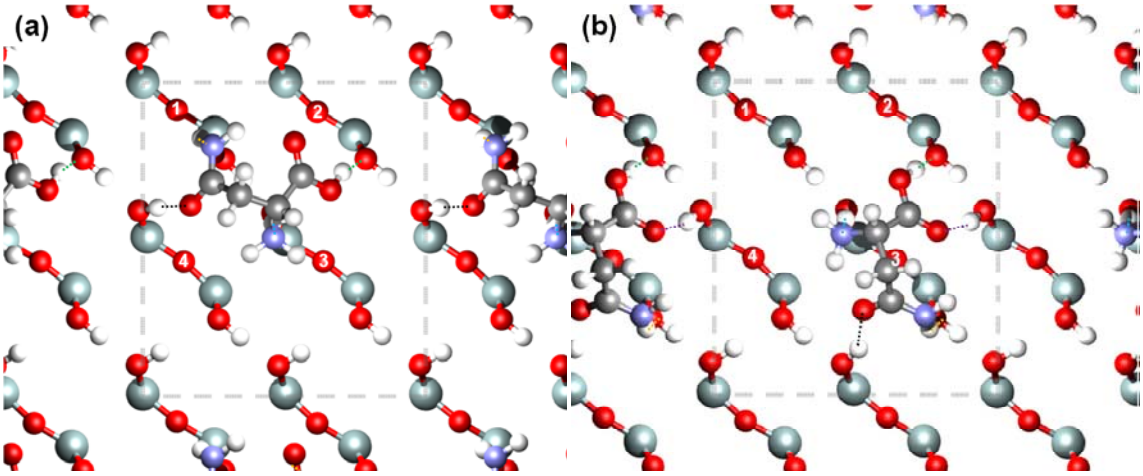

Figure 4.7: Top views of the most stable DFT optimized geometry of absorbed (a) *R*- and (b) *S*-asparagine on the hydroxylated α-quartz $(10\bar{1}0)$. Hydrogen bonds and atoms are shown in the way as in Fig. 4.6.

The adsorption energy of *R*-asparagine in the most stable configuration (Fig. 4.7a) is 0.72 eV while that of *S*-asparagine (Fig. 4.7b) is 0.76 eV. When zero point energies are included, the adsorption energies are changed to 0.67 eV (0.71 eV) for *R*-asparagine (*S*-asparagine). The enantiospecific energy difference between enantiomers of asparagine is therefore -0.04 eV, both with and without ZPEs.

4.4. Enantiospecific adsorption of amino acids on hydroxylated α-quartz $(10\bar{1}0)$

Here, we will focus more on the enantiospecificity of the amino acids we have examined on hydroxylated α-quartz $(10\bar{1}0)$. Table 4.1 summarizes the enantiospecific energy differences in the lowest energy states of the amino acid enantiomers we have examined on quartz (0001) and quartz $(10\bar{1}0)$. As on quartz (0001), alanine adsorption on the $(10\bar{1}0)$ surface shows only weak enantiospecificity. This implies that a substituted methyl group in the alanine molecule does not have a significant effect upon the

adsorption onto the hydroxylated quartz surfaces. For serine, the magnitude of the enantiospecific energy difference on the two surfaces is similar, but the sign of this energy difference is different on these two surfaces. Unlike the result on quartz (0001)[9], a negligible enantiospecific energy difference of the two cysteine enantiomers is observed on the $(10\bar{1}0)$ surface.

	(0001)			**$(10\bar{1}0)$**				
Amino Acid	Ala	Ser	Cys	Ala	Ser	Cys	Asp	Asn
Enantiospecificity (eV)	< 0.01	-0.05	-0.04	-0.02	0.04	< 0.01	-0.10	-0.04

Table 4.1: The enantiospecific energy differences in the lowest energy states of the adsorbed amino acid enantiomers we have examined are summarized. The data for quartz (0001) are from Chapter 3.

For aspartic acid adsorption, there is an energy difference of -0.10 eV between the lowest energy states of the two enantiomers on quartz $(10\bar{1}0)$. This enantiospecificity is similar in magnitude to the largest enantiospecific energy difference that has been reported to date by DFT calculations on any surface, which is 0.14 eV for the cysteine on Au(17 11 9)[34]. Asparagine adsorption is also enantiospecific by -0.04 eV.

The discussion above has focused on the energy differences between the lowest energy states of the adsorbed enantiomers. As we have shown, however, multiple local minima exist on the surface for each enantiomer of each amino acid. Figure 4.8 shows the energies of these energy minima for each amino acid without including zero point energies. An important feature of this figure is that we can directly associate each configuration for the *R*-enantiomer with a configuration of the *S*-enantiomer that has the same structure on the surface. These associations are shown with dashed lines in Fig. 4.8, and provide evidence (although not a definitive proof) that we have not missed local minima of one of the adsorbed enantiomers in our examination of the complicated potential energy surface defined by these adsorbed molecules.

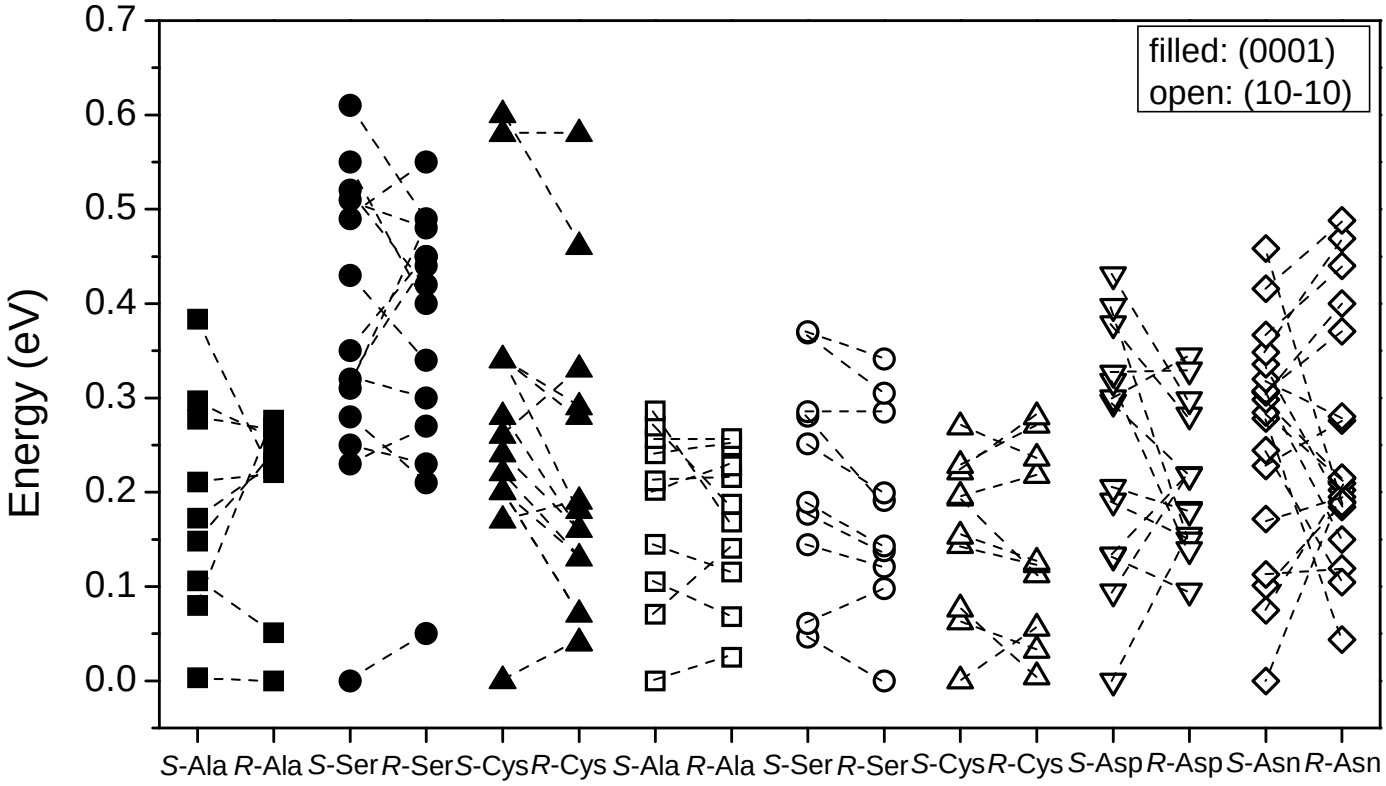

Figure 4.8: Energies of the distinct local minima observed for several amino acids adsorbed on the hydroxylated α-quartz (0001) and $(10\bar{1}0)$ surface measured relative to the energy of the most favorably bound configuration of either enantiomer of the species of interest. The results on (0001) are taken from Chapter 3.

Experimental measurements of molecular binding energies typically probe a thermal average of the available minima. Thus, it would be more experimentally relevant to include these effects when we consider the enantiospecificity of adsorption. Fortunately, it is possible to consider these effects in a straightforward way using ideas from statistical perturbation theory[35-37] once the set of local minima are available for each enantiomer. Using the method described previously[9], we calculated the absolute values of the free energy difference between adsorbed enantiomers, $\left|\Delta A^{R/S}\right|$ as a function of

temperature. The results of these calculations are shown in Fig. 4.9. Our previous results on quartz (0001)[9] are also included for the comparison. Overall, the energy difference between the minimum energy states is a very good approximation to the full free energy difference at all temperatures below room temperature. The enantiospecificity of binding for each amino acid decreases as the temperature increases from 0 to 500 K. The curve for cysteine on quartz $(10\bar{1}0)$ in Fig. 4.9 is non-monotonic because $\Delta A^{R/S} = 0$ when T ≃ 200 K and the sign of this free energy difference changes at this temperature.

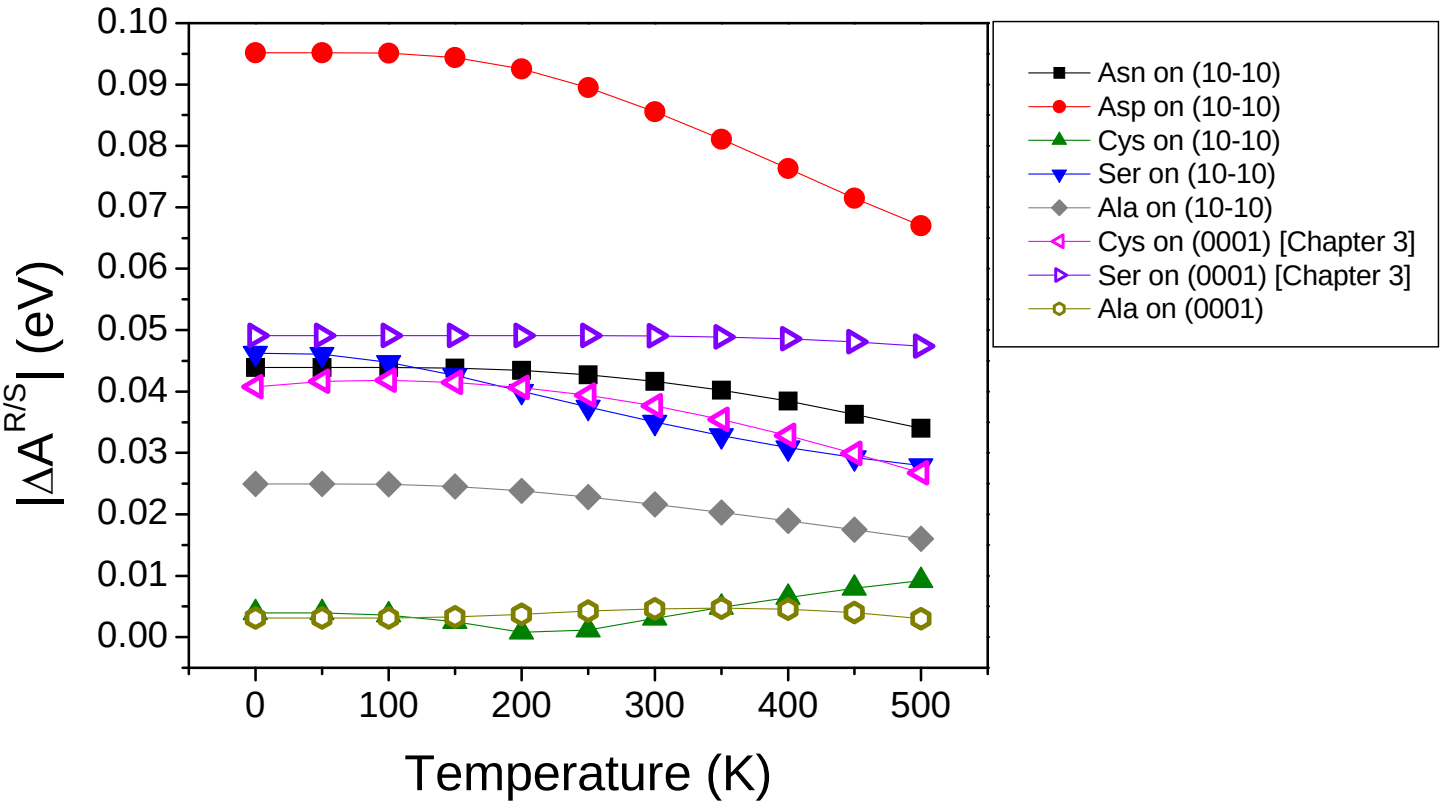

Figure 4.9: Absolute values of the free energy difference between adsorbed enantiomers as a function of temperature. The results on quartz (0001) taken from Chapter 3 are also shown.

The free energy difference for each amino acid except serine and aspartic acid on $(10\bar{1}0)$ changes by ~0.01 eV between 0 and 500 K. The temperature dependence for

serine and aspartic acid is stronger, with the free energy difference changing by 0.02 and 0.03 eV, respectively, as the temperature is increased from 0 to 500 K. This outcome can be understood be examining the distribution of energy states in Fig. 4.8. In the case of aspartic acid, for example, the several lowest energy levels available for the *R*-enantiomer are lower in energy than many states for the *S*-enantiomer except for the minimum energy state of the *S*-aspartic acid. As temperature increases, therefore, the thermal average over these minima reduces the enantiospecificity seen at 0 K favoring *R*-aspartic acid.

4.5. Contributions to the adsorption energy

Here, we describe a decomposition of the adsorption energy to examine how different physical aspects of the adsorption process contribute to the adsorption energy. We computed the energy required for surface deformation, molecular deformation, and surface binding as defined in previous reports[8-9, 38-39]. Briefly, the surface (molecular) deformation energy is the energy difference between the surface (molecule) in its geometry during molecular adsorption and relaxed geometry when no adsorbate is present (in the gas phase). The surface binding energy is then defined as the difference between the net adsorption energy and the net deformation energy[8, 38-39]. The surface binding energy defined in this way is larger in magnitude than the net adsorption energy because of the unfavorable nature of the deformation energies. Only the adsorption energy is experimentally observable, but the other contributions provide insight into the factors that influence adsorption on the surface. The absolute values of the adsorption energies and the contributions to these energies of amino acids we have studied are summarized in Fig. 4.10.

The surface binding energies defined above of glycine, *R*- and *S*-alanine, *S*-serine, and *R*- and *S*-cysteine are very similar at around 1.45 eV. The energies required for the surface deformation in the adsorption of these amino acids are also similar to each other, ranging from 0.41 to 0.44 eV. These surface deformation energies occur because the

surface hydroxyls deform substantially to form hydrogen bonds with the adsorbing molecule. As already discussed in Sec. 4.3, all of these species bind to the surface via three hydrogen bonds. The enantiomers of cysteine have slightly higher adsorption energies because they experience less molecular deformation than the other species. *R*-serine forms an additional hydrogen bond with the surface, giving a surface binding energy ~0.17 eV higher than the amino acids mentioned above. The overall adsorption energy of this molecule, however, does not increase because the larger surface binding energy is compensated by an increase in the molecular deformation energy.

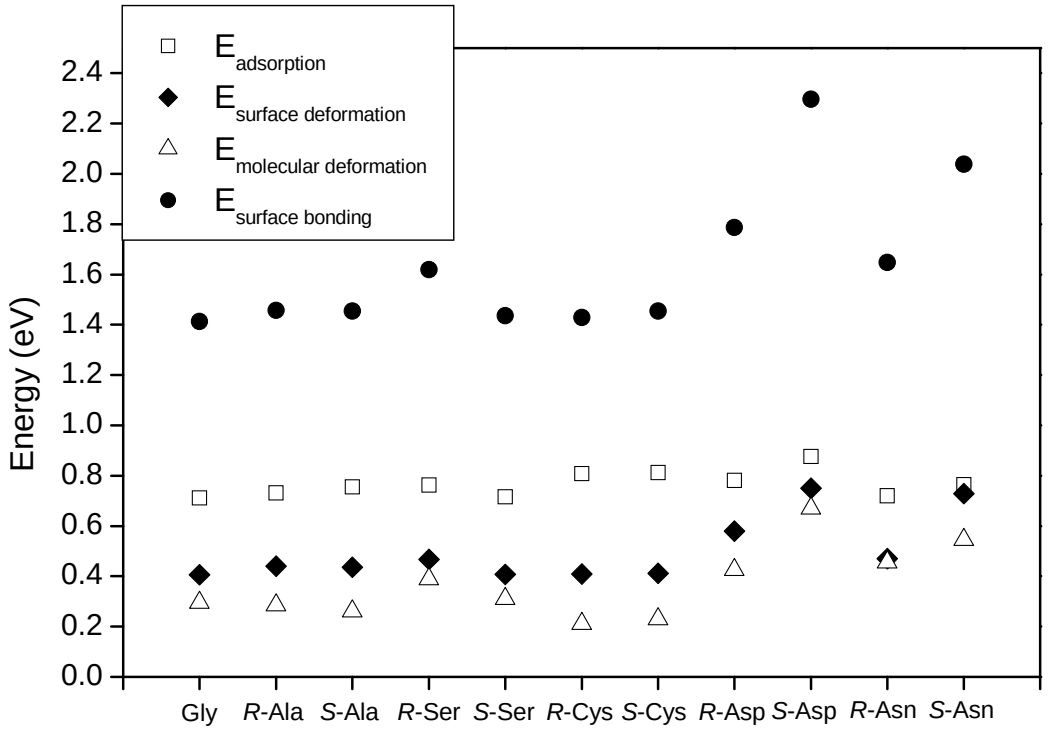

Figure 4.10: The adsorption energies of amino acids α-quartz $(10\bar{1}0)$ and their decomposed energies into surface deformation, molecular deformation, and surface bonding in their absolute values.

As mentioned in Sec. 4.3.3, the most stable adsorbed configurations of *R*- and *S*-enantiomers of aspartic acid and asparagine form four and five kinds of hydrogen bonds with the surface, respectively. This leads to much larger surface binding energies than the

other species, as can be seen in Fig. 4.10. Because the *S*-enantiomers have one more hydrogen bond with the surface, the surface binding energies of the *S*-enantiomers are ~0.5 eV for aspartic acid and ~0.4 eV for asparagine larger than the *R*-enantiomers. The presence of additional hydrogen bonds is associated with increased deformation of both the surface and the adsorbates. For the *S*-enantiomers of both species, the surface deformation energies are ~0.3 eV larger than in the other amino acids we have examined, while for the *R*-enantiomer of aspartic acid (asparagine), they are larger by ~0.15 (~0.05) eV. Similarly, the molecular deformation energies are also larger than the other species by ~0.15 eV (~0.4 eV) for *R*- (*S*-) aspartic acid and ~0.2 eV (~0.3 eV) for *R*- (*S*-) asparagine, respectively.

The results in Fig. 4.10 illustrate how attempting to characterize adsorption strengths based simply upon counting hydrogen bonds would be misleading[9]. In general, an increased number of hydrogen bonds is associated with increased deformation energies, which diminishes the contribution of the hydrogen bonds on the overall adsorption energy. For example, we mentioned above that the most stable configuration of *S*-aspartic acid on quartz $(10\bar{1}0)$ forms five hydrogen bonds with the surface, while the most stable configuration of the *R*-enantiomer has only four hydrogen bonds. Figure 4.8 shows that the state with five hydrogen bonds does have a direct counterpart for the *R*-enantiomer, but this state is 0.11 eV less stable than the configuration with four hydrogen bonds. In this metastable local minimum, the deformation energies associated with the state are sufficiently large that the energy gain from forming an additional hydrogen bond does not lead to overall stabilization of the molecule.

4.6. Conclusion

The adsorption of several amino acids on hydroxylated α-quartz $(10\bar{1}0)$ has been examined using DFT calculations. In order to find the most favorable configurations of a variety of amino acids upon the adsorption, we have used a systematic approach that

included an investigation of a large number of local minima for each molecule. Our results describe the configurations of these molecules in experiments under vacuum conditions since we include no solvent in the calculations.

We found non-negligible differences in adsorption energy between the enantiomers of serine, aspartic acid, and asparagine on the surface. For serine adsorption, the enantiospecific energy differences in the two enantiomers on quartz $(10\bar{1}0)$ has the same magnitude as on quartz (0001), but the opposite sign. This is an example where a different enantiomeric preference exists on different surfaces of a same material. The large enantiospecific energy difference, -0.10 eV, was found for aspartic acid adsorption. This energy difference is comparable to the largest enantiospecific energy differences that have been reported in previous DFT studies on other chiral surfaces: -0.14 eV for the adsorption of cysteine on Au(17 11 9)[34] and 0.13 eV for the adsorption of amino-(fluoro)methoxy on Cu(874)[17]. Negligible differences in adsorption energies between the two enantiomers of alanine and cysteine were found on quartz $(10\bar{1}0)$.

To describe enantiospecific energy differences at finite temperature, we considered a thermal average over multiple states using a simple method that has a well defined meaning in terms of adsorption free energies. Our results showed that the enantiospecificity at 0 K is a useful value for characterizing this phenomenon because the effects of other energy minima at experimentally relevant temperatures are small. Our analysis of the contributions to the adsorption energy demonstrate that although it might be expected that the adsorption energy is correlated in a simple way to the number of bonds with the surface, the associated deformations of the surface and the absorbing molecules during the adsorption process make such a simplistic description of surface bonding inadequate.

References

(1) Downs, R. T.; Hazen, R. M., *J. Mol. Cat. A: Chem.* **2004**, 216, 273-285.
(2) Kahr, B.; Chittenden, B.; Rohl, A., *Chirality* **2006**, 18, 127-133.
(3) Kresse, G.; Furthmuller, J., *Phys. Rev. B* **1996**, 54, 11169-11186.
(4) Kresse, G.; Hafner, J., *Phys. Rev. B* **1993**, 47, 558-561.
(5) Kresse, G.; Hafner, J., *J. Phys.: Condens. Matter* **1994**, 6, 8245-8257.
(6) Sholl, D. S.; Steckel, J. A., *Density functional theory : a practical introduction*. John Wiley & Sons, Inc.: Hoboken, NJ, 2009.
(7) Perdew, J. P.; Chevary, J. A.; Vosko, S. H.; Jackson, K. A.; Pederson, M. R.; Singh, D. J.; Fiolhais, C., *Phys. Rev. B* **1992**, 46, 6671-6687.
(8) Han, J. W.; James, J. N.; Sholl, D. S., *Surf. Sci.* **2008**, 602, 2478-2485.
(9) Han, J. W.; Sholl, D. S., *Langmuir* **2009**, 25, 10737-10745.
(10) Levien, L.; Prewitt, C. T.; Weidner, D. J., *Am. Mineral.* **1980**, 65, 920.
(11) Bengtsson, L., *Phys. Rev. B* **1999**, 59, 12301.
(12) Neugebauer, J.; Scheffler, M., *Phys. Rev. B* **1992**, 46, 16067.
(13) Schlegel, M. L.; Nagy, K. L.; Fenter, P.; Sturchio, N. C., *Geochim. Cosmochim. Acta* **2002**, 66, 3037-3054.
(14) Murashov, V. V., *J. Phys. Chem. B* **2005**, 109, 4144-4151.
(15) Murashov, V. V.; Demchuk, E., *J. Phys. Chem. B* **2005**, 109, 10835-10841.
(16) Šljivancanin, Ž.; Gothelf, K. V.; Hammer, B., *J. Am. Chem. Soc.* **2002**, 124, 14789-14794.
(17) Bhatia, B.; Sholl, D. S., *Angew. Chem. Int. Ed.* **2005**, 44, 7761-7764.
(18) Bhatia, B.; Sholl, D. S., *J. Chem. Phys.* **2008**, 128, 144709.
(19) Rankin, R. B.; Sholl, D. S., *Surf. Sci.* **2005**, 574, L1-L8.
(20) Barlow, S. M.; Louafi, S.; Le Roux, D.; Williams, J.; Muryn, C.; Haq, S.; Raval, R., *Surf. Sci.* **2005**, 590, 243.
(21) Haq, S.; Massey, A.; Moslemzadeh, N.; Robin, A.; Barlow, S. M.; Raval, R., *Langmuir* **2007**, 23, 10694-10700.
(22) Barlow, S. M.; Raval, R., *Curr. Opin. Colloid Interface Sci.* **2008**, 13, 65-73.
(23) Guevremont, J. M.; Strongin, D. R.; Schoonen, M. A. A., *Am. Mineral.* **1998**, 83, 1246-1255.
(24) Hazen, R. M.; Sholl, D. S., *Nat. Mater.* **2003**, 2, 367-374.
(25) Ihs, A.; Lieberg, B., *J. Colloid Interface Sci.* **1991**, 144, 282.
(26) Kuhnle, A.; Linderoth, T. R.; Hammer, B.; Besenbacher, F., *Nature* **2002**, 415, 891-893.
(27) Kuhnle, A.; Linderoth, T. R.; Schunack, M.; Besenbacher, F., *Langmuir* **2006**, 22, 2156.
(28) Kuhnle, A.; Molina, L. M.; Linderoth, T. R.; Hammer, B.; Besenbacher, F., *Phys. Rev. Lett.* **2004**, 93, 086101.
(29) Lopez-Lozano, X.; Perez, L. A.; Garzon, I. L., *Phys. Rev. Lett.* **2006**, 97, -.
(30) Marti, E. M.; Methivier, C.; Pradier, C. M., *Langmuir* **2004**, 20, 10223.
(31) Santos, E.; Avalle, L. B.; Scurtu, R.; Jones, H., *Chem. Phys.* **2007**, 342, 236.
(32) Orme, C. A.; Noy, A.; Wierzbicki, A.; McBride, M. T.; Grantham, M.; Teng, H. H.; Dove, P. M.; DeYoreo, J. J., *Nature* **2001**, 411, 775-779.

(33) Hazen, R. M.; Filley, T. R.; Goodfriend, G. A., *Proc. Nat. Acad. Sci.* **2001**, 98, 5487-5490.
(34) Greber, T.; Šljivancanin, Ž.; Schillinger, R.; Wider, J.; Hammer, B., *Phys. Rev. Lett.* **2006**, 96, 056103.
(35) Jorgensen, W. L.; Ravimohan, C., *J. Chem. Phys.* **1985**, 83, 3050-3054.
(36) Jorgensen, W. L., *Adv. Chem. Phys.* **1988**, 70, 469.
(37) Jorgensen, W. L., *Acc. Chem. Res.* **1989**, 22, 184-189.
(38) Barbosa, L. A. M. M.; Sautet, P., *J. Am. Chem. Soc.* **2001**, 123, 6639-6648.
(39) Rankin, R. B.; Sholl, D. S., *Surf. Sci.* **2004**, 548, 301-308.

Appendix 4.A: Structural information for amino acid adsorption in their most stable states on hydroxylated α-quartz $(10\bar{1}0)$

Table 4.A.1 lists structural information for hydroxylated α-quartz $(10\bar{1}0)$ surface upon the adsorption of amino acids. The structural information for the bare surface is also included.

Table 4.A.1: Selected bond lengths or angles of the DFT-optimized geometries of adsorbed amino acids on hydroxylated α-quartz $(10\bar{1}0)$. Structural information for the bare surface is also included.

	SiOH	*d*(O-H) /Å	*d*(H…O) /Å	*d*(Si-O) /Å	∠(O-H…O) /°	∠(Si-O-H) /°	carboxyl group $d(H_{surf}…O_{mole})$/Å $d(O_{surf}…H_{mole})$/Å	amine group $d(H_{surf}…N_{mole})$/Å	side chain $d(H_{surf}…O_{mole})$/Å $d(O_{surf}…H_{mole})$/Å
Bare surface	**a**	0.98	2.52	1.65	155	116	-	-	-
	b	0.99	1.72	1.62	177	120			
Gly	**1a/b**	0.98, 1.01	2.28, 1.62	1.66, 1.62	158, 178	115, 119	2.61	1.52	-
	2a/b	0.98, 1.00	2.89, 1.69	1.65, 1.61	137, 179	122, 119			
	3a/b	1.07, 1.00	3.25, 1.64	1.62, 1.64	108, 179	124, 120	1.67		-
	4a/b	0.98, 1.00	2.37, 1.71	1.66, 1.62	157, 176	115, 119			
***R*-Ala**	**1a/b**	0.98, 1.01	2.27, 1.61	1.66, 1.62	158, 178	115, 119	2.58	1.50	-
	2a/b	0.98, 0.99	2.90, 1.69	1.65, 1.61	148, 179	122, 119			
	3a/b	1.08, 1.01	3.27, 1.64	1.61, 1.64	107, 179	123, 121	1.65		-
	4a/b	0.98, 0.99	2.36, 1.71	1.65, 1.62	157, 175	115, 119			
***S*-Ala**	**1a/b**	0.98, 1.01	2.28, 1.62	1.66, 1.62	159, 179	115, 119	2.48	1.51	-
	2a/b	0.98, 0.99	2.91, 1.70	1.65, 1.61	148, 179	123, 120			
	3a/b	1.07, 1.00	3.29, 1.63	1.61, 1.64	106, 179	123, 120	1.67		-
	4a/b	0.98, 1.00	2.31, 1.70	1.65, 1.62	158, 173	114, 119			
***R*-Ser**	**1a/b**	0.98, 1.01	2.48, 1.62	1.66, 1.62	152, 179	116, 119	1.86	1.59	-
	2a/b	0.99, 0.99	3.17, 1.72	1.64, 1.61	127, 175	128, 120			
	3a/b	1.05, 1.00	3.64, 1.69	1.62, 1.62	93, 177	122, 121	1.64		1.92
	4a/b	0.98, 1.01	2.30, 1.59	1.65, 1.65	158, 175	116, 117			
***S*-Ser**	**1a/b**	0.99, 1.01	2.24, 1.62	1.66, 1.62	159, 179	115, 119	2.51	1.53	-
	2a/b	0.98, 0.99	2.94, 1.70	1.65, 1.61	147, 179	122, 120			
	3a/b	1.07, 1.01	3.31, 1.63	1.62, 1.64	106, 178	123, 120	1.66		-
	4a/b	0.98, 1.00	2.32, 1.71	1.65, 1.63	157, 173	115, 119			
***R*-Cys**	**1a/b**	0.99, 1.01	2.23, 1.62	1.66, 1.62	159, 179	115, 119	2.45	1.52	-
	2a/b	0.98, 0.99	2.94, 1.70	1.65, 1.61	148, 179	123, 119			
	3a/b	1.07, 1.01	3.30, 1.63	1.62, 1.64	106, 178	123, 120	1.66		-
	4a/b	0.98, 1.00	2.32, 1.71	1.62, 1.62	157, 173	115, 119			
***S*-Cys**	**1a/b**	0.99, 1.01	2.22, 1.63	1.66, 1.62	160, 179	115, 120	2.40	1.54	-
	2a/b	0.98, 0.99	2.99, 1.70	1.65, 1.61	146, 179	123, 120			
	3a/b	1.06, 1.01	3.35, 1.62	1.62, 1.64	104, 179	124, 121	1.63		-
	4a/b	0.98, 1.00	2.30, 1.71	1.65, 1.62	158, 173	115, 119			

***R*-Asp**	**1a/b**	0.98, 1.00	2.38, 1.66	1.66, 1.60	154, 178	115, 121	-	1.68	1.92
	2a/b	0.97, 0.99	3.10, 1.73	1.66, 1.60	135, 173	119, 122			
	3a/b	1.03, 1.01	3.78, 1.61	1.61, 1.64	104, 179	126, 121	1.81		1.55
	4a/b	0.99, 1.00	4.72, 1.66	1.64, 1.65	130, 177	120, 117			
***S*-Asp**	**1a/b**	0.99, 1.00	2.04, 1.69	1.66, 1.60	163, 177	114, 121	1.74	1.65	2.01
	2a/b	0.99, 1.01	2.94, 1.61	1.64, 1.64	142, 171	128, 118			
	3a/b	1.03, 1.01	4.10, 1.58	1.62, 1.64	112, 178	125, 119	1.56		1.61
	4a/b	1.00, 1.00	4.47, 1.70	1.64, 1.63	137, 171	123, 117			
***R*-Asn**	**1a/b**	0.98, 1.01	2.42, 1.60	1.66, 1.60	156, 177	115, 125	-	1.61	1.91
	2a/b	0.98, 1.00	2.49, 1.71	1.66, 1.63	160, 177	114, 121			
	3a/b	1.04, 0.99	4.13, 1.71	1.62, 1.63	112, 176	121, 119	1.74		2.17
	4a/b	1.00, 0.99	3.11, 1.72	1.64, 1.63	125, 175	121, 118			
***S*-Asn**	**1a/b**	0.99, 1.00	2.05, 1.66	1.66, 1.60	165, 177	114, 122	1.81	1.61	1.98
	2a/b	0.99, 1.01	3.05, 1.64	1.64, 1.64	137, 170	128, 119			
	3a/b	1.04, 1.00	4.06, 1.62	1.62, 1.62	114, 177	122, 119	1.58		1.95
	4a/b	0.99, 1.00	4.56, 1.69	1.64, 1.64	130, 173	123, 117			

Appendix 4.B: Coordinates for glycine and alanine adsorption adsorbed on hydroxylated α-quartz ($10\bar{1}0$)

This appendix lists the coordinates for the most stable structures of glycine and alanine discussed in this Chapter. The coordinates for each molecule are defined for a single supercell of a (2×2) surface unit cell with all coordinates in Å. The shaded sections of the table give the coordinates of the adsorbate; all other coordinates define the portion of the surface atoms. A table defining unit cell vectors for supercell is also listed in Å.

Table 4.B.1: Unit cell vectors of supercell used for calculations in this Chapter. (in Å)

	x	y	z
a	10.112	0.000	0.000
b	-10.112	11.122	0.000
c	0.000	0.000	26.562

Table 4.B.2: Coordinates for the most stable glycine adsorbed on hydroxylated α-quartz $(10\bar{1}0)$. This configuration is shown in Fig. 4.2.

Atom	x	y	z	Atom	x	y	z	Atom	x	y	z
C	-0.546	4.728	14.666	O	0.986	1.875	9.036	O	-2.562	3.723	1.084
C	-0.103	3.405	14.060	O	6.012	1.845	8.998	O	2.494	3.723	1.084
H	-0.447	6.742	14.147	O	-4.055	7.455	8.984	O	-7.618	9.284	1.084
H	0.752	5.838	13.479	O	0.942	7.405	9.085	O	-2.562	9.284	1.084
H	-1.626	4.685	14.834	O	4.162	-0.083	8.934	O	1.164	1.699	0.219
H	-0.040	4.852	15.637	O	9.235	-0.036	9.038	O	6.221	1.699	0.219
H	1.402	2.701	13.074	O	-0.913	5.472	8.987	O	-3.892	7.260	0.219
N	-0.240	5.832	13.731	O	4.196	5.525	8.958	O	1.164	7.260	0.219
O	-0.831	2.435	13.901	O	-0.962	1.919	7.260	O	4.085	0.041	0.174
O	1.191	3.457	13.710	O	4.058	1.917	7.249	O	9.141	0.041	0.174
				O	-6.028	7.493	7.249	O	-0.972	5.602	0.174
				O	-0.961	7.481	7.263	O	4.085	5.602	0.174
H	4.427	0.599	11.806	O	0.930	0.079	7.103	Si	1.251	2.822	10.323
H	-0.892	0.513	12.142	O	6.000	0.099	7.073	Si	6.272	2.729	10.333
H	-1.020	5.714	12.432	O	-4.105	5.662	7.076	Si	-3.824	8.323	10.342
H	-5.663	6.154	11.841	O	0.933	5.644	7.103	Si	1.238	8.350	10.381
H	2.349	1.218	11.584	O	-2.724	3.583	6.235	Si	-1.298	4.630	10.329
H	7.167	1.137	11.699	O	2.332	3.589	6.231	Si	3.816	4.673	10.271
H	-2.853	6.687	11.604	O	-7.779	9.150	6.231	Si	-6.324	10.205	10.263
H	2.360	6.828	11.637	O	-2.722	9.146	6.236	Si	-1.270	10.213	10.351
H	0.392	1.075	0.160	O	-0.194	3.807	5.545	Si	0.016	0.953	8.113
H	5.448	1.075	0.160	O	4.862	3.807	5.545	Si	5.059	0.947	8.069
H	-4.664	6.636	0.160	O	-5.251	9.368	5.545	Si	-5.020	6.538	8.073
H	0.392	6.636	0.160	O	-0.194	9.368	5.545	Si	0.001	6.497	8.123
H	3.300	0.533	-0.147	O	-1.579	1.744	4.697	Si	-1.364	2.762	5.939
H	8.356	0.533	-0.147	O	3.477	1.744	4.697	Si	3.687	2.767	5.930
H	-1.756	6.094	-0.147	O	-6.635	7.305	4.697	Si	-6.423	8.330	5.930
H	3.300	6.094	-0.147	O	-1.579	7.305	4.697	Si	-1.363	8.321	5.941
O	1.602	1.889	11.626	O	1.550	-0.086	4.532	Si	-3.897	4.630	5.855
O	6.387	1.750	11.622	O	6.606	-0.086	4.532	Si	1.159	4.630	5.855
O	-3.622	7.340	11.608	O	-3.506	5.475	4.532	Si	-8.954	10.191	5.855
O	1.604	7.473	11.684	O	1.550	5.475	4.532	Si	-3.897	10.191	5.855
O	3.598	0.155	11.517	O	1.626	1.918	2.835	Si	2.531	0.892	3.706
O	8.512	0.092	11.618	O	6.683	1.918	2.835	Si	7.587	0.892	3.706
O	-1.622	5.637	11.550	O	-3.430	7.479	2.835	Si	-2.525	6.453	3.706
O	3.623	5.715	11.542	O	1.626	7.479	2.835	Si	2.531	6.453	3.706
O	-0.063	3.652	10.733	O	3.486	-0.018	2.756	Si	1.287	2.726	1.468
O	4.976	3.638	10.656	O	8.542	-0.018	2.756	Si	6.343	2.726	1.468
O	-5.155	9.182	10.671	O	-1.570	5.543	2.756	Si	-3.769	8.287	1.468
O	-0.069	9.224	10.761	O	3.486	5.543	2.756	Si	1.287	8.287	1.468
O	-2.578	3.687	10.015	O	-0.024	3.652	1.716	Si	-1.284	4.614	1.466
O	2.440	3.881	10.009	O	5.033	3.652	1.716	Si	3.772	4.614	1.466
O	-7.698	9.420	10.008	O	-5.080	9.213	1.716	Si	-6.340	10.175	1.466
O	-2.609	9.367	10.064	O	-0.024	9.213	1.716	Si	-1.284	10.175	1.466

Table 4.B.3: Coordinates for the most stable *R*-alanine adsorbed on hydroxylated α-quartz $(10\bar{1}0)$. This configuration is shown in Fig. 4.3(a).

Atom	x	y	z	Atom	x	y	z	Atom	x	y	z
C	0.147	4.910	16.039	O	-7.697	9.419	10.005	O	-0.024	9.213	1.716
C	-0.535	4.718	14.684	O	-2.607	9.366	10.061	O	-2.562	3.723	1.084
C	-0.102	3.403	14.038	O	0.988	1.877	9.031	O	2.494	3.723	1.084
H	-0.481	6.723	14.134	O	6.010	1.843	8.998	O	-7.618	9.284	1.084
H	0.736	5.837	13.468	O	-4.054	7.457	8.982	O	-2.562	9.284	1.084
H	-1.622	4.656	14.810	O	0.942	7.405	9.085	O	1.164	1.699	0.219
H	1.396	2.691	13.045	O	4.162	-0.087	8.929	O	6.221	1.699	0.219
H	-0.196	5.838	16.512	O	9.237	-0.036	9.040	O	-3.892	7.260	0.219
H	-0.089	4.080	16.716	O	-0.912	5.472	8.985	O	1.164	7.260	0.219
H	1.235	4.956	15.918	O	4.198	5.527	8.959	O	4.085	0.041	0.174
N	-0.257	5.813	13.722	O	-0.963	1.918	7.259	O	9.141	0.041	0.174
O	-0.841	2.444	13.859	O	4.058	1.917	7.249	O	-0.972	5.602	0.174
O	1.193	3.443	13.691	O	-6.027	7.493	7.249	O	4.085	5.602	0.174
				O	-0.960	7.481	7.263	Si	1.252	2.823	10.318
				O	0.929	0.079	7.103	Si	6.273	2.728	10.332
H	4.432	0.601	11.801	O	6.001	0.099	7.072	Si	-3.823	8.323	10.341
H	-0.894	0.519	12.142	O	-4.105	5.663	7.075	Si	1.239	8.350	10.381
H	-1.029	5.695	12.439	O	0.934	5.646	7.102	Si	-1.299	4.629	10.326
H	-5.656	6.156	11.836	O	-2.725	3.583	6.237	Si	3.818	4.674	10.271
H	2.355	1.219	11.578	O	2.332	3.589	6.233	Si	-6.322	10.204	10.261
H	7.165	1.137	11.701	O	-7.780	9.150	6.233	Si	-1.269	10.213	10.352
H	-2.854	6.681	11.599	O	-2.723	9.145	6.239	Si	0.017	0.954	8.112
H	2.362	6.828	11.638	O	-0.194	3.807	5.545	Si	5.058	0.946	8.067
H	0.392	1.075	0.160	O	4.862	3.807	5.545	Si	-5.019	6.540	8.073
H	5.448	1.075	0.160	O	-5.251	9.368	5.545	Si	0.002	6.497	8.123
H	-4.664	6.636	0.160	O	-0.194	9.368	5.545	Si	-1.365	2.762	5.939
H	0.392	6.636	0.160	O	-1.579	1.744	4.697	Si	3.686	2.767	5.930
H	3.300	0.533	-0.147	O	3.477	1.744	4.697	Si	-6.424	8.330	5.930
H	8.356	0.533	-0.147	O	-6.635	7.305	4.697	Si	-1.363	8.321	5.942
H	-1.756	6.094	-0.147	O	-1.579	7.305	4.697	Si	-3.897	4.630	5.855
H	3.300	6.094	-0.147	O	1.550	-0.086	4.532	Si	1.159	4.630	5.855
O	1.605	1.888	11.619	O	6.606	-0.086	4.532	Si	-8.954	10.191	5.855
O	6.384	1.748	11.620	O	-3.506	5.475	4.532	Si	-3.897	10.191	5.855
O	-3.623	7.337	11.604	O	1.550	5.475	4.532	Si	2.531	0.892	3.706
O	1.606	7.472	11.684	O	1.626	1.918	2.835	Si	7.587	0.892	3.706
O	3.601	0.159	11.512	O	6.683	1.918	2.835	Si	-2.525	6.453	3.706
O	8.512	0.091	11.620	O	-3.430	7.479	2.835	Si	2.531	6.453	3.706
O	-1.626	5.635	11.545	O	1.626	7.479	2.835	Si	1.287	2.726	1.468
O	3.629	5.713	11.545	O	3.486	-0.018	2.756	Si	6.343	2.726	1.468
O	-0.063	3.651	10.731	O	8.542	-0.018	2.756	Si	-3.769	8.287	1.468
O	4.978	3.639	10.656	O	-1.570	5.543	2.756	Si	1.287	8.287	1.468
O	-5.154	9.182	10.673	O	3.486	5.543	2.756	Si	-1.284	4.614	1.466
O	-0.069	9.223	10.764	O	-0.024	3.652	1.716	Si	3.772	4.614	1.466
O	-2.577	3.684	10.010	O	5.033	3.652	1.716	Si	-6.340	10.175	1.466
O	2.441	3.883	10.006	O	-5.080	9.213	1.716	Si	-1.284	10.175	1.466

Table 4.B.4: Coordinates for the most stable *S*-alanine adsorbed on hydroxylated α-quartz $(10\bar{1}0)$. This configuration is shown in Fig. 4.3(b).

Atom	x	y	z	Atom	x	y	z	Atom	x	y	z
C	-2.071	4.635	15.000	O	-7.701	9.419	10.005	O	-0.024	9.213	1.716
C	-0.589	4.664	14.680	O	-2.603	9.384	10.081	O	-2.562	3.723	1.084
C	-0.101	3.367	14.030	O	1.005	1.901	9.016	O	2.494	3.723	1.084
H	-0.516	6.678	14.165	O	6.004	1.837	9.003	O	-7.618	9.284	1.084
H	0.709	5.802	13.499	O	-4.037	7.478	8.964	O	-2.562	9.284	1.084
H	-0.005	4.783	15.609	O	0.942	7.405	9.089	O	1.164	1.699	0.219
H	1.433	2.720	13.062	O	4.154	-0.101	8.906	O	6.221	1.699	0.219
H	-2.663	4.485	14.091	O	9.256	-0.016	9.064	O	-3.892	7.260	0.219
H	-2.299	3.817	15.689	O	-0.914	5.475	8.981	O	1.164	7.260	0.219
H	-2.377	5.579	15.469	O	4.205	5.553	8.967	O	4.085	0.041	0.174
N	-0.285	5.777	13.740	O	-0.962	1.917	7.260	O	9.141	0.041	0.174
O	-0.798	2.385	13.815	O	4.059	1.919	7.248	O	-0.972	5.602	0.174
O	1.200	3.459	13.711	O	-6.027	7.500	7.249	O	4.085	5.602	0.174
				O	-0.959	7.483	7.262	Si	1.269	2.841	10.311
				O	0.929	0.078	7.105	Si	6.278	2.731	10.329
H	4.440	0.604	11.779	O	6.004	0.102	7.070	Si	-3.818	8.333	10.333
H	-0.892	0.548	12.154	O	-4.105	5.664	7.074	Si	1.239	8.347	10.386
H	-1.046	5.681	12.442	O	0.936	5.647	7.102	Si	-1.294	4.629	10.320
H	-5.624	6.183	11.827	O	-2.725	3.582	6.239	Si	3.834	4.694	10.277
H	2.370	1.237	11.567	O	2.332	3.589	6.232	Si	-6.325	10.202	10.247
H	7.175	1.146	11.703	O	-7.780	9.150	6.232	Si	-1.259	10.225	10.369
H	-2.863	6.677	11.586	O	-2.723	9.145	6.239	Si	0.027	0.963	8.116
H	2.375	6.835	11.649	O	-0.194	3.807	5.545	Si	5.056	0.944	8.063
H	0.392	1.075	0.160	O	4.862	3.807	5.545	Si	-5.010	6.553	8.069
H	5.448	1.075	0.160	O	-5.251	9.368	5.545	Si	0.004	6.500	8.121
H	-4.664	6.636	0.160	O	-0.194	9.368	5.545	Si	-1.365	2.762	5.940
H	0.392	6.636	0.160	O	-1.579	1.744	4.697	Si	3.686	2.768	5.929
H	3.300	0.533	-0.147	O	3.477	1.744	4.697	Si	-6.425	8.331	5.929
H	8.356	0.533	-0.147	O	-6.635	7.305	4.697	Si	-1.363	8.321	5.941
H	-1.756	6.094	-0.147	O	-1.579	7.305	4.697	Si	-3.897	4.630	5.855
H	3.300	6.094	-0.147	O	1.550	-0.086	4.532	Si	1.159	4.630	5.855
O	1.627	1.912	11.614	O	6.606	-0.086	4.532	Si	-8.954	10.191	5.855
O	6.398	1.762	11.624	O	-3.506	5.475	4.532	Si	-3.897	10.191	5.855
O	-3.634	7.329	11.587	O	1.550	5.475	4.532	Si	2.531	0.892	3.706
O	1.610	7.469	11.688	O	1.626	1.918	2.835	Si	7.587	0.892	3.706
O	3.606	0.170	11.488	O	6.683	1.918	2.835	Si	-2.525	6.453	3.706
O	8.521	0.102	11.636	O	-3.430	7.479	2.835	Si	2.531	6.453	3.706
O	-1.630	5.630	11.541	O	1.626	7.479	2.835	Si	1.287	2.726	1.468
O	3.659	5.731	11.554	O	3.486	-0.018	2.756	Si	6.343	2.726	1.468
O	-0.053	3.658	10.724	O	8.542	-0.018	2.756	Si	-3.769	8.287	1.468
O	4.992	3.653	10.654	O	-1.570	5.543	2.756	Si	1.287	8.287	1.468
O	-5.155	9.185	10.666	O	3.486	5.543	2.756	Si	-1.284	4.614	1.466
O	-0.068	9.220	10.772	O	-0.024	3.652	1.716	Si	3.772	4.614	1.466
O	-2.569	3.680	10.000	O	5.033	3.652	1.716	Si	-6.340	10.175	1.466
O	2.455	3.908	10.008	O	-5.080	9.213	1.716	Si	-1.284	10.175	1.466

Appendix 4.C: Coordinates for serine and cysteine adsorption adsorbed on hydroxylated α-quartz $(10\bar{1}0)$

Similar to Appendix 4.B but for serine and cysteine.

Table 4.C.1: Coordinates for the most stable *R*-serine adsorbed on hydroxylated α-quartz $(10\bar{1}0)$. This configuration is shown in Fig. 4.4(a).

Atom	x	y	z	Atom	x	y	z	Atom	x	y	z
C	0.767	3.584	15.011	O	-7.684	9.373	10.009	O	-0.024	9.213	1.716
C	-0.680	3.973	14.699	O	-2.567	9.318	10.002	O	-2.562	3.723	1.084
C	-1.402	2.893	13.890	O	1.015	1.902	9.023	O	2.494	3.723	1.084
H	0.229	5.577	13.784	O	5.987	1.782	9.035	O	-7.618	9.284	1.084
H	-1.199	5.990	14.534	O	-4.063	7.453	8.973	O	-2.562	9.284	1.084
H	1.147	4.256	15.792	O	0.937	7.402	9.097	O	1.164	1.699	0.219
H	0.797	2.555	15.398	O	4.120	-0.105	8.907	O	6.221	1.699	0.219
H	1.502	3.011	13.252	O	9.252	-0.001	9.069	O	-3.892	7.260	0.219
H	-1.235	4.058	15.647	O	-0.957	5.519	8.983	O	1.164	7.260	0.219
H	-3.085	2.602	12.957	O	4.223	5.499	8.942	O	4.085	0.041	0.174
N	-0.731	5.273	13.980	O	-0.958	1.921	7.262	O	9.141	0.041	0.174
O	-0.873	1.834	13.549	O	4.063	1.923	7.250	O	-0.972	5.602	0.174
O	-2.659	3.238	13.624	O	-6.028	7.480	7.241	O	4.085	5.602	0.174
O	1.617	3.757	13.889	O	-0.955	7.495	7.259	Si	1.251	2.854	10.324
				O	0.929	0.078	7.106	Si	6.257	2.749	10.292
H	4.372	0.530	11.874	O	5.996	0.095	7.075	Si	-3.811	8.325	10.319
H	-1.143	0.535	12.245	O	-4.078	5.666	7.073	Si	1.231	8.335	10.405
H	-1.324	5.397	12.513	O	0.925	5.640	7.109	Si	-1.325	4.634	10.290
H	-5.622	6.199	11.813	O	-2.726	3.578	6.233	Si	3.810	4.695	10.276
H	2.315	1.274	11.607	O	2.333	3.590	6.230	Si	-6.333	10.189	10.254
H	7.176	1.066	11.561	O	-7.779	9.149	6.231	Si	-1.269	10.209	10.351
H	-2.878	6.681	11.595	O	-2.723	9.147	6.234	Si	0.034	0.970	8.122
H	2.319	6.814	11.700	O	-0.194	3.807	5.545	Si	5.033	0.923	8.064
H	0.392	1.075	0.160	O	4.862	3.807	5.545	Si	-5.013	6.530	8.063
H	5.448	1.075	0.160	O	-5.251	9.368	5.545	Si	-0.002	6.510	8.123
H	-4.664	6.636	0.160	O	-0.194	9.368	5.545	Si	-1.363	2.761	5.940
H	0.392	6.636	0.160	O	-1.579	1.744	4.697	Si	3.686	2.769	5.929
H	3.300	0.533	-0.147	O	3.477	1.744	4.697	Si	-6.423	8.328	5.930
H	8.356	0.533	-0.147	O	-6.635	7.305	4.697	Si	-1.363	8.324	5.938
H	-1.756	6.094	-0.147	O	-1.579	7.305	4.697	Si	-3.897	4.630	5.855
H	3.300	6.094	-0.147	O	1.550	-0.086	4.532	Si	1.159	4.630	5.855
O	1.613	1.979	11.640	O	6.606	-0.086	4.532	Si	-8.954	10.191	5.855
O	6.488	1.808	11.627	O	-3.506	5.475	4.532	Si	-3.897	10.191	5.855
O	-3.639	7.341	11.591	O	1.550	5.475	4.532	Si	2.531	0.892	3.706
O	1.568	7.462	11.714	O	1.626	1.918	2.835	Si	7.587	0.892	3.706
O	3.558	0.133	11.505	O	6.683	1.918	2.835	Si	-2.525	6.453	3.706
O	8.392	0.049	11.605	O	-3.430	7.479	2.835	Si	2.531	6.453	3.706
O	-1.671	5.598	11.544	O	1.626	7.479	2.835	Si	1.287	2.726	1.468
O	3.662	5.751	11.529	O	3.486	-0.018	2.756	Si	6.343	2.726	1.468
O	-0.104	3.649	10.684	O	8.542	-0.018	2.756	Si	-3.769	8.287	1.468
O	4.954	3.621	10.663	O	-1.570	5.543	2.756	Si	1.287	8.287	1.468
O	-5.115	9.224	10.661	O	3.486	5.543	2.756	Si	-1.284	4.614	1.466
O	-0.057	9.245	10.775	O	-0.024	3.652	1.716	Si	3.772	4.614	1.466

O	-2.608	3.698	9.930	O	5.033	3.652	1.716	Si	-6.340	10.175	1.466
O	2.411	3.953	10.006	O	-5.080	9.213	1.716	Si	-1.284	10.175	1.466

Table 4.C.2: Coordinates for the most stable *S*-serine adsorbed on hydroxylated α-quartz $(10\bar{1}0)$. This configuration is shown in Fig. 4.4(b).

Atom	x	y	z	Atom	x	y	z	Atom	x	y	z
C	-2.151	4.636	15.000	O	-7.707	9.421	10.008	O	-0.024	9.213	1.716
C	-0.651	4.652	14.701	O	-2.607	9.380	10.063	O	-2.562	3.723	1.084
C	-0.203	3.340	14.059	O	1.003	1.905	9.022	O	2.494	3.723	1.084
H	-0.508	6.665	14.200	O	5.999	1.839	9.001	O	-7.618	9.284	1.084
H	0.677	5.746	13.527	O	-4.039	7.475	8.963	O	-2.562	9.284	1.084
H	-0.105	4.749	15.655	O	0.938	7.405	9.089	O	1.164	1.699	0.219
H	1.318	2.644	13.074	O	4.151	-0.101	8.906	O	6.221	1.699	0.219
H	-2.710	4.432	14.073	O	9.254	-0.008	9.069	O	-3.892	7.260	0.219
H	-2.378	2.811	15.625	O	-0.917	5.471	8.986	O	1.164	7.260	0.219
H	-2.456	5.622	15.375	O	4.202	5.554	8.965	O	4.085	0.041	0.174
N	-0.317	5.757	13.769	O	-0.961	1.919	7.260	O	9.141	0.041	0.174
O	-0.948	2.383	13.858	O	4.057	1.918	7.247	O	-0.972	5.602	0.174
O	1.090	3.378	13.732	O	-6.030	7.501	7.248	O	4.085	5.602	0.174
O	-2.471	3.700	16.021	O	-0.961	7.481	7.262	Si	1.277	2.840	10.318
				O	0.929	0.078	7.108	Si	6.280	2.722	10.330
H	4.439	0.612	11.772	O	6.003	0.102	7.070	Si	-3.822	8.333	10.329
H	-0.927	0.531	12.164	O	-4.106	5.663	7.075	Si	1.233	8.348	10.386
H	-1.072	5.673	12.444	O	0.933	5.644	7.105	Si	-1.287	4.620	10.325
H	-5.633	6.185	11.836	O	-2.725	3.583	6.241	Si	3.841	4.696	10.278
H	2.367	1.231	11.580	O	2.332	3.590	6.233	Si	-6.329	10.203	10.248
H	7.137	1.119	11.704	O	-7.781	9.151	6.233	Si	-1.267	10.223	10.365
H	-2.869	6.678	11.583	O	-2.723	9.145	6.240	Si	0.027	0.966	8.118
H	2.365	6.835	11.651	O	-0.194	3.807	5.545	Si	5.053	0.943	8.062
H	0.392	1.075	0.160	O	4.862	3.807	5.545	Si	-5.014	6.553	8.067
H	5.448	1.075	0.160	O	-5.251	9.368	5.545	Si	0.000	6.497	8.123
H	-4.664	6.636	0.160	O	-0.194	9.368	5.545	Si	-1.365	2.762	5.939
H	0.392	6.636	0.160	O	-1.579	1.744	4.697	Si	3.686	2.768	5.928
H	3.300	0.533	-0.147	O	3.477	1.744	4.697	Si	-6.425	8.332	5.927
H	8.356	0.533	-0.147	O	-6.635	7.305	4.697	Si	-1.364	8.321	5.941
H	-1.756	6.094	-0.147	O	-1.579	7.305	4.697	Si	-3.897	4.630	5.855
H	3.300	6.094	-0.147	O	1.550	-0.086	4.532	Si	1.159	4.630	5.855
O	1.621	1.905	11.622	O	6.606	-0.086	4.532	Si	-8.954	10.191	5.855
O	6.364	1.741	11.623	O	-3.506	5.475	4.532	Si	-3.897	10.191	5.855
O	-3.635	7.333	11.586	O	1.550	5.475	4.532	Si	2.531	0.892	3.706
O	1.600	7.470	11.688	O	1.626	1.918	2.835	Si	7.587	0.892	3.706
O	3.604	0.172	11.488	O	6.683	1.918	2.835	Si	-2.525	6.453	3.706
O	8.492	0.085	11.639	O	-3.430	7.479	2.835	Si	2.531	6.453	3.706
O	-1.643	5.620	11.544	O	1.626	7.479	2.835	Si	1.287	2.726	1.468
O	3.654	5.731	11.554	O	3.486	-0.018	2.756	Si	6.343	2.726	1.468
O	-0.030	3.678	10.744	O	8.542	-0.018	2.756	Si	-3.769	8.287	1.468
O	5.015	3.673	10.654	O	-1.570	5.543	2.756	Si	1.287	8.287	1.468
O	-5.157	9.185	10.665	O	3.486	5.543	2.756	Si	-1.284	4.614	1.466
O	-0.073	9.224	10.770	O	-0.024	3.652	1.716	Si	3.772	4.614	1.466
O	-2.537	3.637	10.011	O	5.033	3.652	1.716	Si	-6.340	10.175	1.466
O	2.471	3.895	10.011	O	-5.080	9.213	1.716	Si	-1.284	10.175	1.466

Table 4.C.3: Coordinates for the most stable *R*-cysteine adsorbed on hydroxylated α-quartz $(10\bar{1}0)$. This configuration is shown in Fig. 4.5(a).

Atom	x	y	z	Atom	x	y	z	Atom	x	y	z
C	-2.137	4.693	14.986	O	-7.703	9.419	10.009	O	-0.024	9.213	1.716
C	-0.642	4.657	14.687	O	-2.605	9.379	10.067	O	-2.562	3.723	1.084
C	-0.201	3.350	14.018	O	1.004	1.904	9.021	O	2.494	3.723	1.084
H	-0.474	6.670	14.174	O	5.999	1.839	9.000	O	-7.618	9.284	1.084
H	0.697	5.732	13.500	O	-4.038	7.474	8.963	O	-2.562	9.284	1.084
H	-0.079	4.747	15.630	O	0.939	7.404	9.089	O	1.164	1.699	0.219
H	1.341	2.670	13.066	O	4.153	-0.101	8.907	O	6.221	1.699	0.219
H	-2.715	4.459	14.086	O	9.254	-0.007	9.070	O	-3.892	7.260	0.219
H	-2.441	2.456	15.684	O	-0.917	5.471	8.982	O	1.164	7.260	0.219
H	-2.416	5.704	15.310	O	4.202	5.555	8.965	O	4.085	0.041	0.174
N	-0.296	5.758	13.747	O	-0.960	1.919	7.261	O	9.141	0.041	0.174
O	-0.945	2.416	13.741	O	4.057	1.918	7.247	O	-0.972	5.602	0.174
O	1.106	3.390	13.738	O	-6.029	7.502	7.249	O	4.085	5.602	0.174
S	-2.647	3.607	16.354	O	-0.961	7.482	7.262	Si	1.278	2.841	10.316
				O	0.928	0.078	7.108	Si	6.281	2.722	10.330
H	4.441	0.610	11.774	O	6.003	0.102	7.070	Si	-3.821	8.333	10.329
H	-0.931	0.552	12.154	O	-4.106	5.664	7.075	Si	1.235	8.349	10.385
H	-1.063	5.678	12.433	O	0.934	5.645	7.104	Si	-1.286	4.620	10.321
H	-5.631	6.186	11.834	O	-2.725	3.583	6.239	Si	3.842	4.697	10.278
H	2.369	1.235	11.581	O	2.332	3.590	6.232	Si	-6.327	10.204	10.249
H	7.137	1.120	11.706	O	-7.780	9.151	6.231	Si	-1.266	10.224	10.366
H	-2.866	6.679	11.581	O	-2.723	9.145	6.238	Si	0.027	0.966	8.118
H	2.368	6.836	11.649	O	-0.194	3.807	5.545	Si	5.053	0.943	8.062
H	0.392	1.075	0.160	O	4.862	3.807	5.545	Si	-5.013	6.553	8.067
H	5.448	1.075	0.160	O	-5.251	9.368	5.545	Si	0.001	6.498	8.122
H	-4.664	6.636	0.160	O	-0.194	9.368	5.545	Si	-1.365	2.762	5.939
H	0.392	6.636	0.160	O	-1.579	1.744	4.697	Si	3.686	2.768	5.928
H	3.300	0.533	-0.147	O	3.477	1.744	4.697	Si	-6.425	8.332	5.927
H	8.356	0.533	-0.147	O	-6.635	7.305	4.697	Si	-1.363	8.321	5.940
H	-1.756	6.094	-0.147	O	-1.579	7.305	4.697	Si	-3.897	4.630	5.855
H	3.300	6.094	-0.147	O	1.550	-0.086	4.532	Si	1.159	4.630	5.855
O	1.624	1.910	11.621	O	6.606	-0.086	4.532	Si	-8.954	10.191	5.855
O	6.363	1.740	11.622	O	-3.506	5.475	4.532	Si	-3.897	10.191	5.855
O	-3.634	7.333	11.587	O	1.550	5.475	4.532	Si	2.531	0.892	3.706
O	1.602	7.470	11.687	O	1.626	1.918	2.835	Si	7.587	0.892	3.706
O	3.606	0.172	11.489	O	6.683	1.918	2.835	Si	-2.525	6.453	3.706
O	8.493	0.085	11.640	O	-3.430	7.479	2.835	Si	2.531	6.453	3.706
O	-1.642	5.623	11.537	O	1.626	7.479	2.835	Si	1.287	2.726	1.468
O	3.655	5.732	11.554	O	3.486	-0.018	2.756	Si	6.343	2.726	1.468
O	-0.028	3.680	10.738	O	8.542	-0.018	2.756	Si	-3.769	8.287	1.468
O	5.017	3.674	10.653	O	-1.570	5.543	2.756	Si	1.287	8.287	1.468
O	-5.155	9.186	10.664	O	3.486	5.543	2.756	Si	-1.284	4.614	1.466
O	-0.071	9.225	10.769	O	-0.024	3.652	1.716	Si	3.772	4.614	1.466
O	-2.536	3.636	10.012	O	5.033	3.652	1.716	Si	-6.340	10.175	1.466
O	2.472	3.895	10.011	O	-5.080	9.213	1.716	Si	-1.284	10.175	1.466

Table 4.C.4: Coordinates for the most stable *S*-cysteine adsorbed on hydroxylated α-quartz $(10\bar{1}0)$. This configuration is shown in Fig. 4.5(b).

Atom	x	y	z	Atom	x	y	z	Atom	x	y	z
C	0.059	4.716	16.106	O	-7.703	9.419	10.010	O	-0.024	9.213	1.716
C	-0.587	4.574	14.715	O	-2.604	9.384	10.075	O	-2.562	3.723	1.084
C	-0.088	3.306	14.022	O	1.009	1.904	9.017	O	2.494	3.723	1.084
H	-0.636	6.582	14.297	O	6.003	1.835	8.998	O	-7.618	9.284	1.084
H	0.649	5.814	13.593	O	-4.036	7.478	8.963	O	-2.562	9.284	1.084
H	-1.671	4.464	14.832	O	0.938	7.406	9.091	O	1.164	1.699	0.219
H	1.453	2.694	13.033	O	4.153	-0.103	8.904	O	6.221	1.699	0.219
H	-0.199	3.846	16.722	O	9.255	-0.006	9.073	O	-3.892	7.260	0.219
H	1.150	4.756	16.025	O	-0.918	5.473	9.001	O	1.164	7.260	0.219
H	0.515	6.994	16.732	O	4.205	5.558	8.964	O	4.085	0.041	0.174
N	-0.346	5.721	13.821	O	-0.960	1.919	7.261	O	9.141	0.041	0.174
O	-0.792	2.335	13.777	O	4.056	1.918	7.247	O	-0.972	5.602	0.174
O	1.210	3.410	13.711	O	-6.027	7.503	7.249	O	4.085	5.602	0.174
S	-0.525	6.189	17.021	O	-0.961	7.479	7.264	Si	1.269	2.849	10.309
				O	0.928	0.077	7.107	Si	6.260	2.726	10.327
H	4.455	0.610	11.765	O	6.004	0.101	7.069	Si	-3.817	8.334	10.331
H	-0.929	0.550	12.175	O	-4.105	5.665	7.074	Si	1.234	8.350	10.389
H	-1.091	5.636	12.471	O	0.929	5.641	7.107	Si	-1.303	4.617	10.334
H	-5.621	6.189	11.821	O	-2.725	3.583	6.239	Si	3.822	4.703	10.272
H	2.404	1.244	11.553	O	2.333	3.590	6.232	Si	-6.324	10.202	10.247
H	7.138	1.132	11.704	O	-7.780	9.151	6.232	Si	-1.264	10.230	10.374
H	-2.868	6.677	11.595	O	-2.723	9.145	6.239	Si	0.028	0.965	8.118
H	2.367	6.837	11.653	O	-0.194	3.807	5.545	Si	5.054	0.942	8.061
H	0.392	1.075	0.160	O	4.862	3.807	5.545	Si	-5.010	6.555	8.067
H	5.448	1.075	0.160	O	-5.251	9.368	5.545	Si	-0.001	6.495	8.129
H	-4.664	6.636	0.160	O	-0.194	9.368	5.545	Si	-1.364	2.762	5.940
H	0.392	6.636	0.160	O	-1.579	1.744	4.697	Si	3.686	2.768	5.929
H	3.300	0.533	-0.147	O	3.477	1.744	4.697	Si	-6.425	8.332	5.928
H	8.356	0.533	-0.147	O	-6.635	7.305	4.697	Si	-1.363	8.320	5.943
H	-1.756	6.094	-0.147	O	-1.579	7.305	4.697	Si	-3.897	4.630	5.855
H	3.300	6.094	-0.147	O	1.550	-0.086	4.532	Si	1.159	4.630	5.855
O	1.665	1.927	11.606	O	6.606	-0.086	4.532	Si	-8.954	10.191	5.855
O	6.359	1.745	11.619	O	-3.506	5.475	4.532	Si	-3.897	10.191	5.855
O	-3.635	7.331	11.586	O	1.550	5.475	4.532	Si	2.531	0.892	3.706
O	1.602	7.471	11.691	O	1.626	1.918	2.835	Si	7.587	0.892	3.706
O	3.617	0.173	11.486	O	6.683	1.918	2.835	Si	-2.525	6.453	3.706
O	8.499	0.096	11.645	O	-3.430	7.479	2.835	Si	2.531	6.453	3.706
O	-1.646	5.605	11.567	O	1.626	7.479	2.835	Si	1.287	2.726	1.468
O	3.661	5.736	11.553	O	3.486	-0.018	2.756	Si	6.343	2.726	1.468
O	-0.064	3.645	10.736	O	8.542	-0.018	2.756	Si	-3.769	8.287	1.468
O	4.967	3.644	10.637	O	-1.570	5.543	2.756	Si	1.287	8.287	1.468
O	-5.155	9.183	10.665	O	3.486	5.543	2.756	Si	-1.284	4.614	1.466
O	-0.070	9.228	10.773	O	-0.024	3.652	1.716	Si	3.772	4.614	1.466
O	-2.581	3.672	10.011	O	5.033	3.652	1.716	Si	-6.340	10.175	1.466
O	2.425	3.948	10.002	O	-5.080	9.213	1.716	Si	-1.284	10.175	1.466

Appendix 4.D: Coordinates for aspartic acid and asparagine adsorption adsorbed on hydroxylated α-quartz $(10\bar{1}0)$

Similar to Appendix 4.B but for aspartic acid and asparagine.

Table 4.D.1: Coordinates for the most stable *R*-aspartic acid adsorbed on hydroxylated α-quartz $(10\bar{1}0)$. This configuration is shown in Fig. 4.6(a).

Atom	x	y	z	Atom	x	y	z	Atom	x	y	z
C	0.044	3.893	15.470	O	-2.284	3.512	10.054	O	-5.080	9.213	1.716
C	-1.385	4.368	15.150	O	2.792	3.541	9.823	O	-0.024	9.213	1.716
C	-2.255	3.216	14.627	O	-7.655	9.431	9.953	O	-2.562	3.723	1.084
C	0.859	3.551	14.240	O	-2.600	9.441	9.909	O	2.494	3.723	1.084
H	-0.613	6.165	14.479	O	1.007	1.906	8.919	O	-7.618	9.284	1.084
H	-2.243	6.028	14.255	O	6.049	1.900	9.002	O	-2.562	9.284	1.084
H	0.569	4.677	16.024	O	-3.983	7.445	8.964	O	1.164	1.699	0.219
H	-1.838	4.641	16.119	O	0.973	7.427	9.055	O	6.221	1.699	0.219
H	-3.389	2.785	13.106	O	4.246	-0.066	8.968	O	-3.892	7.260	0.219
H	-0.040	3.000	16.100	O	9.250	0.035	9.049	O	1.164	7.260	0.219
H	1.018	2.194	12.853	O	-0.895	5.509	8.999	O	4.085	0.041	0.174
N	-1.359	5.514	14.224	O	-5.944	5.689	9.152	O	9.141	0.041	0.174
O	-2.310	2.124	15.169	O	-1.001	1.916	7.243	O	-0.972	5.602	0.174
O	-2.961	3.576	13.543	O	4.099	1.914	7.244	O	4.085	5.602	0.174
O	1.764	4.265	13.799	O	-6.013	7.489	7.258	Si	1.429	2.765	10.204
O	0.482	2.395	13.701	O	-0.959	7.484	7.258	Si	6.419	2.768	10.315
				O	0.916	0.075	7.088	Si	-3.737	8.340	10.301
				O	6.040	0.108	7.078	Si	1.276	8.370	10.351
H	4.453	0.503	11.873	O	-4.168	5.596	7.128	Si	-1.102	4.601	10.330
H	-0.929	0.239	12.263	O	0.939	5.646	7.100	Si	3.893	4.621	10.329
H	-1.335	5.386	12.552	O	-2.721	3.595	6.231	Si	-6.266	10.169	10.257
H	2.894	4.895	12.383	O	2.334	3.585	6.235	Si	-1.257	10.220	10.299
H	2.411	1.127	11.529	O	-7.778	9.148	6.237	Si	0.008	0.973	8.073
H	7.199	1.095	11.662	O	-2.724	9.142	6.231	Si	5.108	0.967	8.077
H	-2.636	6.766	11.530	O	-0.194	3.807	5.545	Si	-5.022	6.546	8.124
H	2.310	6.807	11.652	O	4.862	3.807	5.545	Si	0.020	6.518	8.115
H	0.392	1.075	0.160	O	-5.251	9.368	5.545	Si	-1.371	2.769	5.927
H	5.448	1.075	0.160	O	-0.194	9.368	5.545	Si	3.693	2.765	5.933
H	-4.664	6.636	0.160	O	-1.579	1.744	4.697	Si	-6.421	8.324	5.938
H	0.392	6.636	0.160	O	3.477	1.744	4.697	Si	-1.363	8.324	5.938
H	3.300	0.533	-0.147	O	-6.635	7.305	4.697	Si	-3.897	4.630	5.855
H	8.356	0.533	-0.147	O	-1.579	7.305	4.697	Si	1.159	4.630	5.855
H	-1.756	6.094	-0.147	O	1.550	-0.086	4.532	Si	-8.954	10.191	5.855
H	3.300	6.094	-0.147	O	6.606	-0.086	4.532	Si	-3.897	10.191	5.855
O	1.645	1.783	11.501	O	-3.506	5.475	4.532	Si	2.531	0.892	3.706
O	6.456	1.769	11.631	O	1.550	5.475	4.532	Si	7.587	0.892	3.706
O	-3.346	7.467	11.583	O	1.626	1.918	2.835	Si	-2.525	6.453	3.706
O	1.640	7.537	11.668	O	6.683	1.918	2.835	Si	2.531	6.453	3.706
O	3.631	0.084	11.541	O	-3.430	7.479	2.835	Si	1.287	2.726	1.468
O	8.487	0.043	11.613	O	1.626	7.479	2.835	Si	6.343	2.726	1.468
O	-1.460	5.590	11.553	O	3.486	-0.018	2.756	Si	-3.769	8.287	1.468
O	3.321	5.401	11.648	O	8.542	-0.018	2.756	Si	1.287	8.287	1.468
O	0.265	3.784	10.657	O	-1.570	5.543	2.756	Si	-1.284	4.614	1.466

O	5.266	3.837	10.672	O	3.486	5.543	2.756	Si	3.772	4.614	1.466
O	-5.101	9.143	10.663	O	-0.024	3.652	1.716	Si	-6.340	10.175	1.466
O	-0.047	9.248	10.702	O	5.033	3.652	1.716	Si	-1.284	10.175	1.466

Table 4.D.2: Coordinates for the most stable *S*-aspartic acid adsorbed on hydroxylated α-quartz $(10\bar{1}0)$.

This configuration is shown in Fig. 4.6(b).

Atom	x	y	z	Atom	x	y	z	Atom	x	y	z
C	-0.085	3.526	15.302	O	-2.292	3.464	10.103	O	-5.080	9.213	1.716
C	-0.282	5.004	14.937	O	2.782	3.573	9.914	O	-0.024	9.213	1.716
C	0.822	5.599	14.054	O	-7.668	9.504	9.943	O	-2.562	3.723	1.084
C	0.022	2.573	14.127	O	-2.582	9.456	9.990	O	2.494	3.723	1.084
H	-2.292	4.614	14.555	O	1.029	1.944	8.893	O	-7.618	9.284	1.084
H	-1.870	6.213	14.380	O	6.046	1.956	8.944	O	-2.562	9.284	1.084
H	-0.941	3.219	15.919	O	-3.957	7.445	8.967	O	1.164	1.699	0.219
H	-0.252	5.563	15.888	O	0.965	7.442	9.070	O	6.221	1.699	0.219
H	1.108	7.220	12.997	O	4.263	-0.048	8.948	O	-3.892	7.260	0.219
H	0.821	3.434	15.908	O	-0.820	0.041	9.087	O	1.164	7.260	0.219
H	1.347	1.743	13.039	O	-0.889	5.501	9.043	O	4.085	0.041	0.174
N	-1.561	5.250	14.231	O	-5.935	5.659	9.071	O	9.141	0.041	0.174
O	1.777	4.952	13.620	O	-1.001	1.909	7.247	O	-0.972	5.602	0.174
O	0.576	6.876	13.806	O	4.082	1.912	7.231	O	4.085	5.602	0.174
O	-0.920	2.310	13.372	O	-5.994	7.508	7.257	Si	1.430	2.747	10.232
O	1.237	2.050	14.000	O	-0.960	7.477	7.266	Si	6.387	2.742	10.324
				O	0.917	0.073	7.092	Si	-3.730	8.343	10.311
				O	6.047	0.114	7.069	Si	1.273	8.438	10.320
H	4.556	0.624	11.729	O	-4.133	5.623	7.106	Si	-1.117	4.559	10.359
H	-1.042	0.737	12.124	O	0.930	5.639	7.112	Si	3.917	4.657	10.308
H	-1.493	5.273	12.581	O	-2.723	3.590	6.228	Si	-6.243	10.201	10.241
H	2.945	5.211	12.358	O	2.335	3.590	6.229	Si	8.863	-0.847	10.370
H	2.476	1.089	11.450	O	-7.778	9.146	6.234	Si	0.023	0.982	8.084
H	7.066	1.044	11.670	O	-2.724	9.140	6.232	Si	5.116	0.989	8.056
H	-2.663	6.758	11.551	O	-0.194	3.807	5.545	Si	-4.994	6.559	8.106
H	2.488	6.890	11.496	O	4.862	3.807	5.545	Si	0.010	6.507	8.133
H	0.392	1.075	0.160	O	-5.251	9.368	5.545	Si	-1.370	2.765	5.932
H	5.448	1.075	0.160	O	-0.194	9.368	5.545	Si	3.690	2.768	5.928
H	-4.664	6.636	0.160	O	-1.579	1.744	4.697	Si	-6.419	8.327	5.936
H	0.392	6.636	0.160	O	3.477	1.744	4.697	Si	-1.362	8.320	5.943
H	3.300	0.533	-0.147	O	-6.635	7.305	4.697	Si	-3.897	4.630	5.855
H	8.356	0.533	-0.147	O	-1.579	7.305	4.697	Si	1.159	4.630	5.855
H	-1.756	6.094	-0.147	O	1.550	-0.086	4.532	Si	-8.954	10.191	5.855
H	3.300	6.094	-0.147	O	6.606	-0.086	4.532	Si	-3.897	10.191	5.855
O	1.660	1.687	11.459	O	-3.506	5.475	4.532	Si	2.531	0.892	3.706
O	6.300	1.672	11.554	O	1.550	5.475	4.532	Si	7.587	0.892	3.706
O	-3.373	7.456	11.599	O	1.626	1.918	2.835	Si	-2.525	6.453	3.706
O	1.761	7.581	11.624	O	6.683	1.918	2.835	Si	2.531	6.453	3.706
O	3.728	0.122	11.522	O	-3.430	7.479	2.835	Si	1.287	2.726	1.468
O	8.482	0.104	11.648	O	1.626	7.479	2.835	Si	6.343	2.726	1.468
O	-1.492	5.542	11.588	O	3.486	-0.018	2.756	Si	-3.769	8.287	1.468
O	3.423	5.583	11.565	O	8.542	-0.018	2.756	Si	1.287	8.287	1.468
O	0.255	3.753	10.680	O	-1.570	5.543	2.756	Si	-1.284	4.614	1.466
O	5.272	3.863	10.671	O	3.486	5.543	2.756	Si	3.772	4.614	1.466
O	-5.122	9.119	10.617	O	-0.024	3.652	1.716	Si	-6.340	10.175	1.466
O	-0.049	9.255	10.760	O	5.033	3.652	1.716	Si	-1.284	10.175	1.466

Table 4.D.3: Coordinates for the most stable *R*-aspragine adsorbed on hydroxylated α-quartz $(10\bar{1}0)$.

This configuration is shown in Fig. 4.7(a).

Atom	x	y	z	Atom	x	y	z	Atom	x	y	z
C	-2.811	6.189	15.577	O	-2.290	3.475	9.931	O	-5.080	9.213	1.716
C	-1.447	5.726	15.043	O	2.747	3.713	10.101	O	-0.024	9.213	1.716
C	-0.603	6.863	14.443	O	-7.631	9.400	10.014	O	-2.562	3.723	1.084
C	-3.799	6.621	14.498	O	-2.548	9.516	9.916	O	2.494	3.723	1.084
H	-2.431	4.090	14.226	O	1.081	2.009	8.942	O	-7.618	9.284	1.084
H	-0.777	4.040	14.036	O	6.019	1.847	9.020	O	-2.562	9.284	1.084
H	-3.266	5.361	16.132	O	-3.994	7.558	8.857	O	1.164	1.699	0.219
H	-0.874	5.367	15.915	O	1.035	7.376	9.070	O	6.221	1.699	0.219
H	0.879	7.006	13.147	O	4.166	-0.058	8.944	O	-3.892	7.260	0.219
H	-2.638	7.012	16.279	O	-0.709	0.032	9.067	O	1.164	7.260	0.219
H	-4.186	8.196	13.310	O	-0.896	5.534	9.009	O	4.085	0.041	0.174
H	-2.943	8.455	14.484	O	-5.864	5.649	9.122	O	9.141	0.041	0.174
N	-1.596	4.650	14.037	O	-0.948	1.918	7.252	O	-0.972	5.602	0.174
N	-3.777	7.937	14.206	O	4.088	1.928	7.245	O	4.085	5.602	0.174
O	-0.848	8.056	14.580	O	-6.057	7.472	7.251	Si	1.411	2.814	10.326
O	0.435	6.358	13.776	O	-0.927	7.506	7.271	Si	6.448	2.712	10.319
O	-4.562	5.797	13.951	O	0.986	0.110	7.082	Si	-3.708	8.409	10.207
				O	6.004	0.097	7.077	Si	1.311	8.327	10.359
H	4.457	0.557	11.860	O	-4.139	5.633	7.099	Si	-1.160	4.584	10.297
H	-0.616	0.530	11.953	O	0.938	5.642	7.099	Si	4.005	4.687	10.411
H	-1.631	5.165	12.508	O	-2.722	3.586	6.238	Si	-6.264	10.205	10.270
H	-5.737	5.719	12.454	O	2.334	3.588	6.231	Si	8.949	-0.889	10.305
H	2.289	1.156	11.627	O	-7.784	9.144	6.232	Si	0.112	1.026	8.092
H	7.324	1.112	11.675	O	-2.721	9.144	6.235	Si	5.073	0.958	8.075
H	-2.678	6.728	11.433	O	-0.194	3.807	5.545	Si	-5.014	6.564	8.092
H	2.472	6.815	11.676	O	4.862	3.807	5.545	Si	0.038	6.515	8.119
H	0.392	1.075	0.160	O	-5.251	9.368	5.545	Si	-1.363	2.762	5.939
H	5.448	1.075	0.160	O	-0.194	9.368	5.545	Si	3.690	2.768	5.930
H	-4.664	6.636	0.160	O	-1.579	1.744	4.697	Si	-6.427	8.326	5.933
H	0.392	6.636	0.160	O	3.477	1.744	4.697	Si	-1.361	8.323	5.942
H	3.300	0.533	-0.147	O	-6.635	7.305	4.697	Si	-3.897	4.630	5.855
H	8.356	0.533	-0.147	O	-1.579	7.305	4.697	Si	1.159	4.630	5.855
H	-1.756	6.094	-0.147	O	1.550	-0.086	4.532	Si	-8.954	10.191	5.855
H	3.300	6.094	-0.147	O	6.606	-0.086	4.532	Si	-3.897	10.191	5.855
O	1.512	1.773	11.570	O	-3.506	5.475	4.532	Si	2.531	0.892	3.706
O	6.557	1.742	11.624	O	1.550	5.475	4.532	Si	7.587	0.892	3.706
O	-3.364	7.463	11.445	O	1.626	1.918	2.835	Si	-2.525	6.453	3.706
O	1.705	7.462	11.686	O	6.683	1.918	2.835	Si	2.531	6.453	3.706
O	3.642	0.105	11.556	O	-3.430	7.479	2.835	Si	1.287	2.726	1.468
O	8.692	0.077	11.625	O	1.626	7.479	2.835	Si	6.343	2.726	1.468
O	-1.631	5.525	11.531	O	3.486	-0.018	2.756	Si	-3.769	8.287	1.468
O	3.703	5.625	11.723	O	8.542	-0.018	2.756	Si	1.287	8.287	1.468
O	0.190	3.799	10.707	O	-1.570	5.543	2.756	Si	-1.284	4.614	1.466
O	5.314	3.795	10.692	O	3.486	5.543	2.756	Si	3.772	4.614	1.466
O	-5.051	9.215	10.638	O	-0.024	3.652	1.716	Si	-6.340	10.175	1.466
O	-0.036	9.148	10.707	O	5.033	3.652	1.716	Si	-1.284	10.175	1.466

Table 4.D.4: Coordinates for the most stable *S*-aspragine adsorbed on hydroxylated α-quartz $(10\bar{1}0)$. This configuration is shown in Fig. 4.7(b).

Atom	x	y	z	Atom	x	y	z	Atom	x	y	z
C	-0.034	3.409	15.449	O	-2.259	3.452	10.088	O	-5.080	9.213	1.716
C	-0.402	4.783	14.869	O	2.806	3.602	9.910	O	-0.024	9.213	1.716
C	0.724	5.417	14.030	O	-7.631	9.470	9.998	O	-2.562	3.723	1.084
C	0.107	2.332	14.385	O	-2.545	9.485	9.943	O	2.494	3.723	1.084
H	-1.901	3.741	13.902	O	1.055	1.999	8.851	O	-7.618	9.284	1.084
H	-2.399	5.246	14.458	O	6.048	1.942	8.960	O	-2.562	9.284	1.084
H	-0.842	3.104	16.128	O	-3.933	7.483	8.923	O	1.164	1.699	0.219
H	-0.569	5.473	15.707	O	0.969	7.455	9.067	O	6.221	1.699	0.219
H	0.985	7.034	12.937	O	4.255	-0.053	8.946	O	-3.892	7.260	0.219
H	0.885	3.496	16.040	O	-0.773	0.101	9.146	O	1.164	7.260	0.219
H	2.118	2.268	14.640	O	-0.881	5.502	9.006	O	4.085	0.041	0.174
H	1.489	1.335	13.330	O	-5.911	5.714	9.132	O	9.141	0.041	0.174
N	-1.630	4.724	14.040	O	-1.002	1.905	7.245	O	-0.972	5.602	0.174
N	1.325	1.784	14.234	O	4.091	1.915	7.233	O	4.085	5.602	0.174
O	1.758	4.818	13.707	O	-6.000	7.503	7.256	Si	1.452	2.765	10.218
O	0.418	6.658	13.705	O	-0.956	7.483	7.261	Si	6.414	2.747	10.322
O	-0.878	1.975	13.698	O	0.913	0.070	7.097	Si	-3.687	8.366	10.274
				O	6.046	0.113	7.070	Si	1.284	8.423	10.337
H	4.606	0.633	11.717	O	-4.151	5.606	7.119	Si	-1.097	4.569	10.325
H	-1.048	0.608	12.279	O	0.947	5.653	7.104	Si	3.943	4.668	10.331
H	-1.505	5.240	12.524	O	-2.721	3.592	6.227	Si	-6.215	10.200	10.256
H	2.959	5.143	12.392	O	2.335	3.589	6.227	Si	8.890	-0.831	10.390
H	2.493	1.124	11.411	O	-7.779	9.147	6.234	Si	0.043	1.006	8.090
H	7.104	1.062	11.685	O	-2.724	9.141	6.229	Si	5.116	0.985	8.061
H	-2.607	6.775	11.508	O	-0.194	3.807	5.545	Si	-4.988	6.572	8.112
H	2.480	6.865	11.529	O	4.862	3.807	5.545	Si	0.024	6.520	8.120
H	0.392	1.075	0.160	O	-5.251	9.368	5.545	Si	-1.369	2.764	5.933
H	5.448	1.075	0.160	O	-0.194	9.368	5.545	Si	3.691	2.768	5.929
H	-4.664	6.636	0.160	O	-1.579	1.744	4.697	Si	-6.420	8.326	5.936
H	0.392	6.636	0.160	O	3.477	1.744	4.697	Si	-1.362	8.323	5.940
H	3.300	0.533	-0.147	O	-6.635	7.305	4.697	Si	-3.897	4.630	5.855
H	8.356	0.533	-0.147	O	-1.579	7.305	4.697	Si	1.159	4.630	5.855
H	-1.756	6.094	-0.147	O	1.550	-0.086	4.532	Si	-8.954	10.191	5.855
H	3.300	6.094	-0.147	O	6.606	-0.086	4.532	Si	-3.897	10.191	5.855
O	1.671	1.698	11.422	O	-3.506	5.475	4.532	Si	2.531	0.892	3.706
O	6.344	1.704	11.580	O	1.550	5.475	4.532	Si	7.587	0.892	3.706
O	-3.326	7.467	11.545	O	1.626	1.918	2.835	Si	-2.525	6.453	3.706
O	1.725	7.524	11.635	O	6.683	1.918	2.835	Si	2.531	6.453	3.706
O	3.771	0.134	11.529	O	-3.430	7.479	2.835	Si	1.287	2.726	1.468
O	8.476	0.075	11.691	O	1.626	7.479	2.835	Si	6.343	2.726	1.468
O	-1.477	5.566	11.540	O	3.486	-0.018	2.756	Si	-3.769	8.287	1.468
O	3.449	5.546	11.627	O	8.542	-0.018	2.756	Si	1.287	8.287	1.468
O	0.276	3.776	10.671	O	-1.570	5.543	2.756	Si	-1.284	4.614	1.466
O	5.308	3.877	10.667	O	3.486	5.543	2.756	Si	3.772	4.614	1.466
O	-5.073	9.138	10.615	O	-0.024	3.652	1.716	Si	-6.340	10.175	1.466
O	-0.022	9.266	10.769	O	5.033	3.652	1.716	Si	-1.284	10.175	1.466

CHAPTER 5

STEP DECORATION OF CHIRAL METAL SURFACES

5.A. Step decoration thermodynamics

5.A.1. Introduction[†]

Intrinsically chiral surfaces are crystal planes with a surface structure lacking mirror symmetry[1-20], which can be created by cutting a single crystal along certain high Miller index directions. Multiple experiments and theoretical studies have shown that intrinsically chiral surfaces can provide enantiospecificity for chiral molecules[2-10, 12-18, 20]. It would be useful to control the catalytic reactivity or tune the chemistry of intrinsically chiral surfaces with the goal of enhancing the enantiospecificity of these surfaces. Two possible approaches that can be considered towards this goal are to change the surface orientation or to make surfaces decorated with impurities. In general, fabricating decorated surfaces is possibly the more flexible of these approaches. This idea is closely related to the general concept of using bimetallics rather than pure metals in heterogeneous catalysis, where the simultaneous presence of two metal species opens up a wide range of potentially useful catalytic phenomena. Unfortunately, little fundamental information is available to indicate how this idea could be pursued for highly stepped surface.

[†] The results described in 5.A. have been published in Han, J. W.; Kitchin, J. R.; Sholl, D. S., *J. Chem. Phys.* **2009**, 130, 124710.

In this Section, we consider the decoration of chiral stepped metal surfaces with an additional metal species. For this idea to affect enantiospecific adsorption on a chiral surface, it would be desirable for the impurities deposited on a surface to preferentially decorate the kinked step edges that make the surface chiral. This outcome is not necessarily guaranteed, however. In fact, there are at least three possibilities after step decoration; the impurities can prefer to remain in the kinked sites, they may prefer to be located in the surface terrace, or they may dissolve into the bulk. The surface segregation energy, which is the energy required for moving an impurity from the inside of a host metal to the surface[23-24], plays a key role in determining which phenomenon is dominant. Therefore, if we know surface segregation energies, we can infer the tendency of the movement of an impurity after step decoration.

First-principles calculations of surface segregation energy have proven to be useful in screening potential surface/impurity combinations. An important set of calculations was performed by Ruban *et al.*[23-24], who calculated 552 surface segregation energies of single transition metal impurities in transition-metal hosts. That work only examined flat surfaces, so it is not obvious without further work how these results are related to the concept of decorating undercoordinated sites on stepped surfaces.

We want to study the tendency of surface segregation of isolated metal impurities on chiral metal surfaces. The aim of our work was to establish a database describing surface segregation on chiral surfaces focusing on which impurity atoms will segregate to the kinked step edges. We pursued this task by performing a large number of Density Functional Theory (DFT) calculations to theoretically predict surface segregation for selected examples. We have subsequently used these calculation results to develop a

correlation that makes predictions of surface segregation phenomena on flat and stepped surfaces for all combinations of 3d, 4d, and 5d metals. We limit our attention to the enthalpic contributions to surface segregation energies in these materials. The configurational entropy associated with the large number of possible sites for an impurity in a bulk material means that the free energy for surface segregation always favors dissolution of an impurity into the bulk relative to a prediction made using the enthalpic contributions alone. In general, the balance between this entropic effect and the enthalpic contributions to surface segregation control the net concentration difference between bulk and surface sites. We also limited our attention to the behavior of isolated impurity atoms, which means we cannot comment on the possibility of aggregation of impurities on surfaces. Both of these restrictions are consistent with the treatment of surface segregation energies by Ruban *et al.*[23-24].

5.A.2. Theory

The surface segregation energy of an isolated impurity is defined as the energy needed to transfer an impurity atom from the bulk to the surface[23-28]. It can be calculated as the difference between the total energy derivatives of the surface and the bulk with respect to impurity concentration in the single impurity limit[23-24, 27-30]. That is,

$$\varepsilon_{segr} \equiv \left.\frac{\partial \varepsilon_{surf}}{\partial c_{surf}}\right|_{c\to 0} - \left.\frac{\partial \varepsilon_{bulk}}{\partial c_{bulk}}\right|_{c\to 0}, \tag{5.1}$$

where $\varepsilon_{surf/bulk}$ is the total energy per atom of a surface/bulk system and $c_{surf/bulk}$ the impurity concentration of the surface/bulk system. In order to calculate this with DFT, each derivative term of Eq. (5.1) may be written as

$$\left.\frac{\partial \varepsilon_{surf/bulk}}{\partial c_{surf/bulk}}\right|_{c\to 0} \approx \frac{\left[\frac{1}{K}E\left(\frac{1}{K}\right)-\frac{1}{K}E(0)\right]}{\left(\frac{1}{K}\right)} = E\left(\frac{1}{K}\right)-E(0), \tag{5.2}$$

where $E\left(\frac{x}{K}\right)$ is a DFT total energy for a supercell containing K atoms including x impurity atoms. For large enough supercells, the dilute concentration limit is satisfied and Eq. (5.2) is accurate. Combining Eqs. (5.1) and (5.2),

$$\varepsilon_{segr} \approx \left[E_{surf}\left(\frac{1}{M}\right)-E_{surf}(0)\right]-\left[E_{bulk}\left(\frac{1}{N}\right)-E_{bulk}(0)\right]. \tag{5.3}$$

Here, the surface (bulk) supercell contains M (N) atoms. Rearranging Eq. (5.3),

$$\varepsilon_{segr} \approx \left[E_{surf}\left(\frac{1}{M}\right)+E_{bulk}(0)\right]-\left[E_{surf}(0)+E_{bulk}\left(\frac{1}{N}\right)\right] \tag{5.4}$$

In Eq. (5.4), each pair of terms in square brackets corresponds to a set of DFT calculation with $M+N$ total atoms and one impurity. With this definition, a negative ε_{segr} indicates that the impurity remaining on the surface is preferred energetically to the impurity dissolving into the bulk.

As mentioned above, this approach only examines the enthalpic contributions to surface segregation energies. Generically, an impurity in the bulk of a material will always have a larger configurational entropy than an atom on a surface, so this entropy will reduce the tendency for surface segregation to occur when the free energy for this segregation is considered. Our treatment also neglects contributions to the free energy of surface segregation energy due to vibrational degrees of freedom in the bulk material or the free surface.

We performed plane wave DFT calculations using the Vienna *ab initio* Simulation Package (VASP) with the ultrasoft pseudopotentials available in this package[31-32]. These calculations used the generalized gradient approximation (GGA) with the Perdew-Wang 91[33] functional and a plane wave expansion with a cutoff of 241.6 eV.

During geometry optimization calculations, this cutoff energy was increased by 30%. Total energy calculations were conducted using the residual minimization method for electronic relaxation, accelerated using Methfessel-Paxton Fermi-level smearing with a width of 0.2 eV. Geometries were relaxed using the conjugate gradient algorithm until the forces on all the unconstrained atoms were less than 0.03 eV/Å. The unit cell and *k*-point mesh used for the surface calculation in each individual case are given below in the details for each calculation. For all surfaces, the supercell consisted of layers that had a thickness equivalent to six layers of the (111) supercell and a vacuum spacing of 14 Å. We embedded each impurity in the top and bottom layer in order to cancel out any dipole effects. This approach introduces an additional factor of two into the first square bracket in Eq. (5.3). For all bulk calculations, a 3×3×3 Monkhorst-Pack *k*-point mesh was used with a 4×4×4 primitive supercell. For both surface and bulk calculations, the DFT-optimized lattice constants, which are listed below in the details of each calculation, were used. In all surface calculations, the lattice constant in the plane of the surface was fixed at the DFT-optimized value of the pure metal. In bulk calculations that included impurities, the lattice constant of the material was fully relaxed.

5.A.3. Results and discussion

5.A.3.1. Direct DFT calculations of surface segregation energies

The method described in Section 5.A.2 for calculating Eq. (5.1) with DFT calculations is different from some previous approaches[23-30, 34-35]. To compare our approach with previous calculations, we compared selected results for flat surfaces with the results of Ruban *et al*. [23-24] Ruban *et al.* performed DFT within the local density approximation in conjunction with a Green's function technique to calculate the surface segregation energy of an isolated impurity on the most closely packed surface of the host metal[23-24]. Their results are in good agreement with available experimental data and

previous DFT calculations[36-37]. We calculated the surface segregation energies of several impurities on Cu, Rh, Pd, and Ir(111) surfaces. In all, 19 impurity/surface combinations were included in this comparison, including examples with strong tendencies towards segregation, strong tendencies towards anti-segregation, and examples with small segregation energies. A 4×4×1 *k*-point mesh and a (3×3) surface unit cell were used for these surface calculations. The DFT-optimized lattice constants used for Cu, Rh, Pd, and Ir were 3.64, 3.85, 3.96, and 3.89 Å, in good agreement with the experimental values of 3.62, 3.80, 3.89, and 3.84 Å[38], respectively. Figure 5.1 compares our results with the previous calculations of Ruban *et al.*; the root mean square deviation is 0.12 eV/atom.

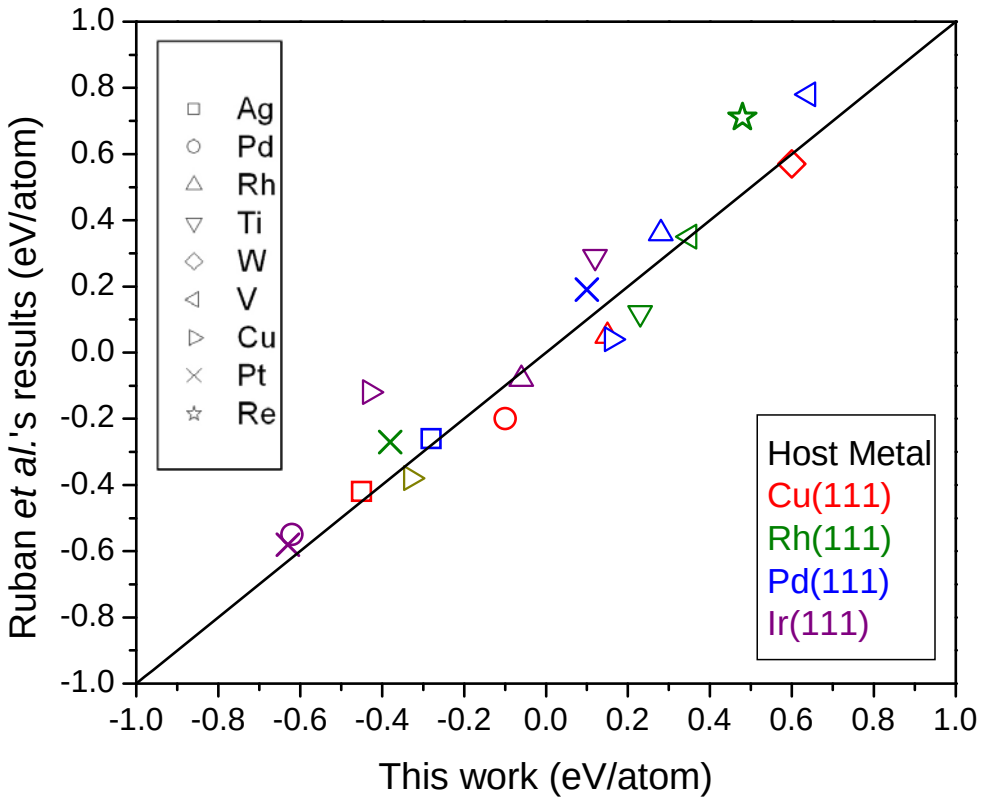

Figure 5.1: Comparison of our surface segregation energies results on Cu, Rh, Pd, and Ir(111) surfaces with Ruban *et al.*[23-24]

The main aim of our calculations was to examine the segregation tendencies of impurity atoms on stepped surfaces. To do this, we examined a range of flat and stepped surfaces of fcc metals. Specifically, we examined the flat (110), (100), and (111) surfaces, which have 7, 8, and 9 coordinated sites, respectively, the stepped (322) surface, an achiral stepped surface with a (111) terrace and 7, 9, and 10 coordinated sites, and the chiral stepped (643) surface. The latter surface has sites with coordinations from 6-11. A 4×4×1 *k*-point mesh was used for the (110), (100), and (111) surfaces with a (3×3) surface unit cell. A 2×5×1 *k*-point mesh was used for the (322) surfaces with a (3×1) surface unit cell, and a 3×3×1 *k*-point mesh for the (643) surfaces with a (1×1) surface unit cell. Convergence tests indicated these results were well converged in *k*-space.

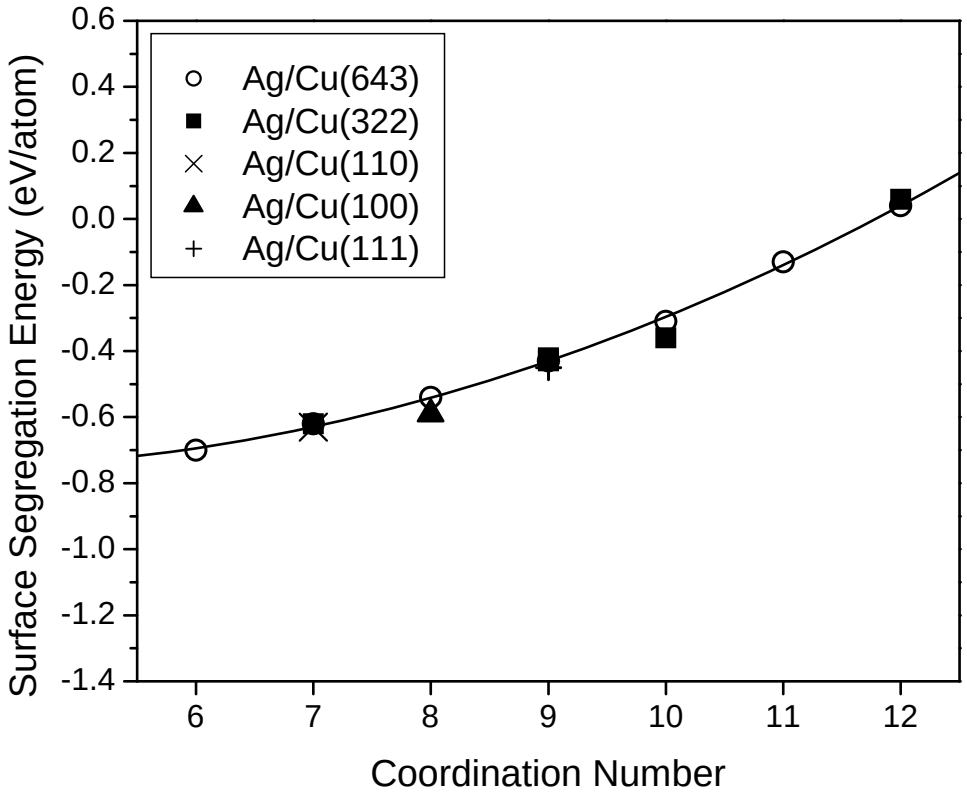

Figure 5.2: Surface segregation energies of a Ag impurity on Cu surfaces.

For illustrative purposes, we first describe the surface segregation energies of a Ag impurity on Cu surfaces. Figure 5.2 shows the surface segregation energies for a Ag atom on various surface sites of the five Cu surfaces as a function of the coordination number (CN) of these sites. In Fig. 5.2, each symbol corresponds to each surface orientation and the black line is a quadratic fit to the data. The sites with CN = 6 are the kinked step sites on Cu(643) and the sites with CN = 12 are subsurface sites. As mentioned in Sec. 5.2, a negative surface segregation energy implies that segregation of an impurity towards the surface is enthalpically favored. The fact the segregation energy decreases and is negative as the coordination number is reduced indicates that on a stepped surface such as Cu(643), the sites with the lowest coordination will be preferentially decorated by Ag impurities compared to other sites on the surface.

We have performed calculations similar to those in Fig. 5.2 for four fcc host materials: Cu, Rh, Pd, and Ir. For each host, five impurities with various magnitudes of surface segregation energies for the (111) surface of the host as calculated by Ruban *et al.*[23-24] were chosen. Specifically, we examined Ag, Pd, Rh, Ti, and W impurities on Cu surfaces (Fig. 5.3a), Cu, Pt, Ti, V, and Re impurities on Rh surfaces (Fig. 5.3b), Ag, Cu, Pt, Rh, and V impurities on Pd surfaces (Fig. 5.3c), and Pd, Pt, Cu, Rh, and Ti impurities on Ir surfaces (Fig. 5.3d). In Fig. 5.3, each color corresponds to an impurity and each symbol to site on a specific surface. The curves associated with each data set are quadratic fits to the DFT data for each impurity/host combination. Clean Ir(110) is known to reconstruct, but our calculations examined the unreconstructed surface.

From these results, we can predict the possibility of step decoration for each binary pair. A negative value at CN = 6 indicates segregation of an impurity would occur at the kinked step site. Therefore, it would be possible to decorate the kinked step site with Ag impurities on Cu surfaces, Cu and Pt impurities on Rh, Ag impurities on Pd, and Pd, Pt, Cu, and Rh impurities on Ir. On the other hand, due to positive values at CN = 6, the examples below would be expected to dissolve into the bulk of each host after step

decoration; Rh, Ti, and W impurities on Cu hosts, Ti, V, and Re impurities on Rh, Pt, Rh, and V impurities on Pd, and Ti impurities on Ir. It is also interesting to note that a Pd impurity on Cu surfaces does not show a strong CN dependency of its surface segregation, and vice versa.

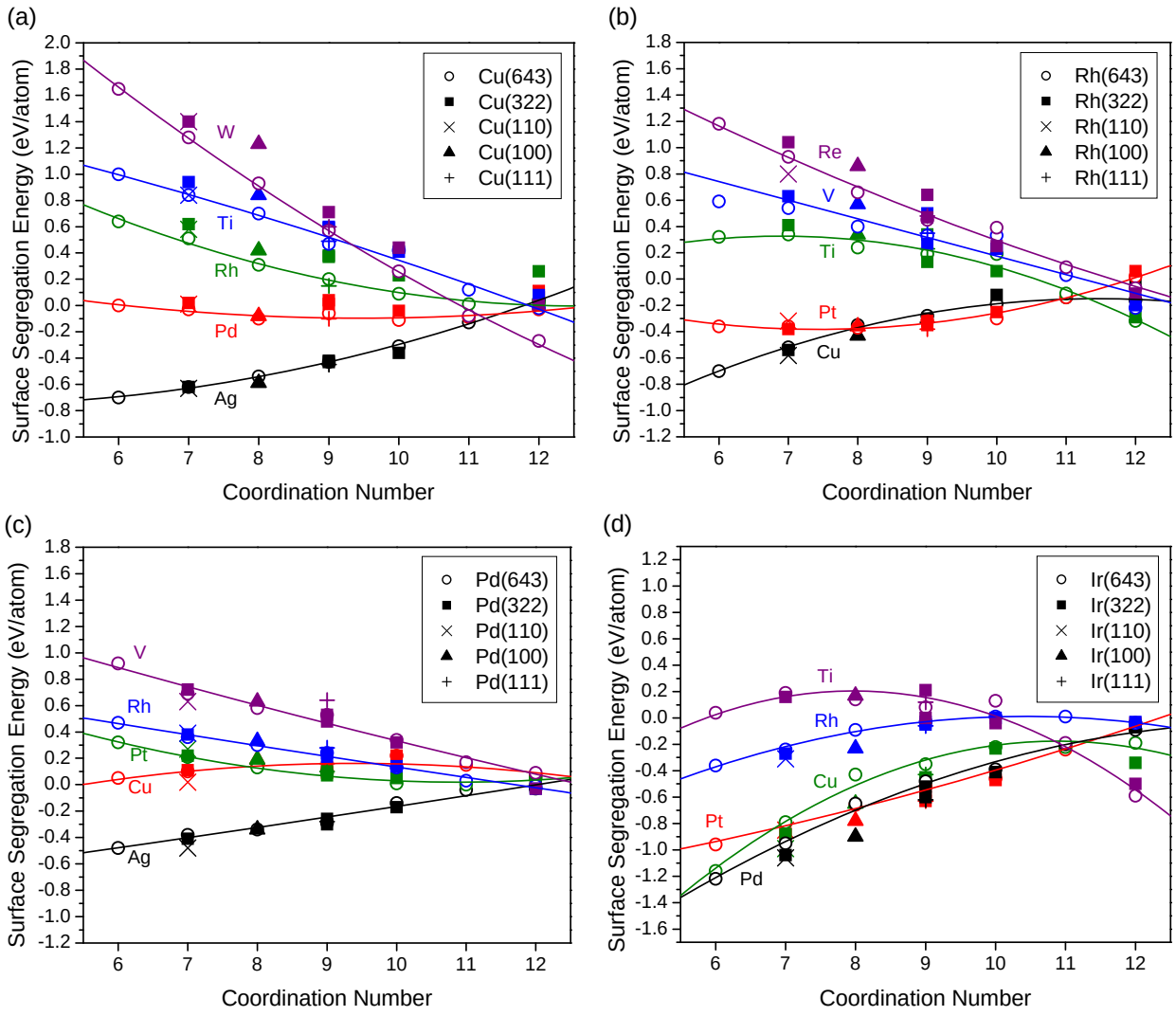

Figure 5.3: Surface segregation energies of 5 impurities on (a) Cu, (b) Rh, (c) Pd, and (d) Ir surfaces.

Our results at CN = 12 are around zero, but are not exactly zero. If surface segregation energies at CN = 12 are measured in the bulk, they should be zero according to the definition of surface segregation in Eq. (1). However, we have calculated surface

segregation of CN = 12 using subsurface sites that are right underneath the top surface layer. Even though these sites have CN = 12, they may not be entirely in the bulk environment. Several reports have discussed segregation of the impurities in subsurface layers[25, 27, 30, 35, 39]. These previous reports have also shown that those surface segregation energies come to zero from ~5th layer depth from the top surface[25, 30, 39].

5.A.3.2. Development of a model for predicting surface segregation on stepped surfaces

Up to this point, we used DFT calculations of surface segregation energy to consider possible surface/impurity combinations for decorating surface steps. To consider the full range of binary transition metal pairs that exist, however, would require a huge number of DFT calculations. It is therefore worthwhile examining our DFT data to understand the physical trends that govern these results and to develop a model that can be applied to a larger group of surfaces.

5.A.3.2.1. Factors controlling segregation thermodynamics

In developing a model for surface segregation energies, it is critical to understand the physical origins of segregation. Here, we describe contributions to these phenomena that have been observed in earlier work. Our observation that the surface segregation energy is strongly dependent on the coordination number (CN) is consistent with previous reports[40-45]. This is physically plausible if segregation is described with a simple bond counting model[40-43]. The bond strength difference between the host and impurity is also an important factor in surface segregation[40-42, 45]. There are multiple ways to characterize the bond strength of metals. High surface free energies are associated with high bond strengths and the surface free energy of a solid metal is approximately 1.2 times of that of liquid[21]. Thus, liquid surface tension can be used as a gauge of bond strength. The cohesive energy[46] or melting points of metals can also be used as a measure. These three approaches to describing bond strengths all show similar trends.

This means that using one method is sufficient to investigate the correlation of bond strength with surface segregation. We used liquid surface tension data[21], which is listed in Table 5.A.1 of the Appendix 5.A.

The atomic size difference between host and impurity atoms has also been considered as another factor of surface segregation[40-42, 45, 47-48]. A large size mismatch between host and impurity atoms causes strain. It is typically expected that atoms of the component which has the larger radius segregate to the surface[47-48]. The nearest neighbor distance between atoms in the bulk[49] or the atomic radius[50] can be used as measures of atomic size. The Wigner-Seitz radius is a similar quantity[51]. All of these three definitions of atomic size are similar, so we used Wigner-Seitz radii[22] as the atomic size as listed in Table 5.A.2 of the Appendix 5.A.

A final property that can play a role in surface segregation are effects related to the metal *d*-bands[23-24, 43-44]. Ruban *et al.* showed that surface segregation energy is related to the *d*-band width of metals[23-24]. In turn, Kitchin *et al.* showed that the *d*-band width is related to the *d*-band center[52], which is defined as the centroid of the *d*-band density of states in an atomic sphere centered at a surface atom[22]. This implies that the *d*-band center should be correlated with surface segregation. When surface sites are doped with a second metal atom, the shift in the *d*-band center from the pure surface occurs. We used these shifts in *d*-band centers of surface impurities relative to the clean metal values to represent *d*-band properties. We performed simple DFT calculations to obtain *d*-band center values on the close-packed surfaces of all the materials described below. For all calculations, the supercell consisted of 6 layers and a vacuum spacing of 14 Å as before. A (3×3) surface unit cell was used for fcc(111) and hcp(0001) surfaces and a (2×2) surface unit cell for bcc(110) surface. Spin-polarization effects were considered in the calculations for all impurities on Fe, Co, and Ni hosts and Fe, Co, and Ni impurities on all host materials. Crucially for the efficiency of this approach, no surface relaxation was included in these calculations. The results are listed in Table 5.A.3 of the Appendix 5.A.

5.A.3.2.2. Correlations for predicting step decoration thermodynamics

A wide range of correlations between our DFT data in Sec. 5.A.3.1 and the factors described in Sec. 5.A.3.2.1 were investigated. Among all the expressions we examined, the most effective correlation for a surface site with coordination number *CN* was

$$\varepsilon_{segr} = \Delta CN \times \left(0.158 \times \Delta\varepsilon + 0.062 \times \Delta d\right) \text{-} 0.060\,, \tag{5.5}$$

where ΔCN is 12 - *CN*, $\Delta\varepsilon$ is the bond strength difference, and Δd the shift in *d*-band center between the impurity on the flat unrelaxed surface and the pure flat surface, respectively, with all energies in eV. The details of our calculations to determine the most effective correlation are in the Appendix 5.A. These calculations compared possible models with different numbers of model parameters using the Leave One Out method[53-55]. It is interesting to note that including the atomic size term discussed above does not significantly improve the description of the data. This may be explained by noting that the *d*-band center depends sensitively on atomic size[22], so little additional information is gained by including atomic size in an expression that already incorporates a *d*-band center term. A number of the data sets for individual impurity/surface pairs show indications of a nonlinear dependence of the segregation energy on coordination number (see Figs. 5.2 and 5.3). Including a quadratic dependence of the segregation energy on coordination number did not, however, improve the description of the overall data set in a statistical way, so the expression above involves only a linear dependence on the coordination number.

An important feature of Eq. (5.5) is that it makes predictions about a range of surface sites. For example, using CN = 9 for fcc and hcp, CN = 6 for bcc into Eq. (5.5), we can predict the surface segregation energy on close packed surfaces of these hosts. The segregation energy associated with kinked stepped sites is predicted by Eq. (5.5) with CN = 6 for fcc and hcp hosts and CN = 4 for bcc hosts. This expression can also be used to describe the relative energies of pairs of surface sites with different coordination

numbers. For instance, based on Eq. (5.5), for an fcc material, the energy difference between an impurity on a (111) terrace site (CN = 9) and a kinked step site (CN = 6) is same as that of an impurity from the bulk (CN = 12) to the (111) terrace (CN = 9). This means that the extensive data compiled by Ruban *et al.*[23-24] for the latter case can also be interpreted in terms of the distribution of impurity atoms among less coordinated surface sites.

In this Section, our focus has been concentrated on predicting the possibility of step decoration. Below, we use the correlation defined above to examine the surface segregation energies of a wide range of surface/impurity pairs on the kinked stepped surfaces.

5.A.3.3. Possible step decorations on the kinked step site

5.A.3.3.1. Application of the correlation to fcc, Fe, Co, and Ru hosts

In order to test the suitability of Eq. (5.5) for a broader data set, we compared the predictions of this correlation with Ruban *et al.*'s data for atomically flat surfaces[23-24]. This comparison was first performed with binary pairs of all fcc transition metals and Fe, Co, and Ru. Figure 5.4 shows this comparison. Two available surface core level shifts (SCLS) experimental data points[56], which provide quantitatively reliable values of segregation energy[23-24], are also included in Fig. 5.4. In the Z+1 approximation, the SCLS can be interpreted as the segregation energy of an atomic number (Z+1) substitutional impurity in an atomic number Z host metal[23-24, 56]. Overall, there is good agreement between Eq. (5.5) and Ruban *et al.*'s data and good agreement with the experimental values is observed. The standard deviation between our correlation and Ruban *et al.*'s data[23-24] is 0.26 eV/atom. When considering the surface segregation properties of many impurity/host pairs semi-quantitatively, the sign of the surface segregation energy is perhaps the most fundamental property of interest. Figure 5.4 suggests that when the

absolute value of the surface segregation energy is larger than ~0.26 eV/atom, our correlation can reliably predict the sign of surface segregation energy.

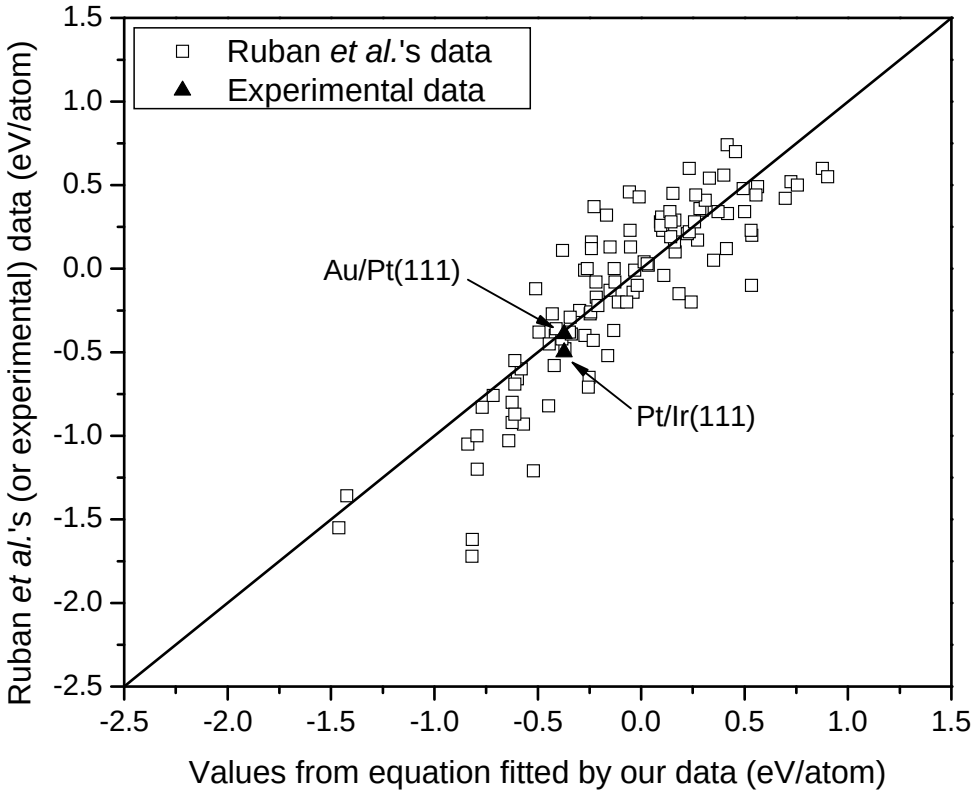

Figure 5.4: Comparison of surface segregation energies of binary pairs of all fcc transition metals and Fe, Co, and Ru from our correlation with previous DFT and experimental data on the close packed surfaces. Open squares are for Ruban *et al.*'s data[23-24] and filled triangles for experimental data[56].

Using Eq. (5.5), the possibility of decorating kink sites on chiral surfaces for a large number of examples can be assessed without further DFT calculations of surface segregation. Figure 5.5 shows the outcome of this analysis for 88 examples. In Fig. 5.5, each color corresponds to the magnitude of each bimetallic pair's surface segregation energy for a kinked step site. Red colors indicate pairs with negative segregation energies, that is, examples where selective step edge decoration may be thermodynamically favored, while blue colors correspond to positive segregation

energies. A number of entries in Fig. 5.5 are white; these are examples where we cannot reliably make a prediction using Eq. (5.5) because the absolute values of surface segregation energy from this expression are less than 0.26 eV/atom.

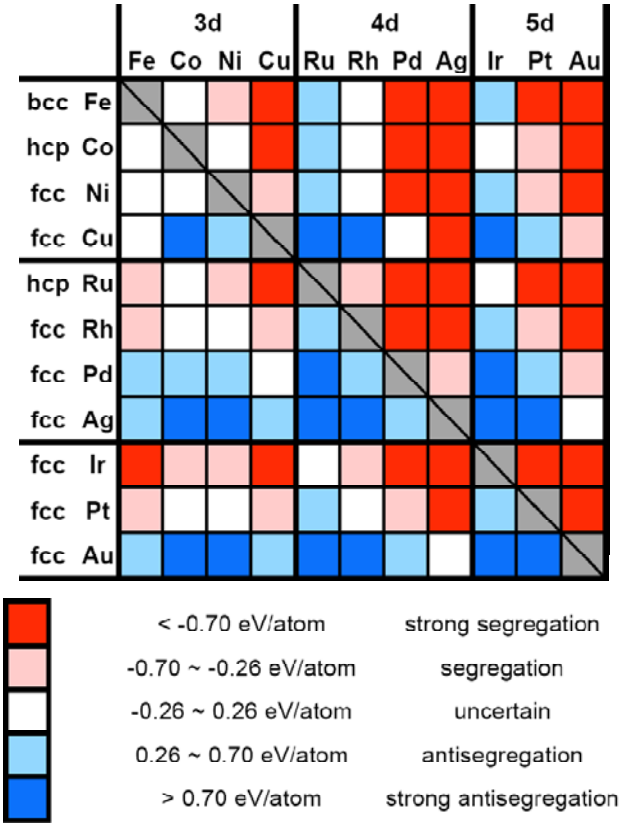

Figure 5.5: Results for binary pairs of all fcc transition metals and Fe, Co, and Ru. These results were gained from Eq. (5.5) by substituting *CN* to 6. The sites with CN = 6 correspond to kinked sites for fcc or hcp metals.

5.A.3.3.2. Application of the correlation to a larger class of metals

We also applied Eq. (5.5) to the full range of 3d, 4d, and 5d metals. Similarly to Sec. 5.A.3.3.1, we compared the results on the close packed surfaces from our correlation with Ruban *et al.*[23-24] and six SCLS experimental measurements[56]. This comparison is shown in Fig. 5.6. Good agreement with the experimental values is observed, but the agreement with Ruban *et al.*'s data[23-24] is not quite as good as for the smaller data set examined in Fig. 5.5. The scattering mainly comes from surface segregation on bcc(110)

surfaces. This presumably occurred because we only used DFT data from surface segregation on fcc hosts to construct our correlation. Nevertheless, when the absolute value of the surface segregation energy is larger than ~0.54 eV/atom, the standard deviation between our correlation's predictions and Ruban *et al.*'s data, we still reliably predict the sign of surface segregation for any combination of the 3d, 4d, and 5d metals.

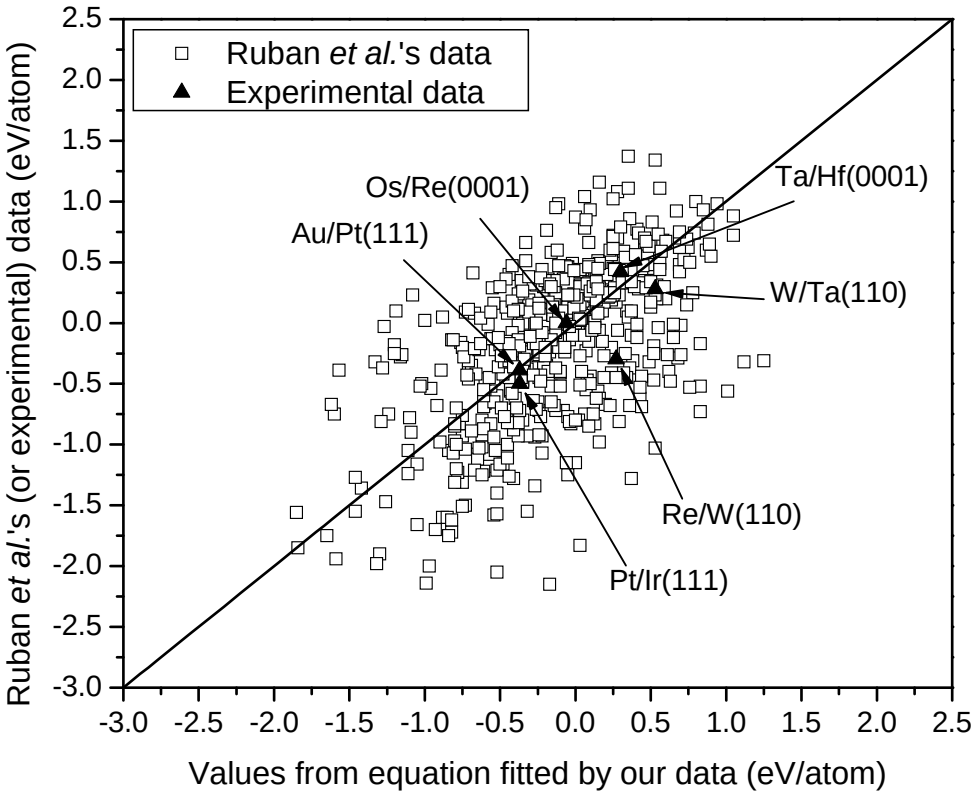

Figure 5.6: Comparison of surface segregation energies of binary pairs of whole 3d, 4d, and 5d transition metals from our correlation with previous DFT and experimental data on the close packed surfaces. Open squares are for Ruban *et al.*'s data[23-24] and filled triangles for experimental data[56].

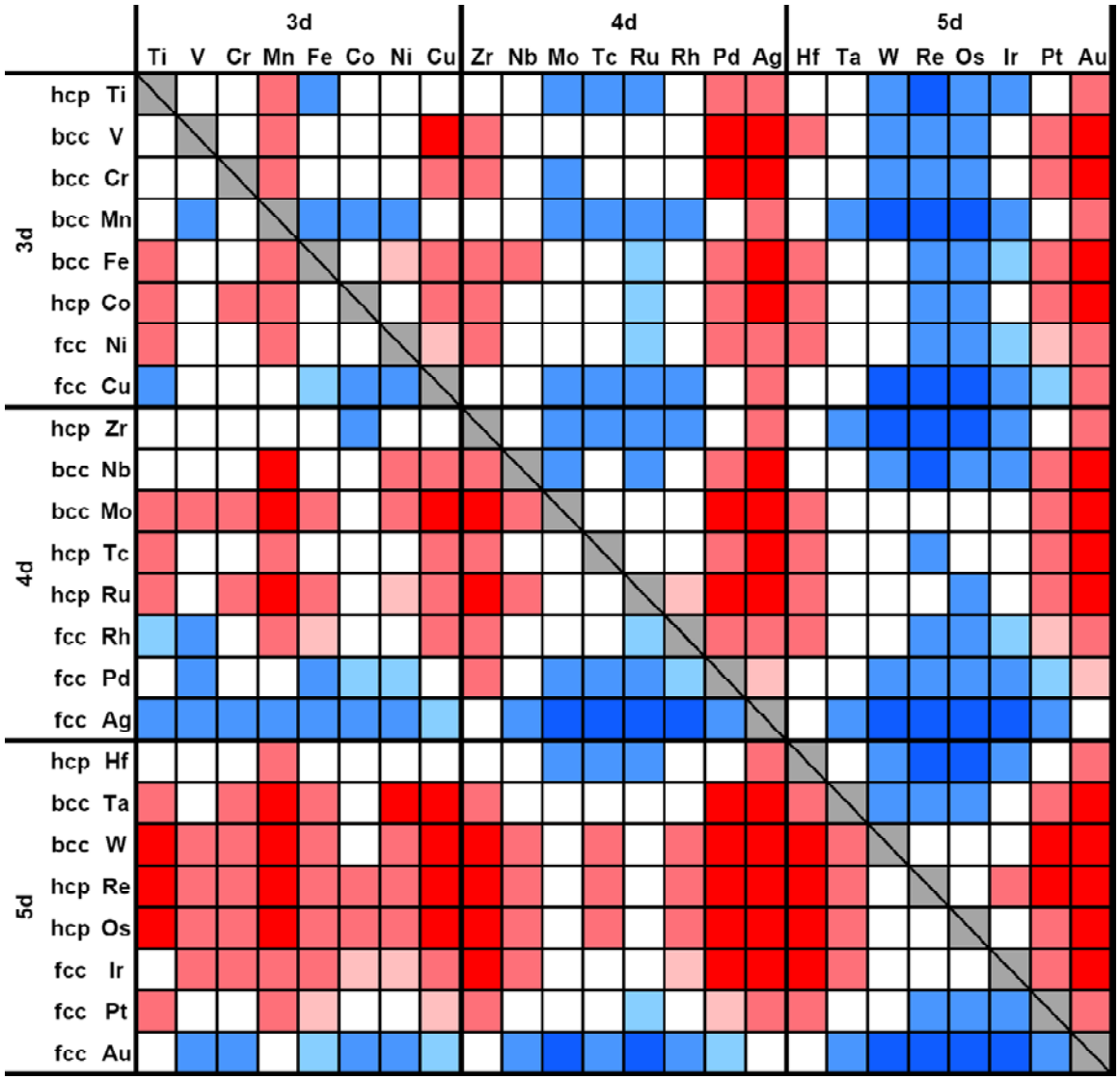

Figure 5.7: Results for binary pairs of all 3d, 4d, and 5d transition metals. These results were gained from Eq. (5.5) by substituting *CN* to 6 (fcc or hcp) or 4 (bcc). The sites with CN = 6 (4) correspond to kinked sites for fcc or hcp (bcc) metals.

The results of our DFT-based correlation are summarized in Fig. 5.7. The numbers used for Fig. 5.7 are also listed in Table 5.A.8 of the Appendix 5.A. These results are obtained from Eq. (5.5) by setting CN to 6 (fcc or hcp) or 4 (bcc) to consider kinked sites on the surfaces. For the full range of 3d, 4d, and 5d metals, predictions in this figure are limited to cases where $|\varepsilon_{segr}|$ is larger than 0.54 eV/atom. For the materials shown in Fig. 5.5, results for the range of $0.26 \leq |\varepsilon_{segr}| \leq 0.54$ eV/atom are included in Fig. 5.7. Figure 5.7 also includes predictions from the direct DFT results we described in Sec. 5.3.1. In all, a firm prediction can be made for 347 impurity/host pairs. Of these, 206 pairs are predicted to be situations where it may be thermodynamically favorable to selectively decorate undercoordinated step sites. For the remaining 141 pairs, this kind of step decoration is predicted to be thermodynamically unfavorable. We can expect that step decoration is favored for many impurities on Mo, Ru, W, Re, Os, and Ir surfaces, while it would be unstable for almost all impurities on Ag and Au.

5.A.4. Conclusion

We have examined step decoration thermodynamics using DFT calculations. Our calculations have identified many "step decorators" that are stable with respect to segregation into other surface sites or the bulk. Our work has used two approaches to contribute to the goal of controlling step decoration of chiral metal surfaces. First, we used detailed DFT calculations for dozens of examples to show that examples exist where decoration of kink sites on chiral surfaces is thermodynamically stable. Prior to these calculations, no evidence was available to support or disprove this claim. Second, based on the DFT data, we developed a robust correlation suitable for characterizing surface segregation on stepped surfaces. This correlation was a useful tool for considering step decoration for hundreds of examples. Figure 5.7 showed the final results of this investigation.

When we predict or explain the results of step decoration only with Fig. 5.7, we

should be appropriately cautious, noting that this treatment did not consider the kinetics of the deposition, diffusion and growth that will be relevant in specific experiments. In addition, in examples where strong segregation of impurities is predicted, aggregation of impurities on the surface might occur. Even though our results neglected these effects, they still provide a useful basis for selecting surface/impurity pairs where these other aspects of step decoration could fruitfully be pursued.

Decoration of step edges on chiral metal surfaces may be an interesting avenue for tuning the surface chemistry of these materials. Chiral metal surfaces tuned by stable step decorations (such as the red colored bimetallic pairs in Fig. 5.7) may show enhanced enantiospecificity for chiral molecules binding on these surfaces. Further investigations would be necessary to find whether the adsorption of chiral molecules on step decorated chiral metal surfaces yields significantly different binding energies for two enantiomers of an adsorbing molecule or not. These results could then be compared to previous DFT calculations of small molecule adsorption on the pure chiral surfaces[12-13, 17-18, 57].

This kind of step decoration we have discussed here may also be applied to the development of tailored bimetallic nanoparticles for heterogeneous catalysis applications. Because nanoparticles usually have a large number of step edge and other undercoordinated surface sites, stable step decoration of a second metal on the surfaces would considerably affect their reactivity as catalysts. Our results may be useful for providing insight into materials where these kinds of effects can be contemplated.

5.B. The importance of kinetics in surface alloying: A comparison of the diffusion pathways of Pd and Ag atoms on Cu(111)

5.B.1. Introduction[‡]

The enantioselectivity of intrinsically chiral Cu surfaces has been demonstrated in vacuum experiments[2-7, 58] and studied using theoretical models[17-18, 59]. From our results regarding step decoration, Ag, Au, and Pd could potentially be used to decorate the kinked step of Cu surface. It is therefore interesting to examine how the interaction of chiral molecules would be changed by decoration of Cu surface with Ag or Pd. In order to create experimentally relevant step decorated surfaces, it is not enough to know only the thermodynamics of step decoration by investigating surface segregation. It is also important to understand surface diffusion, since this process controls morphology and crystalline structure of solid surfaces during synthesis or annealing[60-61]. One of decisive factors in these phenomena is the energy barrier experienced by the diffusion atom at the step edge. This barrier is known as the Ehrlich-Schwoebel (ES) barrier[62-63]. Measuring the ES barrier of Ag or Pd adatom across the step of a Cu surface would be useful for understanding the kinetics of surface alloying. In general, if this barrier is small, an adatom can descend over the step edge to the lower terrace, so the growth during deposition is expected to be two dimensional. However, if the adatom encounters a high energy barrier at the step edge, the growth might be three dimensional. Because the ES barrier depends on the types of adatom, we may need different experimental approaches for each impurity in order to design step decorated surfaces.

[‡] The results described in 5.B. have been published in Bellisario, D. O.; Han, J. W.; Tierney, H. L.; Baber, A. E.; Sholl, D. S.; Sykes, E. C. H., *J. Phys. Chem. C* **2009**, 113, 12863-12869.

This research was also motivated by the Sykes group's experimental result for Pd and Ag alloying on stepped Cu(111) surface[64]. They demonstrated from low-temperature scanning tunneling microscopy that physical vapor deposition of Pd and Ag at or above room temperature yields remarkably different surface alloys: Pd predominantly incorporates at the nearest ascending Cu step edge whereas Ag appears to be able to traverse step edges rather easily and alloys into terraces both above and below its initial adsorption site. Combining theory and experiment can play an important role for understanding complicated surface alloying mechanisms. In this Section, we present DFT calculations to illustrate how both the kinetics and the thermodynamics of the process must be considered to fully understand experimental observations.

5.B.2. Computational methods

Plane wave DFT calculations have been performed using the Vienna *ab initio* simulation package (VASP) with the ultrasoft pseudopotentials available in this package[31-32]. In all calculations, we have used the generalized gradient approximation (GGA) with the Perdew-Wang 91[33] functional and a plane wave cutoff energy of 241.6 eV. The geometries of the structures in our calculations were relaxed using a conjugate gradient algorithm until the forces on all the unconstrained atoms were less than 0.03 eV/Å. In order to represent the diffusion of an adatom at the stepped and kinked sites on Cu, we have used Cu(322) and Cu(643) surfaces, respectively. Cu(322) has steps with {100} microfacets on a (111) terrace, while Cu(643) has steps with both {100} and {110} microfacets on a (111) terrace, so these two steps are representative of the full range of step orientations that can exist on a (111) terrace. A 2×5×1 *k*-point mesh was used for the (322) surfaces with a (3×1) surface unit cell and a 3×3×1 *k*-point mesh for the (643) surfaces with a (1×1) surface. The surface unit cells were defined using the

DFT-optimized Cu lattice constant and the slab thickness for each surface was ~10.5 Å separated by a vacuum spacing of ~14 Å in the direction of the surface normal. No atoms were constrained during calculations with these supercells.

The nudged elastic band (NEB) method has been employed to investigate diffusion pathways of adatoms on those surfaces[65-66]. Initial approximations to reaction paths were obtained by linear interpolation between energy minima. The same set of *k*-points and energy cutoff were used for NEB calculations as were mentioned above. The total number of intermediate images we used for Figures 5.11, 5.12, and 5.13 was 18, 22, and 19, respectively, which is sufficient to map the minimum energy path (MEP) accurately. For Figures 5.11-13, we defined the reaction coordinates by defining a straight line between the initial and final position of the diffusing atom in the plane of the surface and projecting the full coordinates of each NEB image onto that line.

5.B.3. Results

The Sykes group's STM results suggested that in the case of Ag, adatoms crossed step edges during the process of alloying[64]. In contrast, Pd adatoms were mostly incorporated into the nearest ascending step edge, unless very wide terraces were involved. To explore these observations with DFT, diffusion barriers for Ag and Pd on Cu(111) were calculated both on the flat terraces and for a variety of step edge types. Diffusion pathways of Ag (A) and Pd (B) on Cu(322) are shown in Figures 5.8 and 5.9. The energy of the initial configuration, corresponding to the adatom in an fcc hollow site close to the upper step edge on this stepped surface, was defined to be zero for each set of calculations. It is known that there are two possible diffusion mechanisms for adatom motion across a step edge; hopping and exchange[67-68]. Both cases have been examined in order to investigate which mechanism is more favorable in this system. The diffusion of the adatom via the hopping (exchange) mechanism is plotted in Figure 5.8 (Figure 5.9). The results shown in Figure 5.8 reveal that adatom diffusion across the step via a hopping

mechanism involves a Ehrlich-Schwoebel (ES) barrier[69] of 0.45 eV (0.68 eV) for Ag (Pd). After crossing the step, the adatom is in a more coordinated site ((b) in Figure 5.8) compared with its initial site on a terrace ((a) in Figure 5.8). Due to its higher coordination, site b is the most stable site in the diffusion pathway for hopping over a step edge that we examined. In order for a Ag (Pd) adatom to escape from site b, an energy of ~0.4 eV (~0.8 eV) is required. In moving from (c) to (d) to (e) in Figure 5.8, an adatom diffuses away on the terrace and arrives at an energetically equivalent site to the starting point but on the lower terrace. This cycle would then be repeated if an adatom diffused down another step.

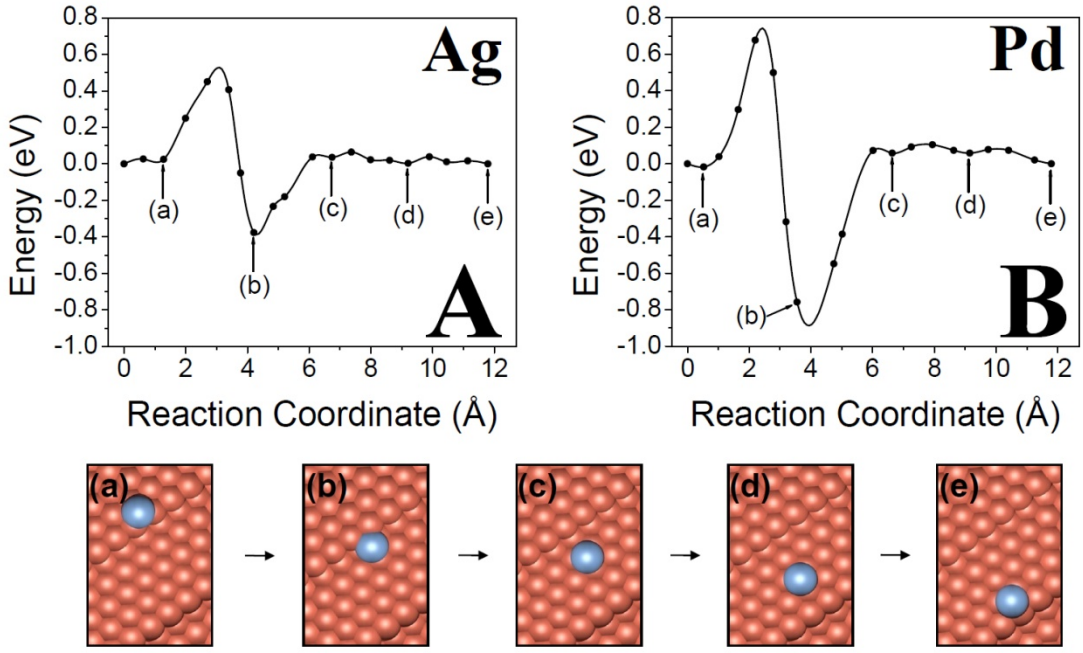

Figure 5.8: Nudged elastic band results for the diffusion of Ag (A) and Pd (B) on Cu(322) by a hopping mechanism. The energy of the adatom on the lower terrace away from the step edge (final position) is the same as the starting point on the upper terrace (initial position). DFT predicts that the Ehrlich-Schwoebel barrier at the Cu(322) step edge is 0.45 eV for Ag and 0.68 eV for Pd.

In contrast to hopping, for the diffusion via an exchange mechanism the diffusing adatom must undergo two separate processes to get to a point equivalent to position b in Figure 5.8. First, the adatom displaces a step edge Cu atom beneath it and assumes its

position (step (a) to (b) in Figure 5.9). Then, the adatom diffuses out towards the lower terrace and the displaced Cu atom returns to its original position (step (b) to (c) in Figure 5.9). The Ehrlich-Schwoebel barriers during this process, that is, the diffusion barrier from (a) to (b) in Figure 5.12, are 0.45 eV (0.21 eV) for Ag (Pd). In order for an Ag (Pd) adatom to diffuse from (b) to (c) in Figure 5.9, an energy barrier of 0.67 eV (1.04 eV) must be overcome. Once the adatom arrives at (c) in Figure 5.9, the remainder of the pathway is the same as in the hopping mechanism. Thus, the pathway from (c) to (e) in Figure 5.8 is equivalent to that from (d) to (f) in Figure 5.9. Comparing the Ehrlich-Schwoebel barriers via both mechanisms, we see that the barrier is the same for Ag adatoms, but the exchange mechanism is more favorable for Pd adatoms.

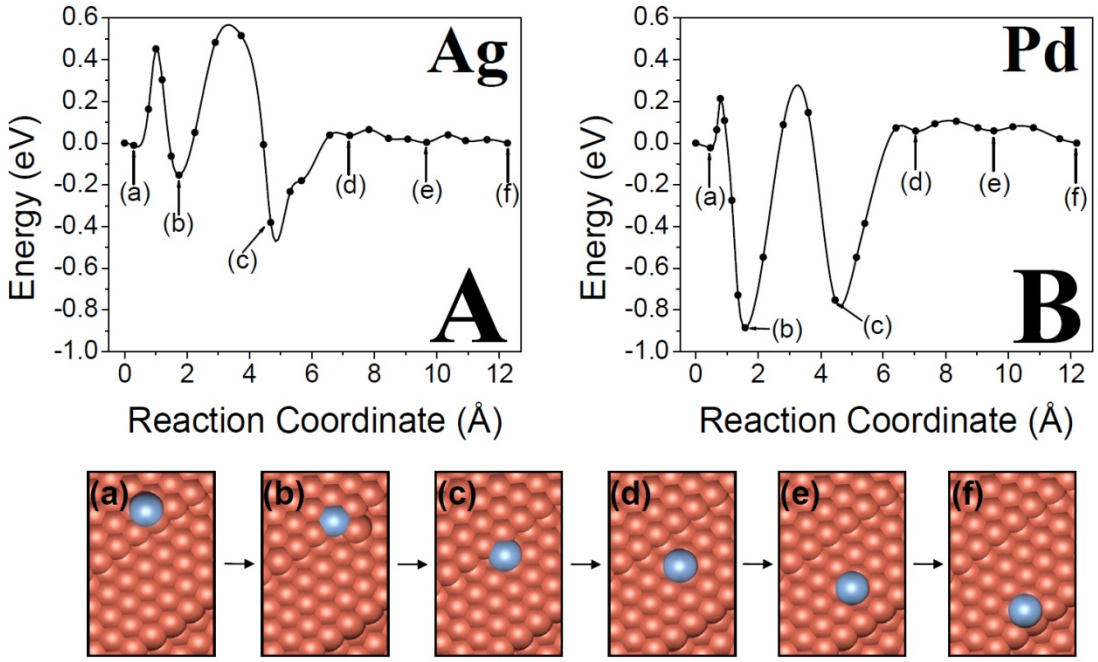

Figure 5.9: Nudged elastic band results for diffusion of Ag (A) and Pd (B) on Cu(322) by an exchange mechanism. The energy of the adatom on the lower terrace away from the step edge (final position) is the same as the starting point on the upper terrace (initial position). The Ehrlich-Schwoebel barrier on step edge is 0.45 eV (A) and 0.21 eV (B), respectively. Unlike the hopping mechanism, a second barrier (step b to c) must be overcome in order to fully clear the step edge.

While Cu(322) is a reasonable model for understanding the diffusion of adatoms across step edges, the shape of Cu step edges at room temperature is in constant flux[70-75]. For this reason DFT calculations were performed for the exchange mechanism occurring at kink sites. Because the Ehrlich-Schwoebel barrier for the exchange mechanism is much lower than the hopping mechanism for Pd on Cu(322), only the exchange mechanism was investigated for this case. As can be seen in Figure 5.10, the starting point for the adatom is on a fcc hollow site just above the kink site. This diffusion path also has two stages. From (a) to (b) in Figure 5.10, the adatom displaces the Cu kink site atom and assumes the Cu atom's original position. During this process, the Ehrlich-Schwoebel barrier for an Ag (Pd) adatom was 0.31 eV (0.09 eV). Then, from (b) to (c), the displaced Cu atom assumes its original position and the adatom moves onto the lower terrace. The energy barrier of this process was found to be 0.78 eV (0.96 eV) for Ag (Pd) adatom. Similar to the situation for Cu(322), in order for an adatom to move away from the step, i.e. from (c) to (d), an energy of ~0.4 eV (~0.8 eV) is needed because (c) is the more coordinated, stable site. From (d) to (f) in Figure 5.10, the adatom diffuses away on the terrace and arrives at an equivalent site to the starting point, but on the lower terrace. Similar to the exchange mechanism on Cu(322), the Ehrlich-Schwoebel barrier of Ag was found to be 0.22 eV larger than that of Pd. Interestingly, it has been observed experimentally in the case of Mn on Cu(100) that the amount of alloy formation in lower terraces can be correlated with the kink density at steps[76]. Our DFT results provide an example of how this observation can arise and suggest that the barrier for incorporating into the lower step edge at kink sites is ~0.1 eV lower than on straight step edges for both Pd and Ag.

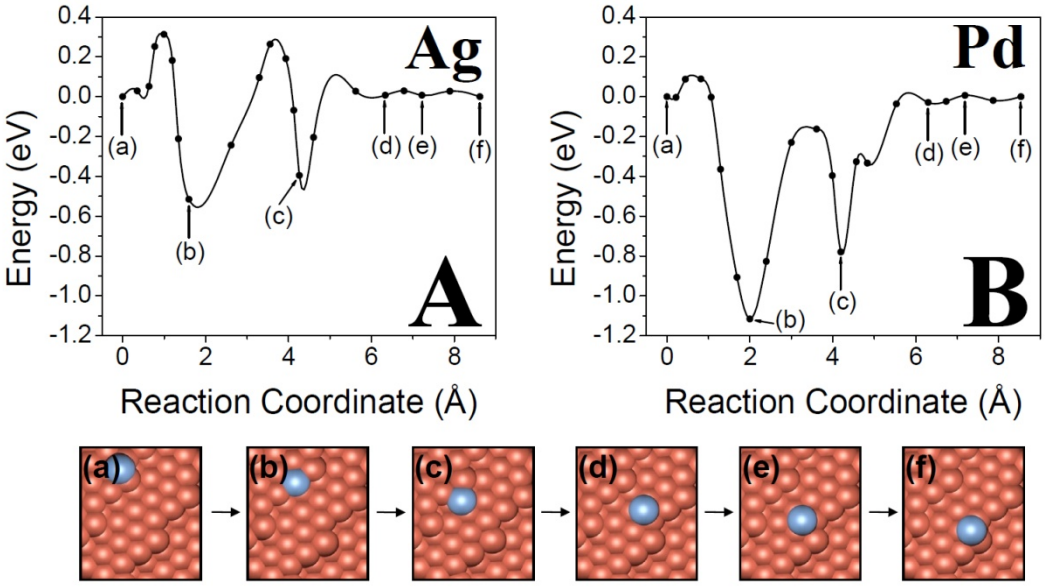

Figure 5.10: Nudged elastic band results for diffusion of Ag (A) and Pd (B) on Cu(643) by an exchange mechanism. The energy of the adatom on the lower terrace away from the step edge (final position) is the same as the starting point on the upper terrace (initial position). The Ehrlich-Schwoebel barrier was calculated to be 0.31 eV (A) and 0.09 eV (B), respectively. The second energetic barrier occurs when the adatom moves out of the step edge (step b to c).

5.B.4. Discussion

In the Sykes group examination of alloying of low concentrations of Pd and Ag in Cu(111) with STM, several important differences were observed[64]. It appears that the main mechanism for Pd incorporation in the surface is alloying into ascending step edges. Only when very large terraces are involved does any Pd become incorporated below the step edges. In contrast, Ag alloys both above and below step edges. In order to quantify the energetics of the initial stages of alloying, DFT calculations were performed on both stepped and kinked Cu surfaces. The DFT calculations confirm that there are several available pathways by which adatoms can either cross step edges or become incorporated into the step edges themselves. While we have presented the progression of an adatom across and/or into a step edge, microscopic reversibility allows us to examine exactly the same energetics for the reverse process i.e. an adatom approaching a step edge from the lower terrace and either alloying into it, or hopping onto the upper terrace.

The first important point that emerges from our calculations is that for all three mechanisms studied (hopping, exchange at straight steps, and exchange at kinked steps) the potential wells are deeper for Pd than for Ag. For example, a Pd atom is ~0.8 eV more stable when coordinated to a step edge relative to the most stable site on a flat terrace (Figures 5.8B, 5.9B and 5.10B). In contrast, the same energy difference for Ag is only ~0.4 eV. This large difference means that, unlike Ag, once Pd becomes associated with a step edge it is unlikely to leave it. At 300 K (assuming a pre-exponential factor of 10^{12}), a Ag adatom would have an average residence time at the step edge of ~ 5 μs as compared with Pd's residence time of ~28 s. This long residence time for Pd atoms at step edges means that once they contact their nearest ascending step edge they remain there on a long timescale and are presumably incorporated further into the brim of the step edge via step fluctuations and vacancy mediated diffusion[70-78]. Ag, on the other hand, can bind and detach from a step with great frequency during the alloying process because of its weaker binding to step edges.

Figure 5.11 shows a schematic of the proposed alloying process for both Pd and Ag atoms. After evaporation the metal atoms diffuse randomly over the terrace they initially land on. If Pd encounters an ascending step edge it remains there and is incorporated in the brim via step fluctuations and vacancy mediated diffusion[70-78]. On the other hand Ag can fairly easily detach from ascending step edges and diffuse back onto the terrace. During their random walk Pd and Ag atoms will also encounter descending step edges. Unlike binding to ascending step edges, traversing descending step edges is an activated process (see Figures 5.8-10). Therefore, depending on the barrier height, some diffusing adatoms may occasionally cross down step edges while most are reflected back onto the terrace. Of the three mechanisms we have considered, the lowest barrier available to Ag is to traverse a descending step edge via the exchange mechanism at a kink site (0.3 eV, Figure 5.10A). Crossing this barrier leads to an end point at which the adatom is incorporated into the lower step edge. Figure 5.9 reveals that a similar process

for Ag at a straight step would have a slightly higher barrier of 0.4 eV. In contrast, both of these mechanisms for step crossing offer Pd an even lower energy barrier; 0.2 eV for exchange at the straight step and 0.1 eV for the kinked step.

From these results one would naively expect to observe more Pd to accumulate below step edges, however, both the average residence times at ascending step edges and the probability of crossing descending step edges must be taken into account to fully understand the situation. While Pd is more likely to cross down a descending step edge, it binds essentially irreversibility to ascending steps; this binding limits the number of attempts a Pd adatom makes at crossing a descending step edge to those attempts made before the binding event occurs. Conversely Ag can bind and detach from ascending steps many times during the alloying process and thus each Ag atom will have many attempts at crossing descending step edges; this more than compensates for the higher reflection probability for Ag off of descending step edges. In a simplistic 1D case, when Pd or Ag adatoms diffuse towards a descending step edge they are presented with two barriers: the diffusion barrier back onto the terrace, or the Ehrlich-Schwoebel barrier for crossing down the step edge. Our DFT calculations reveal that the diffusion barriers on the Cu(111) terrace are small and almost the same for Ag (0.040 eV) and Pd (0.035 eV) whereas the Ehrlich-Schwoebel barriers via the lowest energy pathway are 0.3 eV for Ag and 0.1 eV for Pd. A simplistic Arrhenius rate calculation reveals that at room temperature the probability for a Pd atom to cross a step edge is ~ 5 % vs. 0.005 % for an Ag atom. While the probability for Ag is much lower than that for Pd, the fact that Ag is relatively weakly bound to ascending step edges means that over the course of the alloying process (tens of minutes) the Ag adatoms have many attempts ($>10^8$) at crossing down step edges. While this 1D model of competing processes is simplistic, the very large differences in rates of the various processes for Ag and Pd are sufficient to explain the differences between the final alloying positions of Ag and Pd observed experimentally. The unusually large Pd brims experimentally observed at the edge of

very large Cu(111) terraces can also be explained within this model. A large terrace will have a large number of Pd atoms incident upon it. Therefore, the large flux of Pd atoms incident upon the descending step will contribute to the formation of an unusually large brim. Additionally, the large spatial gap between the ascending and descending step edges of a large terrace increases the likelihood that adatoms reflected from the descending step will return before diffusing to the distant ascending step edge. While the experiments were performed at relativity low coverages and the DFT models considered just one atom, the processes at play (crossing the Ehrlich-Schwoebel barrier and exchanging into the step edge) are essentially the same regardless of coverage except that the energetics of each process will change slightly as the surface becomes more alloyed.

5.B.5. Conclusion

In this Section we have performed DFT calculations to compare and contrast how the initial stages of alloying occur in both Pd/Cu(111) and Ag/Cu(111) systems. Our results combined with experimental observations show that Pd and Ag behave very differently in the initial stages of alloying on Cu(111). Our data reveals how the Ehrlich-Schwoebel barrier at step edges affects the initial stages of surface alloy formation. It appears that the strong binding of Pd to ascending step edges leads to incorporation of most of the Pd incident on a terrace in brims at the upper terraces. Ag on the other hand binds more weakly to these sites and hence has many opportunities to attempt to traverse the Ehrlich-Schwoebel barrier. These results have implications for many alloy systems in which surface diffusion of the constituent metals is necessary for the particles to remain active and also for systems in which such diffusion is detrimental in terms of surface segregation of the inactive element.

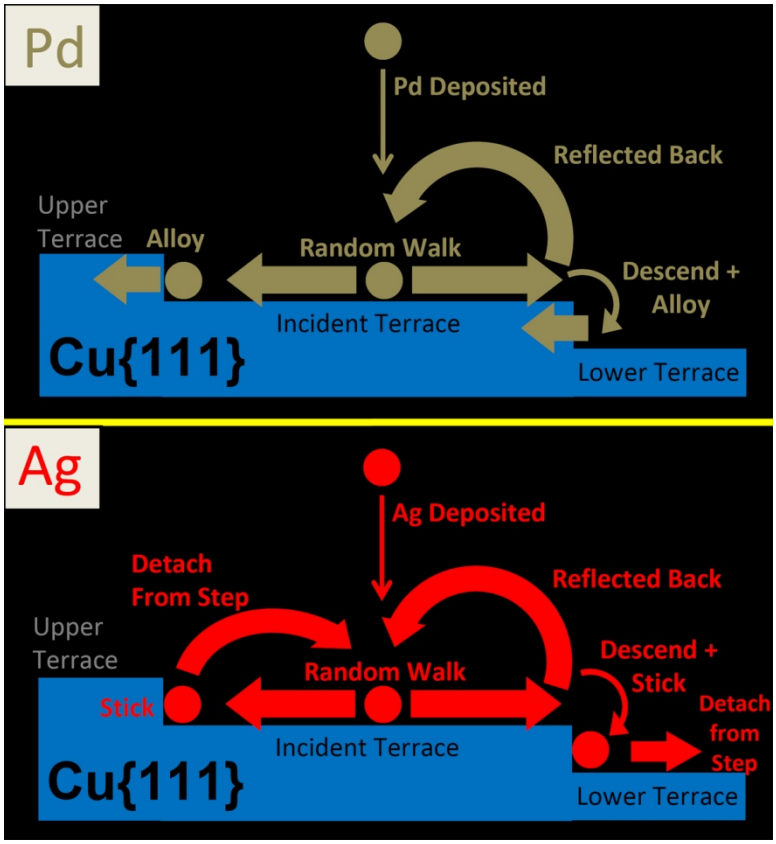

Figure 5.11: Schematic of the proposed mechanism of Ag and Pd alloying with Cu(111). The thickness of the arrows indicates the relative number of events. Pd atoms bind irreversibly to ascending step edges and hence have at most only a very small number of chances to cross to the lower terrace. The crossing process, unlike binding to ascending step edges, is activated and hence most atoms are reflected back onto the terrace. In contrast Ag binds more weakly to ascending step edges and can have multiple attempts to cross step edges.

References

(1) McFadden, C. F.; Cremer, P. S.; Gellman, A. J., *Langmuir* **1996**, 12, 2483-2487.
(2) Gellman, A. J.; Horvath, J. D.; Buelow, M. T., *J. Mol. Catal. A* **2001**, 167, 3-11.
(3) Horvath, J. D.; Gellman, A. J., *J. Am. Chem. Soc.* **2001**, 123, 7953-7954.
(4) Horvath, J. D.; Gellman, A. J., *J. Am. Chem. Soc.* **2002**, 124, 2384-2392.
(5) Horvath, J. D.; Koritnik, A.; Kamakoti, P.; Sholl, D. S.; Gellman, A. J., *J. Am. Chem. Soc.* **2004**, 126, 14988-14994.
(6) Rampulla, D. M.; Francis, A. J.; Knight, K. S.; Gellman, A. J., *J. Phys. Chem. B* **2006**, 110, 10411-10420.
(7) Rampulla, D. M.; Gellman, A. J., *Surf. Sci.* **2006**, 600, 2823-2829.
(8) Ahmadi, A.; Attard, G.; Feliu, J.; Rodes, A., *Langmuir* **1999**, 15, 2420-2424.
(9) Attard, G. A.; Ahmadi, A.; Feliu, J.; Rodes, A.; Herrero, E.; Blais, S.; Jerkiewicz, G., *J. Phys. Chem. B* **1999**, 103, 1381-1385.
(10) Attard, G. A., *J. Phys. Chem. B* **2001**, 105, 3158-3167.
(11) Kara, A.; Rahman, T. S., *J. Phys.: Condens. Matter* **2006**, 18, 8883-8890.
(12) Šljivancanin, Ž.; Gothelf, K. V.; Hammer, B., *J. Am. Chem. Soc.* **2002**, 124, 14789-14794.
(13) Greber, T.; Šljivancanin, Ž.; Schillinger, R.; Wider, J.; Hammer, B., *Phys. Rev. Lett.* **2006**, 96, 056103.
(14) Schillinger, R.; Šljivancanin, Ž.; Hammer, B.; Greber, T., *Phys. Rev. Lett.* **2007**, 98, 136102-4.
(15) Kuhnle, A.; Linderoth, T. R.; Besenbacher, F., *J. Am. Chem. Soc.* **2006**, 128, 1076-1077.
(16) Sholl, D. S., *Langmuir* **1998**, 14, 862-867.
(17) Bhatia, B.; Sholl, D. S., *Angew. Chem. Int. Ed.* **2005**, 44, 7761-7764.
(18) Bhatia, B.; Sholl, D. S., *J. Chem. Phys.* **2008**, 128, 144709-1~144709-9.
(19) Baber, A. E.; Gellman, A. J.; Sholl, D. S.; Sykes, E. C. H., *J. Phys. Chem. C* **2008**, 112, 11086-11089.
(20) Gladys, M. J.; Stevens, A. V.; Scott, N. R.; Jones, G.; Batchelor, D.; Held, G., *J. Phys. Chem. C* **2007**, 111, 8331-8336.
(21) Murr, L. E., *Interfacial Phenomena in Metals and Alloys*. Addison-Wesley: Reading, MA, 1975.
(22) Ruban, A.; Hammer, B.; Stoltze, P.; Skriver, H. L.; Nørskov, J. K., *J. Mol. Catal. A* **1997**, 115, 421-429.
(23) Ruban, A. V.; Skriver, H. L., *Comput. Mater. Sci.* **1999**, 15, 119-143.
(24) Ruban, A. V.; Skriver, H. L.; Nørskov, J. K., *Phys. Rev. B* **1999**, 59, 15990.
(25) Jiang, C.; Gleeson, B., *Acta Materialia* **2007**, 55, 1641-1647.
(26) Saul, A.; Weissmann, M., *Phys. Rev. B* **1999**, 60, 4982-4987.
(27) Ropo, M.; Kokko, K.; Vitos, L.; Kollar, J., *Phys. Rev. B* **2005**, 71, 045411.
(28) Ropo, M.; Kokko, K.; Vitos, L.; Kollar, J.; Johansson, B., *Surf. Sci.* **2006**, 600, 904-913.
(29) Hugosson, H. W.; Eriksson, O.; Jansson, U.; Abrikosov, I. A., *Surf. Sci.* **2005**, 585, 101-107.
(30) Ponomareva, A. V.; Skorodumova, N. V.; Vekilov, Y. K.; Abrikosov, I. A., *Phys. Rev. B* **2007**, 75, 245406.

(31) Kresse, G.; Furthmüller, J., *Comput. Mater. Sci.* **1996**, 6, 15.
(32) Kresse, G.; Hafner, J., *Phys. Rev. B* **1993**, 48, 13115-13118.
(33) Perdew, J. P.; Chevary, J. A.; Vosko, S. H.; Jackson, K. A.; Pederson, M. R.; Singh, D. J.; Fiolhais, C., *Phys. Rev. B* **1992**, 46, 6671-6687.
(34) Qin, F.; Jiang, C.; Anderegg, J. W.; Jenks, C. J.; Gleeson, B.; Sordelet, D. J.; Thiel, P. A., *Surf. Sci.* **2007**, 601, 376-380.
(35) Løvvik, O. M., *Surf. Sci.* **2005**, 583, 100-106.
(36) Howe, J. M., *Interfaces in Materials*. John Wiley & Sons: New York, 1997.
(37) Nonas, B.; Wildberger, K.; Zeller, R.; Dederichs, P. H., *Phys. Rev. Lett.* **1998**, 80, 4574 - 4577.
(38) *ASM materials information [electronic resource] : ASM handbooks online*. ASM International: Materials Park, OH, 2002; Vol. 2.
(39) Ruban, A. V.; Abrikosov, I. A.; Kats, D. Y.; Gorelikov, D.; Jacobsen, K. W.; Skriver, H. L., *Phys. Rev. B* **1994**, 49, 11383.
(40) Abraham, F. F., *Phys. Rev. Lett.* **1981**, 46, 546-549.
(41) Abraham, F. F.; Brundle, C. R., *J. Vac. Sci. Technol.* **1981**, 18, 506-519.
(42) Wandelt, K.; Brundle, C. R., *Phys. Rev. Lett.* **1981**, 46, 1529-1532.
(43) Mukherjee, S.; Moran-Lopez, J. L.; Kumar, V.; Bennemann, K. H., *Phys. Rev. B* **1982**, 25, 730-737.
(44) Lambin, P.; Gaspard, J. P., *J. Phys. F: Metal Phys.* **1980**, 10, 2413-2428.
(45) Tomanek, D.; Aligia, A. A.; Balseiro, C. A., *Phys. Rev. B* **1985**, 32, 5051-5056.
(46) Farid, B.; Godby, R. W., *Phys. Rev. B* **1991**, 43, 14248-14250.
(47) Yamauchi, H., *Phys. Rev. B* **1985**, 31, 7688-7694.
(48) Kiejna, A., *J. Phys.: Condens. Matter* **1990**, 2, 6331-6333.
(49) Winter, M. J., *WebElements :the first periodic table on the WWW* 2007; Vol. 2008.
(50) Clementi, E.; D.L.Raimondi; Reinhardt, W. P., *J. Chem. Phys.* **1967**, 47, 1300.
(51) Sutton, A. P., *Electronic Structure of Materials*. Oxford University Press: New York, 1993.
(52) Kitchin, J. R.; Nørskov, J. K.; Barteau, M. A.; Chen, J. G., *J. Chem. Phys.* **2004**, 120, 10240-10246.
(53) Drautz, R.; Diaz-Ortiz, A., *Phys. Rev. B* **2006**, 73, 224207.
(54) Martens, H. A.; Dardenne, P., *Chemom. Intell. Lab. Syst.* **1998**, 44, 99.
(55) Semidey-Flecha, L.; Sholl, D. S., *J. Chem. Phys.* **2008**, 128, 144701.
(56) Flodstrom, A.; Nyholm, R.; Johansson, B., *Advances in Surface and Interface Science, Volume 1: Techniques*. Plenum Press: New York, 1992.
(57) James, J. N.; Sholl, D. S., *Curr. Opin. Colloid Interface Sci.* **2008**, 13, 60-64.
(58) Horvath, J. D.; Baker, L.; Gellman, A. J., *J. Phys. Chem. C* **2008**, 112, 7637-7643.
(59) Power, T. D.; Sholl, D. S., *J. Vac. Sci. Technol. A* **1999**, 17, 1700-1704.
(60) Huang, H. C., *J. Comput.-Aided Mater. Des.* **2002**, 9, 75.
(61) Xiang, S. K.; Huang, H. C., *Appl. Phys. Lett.* **2008**, 92, 101923.
(62) Ehrlich, G.; Hudda, F. G., *J. Chem. Phys.* **1966**, 44, 1039.
(63) Schwoebel, R. L.; Shipsey, E. J., *J. Appl. Phys.* **1966**, 37, 3682.
(64) Bellisario, D. O.; Han, J. W.; Tierney, H. L.; Baber, A. E.; Sholl, D. S.; Sykes, E. C. H., *J. Phys. Chem. C* **2009**, 113, 12863-12869.
(65) Henkelman, G.; Jonsson, H., *J. Chem. Phys.* **2000**, 113, 9978-9985.

(66) Henkelman, G.; Uberuaga, B. P.; Jónsson, H., *J. Chem. Phys.* **2000**, 113, 9901-9904.
(67) Kim, S. Y.; Lee, I.-H.; Jun, S., *Phys. Rev. B* **2007**, 76, 245408-20.
(68) Leonardelli, G.; Lundgren, E.; Schmid, M., *Surf. Sci.* **2001**, 490, 29-42.
(69) Amar, J. G.; Family, F., *Thin Solid Films* **1996**, 272, 208-222.
(70) Dougherty, D. B.; Bondarchuk, O.; Degawa, M.; Williams, E. D., *Surf. Sci.* **2003**, 527, L213-L218.
(71) Giesen, M.; Dietterle, M.; Stapel, D.; Ibach, H.; Kolb, D. M., *Surf. Sci.* **1997**, 384, 168-178.
(72) Giesenseibert, M.; Jentjens, R.; Poensgen, M.; Ibach, H., *Phys. Rev. Lett.* **1993**, 71, 3521-3524.
(73) Jeong, H. C.; Williams, E. D., *Surf. Sci.* **1999**, 34, 171-294.
(74) Pai, W. W.; Bartelt, N. C.; ReuttRobey, J. E., *Phys. Rev. B* **1996**, 53, 15991-15996.
(75) Pai, W. W.; Ozcomert, J. S.; Bartelt, N. C.; Einstein, T. L.; Reuttrobey, J. E., *Surf. Sci.* **1994**, 309, 747-754.
(76) Flores, T.; Junghans, S.; Wuttig, M., *Surf. Sci.* **1997**, 371, 14-29.
(77) Nagl, C.; Haller, O.; Platzgummer, E.; Schmid, M.; Varga, P., *Surf. Sci.* **1994**, 321, 237-248.
(78) Aaen, A. B.; Laegsgaard, E.; Ruban, A. V.; Stensgaard, I., *Surf. Sci.* **1998**, 408, 43-56.

Appendix 5.A: The procedures used to develop a correlation for predicting step decoration thermodynamics and the data used in Fig. 5.7.

Tables 5.A.1 and 5.A.2 list the liquid surface tension data and Wigner-Seitz radii for pure elements used in our calculations. Table 5.A.3 lists the complete set of *d*-band centers and *d*-band shifts used in our calculations.

Table 5.A.1: Liquid surface tension data for 3d, 4d, and 5d transition metals.[21]

Liquid Surface Tension (J/m^2)							
Ti	**V**	**Cr**	**Mn**	**Fe**	**Co**	**Ni**	**Cu**
1.650	1.950	1.590	1.060	1.880	1.880	1.780	1.300
Zr	**Nb**	**Mo**	**Tc**	**Ru**	**Rh**	**Pd**	**Ag**
1.480	1.900	2.250	2.100	2.250	2.000	1.500	0.895
Hf	**Ta**	**W**	**Re**	**Os**	**Ir**	**Pt**	**Au**
1.630	2.150	2.400	2.700	2.500	2.250	1.800	1.140

Table 5.A.2: Wigner-Seitz radius for 3d, 4d, and 5d transition metals.[22]

Wigner-Seitz radius (au)							
Ti	**V**	**Cr**	**Mn**	**Fe**	**Co**	**Ni**	**Cu**
3.05	2.82	2.68	2.70	2.66	2.62	2.60	2.67
Zr	**Nb**	**Mo**	**Tc**	**Ru**	**Rh**	**Pd**	**Ag**
3.35	3.07	2.99	2.84	2.79	2.81	2.87	3.01
Hf	**Ta**	**W**	**Re**	**Os**	**Ir**	**Pt**	**Au**
3.30	3.07	2.95	2.87	2.83	2.84	2.90	3.00

Table 5.A.3: *d*-band centers and their shift values of 3d, 4d, and 5d binary transition metals on the most closely packed surfaces (in units of eV). The impurity atoms are listed horizontally and the host surfaces are listed vertically. For each host metal, *d*-band center values are listed in the first row and shifts in *d*-band centers of surface impurities relative to the clean metal values are listed in the second row.

	Ti	V	Cr	Mn	Fe	Co	Ni	Cu	Zr	Nb	Mo	Tc	Ru	Rh	Pd	Ag	Hf	Ta	W	Re	Os	Ir	Pt	Au
Ti	-0.96	-0.89	-1.54	-2.31	-0.86	-1.41	-1.33	-2.60	-1.29	-1.28	-1.28	-1.36	-1.52	-1.91	-2.79	-4.79	-1.29	-1.30	-1.35	-1.46	-1.66	-2.07	-2.89	-4.53
		0.20	0.10	-0.53	1.02	0.54	0.33	-0.24	-0.16	0.33	0.79	0.66	0.82	0.27	-1.00	-0.80	-0.04	0.12	0.91	0.88	1.11	0.71	-0.50	-1.22
V	-1.14	-1.09	-1.11	-1.18	-1.76	-1.97	-1.92	-3.12	-1.51	-1.59	-1.75	-1.98	-2.30	-2.78	-3.61	-5.44	-1.47	-1.59	-1.78	-2.06	-2.45	-2.97	-3.81	-5.31
	-0.18		0.53	0.60	0.12	-0.02	-0.26	-0.76	-0.38	0.02	0.32	0.04	0.04	-0.60	-1.82	-1.45	-0.22	-0.17	0.48	0.28	0.32	-0.19	-1.42	-2.00
Cr	-1.60	-1.60	-1.64	-1.68	-2.18	-1.99	-1.93	-3.12	-2.08	-2.25	-2.43	-2.65	-2.89	-3.21	-3.90	-5.57	-2.06	-2.25	-2.50	-2.79	-3.11	-3.53	-4.22	-5.57
	-0.64	-0.51		0.10	-0.30	-0.04	-0.27	-0.76	-0.95	-0.64	-0.36	-0.63	-0.55	-1.03	-2.11	-1.58	-0.81	-0.83	-0.24	-0.45	-0.34	-0.75	-1.83	-2.26
Mn	-1.96	-1.89	-1.84	-1.78	-2.07	-2.00	-1.93	-2.96	-2.50	-2.59	-2.71	-2.82	-2.98	-3.23	-3.79	-5.43	-2.47	-2.62	-2.80	-3.01	-3.26	-3.62	-4.20	-5.46
	-1.00	-0.80	-0.20		-0.19	-0.05	-0.27	-0.60	-1.37	-0.98	-0.64	-0.80	-0.64	-1.05	-2.00	-1.44	-1.22	-1.20	-0.54	-0.67	-0.49	-0.84	-1.81	-2.15
Fe	-2.62	-1.85	-1.45	-1.58	-1.88	-1.89	-1.92	-2.79	-2.32	-2.97	-2.43	-2.95	-2.47	-2.76	-2.92	-5.24	-2.41	-2.46	-2.80	-2.88	-2.10	-3.07	-3.64	-5.10
	-1.66	-0.76	0.19	0.20		0.06	-0.26	-0.43	-1.19	-1.36	-0.36	-0.93	-0.13	-0.58	-1.13	-1.25	-1.16	-1.04	-0.54	-0.54	0.67	-0.29	-1.25	-1.79
Co	-2.01	-1.97	-2.23	-1.46	-1.72	-1.95	-1.89	-2.80	-2.59	-2.65	-2.67	-2.38	-2.22	-2.68	-3.32	-5.18	-2.59	-2.70	-2.82	-2.76	-2.52	-3.06	-3.58	-5.16
	-1.05	-0.88	-0.59	0.32	0.16		-0.23	-0.44	-1.46	-1.04	-0.60	-0.36	0.12	-0.50	-1.53	-1.19	-1.34	-1.28	-0.56	-0.42	0.25	-0.28	-1.19	-1.85
Ni	-2.12	-1.98	-1.53	-1.50	-2.62	-2.16	-1.66	-2.41	-2.63	-2.68	-2.68	-2.36	-2.33	-2.52	-2.99	-4.76	-2.61	-2.74	-2.83	-2.79	-2.61	-2.79	-3.29	-4.65
	-1.16	-0.89	0.11	0.28	-0.74	-0.21		-0.05	-1.50	-1.07	-0.61	-0.34	0.01	-0.34	-1.20	-0.77	-1.36	-1.32	-0.57	-0.45	0.16	-0.01	-0.90	-1.34
Cu	-2.03	-1.41	-1.09	-0.95	-2.54	-0.85	-1.09	-2.36	-2.79	-2.29	-1.92	-1.61	-1.55	-1.76	-2.57	-4.69	-2.88	-2.44	-2.15	-1.86	-1.78	-2.01	-2.75	-4.43
	-1.07	-0.32	0.55	0.83	-0.66	1.10	0.57		-1.66	-0.68	0.15	0.41	0.79	0.42	-0.78	-0.70	-1.63	-1.02	0.11	0.48	0.99	0.77	-0.36	-1.12
Zr	-0.82	-1.26	-1.19	-1.53	-2.34	-0.81	-1.71	-2.26	-1.13	-1.08	-1.03	-1.04	-1.16	-1.46	-2.29	-4.36	-1.14	-1.12	-1.11	-1.15	-1.28	-1.61	-2.37	-4.02
	0.14	-0.17	0.45	0.25	-0.46	1.14	-0.05	0.10		0.53	1.04	0.98	1.18	0.72	-0.50	-0.37	0.11	0.30	1.15	1.19	1.49	1.17	0.02	-0.71
Nb	-1.01	-1.09	-1.48	-2.39	-1.01	-1.14	-3.01	-2.70	-1.35	-1.61	-1.46	-1.60	-1.83	-2.20	-2.98	-4.86	-1.33	-1.38	-1.51	-1.69	-1.97	-2.41	-3.15	-4.64
	-0.05	0.00	0.16	-0.61	0.87	0.81	-1.35	-0.34	-0.22		0.61	0.42	0.51	-0.02	-1.19	-0.87	-0.08	0.04	0.75	0.65	0.80	0.37	-0.76	-1.33
Mo	-1.47	-1.38	-1.34	-1.32	-2.27	-1.85	-1.46	-2.60	-1.94	-1.99	-2.07	-2.14	-2.28	-2.48	-3.11	-4.81	-1.93	-2.02	-2.15	-2.32	-2.52	-2.79	-3.37	-4.61
	-0.51	-0.29	0.30	0.46	-0.39	0.10	0.20	-0.24	-0.81	-0.38		-0.12	0.06	-0.30	-1.32	-0.82	-0.68	-0.60	0.11	0.02	0.25	-0.01	-0.98	-1.30
Tc	-1.56	-1.38	-1.42	-1.37	-2.20	-1.31	-1.62	-2.66	-2.05	-2.00	-1.97	-2.02	-2.17	-2.47	-3.18	-4.89	-2.08	-2.08	-2.11	-2.22	-2.41	-2.76	-3.42	-4.80
	-0.60	-0.29	0.22	0.41	-0.32	0.64	0.04	-0.30	-0.92	-0.39	0.10		0.17	-0.29	-1.39	-0.90	-0.83	-0.66	0.15	0.12	0.36	0.02	-1.03	-1.49
Ru	-1.77	-1.54	-1.67	-2.26	-2.43	-1.39	-1.51	-2.42	-2.33	-2.24	-2.23	-2.26	-2.34	-2.46	-3.00	-4.60	-2.38	-2.35	-2.36	-2.46	-1.51	-2.83	-3.33	-4.55
	-0.81	-0.45	-0.03	-0.48	-0.55	0.56	0.15	-0.06	-1.20	-0.63	-0.16	-0.24		-0.28	-1.21	-0.61	-1.13	-0.93	-0.10	-0.12	1.26	-0.05	-0.94	-1.24
Rh	-1.84	-1.64	-1.65	-1.31	-2.73	-1.13	-1.46	-2.12	-2.41	-2.35	-2.30	-2.21	-2.12	-2.18	-2.58	-4.19	-2.44	-2.45	-2.47	-2.44	-2.43	-2.53	-2.88	-4.08
	-0.88	-0.55	-0.01	0.47	-0.85	0.82	0.20	0.24	-1.28	-0.74	-0.23	-0.19	0.22		-0.79	-0.20	-1.19	-1.03	-0.21	-0.10	0.34	0.25	-0.49	-0.77
Pd	-1.86	-1.61	-1.36	-1.06	-0.93	-1.72	-0.84	-1.44	-2.40	-2.33	-2.14	-1.89	-1.69	-1.60	-1.79	-3.42	-2.42	-2.44	-2.37	-2.20	-2.00	-1.91	-2.06	-3.19
	-0.90	-0.52	0.28	0.72	0.95	0.23	0.82	0.92	-1.27	-0.72	-0.07	0.13	0.65	0.58		0.57	-1.17	-1.02	-0.11	0.14	0.77	0.87	0.33	0.12
Ag	-1.20	-0.80	-0.57	-0.50	-2.42	-1.50	-0.57	-1.83	-1.82	-1.32	-0.93	-0.79	-0.76	-0.93	-1.63	-3.99	-2.03	-1.54	-1.17	-0.95	-0.88	-1.06	-1.69	-3.47
	-0.24	0.29	1.07	1.28	-0.54	0.45	1.09	0.53	-0.69	0.29	1.14	1.23	1.58	1.25	0.16		-0.78	-0.12	1.09	1.39	1.89	1.72	0.70	-0.16
Hf	-0.90	-0.88	-1.76	-1.91	-2.04	-1.49	-1.06	-2.37	-1.26	-1.16	-1.11	-1.13	-1.25	-1.57	-2.43	-4.48	-1.25	-1.23	-1.18	-1.23	-1.37	-1.73	-2.52	-4.17
	0.06	0.21	-0.12	-0.13	-0.16	0.46	0.60	-0.01	-0.13	0.45	0.96	0.89	1.09	0.61	-0.64	-0.49		0.19	1.08	1.11	1.40	1.05	-0.13	-0.86
Ta	-1.05	-1.11	-1.51	-2.03	-2.27	-1.49	-3.78	-2.79	-1.41	-1.40	-1.47	-1.64	-1.87	-2.25	-3.07	-4.98	-1.40	-1.42	-1.52	-1.73	-2.03	-2.45	-3.24	-4.03
	-0.09	-0.02	0.13	-0.25	-0.39	0.46	-2.12	-0.43	-0.28	0.21	0.60	0.38	0.47	-0.07	-1.28	-0.99	-0.15		0.74	0.61	0.74	0.33	-0.85	-0.72
W	-1.59	-1.49	-1.59	-1.44	-2.24	-1.42	-1.68	-2.72	-2.10	-2.09	-2.16	-2.25	-2.39	-2.65	-3.28	-4.96	-2.10	-2.14	-2.26	-2.43	-2.62	-2.95	-3.54	-4.90
	-0.63	-0.40	0.05	0.34	-0.36	0.53	-0.02	-0.36	-0.97	-0.48	-0.09	-0.23	-0.05	-0.47	-1.49	-0.97	-0.85	-0.72		-0.09	0.15	-0.17	-1.15	-1.59
Re	-1.65	-1.45	-1.47	-1.27	-2.13	-1.58	-1.72	-2.78	-2.21	-2.13	-2.09	-2.13	-2.29	-2.62	-3.36	-5.03	-2.25	-2.22	-2.25	-2.34	-2.54	-2.92	-3.62	-4.99
	-0.69	-0.36	0.17	0.51	-0.25	0.37	-0.06	-0.42	-1.08	-0.52	-0.02	-0.11	0.05	-0.44	-1.57	-1.04	-1.00	-0.80	0.01		0.23	-0.14	-1.23	-1.68
Os	-1.94	-1.64	-1.48	-1.39	-2.37	-1.88	-1.64	-2.59	-2.57	-2.40	-2.33	-2.35	-2.47	-2.70	-3.25	-4.82	-2.63	-2.55	-2.51	-2.60	-2.77	-3.07	-3.61	-4.84
	-0.98	-0.55	0.16	0.39	-0.49	0.07	0.02	-0.23	-1.44	-0.79	-0.26	-0.33	-0.13	-0.52	-1.46	-0.83	-1.38	-1.13	-0.25	-0.26		-0.29	-1.22	-1.53
Ir	-2.05	-1.79	-1.56	-1.43	-2.66	-1.98	-1.43	-2.36	-2.71	-2.60	-2.49	-2.38	-2.30	-2.39	-2.85	-4.47	-2.74	-2.72	-2.71	-2.69	-2.66	-2.78	-3.18	-4.42
	-1.09	-0.70	0.08	0.35	-0.78	-0.03	0.23	0.00	-1.58	-0.99	-0.42	-0.36	0.04	-0.21	-1.06	-0.48	-1.49	-1.30	-0.45	-0.35	0.11		-0.79	-1.11
Pt	-2.04	-1.74	-1.40	-1.22	-2.99	-2.14	-1.33	-1.66	-2.70	-2.57	-2.35	-2.11	-1.91	-1.85	-2.10	-3.65	-2.75	-2.70	-2.62	-2.43	-2.28	-2.18	-2.39	-3.52
	-1.08	-0.65	0.24	0.56	-1.11	-0.19	0.33	0.70	-1.57	-0.96	-0.28	-0.09	0.43	0.33	-0.31	0.34	-1.50	-1.28	-0.36	-0.09	0.49	0.60		-0.21
Au	-1.47	-1.10	-0.77	-0.59	-2.62	-1.74	-0.81	-1.69	-2.56	-1.86	-1.36	-1.09	-0.94	-1.05	-1.60	-3.73	-2.78	-2.06	-1.52	-1.24	-1.12	-1.21	-1.74	-3.31
	-0.51	-0.01	0.87	1.19	-0.74	0.21	0.85	0.67	-1.43	-0.25	0.71	0.93	1.40	1.13	0.19	0.26	-1.53	-0.64	0.74	1.10	1.65	1.57	0.65	

In order to determine the most effective correlation, we have considered R^2 values, variances between the original and predicted data, and leave one out (LOO) errors. The LOO method has been used for making a reliable prediction, providing a way to compare models with different numbers of parameter[53-55]. It performs a least squares minimization of the model being considered *X* independent times. In each case, one data point from the complete set of *X* values is left out. The LOO error is defined as

$$R^2_{LOO} = \frac{1}{X}\sum_{k=1}^{X}\left(E_{predicted,k} - E_k\right)^2,$$

where $E_{predicted,k}$ is the value of k^{th} data point predicted by the model fitted to all data except the k^{th} data point and E_k is the k^{th} data point. A model with a low LOO error is a useful one, because it can more accurately predict the missing data point.

We first examined the simple correlations listed in Table 5.A.4. Not surprisingly, most of these simple correlations performed poorly. The two correlations identified by (a) and (b) in Table 5.A.4 were the best among this initial set, and were used as the basis for further development. Retaining the terms shown in (a) and (b) in Table 5.A.4, we developed and tested the more extensive set of expressions listed in Table 5.A.5. For many of these expressions, a lower LOO error could be found by neglecting one or more of the terms in the expression. Terms that were neglected in this way are indicated in Table 5.A.5 in red, and the data shown on the right of this table for each model refers to the model with the lowest LOO error. In Table 5.A.6, Table 5.A.5 was rewritten with removing the red terms from Table 5.A.5 and listing the LOO error values for each model.

We subsequently selected a number of the correlations from Table 5.A.6 with the lowest LOO errors investigated the variances between the values on closely packed surfaces from these equations and Ruban *et al.*'s results[23-24] for all fcc, Fe, Co, and Ru binary pairs. The results from this analysis are listed in Table 5.A.7. Based on these

analyses, we find that including a quadratic term for the coordination number and/or an atomic size term do not improve the quality of the correlation significantly. Instead, surface segregation can be well described simply with an expression involving $\Delta CN \times \Delta\varepsilon$ and $\Delta CN \times \Delta d$ terms. Therefore, we consider the the expression denoted (c) in Table 5.A.7 to be the most effective correlation among those we have examined for describing surface segregation. Finally, Table 5.A.8 lists the segregation energies at kinked sites for binary pairs of all 3d, 4d, and 5d transition metals used in Fig. 5.7.

Table 5.A.4: Simple correlations between surface segregation and each factor.

Correlations	R^2	LOO error	variance
$\varepsilon_{segr} = c_1 \Delta CN + c_2$	0.0863	1.30E-01	0.3517
$\varepsilon_{segr} = c_1 \Delta CN^2 + c_2$	0.0807	1.32E-01	0.3528
$\varepsilon_{segr} = c_1 \Delta CN^2 + c_2 \Delta CN + c_3$	0.0863	1.34E-01	0.3517
$\varepsilon_{segr} = c_1 \Delta\varepsilon + c_2$	0.5137	6.85E-02	0.2559
$\varepsilon_{segr} = c_1 \Delta\sigma + c_2$	0.0010	1.41E-01	0.3676
$\varepsilon_{segr} = c_1 \Delta d + c_2$	0.2776	1.02E-01	0.3124
$\varepsilon_{segr} = c_1 \Delta CN \times \Delta\varepsilon + c_2$ **(f)**	0.8062	2.74E-02	0.1620
$\varepsilon_{segr} = c_1 \Delta CN^2 \times \Delta\varepsilon + c_2$ **(g)**	0.7858	3.06E-02	0.1707
$\varepsilon_{segr} = c_1 \Delta CN \times \Delta\sigma + c_2$	0.0030	1.43E-01	0.3672
$\varepsilon_{segr} = c_1 \Delta CN^2 \times \Delta\sigma + c_2$	0.0013	1.44E-01	0.3675
$\varepsilon_{segr} = c_1 \Delta CN \times \Delta d + c_2$	0.3831	8.81E-02	0.2887
$\varepsilon_{segr} = c_1 \Delta CN^2 \times \Delta d + c_2$	0.3480	9.38E-02	0.2970

Table 5.A.5: The possible correlations extended from Eqs. (a) and (b). Red terms would be removed after LOO analysis.

Correlations	R^2	variance
$\varepsilon_{segr} = c_1 \Delta CN \times \Delta\varepsilon + c_2 \Delta\sigma + c_3$	0.8495	0.1429
$\varepsilon_{segr} = c_1 \Delta CN \times \Delta\varepsilon + c_2 \Delta d + c_3$	0.9040	0.1138
$\varepsilon_{segr} = c_1 \Delta CN \times \Delta\varepsilon + c_2 \Delta\sigma + c_3 \Delta d + c_4$	0.9054	0.1138
$\varepsilon_{segr} = \Delta CN \times (c_1 \Delta\varepsilon + c_2 \Delta\sigma) + c_3$	0.8638	0.1360
$\varepsilon_{segr} = \Delta CN \times (c_1 \Delta\varepsilon + c_2 \Delta d) + c_3$	0.9315	0.0962
$\varepsilon_{segr} = \Delta CN \times (c_1 \Delta\varepsilon + c_2 \Delta\sigma) + c_3 \Delta d + c_4$	0.9145	0.1138
$\varepsilon_{segr} = \Delta CN \times (c_1 \Delta\varepsilon + c_2 \Delta d) + c_3 \Delta\sigma + c_4$	0.9326	0.0962
$\varepsilon_{segr} = \Delta CN \times (c_1 \Delta\varepsilon + c_2 \Delta\sigma + c_3 \Delta d) + c_4$	0.9326	0.0962
$\varepsilon_{segr} = c_1 \Delta CN^2 \times \Delta\varepsilon + c_2 \Delta\sigma + c_3$	0.8179	0.1576
$\varepsilon_{segr} = c_1 \Delta CN^2 \times \Delta\varepsilon + c_2 \Delta d + c_3$	0.9056	0.1134
$\varepsilon_{segr} = c_1 \Delta CN^2 \times \Delta\varepsilon + c_2 \Delta CN \times \Delta\varepsilon + c_3$	0.8113	0.1600
$\varepsilon_{segr} = c_1 \Delta CN^2 \times \Delta\varepsilon + c_2 \Delta CN \times \Delta\sigma + c_3$	0.8353	0.1500
$\varepsilon_{segr} = c_1 \Delta CN^2 \times \Delta\varepsilon + c_2 \Delta CN \times \Delta d + c_3$	0.9201	0.1045
$\varepsilon_{segr} = \Delta CN^2 \times (c_1 \Delta\varepsilon + c_2 \Delta\sigma) + c_3$	0.8256	0.1543
$\varepsilon_{segr} = \Delta CN^2 \times (c_1 \Delta\varepsilon + c_2 \Delta d) + c_3$	0.8909	0.1221
$\varepsilon_{segr} = \Delta CN^2 \times (c_1 \Delta\varepsilon + c_2 \Delta\sigma) + c_3 \times \Delta CN \times \Delta\varepsilon + c_4$	0.8544	0.1425
$\varepsilon_{segr} = \Delta CN^2 \times (c_1 \Delta\varepsilon + c_2 \Delta\sigma) + c_3 \times \Delta CN \times \Delta\sigma + c_4$	0.8392	0.1490
$\varepsilon_{segr} = \Delta CN^2 \times (c_1 \Delta\varepsilon + c_2 \Delta\sigma) + c_3 \times \Delta CN \times \Delta d + c_4$	0.9202	0.1038
$\varepsilon_{segr} = \Delta CN^2 \times (c_1 \Delta\varepsilon + c_2 \Delta d) + c_3 \times \Delta CN \times \Delta\varepsilon + c_4$	0.9161	0.1075
$\varepsilon_{segr} = \Delta CN^2 \times (c_1 \Delta\varepsilon + c_2 \Delta d) + c_3 \times \Delta CN \times \Delta\sigma + c_4$	0.8927	0.1213
$\varepsilon_{segr} = \Delta CN^2 \times (c_1 \Delta\varepsilon + c_2 \Delta d) + c_3 \times \Delta CN \times \Delta d + c_4$	0.9332	0.1038

$\varepsilon_{segr} = c_1 \Delta CN^2 \times \Delta\varepsilon + \Delta CN \times (c_2 \Delta\varepsilon + c_3 \Delta\sigma) + c_4$	0.8677	0.1355
$\varepsilon_{segr} = c_1 \Delta CN^2 \times \Delta\varepsilon + \Delta CN \times (c_2 \Delta\varepsilon + c_3 \Delta d) + c_4$	0.9366	0.0961
$\varepsilon_{segr} = c_1 \Delta CN^2 \times \Delta\varepsilon + \Delta CN \times (c_2 \Delta\sigma + c_3 \Delta d) + c_4$	0.9201	0.1038
$\varepsilon_{segr} = \Delta CN^2 \times (c_1 \Delta\varepsilon + c_2 \Delta\sigma) + \Delta CN \times (c_3 \Delta\varepsilon + c_4 \Delta\sigma) + c_5$	0.8756	0.1307
$\varepsilon_{segr} = \Delta CN^2 \times (c_1 \Delta\varepsilon + c_2 \Delta\sigma) + \Delta CN \times (c_3 \Delta\varepsilon + c_4 \Delta d) + c_5$	0.9366	0.0924
$\varepsilon_{segr} = \Delta CN^2 \times (c_1 \Delta\varepsilon + c_2 \Delta\sigma) + \Delta CN \times (c_3 \Delta\sigma + c_4 \Delta d) + c_5$	0.9242	0.1038
$\varepsilon_{segr} = \Delta CN^2 \times (c_1 \Delta\varepsilon + c_2 \Delta d) + \Delta CN \times (c_3 \Delta\varepsilon + c_4 \Delta\sigma) + c_5$	0.9198	0.1053
$\varepsilon_{segr} = \Delta CN^2 \times (c_1 \Delta\varepsilon + c_2 \Delta d) + \Delta CN \times (c_3 \Delta\varepsilon + c_4 \Delta d) + c_5$	0.9428	0.0928
$\varepsilon_{segr} = \Delta CN^2 \times (c_1 \Delta\varepsilon + c_2 \Delta d) + \Delta CN \times (c_3 \Delta\sigma + c_4 \Delta d) + c_5$	0.9335	0.0953
$\varepsilon_{segr} = \Delta CN^2 \times (c_1 \Delta\varepsilon + c_2 \Delta\sigma + c_3 \Delta d)$ $+\Delta CN \times (c_4 \Delta\varepsilon + c_5 \Delta\sigma + c_6 \Delta d) + c_7$	0.9459	0.0868
$\varepsilon_{segr} = \Delta CN^2 \times (c_1 \Delta\varepsilon + c_2 \Delta\sigma + c_3 \Delta d)$ $+\Delta CN \times (c_4 \Delta\varepsilon + c_5 \Delta\sigma + c_6 \Delta d) + c_7 \Delta\varepsilon + c_8 \Delta\sigma + c_9 \Delta d + c_{10}$	0.9515	0.0813

Table 5.A.6: The correlations which remove red terms in Table 5.A.5. Their LOO errors are also listed.

Correlations	R^2	LOO error	variance
$\varepsilon_{segr} = c_1 \Delta CN \times \Delta\varepsilon + c_2 \Delta\sigma + c_3$	0.8495	2.19E-02	0.1429
$\varepsilon_{segr} = c_1 \Delta CN \times \Delta\varepsilon + c_2 \Delta d + c_3$	0.9040	1.39E-02	0.1138
$\varepsilon_{segr} = \Delta CN \times \left(c_1 \Delta\varepsilon + c_2 \Delta\sigma\right) + c_3$	0.8638	2.01E-02	0.1360
$\varepsilon_{segr} = \Delta CN \times \left(c_1 \Delta\varepsilon + c_2 \Delta d\right) + c_3$	0.9315	9.97E-03	0.0962
$\varepsilon_{segr} = c_1 \Delta CN^2 \times \Delta\varepsilon + c_2 \Delta\sigma + c_3$	0.8179	2.67E-02	0.1576
$\varepsilon_{segr} = c_1 \Delta CN^2 \times \Delta\varepsilon + c_2 \Delta d + c_3$	0.9056	1.38E-02	0.1134
$\varepsilon_{segr} = c_1 \Delta CN^2 \times \Delta\varepsilon + c_2 \Delta CN \times \Delta\varepsilon + c_3$	0.8113	2.73E-02	0.1600
$\varepsilon_{segr} = c_1 \Delta CN^2 \times \Delta\varepsilon + c_2 \Delta CN \times \Delta\sigma + c_3$	0.8353	2.46E-02	0.1500
$\varepsilon_{segr} = \Delta CN^2 \times \left(c_1 \Delta\varepsilon + c_2 \Delta\sigma\right) + c_3$	0.8256	2.63E-02	0.1543
$\varepsilon_{segr} = \Delta CN^2 \times \left(c_1 \Delta\varepsilon + c_2 \Delta d\right) + c_3$	0.8909	1.59E-02	0.1221
$\varepsilon_{segr} = c_1 \Delta CN^2 \times \Delta\sigma + c_2 \times \Delta CN \times \Delta\varepsilon + c_3$	0.8494	2.21E-02	0.1425
$\varepsilon_{segr} = c_1 \Delta CN^2 \times \Delta\varepsilon + c_2 \times \Delta CN \times \Delta\sigma + c_3$	0.8353	2.43E-02	0.1490
$\varepsilon_{segr} = c_1 \Delta CN^2 \times \Delta\varepsilon + c_2 \times \Delta CN \times \Delta d + c_3$	0.9201	1.16E-02	0.1038
$\varepsilon_{segr} = c_1 \Delta CN^2 \times \Delta d + c_2 \Delta CN \times \Delta\varepsilon + c_3$	0.9142	1.24E-02	0.1075
$\varepsilon_{segr} = c_1 \Delta CN^2 \times \Delta\sigma + \Delta CN \times \left(c_2 \Delta\varepsilon + c_3 \Delta\sigma\right) + c_4$	0.8732	1.88E-02	0.1307
$\varepsilon_{segr} = c_1 \Delta CN^2 \times \Delta\varepsilon + \Delta CN \times \left(c_3 \Delta\varepsilon + c_4 \Delta d\right) + c_5$	0.9366	9.33E-03	0.0924
$\varepsilon_{segr} = c_1 \Delta CN^2 \times \Delta d + \Delta CN \times \left(c_3 \Delta\varepsilon + c_4 \Delta\sigma\right) + c_5$	0.9178	1.21E-02	0.1053
$\varepsilon_{segr} = \Delta CN^2 \times \left(c_1 \Delta\varepsilon + c_2 \Delta d\right) + c_3 \Delta CN \times \Delta d + c_4$	0.9332	1.00E-02	0.0953
$\varepsilon_{segr} = \Delta CN^2 \times \left(c_1 \Delta\varepsilon + c_2 \Delta\sigma\right) + \Delta CN \times \left(c_3 \Delta\varepsilon + c_4 \Delta\sigma + c_5 \Delta d\right) + c_6$	0.9446	8.47E-03	0.0868
$\varepsilon_{segr} = \Delta CN^2 \times \left(c_1 \Delta\varepsilon + c_2 \Delta\sigma\right) + \Delta CN \times \left(c_3 \Delta\varepsilon + c_4 \Delta\sigma + c_5 \Delta d\right) + c_6 \Delta\sigma + c_7 \Delta d + c_8$	0.9514	7.81E-03	0.0813

Table 5.A.7: The equations with low LOO errors among the equations in Table 5.A.6. The variances between the values on closely packed surfaces from these equations and Ruban *et al.*'s results for all fcc, Fe, Co, and Ru binary pairs are also listed.

Correlations	variance with Ruban *et al.*[23-24]	R^2	LOO error	variance
$\varepsilon_{segr} = \Delta CN^2 \times (c_1 \Delta\varepsilon + c_2 \Delta\sigma)$ $+\Delta CN \times (c_3 \Delta\varepsilon + c_4 \Delta\sigma + c_5 \Delta d) + c_6 \Delta\sigma + c_7 \Delta d + c_8$	0.2389	0.9514	7.81E-03	0.0813
$\varepsilon_{segr} = \Delta CN^2 \times (c_1 \Delta\varepsilon + c_2 \Delta\sigma)$ $+\Delta CN \times (c_3 \Delta\varepsilon + c_4 \Delta\sigma + c_5 \Delta d) + c_6$	0.2380	0.9446	8.47E-03	0.0868
$\varepsilon_{segr} = c_1 \Delta CN^2 \times \Delta\varepsilon + \Delta CN \times (c_3 \Delta\varepsilon + c_4 \Delta d) + c_5$	0.2549	0.9366	9.33E-03	0.0924
$\varepsilon_{segr} = \Delta CN \times (c_1 \Delta\varepsilon + c_2 \Delta d) + c_3$ **(h)**	0.2488	0.9315	9.97E-03	0.0962
$\varepsilon_{segr} = \Delta CN^2 \times (c_1 \Delta\varepsilon + c_2 \Delta d) + c_3 \times \Delta CN \times \Delta d + c_4$	0.2635	0.9332	1.00E-02	0.0953
$\varepsilon_{segr} = c_1 \Delta CN^2 \times \Delta\varepsilon + c_2 \Delta CN \times \Delta d + c_3$	0.2838	0.9201	1.16E-02	0.1038
$\varepsilon_{segr} = c_1 \Delta CN^2 \times \Delta d + \Delta CN \times (c_3 \Delta\varepsilon + c_4 \Delta\sigma) + c_5$	0.2529	0.9178	1.21E-02	0.1053
$\varepsilon_{segr} = c_1 \Delta CN^2 \times \Delta d + c_2 \Delta CN \times \Delta\varepsilon + c_3$	0.2648	0.9142	1.24E-02	0.1075
$\varepsilon_{segr} = c_1 \Delta CN^2 \times \Delta\varepsilon + c_2 \Delta d + c_3$	0.2780	0.9056	1.38E-02	0.1134
$\varepsilon_{segr} = c_1 \Delta CN \times \Delta\varepsilon + c_2 \Delta d + c_3$	0.2547	0.9040	1.39E-02	0.1138

Table 5.A.8: Surface segregation energies at kinked sites for binary pairs of all 3d, 4d, and 5d transition metals (in unit of eV). These numbers are used for Fig. 5.7.

	Ti	**V**	**Cr**	**Mn**	**Fe**	**Co**	**Ni**	**Cu**	**Zr**	**Nb**	**Mo**	**Tc**	**Ru**	**Rh**	**Pd**	**Ag**	**Hf**	**Ta**	**W**	**Re**	**Os**	**Ir**	**Pt**	**Au**
Ti		0.30	-0.08	-0.82	0.54	0.36	0.19	-0.48	-0.28	0.30	0.80	0.61	0.81	0.37	-0.57	-1.07	-0.09	0.46	0.99	1.26	1.16	0.77	-0.10	-1.00
V	-0.53		-0.25	-0.89	-0.09	-0.16	-0.40	-1.26	-0.84	-0.11	0.48	0.15	0.34	-0.29	-1.53	-2.11	-0.57	0.11	0.75	1.03	0.79	0.23	-0.95	-2.07
Cr	-0.30	0.14		-0.68	0.16	0.29	0.05	-0.80	-0.67	0.02	0.60	0.27	0.50	-0.05	-1.21	-1.72	-0.41	0.24	0.85	1.12	0.92	0.40	-0.70	-1.74
Mn	0.19	0.67	0.51		0.88	0.95	0.72	-0.05	-0.20	0.52	1.13	0.86	1.13	0.61	-0.49	-0.98	0.06	0.73	1.37	1.68	1.52	1.03	-0.02	-1.02
Fe	-1.17	-0.35	-0.33	-1.00		-0.03	-0.31	-1.01	-1.15	-0.71	0.23	-0.24	0.34	-0.19	-1.10	-1.92	-0.95	-0.23	0.33	0.71	1.05	0.26	-0.78	-1.88
Co	-0.67	-0.32	-0.55	-0.72	0.00		-0.24	-0.77	-0.98	-0.43	0.07	0.02	0.33	-0.13	-0.99	-1.43	-0.79	-0.28	0.23	0.56	0.62	0.19	-0.58	-1.45
Ni	-0.61	-0.23	-0.20	-0.64	-0.24	-0.04		-0.53	-0.90	-0.34	0.16	0.12	0.39	0.02	-0.77	-1.18	-0.71	-0.20	0.32	0.65	0.68	0.38	-0.37	-1.16
Cu	1.00	0.44	0.42	0.02	0.25	0.90	0.61		-0.50	0.26	0.90	0.85	1.13	0.64	0.00	-0.70	-0.35	0.37	1.65	1.44	1.44	1.13	0.28	-0.63
Zr	0.15	0.32	0.21	-0.37	0.15	0.74	0.21	-0.19		0.53	1.05	0.89	1.11	0.70	-0.23	-0.75	0.12	0.69	1.24	1.54	1.46	1.10	0.25	-0.65
Nb	-0.40	0.00	-0.37	-1.42	0.34	0.31	-0.88	-0.99	-0.70		0.68	0.40	0.63	0.06	-1.15	-1.76	-0.44	0.28	0.94	1.27	1.09	0.56	-0.56	-1.68
Mo	-1.07	-0.58	-0.75	-1.34	-0.72	-0.48	-0.56	-1.38	-1.43	-0.69		-0.31	-0.03	-0.52	-1.66	-2.18	-1.18	-0.48	0.18	0.52	0.38	-0.07	-1.11	-2.10
Tc	-0.71	-0.31	-0.46	-0.89	-0.39	-0.03	-0.35	-0.93	-0.99	-0.39	0.12		0.14	-0.26	-1.14	-1.54	-0.81	-0.26	0.28	0.55	0.45	0.09	-0.73	-1.52
Ru	-0.93	-0.51	-0.70	-1.37	-0.61	-0.20	-0.45	-0.98	-1.23	-0.63	-0.12	-0.29		-0.40	-1.22	-1.57	-1.07	-0.50	0.04	0.32	0.64	-0.08	-0.83	-1.57
Rh	0.32	0.59	-0.45	-0.78	-0.49	0.13	-0.19	-0.70	-1.03	-0.43	0.09	-0.04	0.26		-0.83	-1.18	-0.85	-0.30	0.24	1.18	0.54	0.27	-0.36	-1.16
Pd	-0.25	0.92	0.13	-0.21	0.65	0.39	0.51	0.05	-0.55	0.05	0.62	0.56	0.89	0.47		-0.48	-0.37	0.18	0.75	1.13	1.17	0.97	0.32	-0.36
Ag	0.57	1.05	0.99	0.57	0.67	1.04	1.18	0.52	0.24	1.00	1.65	1.54	1.81	1.45	0.57		0.35	1.09	1.77	2.17	2.16	1.86	1.06	0.11
Hf	-0.02	0.32	-0.14	-0.65	0.12	0.35	0.30	-0.38	-0.25	0.36	0.88	0.71	0.93	0.52	-0.42	-0.94		0.50	1.07	1.36	1.28	0.92	0.05	-0.84
Ta	-0.74	-0.32	-0.70	-1.56	-0.59	-0.17	-1.57	-1.35	-1.05	-0.27	0.36	0.06	0.30	-0.28	-1.51	-2.13	-0.79		0.62	0.94	0.75	0.23	-0.92	-1.69
W	-1.32	-0.83	-1.06	-1.59	-0.90	-0.46	-0.85	-1.63	-1.70	-0.93	-0.29	-0.55	-0.27	-0.80	-1.93	-2.44	-1.45	-0.73		0.27	0.14	-0.33	-1.39	-2.44
Re	-1.31	-0.90	-1.05	-1.43	-0.93	-0.70	-0.95	-1.54	-1.62	-1.01	-0.49	-0.67	-0.47	-0.89	-1.78	-2.16	-1.44	-0.88	-0.34		-0.16	-0.54	-1.37	-2.16
Os	-1.23	-0.79	-0.86	-1.28	-0.83	-0.62	-0.74	-1.28	-1.56	-0.92	-0.39	-0.56	-0.35	-0.73	-1.55	-1.89	-1.40	-0.81	-0.25	0.03		-0.40	-1.18	-1.92
Ir	0.04	-0.60	-0.66	-1.06	-0.70	-0.42	-0.42	-1.16	-1.37	-0.76	-0.22	-0.34	-0.05	-0.36	-1.22	-1.52	-1.20	-0.64	-0.08	0.24	0.22		-0.96	-1.52
Pt	-0.60	-0.16	-0.17	-0.55	-0.39	-0.05	0.04	-0.28	-0.94	-0.32	0.26	0.19	0.53	0.25	-0.46	-0.79	-0.78	-0.20	0.38	0.76	0.78	0.59		-0.76
Au	0.23	0.70	0.69	0.30	0.37	0.72	0.86	0.34	-0.27	0.57	1.25	1.19	1.51	1.17	0.35	-0.20	-0.16	0.66	1.41	1.83	1.84	1.57	0.81	

CHAPTER 6

CHEMICAL SPECIATION OF ADSORBED GLYCINE ON METAL

6.1. Introduction

One potential class of chiral modifiers is the amino acids. Understanding amino acid adsorption on metal surfaces is a useful entry point to investigate the possible phenomena that can arise when chiral molecules form surface adlayers on achiral substrates. Interest in emergent technologies such as biomaterials and biosensors has also motivated efforts to understand the interaction between amino acids and metal surfaces[1-6]. A large number of experiments have probed the formation and properties of amino acids adsorbed on achiral metal surfaces[1-2, 4, 7-16]. In some cases amino acids can form well-ordered overlayers[1-4, 7, 11, 17-23], but many examples also exist with disordered overlayers[24-25]. In some cases, adsorbed amino acids induce faceting of the underlying surface into high Miller index facets that are chiral[4, 19, 26-28].

Amino acids can exist in a various chemical states depending on their environment. In the gas phase, most amino acids exist in their neutral form, $H_2NCHRCOOH$, whereas in their molecular crystals or in aqueous solutions, they are usually zwitterionic, $^{+}H_3NCHRCOO^{-}$[29-30]. Here, R is the functional group that varies among different amino acids. This variety in speciation also occurs when amino acids are adsorbed on metal surfaces. Experiments have reported that amino acids on Cu surfaces dehydrogenate to form $H_2NCHRCOO$ on the surface[1-3, 7, 18, 31-32]. Experimental observations on Pd(111)[33], Pt(111)[34], and Ag(110)[14, 35], however, have shown that adsorbed amino acids on these surfaces are dominated by a zwitterionic form.

Throughout this Chapter we consider glycine, the simplest amino acid. A large number of studies have focused on glycine adsorption on metal surfaces including Cu[1, 7, 10, 31, 36-38], Pd[33], Pt[34, 39], Ag[35, 40], Au[26, 41-42] and binary metal surfaces[9, 43-44]. Although

glycine is achiral, since R = H in the notation above, understanding the structure of adsorbed glycine overlayers has proven to be useful in analyzing the properties of more complex chiral amino acids[3, 5, 27-28, 33, 38, 45-47]. Using density functional theory (DFT) calculations, James and Sholl concluded that at equilibrium, glycine is adsorbed preferentially at low coverage on Cu(110), Cu(100), and Pd(111) in its dehydrogenated form[48]. This conclusion is in disagreement with the experimental observation of zwitterionic glycine on Pd(111)[33].

To reconcile the discrepancy, we test three hypotheses in this Chapter. One possible resolution of this disagreement is that in these experiments the adsorbates are not at equilibrium. If, for example, glycine is initially deposited at low temperature as a zwitterion and a large energy barrier prevents dehydrogenation at the experimental temperature(s), the zwitterionic species would be observed even though it is thermodynamically metastable. It is useful to note in this context that experiments involving glycine on Cu surfaces typically use temperatures of ~400 K for annealing surface layers[1-3, 7, 18, 31-32], but significantly lower annealing temperatures are used on Pd surfaces because of the reactivity of glycine on Pd[33]. A second hypothesis is that the existence of excess H atoms on the surfaces plays a role in glycine speciation. This situation may be especially relevant for Pd(111), since H is well known for binding favorably relative to gaseous H_2 on Pd surfaces and in the bulk of Pd[49-53]. By Le Chatelier's principle, increasing the concentration of adsorbed H could cause more zwitterions to be present on the surface. The last hypothesis we examine is that aggregation of each species could play a decisive role in the speciation of adsorbed glycine. Although the zwitterionic species is thermodynamically metastable at low coverages, it is possible that they might be more preferred on the surfaces to other species once aggregation occurs.

The aim of this Chapter is to test each of the hypothesis described above. We use DFT calculations to characterize the energy barriers and reaction rates for

dehydrogenation of zwitterionic glycine on two surfaces where dehydrogenated glycine is seen experimentally, Cu(110) and Cu(100), and two surfaces that are reported experimentally to adsorb glycine as a zwitterions, Pd(111) and Pt(111). For each surface we use DFT to determine a transition state for dehydrogenation and apply Transition State Theory (TST) to estimate the rate of this reaction at experimentally relevant temperatures. We also discuss how the presence of additional coadsorbed H would influence the thermodynamics on each surface. Lastly, we use Monte Carlo simulations based on data from DFT calculations to test if zwitterions can be adsorbed preferentially due to aggregation.

6.2. Calculation methods

We performed plane wave DFT calculations using the Vienna *ab initio* Simulation Package (VASP) with the ultrasoft pseudopotentials available in this package[54-56]. These calculations used the generalized gradient approximation (GGA) with the Perdew-Wang 91 functional[57] and a plane wave expansion with a cutoff of 396 eV. Total energy calculations were conducted using the residual minimization method for electronic relaxation, accelerated using Methfessel-Paxton Fermi-level smearing with a width of 0.2 eV. Geometries were relaxed using a conjugate gradient algorithm until the forces on all the unconstrained atoms were less than 0.03 eV/Å. The periodicity of the material in the plane of each surface was defined using the DFT-optimized lattice parameter at the bulk material. Our calculations on Cu(100), Pd(111), and Pt(111) were performed using slabs of four layers with the bottom two layers constrained in their bulk positions. For Cu(110), a slab seven layers thick was used with the bottom three layers constrained. A vacuum spacing of 14 Å was used in the direction of the surface normal for all calculations.

Most of our calculations considered the adsorption of glycine on the surfaces at coverages where the adsorbed molecules are well separated. Specifically, we examined

surfaces with one adsorbed glycine in a (3×3) surface unit cell for Cu(100), Pd(111), and Pt(111) and a (3×2) surface unit cell for Cu(110), respectively. This corresponds to overlayers with areas of 56.2, 59.6, 61.1, and 62.1 $Å^2$/molecule for Cu(110), Cu(100), Pd(111), and Pt(111), respectively. For comparison, the dense adlayer that is observed experimentally on Cu(110) has a density of 28.1 $Å^2$/molecule[11]. All calculations sampled reciprocal space with a 3×3×1 Monkhorst-Pack *k*-point mesh[58]. Molecules were placed on only one side of the slab and dipole corrections were applied in computing all of the energies reported below[59-60].

The energy change, ΔE, associated with surface reactions of the form

$$H_3NCH_2COO_{(ads)} \rightleftarrows H_2NCH_2COO_{(ads)} + H_{(ads)} \qquad (6.1)$$

was defined so that negative values indicate that the reaction products are energetically preferred relative to the reactant. Calculations for the products were performed with both adsorbates coadsorbed on the surface with the same surface unit cell as the calculations for the reactants.

All calculations involved supercells in a charge neutral state. In solution, amino acids can exist in an anionic form, $H_2NCH_2COO^-$, with the associated proton, H^+, separated from the molecule. On a metal surface, however, charge transfer between the adsorbed species and the surface controls net charge in the adsorbates. We therefore denote the product in Eq. (6.1) in their neutral state and refer to H_2NCH_2COO as dehydrogenated glycine rather than anionic glycine. It is useful to note in this context that DFT calculations for ordered overlayers of dehydrogenated glycine (and other amino acids) on Cu surfaces have given structures in excellent agreement with experimental observations[27-28, 32, 38, 61-63]. We also present results for adsorption of H_2NCH_2COOH, which we will refer to as the neutral molecular species. This species turns out to play an important role in the behavior of glycine on Pt(111).

The nudged elastic band (NEB) method[64-65] was used to investigate the energy barriers of dehydrogenation reaction of adsorbed glycine. Initial approximations to

reaction paths were obtained by linear interpolation between the lowest energy minima observed for the initial and final states. All adsorbate atoms and the top two (four) slab layers on Cu(100), Pd(111), and Pt(111) (Cu(110)) are fully relaxed during these calculations. In all cases, the six intermediate images were used, which is sufficient to characterize the minimum energy path (MEP). It is of course possible that multiple reaction pathways exist for the processes we consider. Since we cannot rigorously exclude the possibility that other transition states with lower energies exist for the reactions we consider, the reaction rates we estimate below are best viewed as upper bounds on the reaction rates that would be observed if other reaction channels also exist. The zero-point energies associated with H in glycine and on metal surfaces can be appreciable[48, 66-68]. To assess the role of zero point energies in Eq. (6.1), normal modes and vibrational frequencies were calculated within the harmonic approximation using finite difference displacements of 0.03 Å. All adsorbate atoms were included in these calculations but the position of all metal atoms were fixed. Once the normal mode frequencies, v_i, were computed, the total zero-point energy is defined by $\sum_i hv_i / 2$, where the sum is over all normal modes with real vibrational frequencies.

6.3. Results and discussion

6.3.1. DFT results for the kinetics of glycine dehydrogenation on metal surfaces

6.3.1.1. Comparison of the stability of each adsorbed glycine species

We have performed DFT calculations to compare the stability of each adsorbed glycine species (zwitterionic, dehydrogenated, and neutral) on Cu(110), Cu(100), Pd(111), and Pt(111). As initial configurations for glycine adsorption on Cu(110), we used structural details obtained from previous reports for dehydrogenated and zwitterionic molecules on the surface[38, 48, 61-62]. The optimized geometries of zwitterionic

glycine and dehydrogenated glycine coadsorbed with H on Cu(110) are illustrated in Fig. 6.1(a) and (c), respectively. A tridentate configuration is favored for dehydrogenated glycine, with the N and O atoms close to on-top positions[38, 61-62]. This geometry is very similar to what is predicted with DFT and observed experimentally for the ordered overlayer that has an adsorbate density double the value we used here[3, 38, 61-63]. In the zwitterionic species, a bidentate configuration is formed via the two O atoms in the molecule[48]. The H coadsorbed with dehydrogenated glycine prefers the short bridge site[48]. For the neutral species, we used the optimized dehydrogenated glycine structure as an initial configuration after adding a H atom to one O in the carboxyl group. After this calculation, we can observe that only a N atom in the neutral glycine is bound onto the surface as can be seen in Fig. 6.A.1(a) in the Appendix 6.A.

The initial structures of glycine adsorption for both glycine species on Cu(100) were constructed as in previous reports[38, 48]. The adsorption of glycine on Cu(100) can induce spontaneous surface reconstructions featuring intrinsically chiral Cu(3, 1, 17) if annealed at elevated temperatures[4, 7, 27-28]. Here, however, we will not consider the effects of the surface reconstruction. The optimized geometries of zwitterionic and dehydrogenated glycine coadsorbed with H on Cu(100) are shown in Fig. 6.2(a) and (c), respectively. Similarly to Cu(110), two O atoms in the zwitterionic glycine bind to the surface in a bidentate fashion, while a tridentate configuration between the N and O atoms in dehydrogenated glycine and the surface is favored[38, 48]. Each of these bonds can be roughly characterized as being in on-top sites on the surface. The coadsorbed H prefers the four fold-hollow site[48]. Similarly to Cu(110), for the neutral species, we used the optimized dehydrogenated glycine structure as an initial configuration. A unidentate configuration is formed on the surface via the N atom in the neutral glycine (Fig. 6.A.1(b) in the Appendix 6.A).

Glycine forms disordered overlayers on Pd(111)[33]. We performed calculations with one glycine in a (3×3) surface unit cell, corresponding to an isolated adsorbate. We

used the optimized geometries obtained from James and Sholl for dehydrogenated and zwitterionic glycine on Pd(111)[48]. The optimized geometries of zwitterionic and dehydrogenated glycine coadsorbed with H on Pd(111) are illustrated in Fig. 6.3(a) and (c), respectively. Similarly to the two Cu surfaces, the zwitterionic (dehydrogenated) glycine exhibits bidentate (tridentate) bonding with the surface[48]. When H is coadsorbed with dehydrogenated glycine it prefers an fcc hollow site, as is found for isolated H on Pd(111)[49, 69-70]. For the neutral species, we also used the optimized dehydrogenated glycine structure as an initial configuration. The optimized structure shows that only the N atom in the neutral glycine is bonded to the surface as can be seen in Fig. 6.A.1(c) in the Appendix 6.A.

We are not aware of any previous reports of the structure of glycine on Pt(111), although it is known experimentally that glycine adsorbs as intact molecules at all coverages at < 250 K, predominantly in the zwitterionic state[34]. To find the most preferred configuration of dehydrogenated glycine on Pt(111), we took the optimized molecular geometry on Pd(111) and placed the N atom in the molecule above a surface bridge site, top site, a fcc hollow site, and a hcp hollow site, respectively. We also rotated the molecule on each site by increments of 30° up to 120°. This gave 16 initial structures, each of which was optimized with DFT. These calculations converged to 4 distinct states. Unlike the previous surfaces we have examined, the dehydrogenated glycine does not bind to the surface in a tridentate fashion on Pt(111) in this favored geometry. Instead, the lowest energy state has bidentate bonding through the N atom and one O atom. The structure on Pt(111) most similar to the favored configuration on Pd(111) is 0.1 eV less stable than the bidentate state. After determining the most favorable configuration of dehydrogenated glycine on Pt(111), we examined the most preferred adsorption site for a coadsorbed H atom. We investigated the coadsorption of H on every 3 fold-hollow site and top site in a surface unit cell. It is already known that isolated H atoms bind preferentially to fcc sites on Pt(111)[70-71]. We found the same site to be the most stable

location when H is coadsorbed with glycine (Fig. 6.A.3(c) in the Appendix 6.A). We performed DFT calculations using all four stable structures of the dehydrogenated glycine as initial configurations for the zwitterionic glycine. The most favorable structure of zwitterionic glycine on Pt(111) are observed, where the molecule binds in a unidentate fashion (Fig. 6.A.3(a) in the Appendix 6.A). Similarly to dehydrogenated glycine on Pt(111), the zwitterionic structure with bidentate bonding that resembles the most preferred configuration on Pd(111) is ~0.1 eV less stable than the unidentate state. For the neutral glycine, we also used all four stable structures of the dehydrogenated glycine as initial configurations with adding a H atom to one O in the carboxyl group. After these calculations, we can obtain the most stable structure where the neutal glycine adsorbs on the surface via the N atom in the molecule (Fig. 6.A.1(d) in the Appendix 6.A).

Table 6.1 summarizes the relative stability of adsorbed system of three glycine species on each metal surface referenced to the dehydrogenated glycine coadsorbed with H. For all cases, the neutral species is more stable than the zwitterion on the surfaces. For every surface, the neutral molecule, H_2NCH_2COOH, is more stable than the zwitterionic adsorbate. This is a new observation that has not been seen previously because no earlier DFT calculations for these systems examined the neutral molecule. On Cu(110), Cu(100), and Pd(111), the dehydrogenated adsorbate is more stable than the neutral molecule, so the latter state is of limited interest. On Pt(111), however, the neutral molecule is the most stable among the three surface species we examined. We can therefore refine the observations that motivated our work as follows. On Cu(110) and Cu(100), the low coverage adsorbate predicted by DFT to be stable is consistent with experimental observations. On Pd(111) and Pt(111), however, experiments indicate the existence of zwitterionic glycine, whereas DFT calculations at low coverage show either a dehydrogenated or neutral adsorbate is preferred. In the reminder of the Chapter, we explore several possible explanations for this discrepancy.

ΔE (eV)	Cu(110)	Cu(100)	Pd(111)	Pt(111)
Zwitterionic	0.96	0.83	0.48	0.28
Neutral	0.79	0.59	0.18	-0.24
Dehyd w/ H	0.00	0.00	0.00	0.00

Table 6.1: Relative stability of three glycine species on the four surfaces referenced to the dehydrogenated glycine coadsorbed with H. The adsorption of neutral glycine is more (less) stable than that of zwitterionic (dehydrogenated) one on Cu(110), Cu(100), and Pd(111) while it is the most stable on Pt(111).

6.3.1.2. Activation barriers of dehydrogenation reaction on the surfaces

In this section we consider the possibility that formation of dehydrogenated molecules on a surface is kinetically limited. For this description to account for the experimental observations for Pd(111), we must point a process in which molecules arrive at the surface as zwitterions. Below, we examine the formation of a dehydrogenated molecule on Cu(110), Cu(110), and Pd(111) using an adsorbed zwitterion as a starting point.

The energy difference between the coadsorbed state, $H_2NCH_2COO_{(ads)}+H_{(ads)}$, and the zwitterionic state, $H_3NCH_2COO_{(ads)}$, on Cu(110) is ΔE = -0.96 eV (-0.85 eV) with (without) zero-point energy (ZPE) corrections. Figure 6.1 shows the calculated reaction pathway from zwitterionic to dehydrogenated glycine on Cu(110). The calculated activation energy barrier is 0.27 eV. In this case, the ZPE for the transition state and initial state were found to be identical within the precision of our calculations, so the energy barrier is the same with or without ZPEs. The transition state involves rotation of the NH_3 group, with minimal changes in the N-H distances. A local minimum is present along the reaction path (image 5 in Fig. 6.1) associated with an additional small energy barrier as the H atom on the surface moves to its final location on a short bridge site adjacent to the molecule (image 8 in Fig.6.1). Structural information for the initial, transition, and final state are summarized in Table 6.A.1 of the Appendix 6.A.

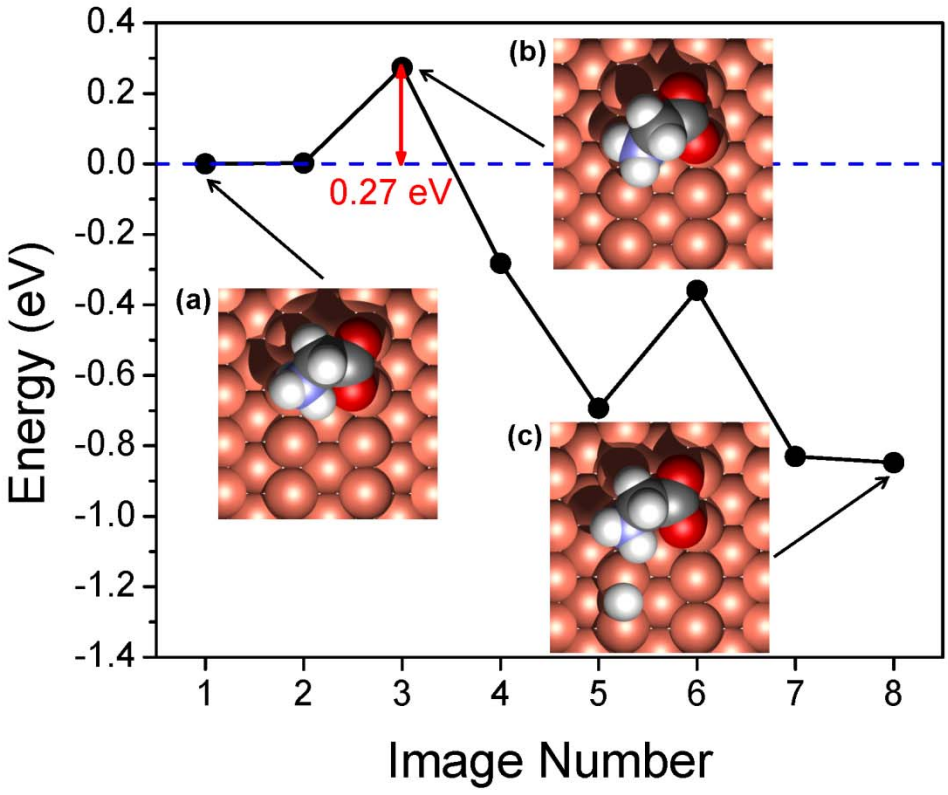

Figure 6.1: H dissociation pathway from zwitterionic to dehydrogenated glycine on Cu(110) without ZPE corrections. Top views of the (a) initial state, (b) transition state, and (c) final state are shown in the insets.

The coadsorbed state is more stable than the zwitterionic state on Cu(100), where the energy difference between them is ΔE = -0.83 eV (-0.63 eV) with (without) ZPE corrections. Figure 6.2 shows the calculated reaction pathway on Cu(100). The geometries for the initial, transition, and final state are shown in the insets of Fig. 6.2. The activation energy barrier is 0.02 eV without ZPE corrections. The ZPE for the transition state is ~0.2 eV smaller than one for the initial state. This implies that there is no energy barrier for this process once ZPEs are considered. Structural information for the initial, transition, and final state is summarized in Table 6.A.2 in the Appendix 6.A.

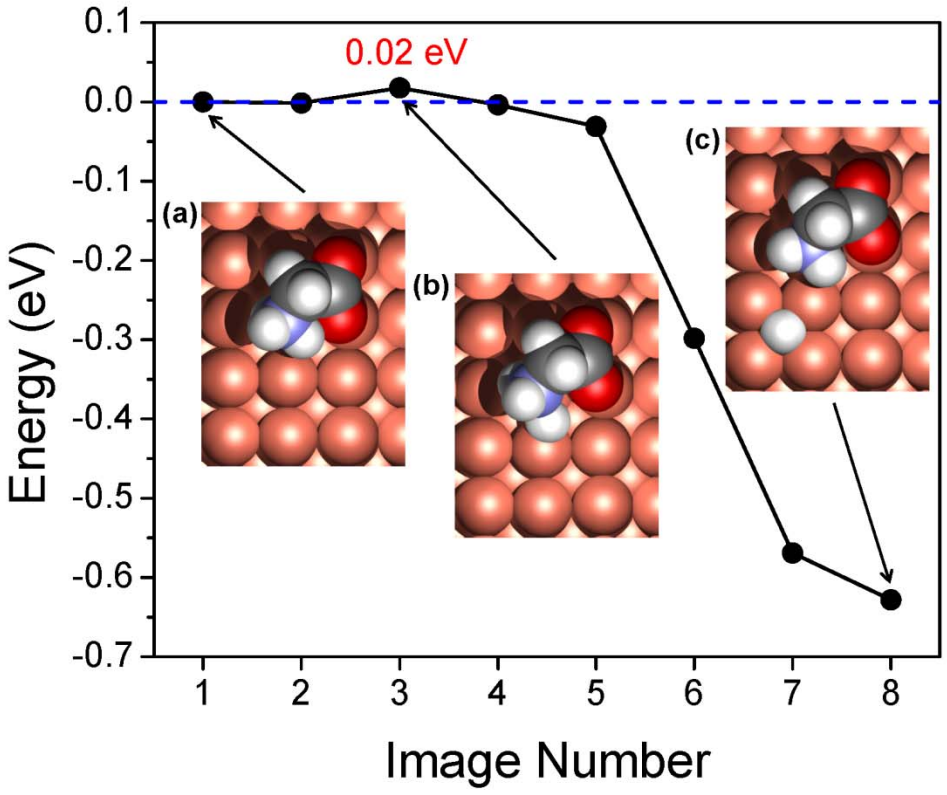

Figure 6.2: H dissociation pathway from zwitterionic to dehydrogenated glycine on Cu(100) without ZPE corrections. Top views of the (a) initial state, (b) transition state, and (c) final state are shown in the insets.

The energy difference between the coadsorbed state and the zwitterionic state on Pd(111) for the most stable state is ΔE = -0.49 eV (-0.36 eV) with (without) ZPE corrections. Figure 6.3 shows the calculated H dissociation pathway starting from zwitterionic glycine on Pd(111) without ZPE corrections. The geometries for the initial, transition, and final state are shown in the insets of Fig. 6.3. This NEB result gives activation energy barrier of 0.52 eV (0.73 eV) with (without) ZPE corrections. As observed on Cu(100), the energy barrier is reduced by ~0.2 eV if we include ZPEs because the ZPE for the transition state is smaller than for the adsorbed zwitterions. During the dehydrogenation reaction, the N atom in the molecule moves by 1.60 Å along

roughly the <110> direction. Structural information for the initial, transition, and final state are available in Table 6.A.3 of the Appendix 6.A.

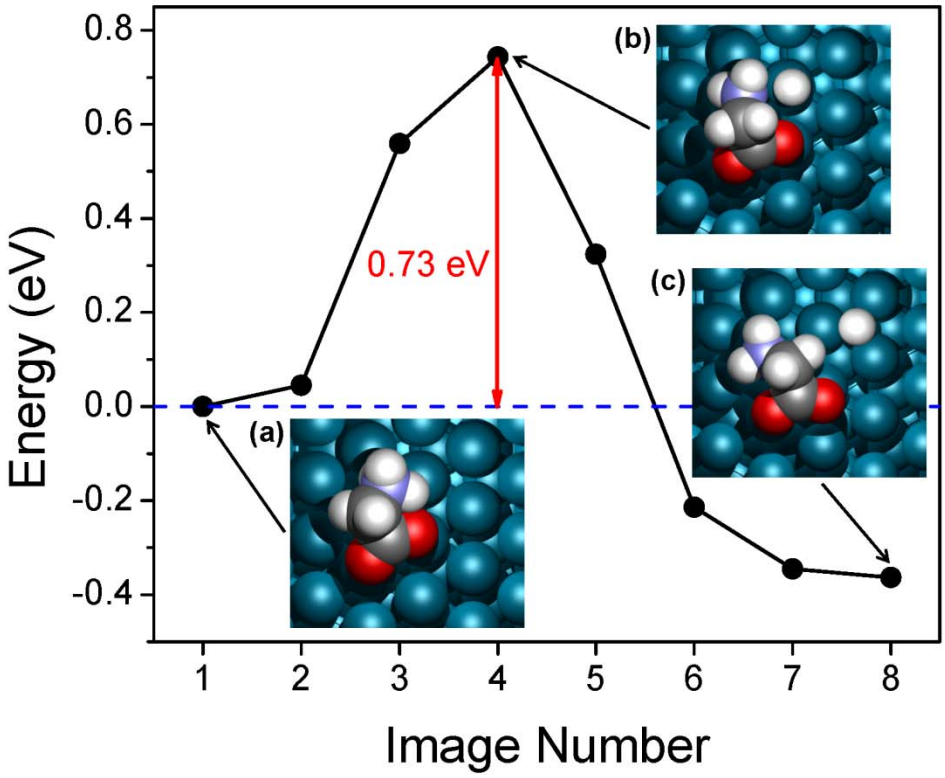

Figure 6.3: H dissociation pathway from zwitterionic to dehydrogenated glycine on Pd(111) without ZPE corrections. Top views of the (a) initial state, (b) transition state, and (c) final state are shown in the insets.

To compare our results with experimental observations, we have estimated surface reaction rates with harmonic transition state theory[72-73] (HTST) using $k = v\exp\left(-\Delta E / k_B T\right)$, where k is the surface reaction rate, k_B is Boltzmann's constant, T is temperature, and ΔE is the zero point energy corrected kinetic barrier calculated by DFT. We assumed that the prefactor, v, defining the reaction rate was 10^{13} s^{-1}. Using k from Eq. (6.2), we have calculated a probability of reaction over the course of the 5 second reaction at a fixed temperature. This quantity was chosen as being representative of the situation observed during temperature ramp used in the experiments for glycine adsorption on Pd(111)[33].

On Cu(110), the reaction probability defined in this way approaches 1 for T~80 K. Experimental observations reported that at liquid nitrogen temperatures (85 K) some glycine remains as the protonated form as it is deposited on a low temperature substrate, but at higher temperatures, the adsorbates is present on the surface in its deprotonated form, with the dissociated H atoms recombining and leaving the surface as H_2[1-3, 74]. The reaction probability in 5 seconds on Pd(111) approaches 1 at T~210 K. Gao *et al.* reported from their X-ray photoelectron spectroscopy (XPS) experiments that above 320 K, zwitterionic glycine begins to decompose and/or convert to the dehydrogenated glycine[33]. The conversion from zwitterionic species to dehydrogenated adsorbates implied by our calculations appears to be entirely consistent with the absence of zwitterions in experiment with Cu(110) and Cu(100). The situation for Pd(111), however, is less clear. Even if one assumes that some unspecified process initially creates zwitterionic molecules on the surface, the kinetic barriers to dehydrogenation do not appear to be so large that they could account for the experimentally observed stability of zwitterions at moderate temperatures.

6.3.2. Equilibrium populations and the effect of excess hydrogen

Here, we discuss the equilibrium thermodynamics associated with the results above. It is plausible that excess hydrogen is present experimentally, especially on Pd(111) since H favorably adsorbs relative to gaseous H_2 on Pd surfaces and in the bulk of Pd[49-53]. We consider both the situation where dehydrogenated glycine and atomic H are present on the surface in stoichiometric quantities and surfaces on which excess H is present. By Le Chatelier's principle, excess hydrogen could shift the equilibrium in Eq. (6.1) towards the reactant so that it causes more zwitterions on the surfaces. To quantify our analysis of Eq. (6.1), we express the total surface coverage of the amino acid, θ_A, as

$$\theta_A = \theta_{DA} + \theta_{ZA}, \tag{6.2}$$

where θ_{DA} and θ_{ZA} are the concentrations of dehydrogenated and zwitterionic glycine. We set θ_A as $1/n$, where n is the total number of surface atoms in the surface unit cell. For the systems described in our DFT calculations, $n = 9$ (6) for Cu(100), Pd(111), and (Cu(110)) using these units. The concentration of hydrogen, θ_H, can be expressed as

$$\theta_H = \theta_{DA} + \alpha, \tag{6.3}$$

where α is the concentration of excess hydrogen. When $\alpha = 0$, the reaction is in its stoichiometric state. The equilibrium constant, K_{eq}, can be then written as

$$K_{eq} = \frac{\theta_{DA}\theta_H}{\theta_{ZA}} = \frac{\theta_{DA}\left(\theta_{DA} + \alpha\right)}{\theta_A - \theta_{DA}} = \exp\left(-\frac{\Delta G}{k_B T}\right), \tag{6.4}$$

where ΔG is Gibbs' free energy change during the reaction.

We have calculated the enthalpy changes for the reaction on each surface we considered in Sec. 6.3. To calculate ΔG, however, entropic contributions should be also addressed. We assume that there is no configurational entropy change due to the adsorbed glycine in Eq. (6.1). The entropy change in this reaction is therefore equal to the configurational entropy of adsorbed H[75-76]

$$\Delta S_{rxn} = k_B \ln N_{config,H} = S_{config,H}, \tag{6.5}$$

Here, ΔS_{rxn} is the entropy change during the reaction and $N_{config,H}$ is the number of possible configurations of H. We assume that one site is available for H per metal atom in the surface. Using Stirling's approximation, this entropy can be written as

$$S_{config,H} = -k_B n[(1 - c\theta_A)\ln(1 - c\theta_A) + c\theta_A \ln c\theta_A)], \tag{6.6}$$

where c is the number of surface atoms unavailable for H adsorption because they are occupied by a glycine molecule. In every case, we take $c = 4$. So, 1-$c\theta_A$ is the fraction of surface sites available for hydrogen. This gives

$$\Delta G \cong \Delta E - TS_{config,H}, \tag{6.7}$$

where ΔE is the classical activation energy after ZPE corrections. Because the vibrational contributions to the internal energy may not be negligible[75, 77], we also add the vibrational contributions at finite temperature, $U_{vib,T}$ to ΔE, where $U_{vib,T} = \sum_i \frac{h\nu_i e^{-h\nu_i/k_BT}}{1-e^{-h\nu_i/k_BT}}$ is obtained from our calculated normal mode frequencies[78-79]. Combining all of these contributions, we express ΔG as

$$\Delta G \cong \Delta E + \Delta U_{vib,T} - TS_{config,H}\,. \tag{6.8}$$

Pd(111)	Temperature (K)	$\log(\theta_{ZA} / \theta_{DA})$	
		Stoichiometric state	H-rich state (α=0.3)
θ_A = 1/9	200	-15.90	-15.43
	400	-9.55	-8.98
	600	-7.31	-6.74
θ_A = 1/100	200	$\theta_{ZA} = 0$	$\theta_{ZA} = 0$
	400	-15.16	-13.71
	600	-12.97	-11.47

Table 6.2: Logarithmic ratios of zwitterionic to dehydrogenated glycine in the stoichiometric and hydrogen-rich states on Pd(111) at three different temperatures. The case where the glycine coverage is reduced to very low levels (θ_A =1/100) is also considered. The concentration of excess hydrogen, α, is assumed to be 0.3 for the hydrogen-rich state.

Using Eq. (6.5)-(6.8), the quadratic equation defined in Eq. (6.4), can be solved to obtain θ_{DA}. Table 6.2 shows the logarithmic ratios of the coverage of zwitterionic to dehydrogenated glycine ($\log(\theta_{ZA} / \theta_{DA})$) in the stoichiometric and hydrogen-rich states on Pd(111) at 200, 400, and 600 K. We also considered a case with very low glycine coverage (θ_A =0.01). It is clear that the dehydrogenated state is overwhelmingly preferred in equilibrium, even at the highest temperature we examined, which is far above the temperature at which reactions leading to further decomposition of glycine occurs[33]. The

presence of excess H, even at the relatively high level shown in the table, does not change the qualitative conclusion that the equilibrium population of the zwitterionic species on this surface is predicted to be effectively zero. On Cu(110) and Cu(100), the enthalpic difference between the zwitterionic and dehydrogenated states favors the latter state more strongly than on Pd(111). That is, the equilibrium population of the zwitterionic state on these surfaces is predicted to be even closer to zero than the results listed in Table 6.2 for Pd(111). It is clear from this discussion that the presence of excess adsorbed H cannot account for the experimental observation of zwitterionic glycine on Pd(111).

6.3.3. Aggregation of glycine species on Pt(111)

An obvious approximation in the DFT calculations described above is that they only examine isolated adsorbates. On Cu(110) and Cu(100), glycine forms ordered adlayers, and DFT calculations accurately describe the structure of these adlayers[38, 61-62]. On Pd(111) and Pt(111), however, no ordering has been reported experimentally. In this section we consider whether aggregation of glycine on Pt(111) is favored and, if so, how it may relate to the speciation of the adsorbed molecules. We examine neutral glycine to compare its stability with adsorbed zwitterions since the former state is the most stable for isolated molecules on Pt(111).

We first performed DFT calculations to obtain the interaction energy for each species using two nearby adsorbates. These calculations were performed using slabs of three layers constrained in their bulk positions; only the adsorbates were relaxed. In order to consider the adsorption of glycine at coverages where pairs of molecules are well separated from their periodic images, we examined surfaces with one adsorbed glycine in a (5×5) surface unit cell that corresponds to overlayers with areas of 172.4 $Å^2$/two aggregates. A 1×1×1 Monkhorst-Pack *k*-point mesh was used for these calculations. To search for the most stable configuration of two glycine molecules in this supercell, eight

possible arrangements of two molecules were optimized using the optimized isolated structure as a starting point. The interaction energy, E_{inter}, was defined by

$$E_{\text{inter}} = (E_{\text{2-ads}} + E_{\text{bare}}) - 2E_{\text{1-ads}} \tag{6.9}$$

Here, $E_{\text{2-ads}}$ ($E_{\text{1-ads}}$) is the total energy of the system containing the two (one) adsorbed molecules and E_{bare} the total energy of the bare surface. The interaction energy for neutral (zwitterionic) glycine in the most stable state we studied is -0.74 (-1.02) eV. In these states, two H-bonds of O-H…O are formed between the neutral glycine aggregates while one N-H…O is formed for the zwitterionic (see Fig. 6.A.2(a) and (c) in Appendix 6.A). We also observed an interaction energy of -0.11 eV associated with N-H…O for a pair of neutral glycine from a less stable configuration of adsorbed two aggregates (see Fig. 6.A.2(b) in Appendix 6.A). We can therefore estimate that for these pairs of molecules the interaction energy due to the one H-bond is -0.37 eV for O-H…O and -0.11 eV for N-H…O in the neutral species, while it is -1.02 eV for N-H…O in the zwitterionic species.

DFT calculations for more than three aggregates of each species are computationally very demanding. Rather than attempting to quantify aggregation with further DFT calculations, we performed Monte Carlo (MC) simulations based on the interaction energies estimated above. To represent the Pt atoms on the (111) surface, we used 20×20 hexagonal lattices with a nearest neighbor distance of ~2.8 Å and periodic boundary conditions. To represent the rotational degrees of freedom of each species, neutral and zwitterionic glycine were modeled as hexagons as shown in Fig. 6.4. Each vertex of these hexagons corresponds to a Pt atom on the surface, and the center of the hexagon is another surface atom. Among the vertices of the hexagon, there are two (one) H-bond donor sites (NH_2 and OH (NH_3)) and one (two) H-bond acceptor sites (O (two Os)) for neutral (zwitterionic) glycine.

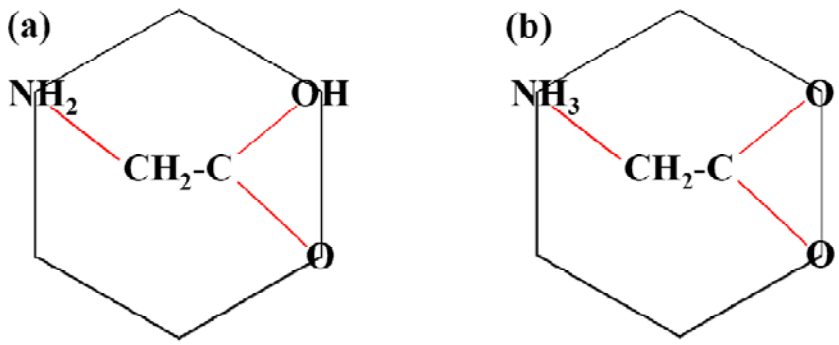

Figure 6.4: The structures of (a) neutral and (b) zwitterionic glycine are modeled as hexagons to represent their six rotational angles. There are two (one) H-bond donor sites and two (two) H-bond acceptor sites for neutral (zwitterionic) glycine.

The interactions between molecules within this simplified model were defined based on the center to center distance between nearby hexagons. For hexagons where this distance was < 5 (> 8) Å, the interaction energy was taken to be infinite (zero). For pairs of hexagons with center to center distances between these two limits, if the distance between a NH_2 (OH) at a vertex in a neutral species and an O atom at a vertex in the other neutral molecule is 2.2-5.2 Å, a H-bond of N-H…O (O-H…O) is considered to form with an interaction energy of -0.11 eV (-0.37 eV). Similarly, if the distance between a NH_3 at a vertex in a zwitterionic species and the an O atom at a vertex in the other zwitterionic molecule is within the same range of distances, a H-bond of N-H…O is assumed to form with the interaction energy of -1.02 eV. Since we regard NH_3, NH_2, or OH as a point in the hexagon, if we consider the actual bond lengths of N-H and O-H (~1 Å, respectively) that would somewhat reach out of the hexagon, the interaction range we used above is reasonable to account for normal H-bonds. For both species, it is possible that each hexagon simultaneously interact with one or more nearby hexagons since it has multiple H-bond accessible points at its vertexes.

MC simulations were performed with the model defined above using a combination of rigid body moves in which hexagons representing adsorbed molecules were moved between adjacent surface sites and rotational moves in which adsorbed

molecules were rotated while holding their central coordinate fixed. The acceptance probability of each move was defined by the Metropolis algorithm[80]. Each MC trajectory began by choosing the orientation and position of each molecule randomly subject to the constraint that no molecules overlapped. Simulations were then performed for 10^9 MC steps at each temperature. After these calculations, we observed that at experimentally relevant temperatures, the molecules typically aggregated into a single cluster. As an example of our MC results, Figure 6.5 shows snapshots of from simulations with 15 molecules of neutral or zwitterionic glycine on 20×20 hexagonal lattices at 300 K. In both cases, all of the molecules in the simulated system are aggregated into a single cluster. It is important to note that we have only considered systems in which all molecules are zwitterions or all molecules are neutral; we have not attempted to simulate mixtures of these two species. The orientations of the molecules within these clusters do not show high levels of long-range order, so our results are consistent with the experimental observation that ordered adlayers are not seen on this surface.

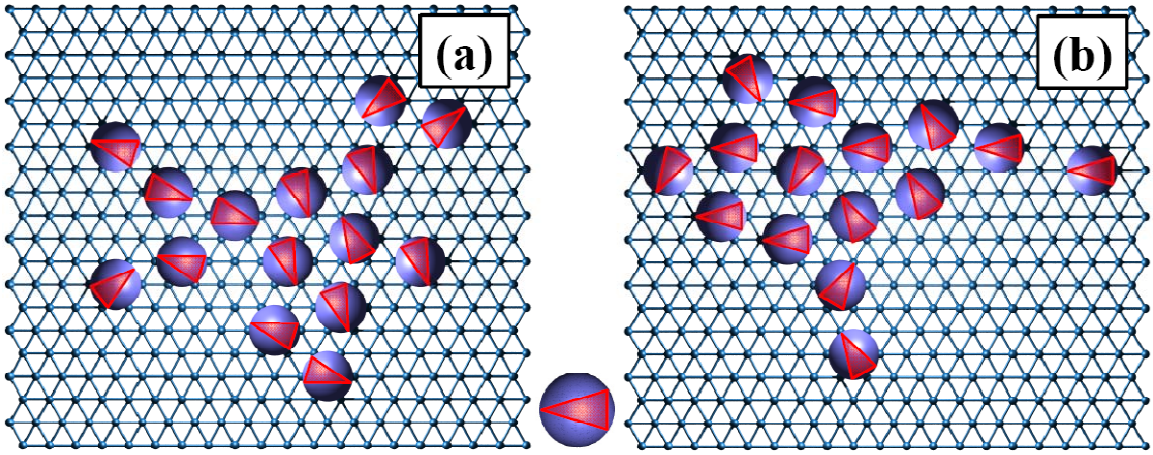

Figure 6.5: Snapshots of aggregations of 15 (a) neutral and (b) zwitterionic glycine molecules on a 20×20 hexagonal lattices at 300 K. The hexagons for modeling each species are shown as spheres for illustrative purposes. The orientation of each molecule is marked as a triangle inside the sphere, with the thin end of the triangle denoting H_2N (H_3N) in the neutral (zwitterionic) molecules.

Figure 6.6 shows our results at 300 K as a function of the number of molecules in our 20×20 simulation volume. For both species, the magnitude of the net interaction energy per molecule increases as the number of available molecules increases. We are particularly interested in the overall energy difference between the adlayers of neutral and zwitterionic molecules. To this end, we define

$$\Delta E_{total} = \Delta E_{single}(DFT) - \frac{1}{n}\Delta E_{inter}(MC)\Big|_n \tag{6.10}$$

where n is the number of molecules in the system, $\Delta E_{single}(DFT)$, is the energy difference between the two adsorbed species as isolated molecules on the surface, and $\Delta E_{inter}(MC)\Big|_n$ is the difference in the averaged total interaction energy observed in our MC simulation. If $\Delta E_{total} = 0$, the two species on the surface would have equal stability once molecule-molecule interactions were taken into account. When small numbers of molecules are present in the system, $\Delta E_{total} > 0$, reflecting the outcome from our earlier calculations that individual neutral adsorbates are energetically favored relative to zwitterionic adsorbates. Once the number of interacting molecules becomes sufficiently large, however, the sign of ΔE_{total} changes sign and the zwitterionic molecules are energetically favored. In the MC simulations shown in Fig. 6.6, this situation occurs once more than 12 molecules are available to interact with one another.

We recognize that our MC model invokes a number of approximations that may introduce some potential inaccuracies. The potential energy we used for attractive interaction associated with H-bonds was assumed to be constant for all bonds within a relatively broad range of distances. This interaction energy would, of course, vary as a function of the distance between the molecules and the molecules' local geometry. Our MC simulation also assumes that the discretized molecular orientations determined from DFT calculations with one and/or two molecules are sufficient to describe the position of

molecules in aggregates of all sizes. As noted above, our model does not consider aggregates that are made up of mixtures of neutral and zwitterionic molecules. Despite these approximations, our results are still meaningful to qualitatively understand the importance of aggregation in stabilizing zwitterions of glycine on Pt(111), as they show both that aggregation is favored under experimentally relevant conditions and that aggregation leads to significant stabilization of zwitterions relative to well separated molecules. In our MC simulations, all the molecules present on the surface aggregated into a single cluster. On a real surface, of course, aggregates of a variety of sizes would be expected, with the distribution and size of these aggregates being influenced by the surface coverage and kinetics of surface diffusion.

The analysis above has only considered the situation where all adsorbed molecules exist in a single layer on the surface. The growth of a second layer of adsorbed amino acids before completion of the first monolayer has been inferred from a number of experiments on several metals[33-34, 45-46]. The formation of H-bonds between first and second layer molecules must play a critical role in this process. The fact that amino acids are found in their zwitterionic form in their molecular crystals[81-82], supports the idea that growth of additional layers on a metal surface will generally favor zwitterionic molecules. Our MC model, however, demonstrates that it is not necessary to invoke the presence of a partial second layer in order to account for the experimental observation of zwitterions on Pt(111).

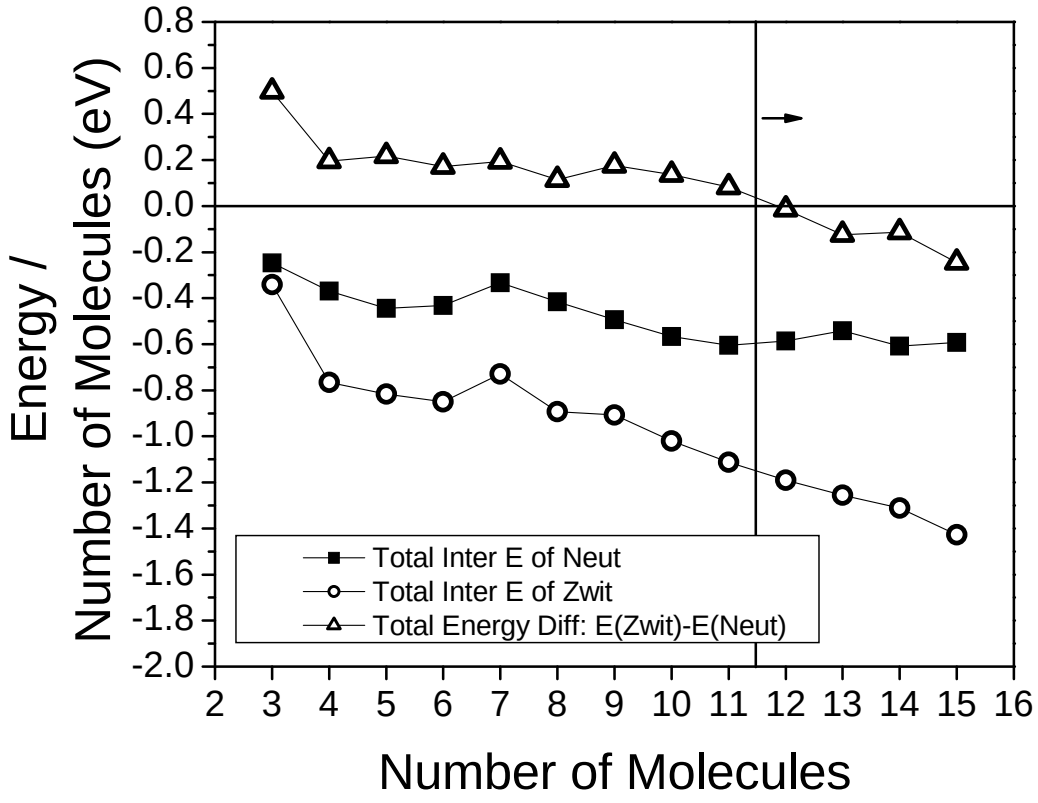

Figure 6.6: Total interaction energy of each species from MC calculations and total energy difference between the two species on the surface calculated by Eq. (6.12) as a function of the number of molecules. Each graph is normalized as the number of molecules. From 12 molecules' aggregates, the zwitterionic aggregations are more preferred to the neutral ones.

6.3.4. Hypothesis regarding structure sensitivity

Understanding the transition states to elementary reaction steps on surfaces is important to predict the kinetics of catalytic reactions and other surface chemical processes. The nature of transition states is commonly classified as either reactant-like, if they occur early in a reaction coordinate, or product-like, if they occur late in the reaction coordinate. Indentifying this lateness of transition states to some types of reaction can be a useful starting point for thinking about their properties and the influence of surfaces on their properties. Gellman has suggested the proposition that surface reactions with

product-like (reactant-like) transition states are relatively sensitive (insensitive) to the nature of the catalyst surface[83-85]. Our results from Sec. 6.3.1 allow us to test this proposition. In order to quantify the lateness of transition states, Manz and Sholl recently proposed a dimensionless reaction coordinate, W, for elementary reactions that has a value of 0 for the reactant state, has a monotonically increasing value along the minimum energy pathway, and a value of 1 for the product state[86]. Using this dimensionless reaction coordinate W, we can classify transition states as early when $W_{TS} < 0.5$, late when $W_{TS} > 0.5$, and equidistant between reactants and products when $W_{TS} = 0.5$. To examine this issue for dehydrogenation of zwitterionic glycine, we used the results from Sec. 6.3.1 and we additionally calculated the kinetic barrier of the dehydrogenation reaction of zwitterionic glycine on Pt(111) in a same way as described for the other surfaces in Sec. 6.3.1 (see Fig. 6.A.3 in Appendix 6.A). Table 6.3 shows the W values we obtained for the dehydrogenation reaction on Cu(110), Cu(100), Pd(111), and Pt(111).

	Cu(110)	**Cu(100)**	**Pd(111)**	**Pt(111)**
W_{TS}	0.22	0.62	0.66	0.62
Transition state	early	late	late	late

Table 6.3: Classification of the lateness of transition states of dehydrogenation reactions on 4 surfaces using the dimensionless reaction coordinate W values.

As mentioned in Sec. 6.3.1, the reaction on Cu(110) has two transition states. The W value is only applicable to elementary reactions, so we considered only the reaction that includes the first transition state and has its product at the image number 5 in Fig. 6.1 to obtain W. This is reasonable because the first reaction on Cu(110) (a state at image number 1 to 5 in Fig. 6.1) is related to the dehydrogenated process but the second reaction (a state at image number 5 to 8 in Fig. 6.1) is simply a diffusion process of the dissociated H atom to find the most stable site on the surface. Except on Cu(110), the

dehydrogenation reactions are classified as being late, implying that the reverse reactions must be characterized as being early.

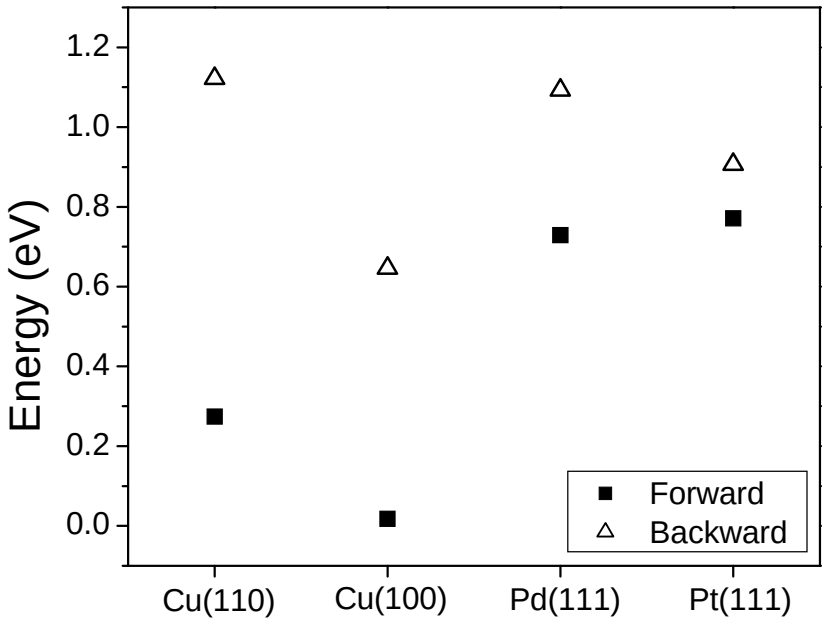

Figure 6.7: Activation energy barriers computed using DFT for forward (filled squares) and backward (open triangles) reaction of dehydrogenation of glycine on four surfaces without zero-point energy corrections, with energies in eV.

Figure 6.7 shows the activation energies without zero-point energy corrections for each forward and reverse reaction we considered. The activation energies for the forward reactions are also listed in Table 6.A.1-4 of the Appendix 6.A. Those for the reverse reactions are calculated to be 1.12, 0.65, 1.09 and 0.91 eV on Cu(110), Cu(100), Pd(111), and Pt(111), respectively. Because only the reaction on Cu(110) has reactant-like (early) transition states, we do not consider the activation energy on this surface to test the proposition stated above. The barriers for the forward reactions vary by 0.75 eV among the three surfaces, while the variation in the reverse reaction barriers is 0.45 eV. These observations are consistent with the hypothesis stated above in that the rates associated

with product-like (late) transition states are correlated with stronger variation between different surfaces than those having reactant-like (early) transition states.

6.4. Conclusion

In this Chapter, we have tested three hypotheses to examine the origin of inconsistency between the experimental and the theoretical reports with regard to the observed species of glycine on Cu(110), Cu(100), Pd(111), and Pt(111). It has been experimentally known that glycine is adsorbed on the Cu(110) and Cu(100) surfaces in its dehydrogenated form at room temperature, whereas it is adsorbed on Pd(111) and Pt(111) in its zwitterionic form. The previous DFT calculations, however, predicted that the dehydrogenated species on Cu(110), Cu(100), and Pd(111) is energetically stable.

Using DFT calculations, we reported that the activation barriers of the reaction on Cu(110) and Cu(100) are quite low, which is in consistent with the absence of zwitterions in experiment with the surfaces. Our calculations showed that although Pd(111) has a higher kinetic barrier than Cu surfaces, it is not large enough to explain the experimentally observed stability of zwitterions at moderate temperature. We then used the equilibrium thermodynamics to investigate if the excess hydrogen on the surface like Pd(111) facilitates the reaction of Eq. (6.1) into the reverse direction so that more zwitterionic forms can be observed. Our results for the fractional concentration of dehydrogenated glycine with excess hydrogen at several temperatures, however, demonstrated that redundant hydrogen would not contribute much to the increase of zwitterionic glycine during the reaction. Lastly, we performed MC simulations to show that above 12 molecules' aggregates of zwitterionic species on Pt(111) would be thermodynamically more stable than the corresponding neutral species. Our results show that the kinetic barrier for dehydrogenation reaction and the formation of glycine aggregates on metal surfaces would play an important role to explain the disagreement between the experimental and the theoretical observations.

Besides the topics described above, we used our results to test the proposition proposed by Gellman. Using the dimensionless reaction coordinate developed recently, we determined the lateness of transition states of the dehydrogenated reactions on the different surfaces. By comparing the lateness of transition states and the variation in the activation barriers of the reactions on different surfaces, we confirmed the proposition that surface reactions with product-like (reactant-like) transition states are relatively sensitive (insensitive) to the nature of the catalyst surface.

Our results for chemical speciation of adsorbed glycine on metal surfaces would provide useful insights for understanding the adsorption of more complicated amino acids that basically include the characteristics of glycine on metal surfaces.

References

(1) Barlow, S. M.; Kitching, K. J.; Haq, S.; Richardson, N. V., *Surf. Sci.* **1998**, 401, 322.
(2) Chen, Q.; Frankel, D. J.; Richardson, N. V., *Surf. Sci.* **2002**, 497, 37.
(3) Kang, J. H.; Toomes, R. L.; Polcik, M.; Kittel, M.; Hoeft, J. T.; V. Efstathiou; Woodruff, D. P.; Bradshaw, A. M., *J. Chem. Phys.* **2003**, 118, 6059.
(4) Zhao, X.; Wang, H.; Zhao, R. G.; Yang, W. S., *Mater. Sci. and Eng. C* **2001**, 16, 41-50.
(5) Humblot, V.; Methivier, C.; Raval, R.; Pradier, C. M., *Surf. Sci.* **2007**, 601, 4189-4194.
(6) Tielens, F.; Humblot, V.; Pradier, C. M., *Surf. Sci.* **2008**, 602, 1032-1039.
(7) Zhao, X.; Gai, Z.; Zhao, R. G.; Yang, W. S.; Sakurai, T., *Surf. Sci.* **1999**, 424, L347-L351.
(8) Zhao, X. Y., *J. Am. Chem. Soc.* **2000**, 122, 12584-12585.
(9) Zhao, X. Y.; Yan, H.; Tu, X. W.; Zhao, R. G.; Yang, W. S., *Langmuir* **2003**, 19, 5542-5545.
(10) Efstathiou, V.; Woodruff, D. P., *Surf. Sci.* **2003**, 531, 304-318.
(11) Toomes, R. L.; Kang, J. H.; Woodruff, D. P.; Polcik, M.; Kittel, M.; Hoeft, J. T., *Surf. Sci.* **2003**, 522, L9-L14.
(12) Dodero, G.; De Michieli, L.; Cavalleri, O.; Rolandi, R.; Oliveri, L.; Dacca, A.; Parodi, R., *Colloids Surf., A* **2000**, 175, 121-128.
(13) Egawa, C.; Iwai, H.; Kabutoya, M.; Oki, S., *Surf. Sci.* **2003**, 532, 233-236.
(14) Jones, T. E.; Baddeley, C. J.; Gerbi, A.; Savio, L.; Rocca, M.; Vattuone, L., *Langmuir* **2005**, 21, 9468-9475.
(15) Chen, Q.; Lee, C. W.; Frankel, D. J.; Richardson, N. V., *PhysChemComm* **1999**, 2, 41 - 44.
(16) Chen, Q.; Frankel, D. J.; Richardson, N. V., *Langmuir* **2001**, 17, 8276-8280.
(17) Barlow, S. M.; Louafi, S.; Le Roux, D.; Williams, J.; Muryn, C.; Haq, S.; Raval, R., *Langmuir* **2004**, 20, 7171-7176.
(18) Booth, N. A.; D.P.Woodruff; Schaff, O.; Giessel, T.; Lindsay, R.; Baumgartel, P.; Bradshaw, A. M., *Surf. Sci.* **1998**, 397, 258.
(19) Zhao, X. Y.; Zhao, R. G.; Yang, W. S., *Surf. Sci.* **1999**, 442, L995-L1000.
(20) Zhao, X. Y.; Zhao, R. G.; Yang, W. S., *Langmuir* **2002**, 18, 433-438.
(21) Marti, E. M.; Barlow, S. M.; Haq, S.; Raval, R., *Surf. Sci.* **2002**, 501, 191-202.
(22) Raval, R., *Cattech* **2001**, 5, 12-28.
(23) Raval, R., *Curr. Opin. Solid St. M.* **2003**, 7, 67-74.
(24) Stacchiola, D.; Burkholder, L.; Zheng, T.; Weinert, M.; Tysoe, W. T., *J. Phys. Chem. B* **2005**, 109, 851-856.
(25) Mulligan, A.; Lane, I.; Rousseau, G. B. D.; Hecht, L.; Johnston, S. M.; Lennon, D.; Kadodwala, M., *Chem. Commun.* **2004**, 2492-2493.
(26) Zhao, X.; Yan, H.; Zhao, R. G.; Yang, W. S., *Langmuir* **2002**, 18, 3910-3915.
(27) Rankin, R. B.; Sholl, D. S., *J. Chem. Phys.* **2006**, 124, 074703.
(28) Rankin, R. B.; Sholl, D. S., *Langmuir* **2006**, 22, 8096-8103.
(29) Barlow, S. M.; Raval, R., *Surf. Sci. Rep.* **2003**, 50, 201-341.
(30) Lambert, J. F., *Orig. Life Evol. Biosph.* **2008**, 38, 211-242.

(31) Hasselstrom, J.; Karis, O.; Weinelt, M.; Wassdahl, N.; Nilsson, A.; Nyberg, M.; Pettersson, L. G. M.; Samant, M. G.; Stohr, J., *Surf. Sci.* **1998**, 407, 221.
(32) Nyberg, M.; Hasselstrom, J.; Karis, O.; Wassdahl, N.; Weinelt, M.; Nilsson, A.; Pettersson, L. G. M., *J. Chem. Phys.* **2000**, 112, 5420-5427.
(33) Gao, F.; Li, Z. J.; Wang, Y. L.; Burkholder, L.; Tysoe, W. T., *J. Phys. Chem. C* **2007**, 111, 9981-9991.
(34) Löfgren, P.; Krozer, A.; Lausmaa, J.; Kasemo, B., *Surf. Sci.* **1997**, 370, 277-292.
(35) Stewart, S.; Fredericks, P. M., *Spectrochim. Acta, Part A* **1999**, 55, 1641-1660.
(36) Atanasoska, L. L.; Buchholz, J. C.; Somorjai, G. A., *Surf. Sci.* **1978**, 72, 189-207.
(37) Ihs, A.; Liedberg, B.; Uvdal, K.; Tornkvist, C.; Bodo, P.; Lundstrom, I., *J. Colloid Interface Sci.* **1990**, 140, 192-206.
(38) Rankin, R. B.; Sholl, D. S., *J. Phys. Chem. B* **2005**, 109, 16764-16773.
(39) Ernst, K. H.; Christmann, K., *Surf. Sci.* **1989**, 224, 277-310.
(40) Lange, W.; Jirikowsky, M.; Benninghoven, A., *Surf. Sci.* **1984**, 136, 419-436.
(41) Liedberg, B.; Lundstrom, I.; Wu, C. R.; Salaneck, W. R., *J. Colloid Interface Sci.* **1985**, 108, 123-132.
(42) Holtkamp, D.; Jirikowsky, M.; Kempken, M.; Benninghoven, A., *J. Vac. Sci. Technol., A* **1985**, 3, 1394-1397.
(43) Tzvetkov, G.; Ramsey, M. G.; Netzer, F. P., *Surf. Sci.* **2003**, 526, 383-393.
(44) Zhao, X. Y.; Rodriguez, J., *Surf. Sci.* **2006**, 600, 2113-2121.
(45) Gao, F.; Li, Z. J.; Wang, Y. L.; Burkholder, L.; Tysoe, W. T., *Surf. Sci.* **2007**, 601, 3276-3288.
(46) Gao, F.; Wang, Y. L.; Burkholder, L.; Tysoe, W. T., *Surf. Sci.* **2007**, 601, 3579-3588.
(47) Barlow, S. M.; Raval, R., *Curr. Opin. Colloid Interface Sci.* **2008**, 13, 65-73.
(48) James, J. N.; Sholl, D. S., *J. Mol. Cat. A: Chem.* **2008**, 281, 44-48.
(49) Conrad, H.; Ertl, G.; Latta, E. E., *Surf. Sci.* **1974**, 41, 435-446.
(50) Pallassana, V.; Neurock, M.; Hansen, L. B.; Hammer, B.; Norskov, J. K., *Phys. Rev. B* **1999**, 60, 6146-6154.
(51) Paul, J. F.; Sautet, P., *Phys. Rev. B* **1996**, 53, 8015.
(52) Nobuhara, K.; Nakanishi, H.; Kasai, H.; Okiji, A., *J. Appl. Phys.* **2000**, 88, 6897-6901.
(53) Felter, T. E.; Foiles, S. M.; Daw, M. S.; Stulen, R. H., *Surf. Sci.* **1986**, 171, L379-L386.
(54) Kresse, G.; Furthmuller, J., *Phys. Rev. B* **1996**, 54, 11169-11186.
(55) Kresse, G.; Hafner, J., *Phys. Rev. B* **1993**, 47, 558-561.
(56) Kresse, G.; Hafner, J., *J. Phys.: Condens. Matter* **1994**, 6, 8245-8257.
(57) Perdew, J. P.; Chevary, J. A.; Vosko, S. H.; Jackson, K. A.; Pederson, M. R.; Singh, D. J.; Fiolhais, C., *Phys. Rev. B* **1992**, 46, 6671-6687.
(58) Monkhorst, H. J.; Pack, J. D., *Phys. Rev. B* **1976**, 13, 5188-5192.
(59) Bengtsson, L., *Phys. Rev. B* **1999**, 59, 12301.
(60) Neugebauer, J.; Scheffler, M., *Phys. Rev. B* **1992**, 46, 16067.
(61) Rankin, R. B.; Sholl, D. S., *Surf. Sci.* **2004**, 548, 301-308.
(62) Rankin, R. B.; Sholl, D. S., *Surf. Sci.* **2005**, 574, L1-L8.
(63) Nyberg, M.; Odelius, M.; Nilsson, A.; Pettersson, L. G. M., *J. Chem. Phys.* **2003**, 119, 12577-12585.

(64) Henkelman, G.; Jónsson, H., *J. Chem. Phys.* **2000**, 113, 9978-9985.
(65) Henkelman, G.; Uberuaga, B. P.; Jónsson, H., *J. Chem. Phys.* **2000**, 113, 9901-9904.
(66) Greeley, J.; Mavrikakis, M., *Surf. Sci.* **2003**, 540, 215-229.
(67) Jiang, D. E.; Carter, E. A., *Surf. Sci.* **2003**, 547, 85-98.
(68) Kamakoti, P.; Sholl, D. S., *J. Membr. Sci.* **2003**, 225, 145-154.
(69) Løvvik, O. M.; Olsen, R. A., *Phys. Rev. B* **1998**, 58, 10890.
(70) Greeley, J.; Mavrikakis, M., *J. Phys. Chem. B* **2005**, 109, 3460-3471.
(71) Badescu, S. C.; Salo, P.; Ala-Nissila, T.; Ying, S. C.; Jacobi, K.; Wang, Y.; Bedurftig, K.; Ertl, G., *Phys. Rev. Lett.* **2002**, 88, 136101.
(72) Fermann, J. T.; Auerbach, S., *J. Chem. Phys.* **2000**, 112, 6787-6794.
(73) Li, X.; Gellman, A. J.; Sholl, D. S., *J. Chem. Phys.* **2007**, 127, 144710.
(74) Nyberg, M.; Hasselstrom, J.; Karis, O.; N.Wassdahl; M.Weinelt; Nilsson, A.; Pettersson, L. G. M., *J. Chem. Phys.* **2000**, 112, 5420.
(75) Alapati, S. V.; Johnson, J. K.; Sholl, D. S., *Phys. Rev. B* **2007**, 76, 104108-8.
(76) Sholl, D. S.; Steckel, J. A., *Density functional theory : a practical introduction*. John Wiley & Sons, Inc.: Hoboken, NJ, 2008.
(77) Alapati, S. V.; Johnson, J. K.; Sholl, D. S., *Phys. Chem. Chem. Phys.* **2007**, 9, 1438-1452.
(78) McQuarrie, D. A.; Simon, J. D., *Molecular Thermodynamics*. University Science Books: Sausalito, CA, 1999.
(79) McQuarrie, D. A., *Statistical Mechanics*. University Science Books: Sausalito, CA, 2000.
(80) Allen, M. P.; Tildesley, D. J., *Computer Simulation of Liquids*. Clarendon Press: Oxford, 1987.
(81) Jonsson, P. G.; Kvick, A., *Acta Cryst. B* **1972**, B 28, 1827-&.
(82) Drebushchak, T. N.; Boldyreva, E. V.; Shutova, E. S., *Acta Cryst. E* **2002**, 58, O634-O636.
(83) Gellman, A. J., *Acc. Chem. Res.* **1999**, 33, 19-26.
(84) Gellman, A. J., *Curr. Opin. Solid State Mater. Sci.* **2001**, 5, 85-90.
(85) Gellman, A. J., *J. Phys. Chem. B* **2002**, 106, 10509-10517.
(86) Manz, T. A.; Sholl, D. S., *J. Comp. Chem.* **2009**, in press.

Appendix 6.A: The optimized geometries of neutral glycine and structural and energetic information during the dehydrogenation reaction on Cu(110), Cu(100), Pd(111), and Pt(111)

The figures below are the optimized geometries of glycine molecules adsorbed on the surfaces described in this Chapter.

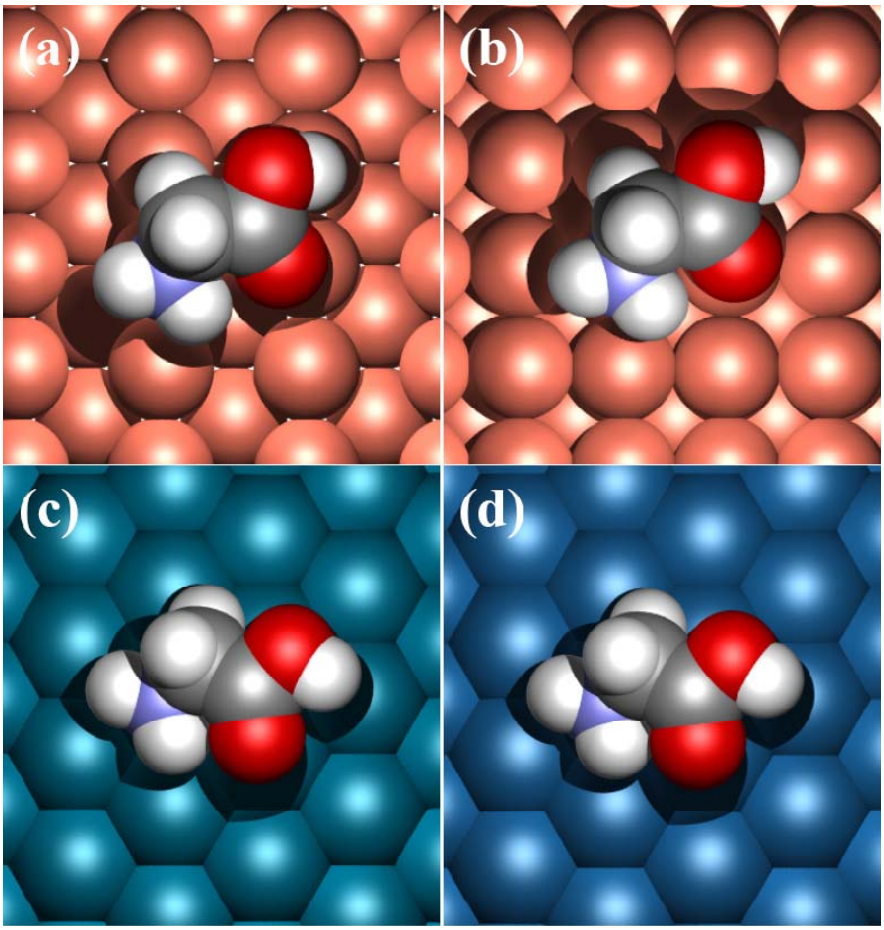

Figure 6.A.1: The optimized geometries of neutral glycine on (a) Cu(110), (b) Cu(100), (c) Pd(111), and (d) Pt(111).

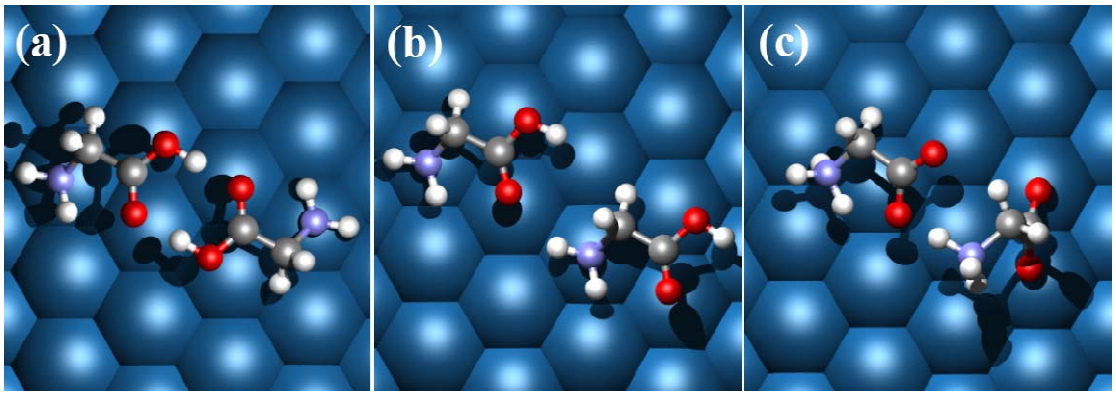

Figure 6.A.2: The optimized geometries of (a) two neutral glycine molecules with two H-bonds of O-H…O, (b) two neutral glycine molecules with a H-bond of N-H…O, and (c) two zwitterionic glycine molecules with a H-bond of N-H…O on Pt(111).

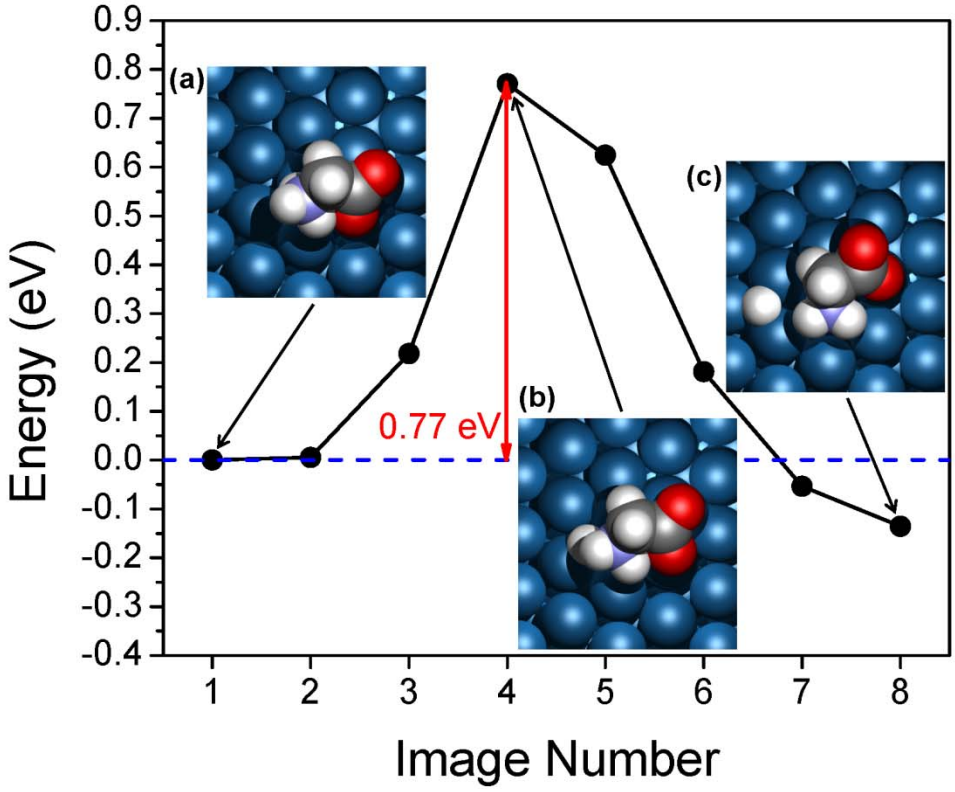

Figure 6.A.3: H dissociation pathway from zwitterionic to dehydrogenated glycine on Pt(111) without ZPE corrections. Top views of the (a) initial state, (b) transition state, and (c) final state are shown in the insets.

The calculated energy difference between the coadsorbed state and the zwitterionic state for the most stable states on Pt(111) is ΔE = -0.28 eV (-0.14 eV) with (without) ZPE

corrections. This energy difference is the smallest among the surfaces we have examined, but like the other three surfaces we have studied, the coadsorbed state on this surface is more stable than the zwitterionic state. The pathway from zwitterionic glycine to the dehydrogenated form on Pt(111) without ZPE corrections is shown in Fig. 6.A.3. The insets of Fig. 6.A.3 denoted as (a), (b), and (c) also show the geometries for the initial, transition, and final state, respectively. The activation energy barrier is 0.59 eV (0.77 eV) with (without) ZPE corrections, which is the highest among the surfaces we have considered. As with Cu(100) and Pd(111), the ZPE for the transition state is ~0.2 eV smaller than for the zwitterionic adsorbate. Glycine changes its position considerably during the dehydrogenation reaction; it rotates roughly by 60°.

Structural and energetic information for the initial, transition, and final state on Cu(110), Cu(100), Pd(111), and Pt(111) during the dehydrogenation reaction is listed in Table 6.A.1-6.A.4.

	Zwitterionic glycine (initial)	Transition state	Glycinate+H (final)
$\Delta E = E_{state} - E_{initial}$	0.00	0.27	-0.96
d(C-N)	1.50	1.52	1.49
d(C-O)	1.26, 1.28	1.26, 1.28	1.27, 1.28
d(C-C)	1.54	1.54	1.52
d(C-H)	1.09, 1.10	1.09, 1.09	1.09, 1.10
d(N-H)	1.03, 1.04, 1.08	1.03, 1.03, 1.07	1.02, 1.02
d(O-Cu)	2.10, 2.11	2.17, 2.04	2.03, 2.01
$d(H_{ads}-Cu)$	-	-	1.65, 1.66
$d(N-H_{ads})$	1.08	1.07	4.08
d(N-Cu)	3.08	2.90	2.12

Table 6.A.1: Structural and energetic properties of adsorbates in the N-H bond breaking process of zwitterionic glycine on Cu(110) including ZPE corrections, with energies in eV and distances in Å.

	Zwitterionic glycine (initial)	Transition state	Glycinate+H (final)
$\Delta E = E_{state} - E_{initial}$	0.00	-0.17	-0.83
d(C-N)	1.50	1.45	1.49
d(C-O)	1.26, 1.28	1.28, 1.27	1.27, 1.28
d(C-C)	1.54	1.53	1.52
d(C-H)	1.09, 1.10	1.10, 1.10	1.09, 1.10
d(N-H)	1.03, 1.04, 1.07	1.02, 1.01	1.02, 1.03
d(O-Cu)	2.12, 2.12	2.00, 2.00	2.04, 2.04
$d(H_{ads}-Cu)$	-	1.67, 1.60	1.85, 1.88, 1.88, 1.98
$d(N-H_{ads})$	1.07	2.56	4.29
d(N-Cu)	3.19	3.12	2.15

Table 6.A.2: Structural and energetic properties of adsorbates in the N-H bond breaking process of zwitterionic glycine on Cu(100) including ZPE corrections, with energies in eV and distances in Å.

	Zwitterionic glycine (initial)	Transition state	Glycinate+H (final)
$\Delta E = E_{state} - E_{initial}$	0.00	0.52	-0.49
d(C-N)	1.50	1.45	1.48
d(C-O)	1.26, 1.28	1.28, 1.27	1.28, 1.27
d(C-C)	1.55	1.54	1.53
d(C-H)	1.09, 1.10	1.10, 1.09	1.10, 1.09
d(N-H)	1.03, 1.04, 1.07	1.02, 1.02	1.02, 1.02
d(O-Pd)	2.30, 2.28	2.13, 2.16	2.18, 2.26
$d(H_{ads}-Pd)$	-	1.54	1.81, 1.82, 1.82
$d(N-H_{ads})$	1.07	2.65	4.73
d(N-Pd)	3.35	3.11	2.20

Table 6.A.3: Structural and energetic properties of adsorbates in the N-H bond breaking process of zwitterionic glycine on Pd(111) including ZPE corrections, with energies in eV and distances in Å.

	Zwitterionic glycine (initial)	Transition state	Glycinate+H (final)
$\Delta E = E_{state} - E_{initial}$	0.00	0.59	-0.28
d(C-N)	1.50	1.46	1.48
d(C-O)	1.31, 1.23	1.32, 1.23	1.32, 1.23
d(C-C)	1.55	1.54	1.53
d(C-H)	1.09, 1.09	1.10, 1.10	1.10, 1.10
d(N-H)	1.03, 1.05, 1.06	1.03, 1.03	1.02, 1.03
d(O-Pt)	2.21, 3.41	2.22, 3.28	2.11, 4.12
$d(H_{ads}-Pt)$	-	1.70, 1.78	1.86, 1.87, 1.88
$d(N-H_{ads})$	1.06	2.17	3.63
d(N-Pt)	3.74	3.49	2.14

Table 6.A.4: Structural and energetic properties of adsorbates in the N-H bond breaking process of zwitterionic glycine on Pt(111) including ZPE corrections, with energies in eV and distances in Å.

Appendix 6.B: Structural information for zwitterionic, dehydrogenated, and neutral glycine adsorption in the most stable states on Cu(110)

This appendix lists the coordinates for the most stable structures of zwitterionic, dehydrogenated, and neutral glycine adsorption on Cu(110) discussed in this Chapter. The coordinates for the adsorbate are defined for a single supercell of a (3×2) surface unit cell with all coordinates in Å. The shaded sections of the table give the coordinates of the adsorbate; all other coordinates define the portion of the surface atoms. A table defining unit cell vectors for supercell is also listed in Å.

Table 6.B.1: Unit cell vectors of supercell used for calculations on Cu(110) with a lattice constant of 3.64 Å. (in Å)

	x	y	z
a	2.000	0.000	0.000
b	0.000	2.121	0.000
c	0.000	0.000	5.965

Table 6.B.2: Coordinates for the most stable zwitterionic glycine adsorbed on Cu(110). This configuration is shown in Fig. 6.1(a).

Atom	x	y	z	Atom	x	y	z	Atom	x	y	z
C	1.470	1.406	11.011	Cu	1.831	1.276	6.472	Cu	0.000	0.000	2.573
C	2.726	1.328	10.123	Cu	1.807	3.837	6.478	Cu	0.000	2.574	2.573
H	0.950	2.356	10.860	Cu	1.809	6.421	6.458	Cu	0.000	5.148	2.573
H	1.720	1.271	12.068	Cu	5.422	1.274	6.464	Cu	3.640	0.000	2.573
H	0.148	0.512	9.613	Cu	5.462	3.846	6.451	Cu	3.640	2.574	2.573
H	1.222	7.203	10.363	Cu	5.445	6.418	6.445	Cu	3.640	5.148	2.573
H	7.118	0.028	11.224	Cu	-0.002	-0.006	5.095	Cu	1.820	1.287	1.286
N	0.586	0.281	10.570	Cu	-0.002	2.559	5.125	Cu	1.820	3.861	1.286
O	3.283	2.411	9.809	Cu	-0.002	5.138	5.126	Cu	1.820	6.435	1.286
O	3.017	0.143	9.743	Cu	3.630	-0.013	5.198	Cu	5.460	1.287	1.286
				Cu	3.631	2.569	5.207	Cu	5.460	3.861	1.286
				Cu	3.630	5.134	5.122	Cu	5.460	6.435	1.286
Cu	-0.040	-0.008	7.564	Cu	1.838	1.284	3.864	Cu	0.000	0.000	0.000
Cu	7.252	2.535	7.627	Cu	1.823	3.851	3.863	Cu	0.000	2.574	0.000
Cu	-0.014	5.135	7.624	Cu	1.827	6.431	3.858	Cu	0.000	5.148	0.000
Cu	3.656	7.668	7.744	Cu	5.440	1.284	3.865	Cu	3.640	0.000	0.000
Cu	3.682	2.600	7.757	Cu	5.452	3.852	3.858	Cu	3.640	2.574	0.000
Cu	3.638	5.131	7.586	Cu	5.449	6.430	3.856	Cu	3.640	5.148	0.000

Table 6.B.3: Coordinates for the most stable dehydrogenated glycine coadsorbed with H on Cu(110). This configuration is shown in Fig. 6.1(c).

Atom	x	y	z	Atom	x	y	z	Atom	x	y	z
C	1.020	1.046	10.580	Cu	1.786	1.296	6.435	Cu	0.000	0.000	2.573
C	2.363	1.164	9.870	Cu	1.832	3.870	6.414	Cu	0.000	2.574	2.573
H	0.485	1.997	10.502	Cu	1.780	6.446	6.446	Cu	0.000	5.148	2.573
H	1.184	0.814	11.645	Cu	5.457	1.294	6.478	Cu	3.640	0.000	2.573
H	6.572	7.637	10.330	Cu	5.409	3.859	6.427	Cu	3.640	2.574	2.573
H	0.695	6.802	10.055	Cu	5.481	6.448	6.456	Cu	3.640	5.148	2.573
N	0.223	7.701	9.912	Cu	-0.015	0.010	5.221	Cu	1.820	1.287	1.286
O	2.787	2.324	9.575	Cu	-0.014	2.574	5.136	Cu	1.820	3.861	1.286
O	2.921	0.056	9.565	Cu	-0.014	5.155	5.133	Cu	1.820	6.435	1.286
				Cu	3.635	0.003	5.194	Cu	5.460	1.287	1.286
H	7.264	3.889	8.754	Cu	3.633	2.560	5.194	Cu	5.460	3.861	1.286
				Cu	3.633	5.167	5.116	Cu	5.460	6.435	1.286
Cu	7.252	0.035	7.808	Cu	1.821	1.279	3.854	Cu	0.000	0.000	0.000
Cu	7.247	2.643	7.656	Cu	1.819	3.859	3.852	Cu	0.000	2.574	0.000
Cu	-0.020	5.119	7.656	Cu	1.811	6.451	3.854	Cu	0.000	5.148	0.000
Cu	3.672	7.680	7.707	Cu	5.454	1.280	3.857	Cu	3.640	0.000	0.000
Cu	3.630	2.599	7.749	Cu	5.454	3.861	3.853	Cu	3.640	2.574	0.000
Cu	3.629	5.156	7.571	Cu	5.461	6.451	3.851	Cu	3.640	5.148	0.000

Table 6.B.4: Coordinates for the most stable neutral glycine adsorbed on Cu(110). This configuration is shown in Fig. 6.A.1(a).

Atom	x	y	z	Atom	x	y	z	Atom	x	y	z
C	0.816	0.953	10.669	Cu	1.817	1.308	6.461	Cu	0.000	0.000	2.573
C	2.289	1.067	10.354	Cu	1.825	3.878	6.445	Cu	0.000	2.574	2.573
H	0.324	1.892	10.383	Cu	1.823	6.452	6.461	Cu	0.000	5.148	2.573
H	0.713	0.841	11.763	Cu	5.470	1.292	6.487	Cu	3.640	0.000	2.573
H	6.557	7.358	10.248	Cu	5.461	3.884	6.436	Cu	3.640	2.574	2.573
H	0.789	6.712	10.033	Cu	5.462	6.463	6.487	Cu	3.640	5.148	2.573
H	3.665	2.375	10.193	Cu	0.000	0.011	5.218	Cu	1.820	1.287	1.286
N	0.223	7.559	9.916	Cu	-0.001	2.581	5.120	Cu	1.820	3.861	1.286
O	2.761	2.302	10.591	Cu	0.000	5.170	5.117	Cu	1.820	6.435	1.286
O	2.973	0.143	9.914	Cu	3.642	0.013	5.177	Cu	5.460	1.287	1.286
				Cu	3.643	2.579	5.108	Cu	5.460	3.861	1.286
				Cu	3.642	5.166	5.122	Cu	5.460	6.435	1.286
Cu	0.018	0.020	7.787	Cu	1.817	1.285	3.861	Cu	0.000	0.000	0.000
Cu	-0.007	2.615	7.598	Cu	1.819	3.868	3.858	Cu	0.000	2.574	0.000
Cu	0.000	5.142	7.588	Cu	1.817	6.449	3.860	Cu	0.000	5.148	0.000
Cu	3.635	0.027	7.707	Cu	5.464	1.284	3.867	Cu	3.640	0.000	0.000
Cu	3.661	2.616	7.579	Cu	5.462	3.868	3.855	Cu	3.640	2.574	0.000
Cu	3.645	5.157	7.612	Cu	5.463	6.450	3.866	Cu	3.640	5.148	0.000

Appendix 6.C: Structural information for zwitterionic, dehydrogenated, and neutral glycine adsorption in the most stable states on Cu(100)

Similar to Appendix 6.B but for Cu(100). The coordinates for the adsorbate are defined for a single supercell of a (3×3) surface unit cell with all coordinates in Å.

Table 6.C.1: Unit cell vectors of supercell used for calculations on Cu(100) with a lattice constant of 3.64 Å. (in Å)

	x	y	z
a	2.121	0.000	0.000
b	0.000	2.121	0.000
c	0.000	0.000	5.346

Table 6.C.2: Coordinates for the most stable zwitterionic glycine adsorbed on Cu(110). This configuration is shown in Fig. 6.2(a).

Atom	x	y	z	Atom	x	y	z	Atom	x	y	z
C	0.574	6.325	8.929	Cu	2.614	0.043	5.578	Cu	5.134	2.567	1.820
C	1.799	6.396	7.998	Cu	5.144	2.573	5.443	Cu	0.000	5.148	1.820
H	0.874	6.268	9.981	Cu	5.187	-0.005	5.447	Cu	0.000	7.715	1.820
H	-0.082	7.185	8.768	Cu	-0.019	2.579	5.421	Cu	2.567	5.148	1.820
H	6.913	4.723	9.270	Cu	-0.028	-0.004	5.412	Cu	2.567	7.715	1.820
H	7.052	5.194	7.632	Cu	6.429	6.438	3.627	Cu	5.134	5.148	1.820
H	0.591	4.370	8.334	Cu	3.844	6.428	3.710	Cu	5.134	7.715	1.820
N	-0.154	5.068	8.558	Cu	3.857	3.875	3.672	Cu	6.409	6.409	0.000
O	2.226	5.254	7.620	Cu	1.327	6.434	3.695	Cu	3.861	6.409	0.000
O	2.194	7.537	7.647	Cu	3.851	1.262	3.678	Cu	3.861	3.861	0.000
				Cu	1.299	3.870	3.656	Cu	1.313	6.409	0.000
				Cu	1.291	1.265	3.670	Cu	3.861	1.313	0.000
Cu	5.210	5.143	5.459	Cu	6.422	3.845	3.623	Cu	1.313	3.861	0.000
Cu	-0.033	5.142	5.373	Cu	6.425	1.291	3.641	Cu	1.313	1.313	0.000
Cu	2.625	5.091	5.547	Cu	0.000	2.567	1.820	Cu	6.409	3.861	0.000
Cu	2.563	2.567	5.405	Cu	2.567	2.567	1.820	Cu	6.409	1.313	0.000

Table 6.C.3: Coordinates for the most stable dehydrogenated glycine coadsorbed with H on Cu(110). This configuration is shown in Fig. 6.2(c).

Atom	x	y	z	Atom	x	y	z	Atom	x	y	z
C	0.577	6.145	8.514	Cu	2.656	0.086	5.547	Cu	5.134	2.567	1.820
C	1.919	6.406	7.843	Cu	5.152	2.565	5.430	Cu	0.000	5.148	1.820
H	0.716	5.931	9.584	Cu	5.217	0.018	5.436	Cu	0.000	7.715	1.820
H	7.660	7.027	8.405	Cu	7.691	2.527	5.416	Cu	2.567	5.148	1.820
H	6.741	4.814	8.137	Cu	7.704	0.032	5.430	Cu	2.567	7.715	1.820
H	0.536	4.169	7.949	Cu	6.473	6.409	3.658	Cu	5.134	5.148	1.820
N	7.684	5.003	7.789	Cu	3.849	6.457	3.692	Cu	5.134	7.715	1.820
O	2.599	5.365	7.548	Cu	3.855	3.862	3.651	Cu	6.409	6.409	0.000
O	2.207	7.604	7.532	Cu	1.300	6.418	3.756	Cu	3.861	6.409	0.000
				Cu	3.854	1.272	3.649	Cu	3.861	3.861	0.000
H	6.479	1.251	6.084	Cu	1.260	3.891	3.710	Cu	1.313	6.409	0.000
				Cu	1.307	1.262	3.646	Cu	3.861	1.313	0.000
Cu	5.164	5.145	5.380	Cu	6.450	3.870	3.647	Cu	1.313	3.861	0.000
Cu	7.658	5.121	5.645	Cu	6.432	1.284	3.564	Cu	1.313	1.313	0.000
Cu	2.658	5.085	5.532	Cu	0.000	2.567	1.820	Cu	6.409	3.861	0.000
Cu	2.566	2.577	5.386	Cu	2.567	2.567	1.820	Cu	6.409	1.313	0.000

Table 6.C.4: Coordinates for the most stable neutral glycine adsorbed on Cu(110). This configuration is shown in Fig. 6.A.1(b).

Atom	x	y	z	Atom	x	y	z	Atom	x	y	z
C	0.567	6.176	8.528	Cu	2.567	0.027	5.382	Cu	5.134	2.567	1.820
C	2.045	6.320	8.272	Cu	5.144	2.565	5.441	Cu	0.000	5.148	1.820
H	0.429	6.079	9.620	Cu	5.139	0.000	5.442	Cu	0.000	7.715	1.820
H	0.051	7.090	8.204	Cu	7.711	2.540	5.416	Cu	2.567	5.148	1.820
H	6.810	4.809	8.056	Cu	7.704	0.024	5.411	Cu	2.567	7.715	1.820
H	0.629	4.195	7.962	Cu	6.449	6.416	3.671	Cu	5.134	5.148	1.820
H	3.425	-0.099	8.166	Cu	3.855	6.429	3.653	Cu	5.134	7.715	1.820
N	0.049	5.021	7.779	Cu	3.854	3.856	3.657	Cu	6.409	6.409	0.000
O	2.756	5.394	7.884	Cu	1.271	6.406	3.693	Cu	3.861	6.409	0.000
O	2.498	-0.158	8.503	Cu	3.863	1.289	3.640	Cu	3.861	3.861	0.000
				Cu	1.274	3.881	3.692	Cu	1.313	6.409	0.000
				Cu	1.276	1.289	3.630	Cu	3.861	1.313	0.000
Cu	5.150	5.147	5.413	Cu	6.448	3.869	3.673	Cu	1.313	3.861	0.000
Cu	7.713	5.150	5.623	Cu	6.416	1.284	3.636	Cu	1.313	1.313	0.000
Cu	2.616	5.140	5.475	Cu	0.000	2.567	1.820	Cu	6.409	3.861	0.000
Cu	2.567	2.559	5.424	Cu	2.567	2.567	1.820	Cu	6.409	1.313	0.000

Appendix 6.D: Structural information for zwitterionic, dehydrogenated, and neutral glycine adsorption in the most stable states on Pd(111)

Similar to Appendix 6.C but for Pd(111).

Table 6.D.1: Unit cell vectors of supercell used for calculations on Pd(111) with a lattice constant of 3.96 Å. (in Å)

	x	y	z
a	1.837	1.061	0.000
b	0.000	2.121	0.000
c	0.000	0.000	5.272

Table 6.D.2: Coordinates for the most stable zwitterionic glycine adsorbed on Pd(111). This configuration is shown in Fig. 6.3(a).

Atom	x	y	z	Atom	x	y	z	Atom	x	y	z
C	0.166	2.587	10.234	Pd	2.463	4.187	6.810	Pd	6.467	5.600	2.286
C	0.825	1.437	9.439	Pd	4.873	5.577	6.834	Pd	1.617	5.600	2.286
H	0.797	4.618	10.504	Pd	0.031	5.557	6.871	Pd	4.042	7.000	2.286
H	0.530	4.181	8.877	Pd	2.463	6.957	6.846	Pd	6.467	8.400	2.286
H	0.292	2.438	11.312	Pd	4.891	8.367	6.855	Pd	1.617	8.400	2.286
H	6.380	6.867	9.983	Pd	0.827	1.377	4.561	Pd	4.042	9.800	2.286
H	1.862	3.564	9.664	Pd	3.247	2.782	4.557	Pd	6.467	11.201	2.286
N	0.871	3.846	9.833	Pd	5.683	4.190	4.569	Pd	0.000	0.000	0.000
O	0.109	0.432	9.186	Pd	0.821	4.202	4.536	Pd	2.425	9.800	0.000
O	2.048	1.654	9.129	Pd	3.247	5.598	4.536	Pd	4.850	11.200	0.000
				Pd	5.660	6.995	4.534	Pd	0.000	2.800	0.000
				Pd	0.814	6.999	4.585	Pd	2.425	4.200	0.000
Pd	0.027	8.352	6.940	Pd	3.243	8.403	4.581	Pd	4.850	5.600	0.000
Pd	2.479	9.769	6.910	Pd	5.675	9.787	4.559	Pd	0.000	5.600	0.000
Pd	4.883	11.176	6.842	Pd	1.617	2.800	2.286	Pd	2.425	7.000	0.000
Pd	0.015	2.788	6.774	Pd	4.042	4.200	2.286	Pd	4.850	8.400	0.000

Table 6.D.3: Coordinates for the most stable dehydrogenated glycine coadsorbed with H on Pd(111). This configuration is shown in Fig. 6.3(c).

Atom	x	y	z	Atom	x	y	z	Atom	x	y	z
C	0.821	2.342	9.955	Pd	2.411	4.219	6.867	Pd	6.475	5.586	2.297
C	1.179	0.999	9.314	Pd	4.847	5.626	6.850	Pd	1.600	5.628	2.297
H	6.848	8.125	9.406	Pd	0.011	5.610	6.837	Pd	4.074	7.056	2.297
H	6.134	6.627	9.290	Pd	2.441	6.997	6.838	Pd	6.475	8.442	2.297
H	1.691	3.002	9.929	Pd	4.854	8.404	6.803	Pd	1.600	8.400	2.297
H	0.504	2.184	10.997	Pd	0.806	1.422	4.623	Pd	4.074	9.829	2.297
N	7.007	7.147	9.155	Pd	3.235	2.808	4.579	Pd	6.475	11.215	2.297
O	0.177	0.244	9.058	Pd	5.669	4.204	4.588	Pd	0.000	0.000	0.000
O	2.399	9.163	9.043	Pd	0.811	4.201	4.579	Pd	2.401	1.386	0.000
				Pd	3.238	5.616	4.537	Pd	4.874	2.814	0.000
H	4.038	4.215	7.667	Pd	5.679	7.010	4.566	Pd	0.000	2.772	0.000
				Pd	0.808	7.020	4.571	Pd	2.401	4.158	0.000
Pd	7.269	12.568	6.900	Pd	3.230	8.419	4.539	Pd	4.874	5.586	0.000
Pd	2.469	9.794	6.877	Pd	5.664	9.819	4.565	Pd	0.000	5.628	0.000
Pd	4.864	11.187	6.892	Pd	1.600	2.772	2.297	Pd	2.401	7.014	0.000
Pd	7.265	7.044	6.974	Pd	4.074	4.200	2.297	Pd	4.874	8.442	0.000

Table 6.D.4: Coordinates for the most stable neutral glycine adsorbed on Pd(111). This configuration is shown in Fig. 6.A.1(c).

Atom	x	y	z	Atom	x	y	z	Atom	x	y	z
C	0.739	3.754	9.939	Pd	2.450	4.235	6.829	Pd	6.475	5.586	2.297
C	2.042	3.071	10.270	Pd	4.846	5.623	6.846	Pd	1.600	5.628	2.297
H	6.164	7.227	9.326	Pd	0.011	5.637	6.853	Pd	4.074	7.056	2.297
H	0.086	1.868	9.459	Pd	2.437	7.023	6.857	Pd	6.475	8.442	2.297
H	0.921	4.674	9.369	Pd	4.848	8.428	6.852	Pd	1.600	8.400	2.297
H	0.269	4.036	10.896	Pd	0.808	1.428	4.608	Pd	4.074	9.829	2.297
H	3.818	3.442	10.797	Pd	3.241	2.820	4.558	Pd	6.475	11.215	2.297
N	7.156	7.033	9.173	Pd	5.665	4.216	4.574	Pd	0.000	0.000	0.000
O	2.193	1.860	10.288	Pd	0.811	4.206	4.590	Pd	2.401	1.386	0.000
O	3.009	3.958	10.590	Pd	3.244	5.629	4.537	Pd	4.874	2.814	0.000
				Pd	5.681	7.021	4.591	Pd	0.000	2.772	0.000
				Pd	0.816	7.020	4.567	Pd	2.401	4.158	0.000
Pd	0.010	0.010	6.864	Pd	3.238	8.427	4.556	Pd	4.874	5.586	0.000
Pd	2.448	1.415	6.858	Pd	5.665	9.824	4.575	Pd	0.000	5.628	0.000
Pd	4.859	2.825	6.868	Pd	1.600	2.772	2.297	Pd	2.401	7.014	0.000
Pd	0.015	2.826	6.991	Pd	4.074	4.200	2.297	Pd	4.874	8.442	0.000

Appendix 6.E: Structural information for zwitterionic, dehydrogenated, and neutral glycine adsorption in the most stable states on Pt(111)

Similar to Appendix 6.C but for Pt(111).

Table 6.E.1: Unit cell vectors of supercell used for calculations on Pt(111) with a lattice constant of 3.99 Å. (in Å)

	x	y	z
a	1.837	1.061	0.000
b	0.000	2.121	0.000
c	0.000	0.000	5.240

Table 6.E.2: Coordinates for the most stable zwitterionic glycine adsorbed on Pt(111). This configuration is shown in Fig. 6.A.3(a).

Atom	x	y	z	Atom	x	y	z	Atom	x	y	z
C	1.052	2.881	10.547	Pt	2.427	4.205	6.873	Pt	1.617	8.401	2.300
C	2.373	2.509	9.852	Pt	7.261	7.005	6.879	Pt	6.467	8.401	2.300
H	6.886	6.559	9.096	Pt	4.869	11.197	6.890	Pt	4.042	7.001	2.300
H	6.490	6.000	10.654	Pt	2.447	9.781	6.981	Pt	1.617	5.600	2.300
H	0.488	1.128	9.723	Pt	7.271	12.577	6.875	Pt	6.467	5.601	2.300
H	0.808	3.913	10.321	Pt	5.660	9.797	4.578	Pt	4.042	4.201	2.300
H	1.135	2.750	11.628	Pt	3.229	8.410	4.606	Pt	1.617	2.800	2.300
N	-0.012	1.989	10.015	Pt	0.811	6.995	4.573	Pt	4.850	8.401	0.000
O	2.292	1.399	9.184	Pt	5.656	6.995	4.568	Pt	2.425	7.001	0.000
O	3.330	3.253	10.006	Pt	3.238	5.598	4.567	Pt	0.000	5.600	0.000
				Pt	0.812	4.199	4.571	Pt	4.850	5.601	0.000
				Pt	5.657	4.197	4.569	Pt	2.425	4.200	0.000
Pt	4.870	8.383	6.892	Pt	3.231	2.786	4.599	Pt	0.000	2.800	0.000
Pt	2.429	6.975	6.883	Pt	0.822	1.396	4.598	Pt	4.850	2.801	0.000
Pt	0.008	5.591	6.895	Pt	6.467	11.201	2.300	Pt	2.425	1.400	0.000
Pt	4.856	5.590	6.893	Pt	4.042	9.801	2.300	Pt	0.000	0.000	0.000

Table 6.E.3: Coordinates for the most stable dehydrogenated glycine coadsorbed with H on Pt(111). This configuration is shown in Fig. 6.A.3(c).

Atom	x	y	z	Atom	x	y	z	Atom	x	y	z
C	0.796	2.351	10.031	Pt	2.416	4.209	6.927	Pt	1.617	8.401	2.300
C	1.176	1.014	9.426	Pt	0.003	2.836	7.014	Pt	6.467	8.401	2.300
H	6.841	8.099	9.396	Pt	4.892	11.159	6.931	Pt	4.042	7.001	2.300
H	6.143	6.603	9.307	Pt	2.492	9.779	6.912	Pt	1.617	5.600	2.300
H	1.654	3.013	10.014	Pt	0.022	8.350	6.943	Pt	6.467	5.601	2.300
H	0.442	2.227	11.062	Pt	5.665	9.803	4.573	Pt	4.042	4.201	2.300
N	7.010	7.121	9.180	Pt	3.233	8.401	4.554	Pt	1.617	2.800	2.300
O	0.194	0.256	9.139	Pt	0.805	7.013	4.576	Pt	4.850	8.401	0.000
O	2.389	9.211	9.163	Pt	5.674	6.988	4.585	Pt	2.425	7.001	0.000
				Pt	3.235	5.588	4.561	Pt	0.000	5.600	0.000
H	4.055	4.195	7.778	Pt	0.814	4.180	4.605	Pt	4.850	5.601	0.000
				Pt	5.675	4.194	4.601	Pt	2.425	4.200	0.000
Pt	4.865	8.399	6.859	Pt	3.237	2.787	4.604	Pt	0.000	2.800	0.000
Pt	2.451	6.978	6.859	Pt	0.806	1.412	4.640	Pt	4.850	2.801	0.000
Pt	0.019	5.603	6.888	Pt	6.467	11.201	2.300	Pt	2.425	1.400	0.000
Pt	4.862	5.622	6.893	Pt	4.042	9.801	2.300	Pt	0.000	0.000	0.000

Table 6.E.4: Coordinates for the most stable neutral glycine adsorbed on Pt(111). This configuration is shown in Fig. 6.A.1(d).

Atom	x	y	z	Atom	x	y	z	Atom	x	y	z
C	0.778	3.631	9.961	Pt	2.463	4.212	6.873	Pt	1.617	8.401	2.300
C	2.070	2.935	10.271	Pt	0.029	2.799	7.012	Pt	6.467	8.401	2.300
H	6.209	7.119	9.356	Pt	4.869	11.202	6.897	Pt	4.042	7.001	2.300
H	0.129	1.770	9.429	Pt	2.460	9.789	6.881	Pt	1.617	5.600	2.300
H	0.954	4.557	9.413	Pt	0.014	8.382	6.885	Pt	6.467	5.601	2.300
H	0.310	3.879	10.923	Pt	5.666	9.801	4.575	Pt	4.042	4.201	2.300
H	3.846	3.289	10.771	Pt	3.238	8.400	4.564	Pt	1.617	2.800	2.300
N	7.192	6.937	9.178	Pt	0.817	7.001	4.566	Pt	4.850	8.401	0.000
O	2.199	1.731	10.274	Pt	5.677	7.001	4.608	Pt	2.425	7.001	0.000
O	3.038	3.803	10.589	Pt	3.239	5.605	4.561	Pt	0.000	5.600	0.000
				Pt	0.806	4.185	4.612	Pt	4.850	5.601	0.000
				Pt	5.665	4.201	4.576	Pt	2.425	4.200	0.000
Pt	4.854	8.411	6.887	Pt	3.243	2.799	4.573	Pt	0.000	2.800	0.000
Pt	2.443	7.001	6.890	Pt	0.808	1.413	4.608	Pt	4.850	2.801	0.000
Pt	0.014	5.620	6.888	Pt	6.467	11.201	2.300	Pt	2.425	1.400	0.000
Pt	4.853	5.591	6.886	Pt	4.042	9.801	2.300	Pt	0.000	0.000	0.000

CHAPTER 7

DENSITY FUNCTIONAL THEORY STUDY OF H AND CO ADSORPTION ON K-PROMOTED MO_2C SURFACES

7.1. Introduction

Transition metal carbides are interesting as catalysts because of their extreme hardness[1], high melting point[2], and excellent electric and thermal conductivities[3]. Within this class of materials, molybdenum carbides have exhibited excellent catalytic behavior in reactions including ammonia synthesis[4], water-gas shift[5], hydrogenation of CO[6-7] or benzene[8-9], hydrodenitrogenation[10], hydrodesulfurization[11], and hydrocarbon isomerization[12]. Molybdenum carbides are potentially promising substitutes for expensive noble metals due to their similar catalytic properties[13], accompanied by resistance to sulfur poisoning[13-14].

In the Mo-C phase diagram at least six different phases have been identified[15], including two phases of Mo_2C (one orthorhombic and one hexagonal). Among these phases, only two types of Mo_2C and one MoC phase are found to be stable at room temperature[15-16]. There is some confusion in the literature regarding the names of Mo_2C phases, with some authors referring to orthogonal Mo_2C as α–Mo_2C[17-21]. We prefer to follow the convention defined by the Joint Committee on Power Diffraction Standards (JCPDS) data files[22-24], in which hexagonal Mo_2C, orthogonal Mo_2C, and hexagonal MoC are denoted α, β, and γ, respectively. Liu *et al.* demonstrated that β–Mo_2C is more stable than α–Mo_2C using density functional theory (DFT) calculations of the formation enthalpy[25]. For this reason, we restrict our attention in this Chapter to the orthogonal phase of Mo_2C, that is, β–Mo_2C.

The surface properties of catalytic materials can be modified by doping with alkali metals[26-32]. Since K is relatively inexpensive, it is widely used as a promoter in

industrial applications. Woo *et al.* reported significant changes in the selectivity to C_1-C_7 linear alcohols production relative to hydrocarbons from synthesis gas for experiments in which molybdenum carbides were promoted with K_2CO_3[14]. Xiang *et al.* have reported in experiments for mixed alcohol synthesis from CO hydrogenation that both β–Mo_2C and α–MoC_{1-x} produced light hydrocarbons and by adding K as a promoter, they showed a distinctive selectivity shift from hydrocarbons to alcohols[28]. In general terms, this promotion effect is thought to be associated with the charge transfer to the catalyst surface due to the exceptionally low ionization potential of K. The addition of alkali promoters generates electrostatic fields at the surface, inducing substantial changes in the process of adsorption and catalytic reactions[31].

Theoretical studies have been applied to a range of physical, chemical, and electronic properties of the molybdenum carbides, including the adsorption and reaction of small species on the surfaces. Hugosson *et al.* have extensively examined the relative stabilities of Mo-C phases and the effect of vacancies on phase stability[15]. Kitchin *et al.* investigated the β–Mo_2C (001) surface along with the close-packed surfaces of other carbides to compare the chemical properties of various carbide surfaces[33]. DFT calculations for the adsorption of small molecules on β–Mo_2C (001) have been also performed, including the adsorption O_2 and CO[34], CO_2, H, CH_x (x=0-3), C_2H_4[20], and methanol[35]. Tominaga *et al.* have studied individual reaction steps associated with several reactions on β–Mo_2C (001) including the water-gas shift reaction[36], CH_4 reforming[37], and hydrodesulfurization of thiophene[38]. In all of these studies, it appears that attention was given to the (001) surface because this is most densely packed surface of β–Mo_2C (001). Recently, Shi *et al.* reported DFT calculations for a range of low-index surfaces of β–Mo_2C[39]. They observed that the mixed Mo/C termination of the (011) surface, not (001), had the lowest surface free energy among the surfaces they considered. None of the existing DFT studies of β–Mo_2C have considered the properties of K as a promoter on the

surface. A small number of DFT calculations are available examining this issue on other materials[40-41].

In this Chapter, we use DFT calculations to probe the properties of K atoms on β–Mo_2C surfaces with the aim of providing fundamental information about this situation that will be useful for considering the mechanistic influence of K promoters in complex catalytic reactions. To make progress towards this goal, we assume that the catalytic activity of Mo_2C is associated with the terraces of stable surfaces of the material rather than being dominated by a rate-determining step dictated by a step edge or other defect. This assumption also underlies the DFT studies listed above, although it is rarely stated explicitly. This assumption means that we confine our attention to the properties of K adsorbed on stable surfaces on typical Mo_2C crystals. We also consider situations where the concentration of K on catalyst particles is low. This choice implies that we must determine what Mo_2C surfaces on a typical catalyst particle bind K most strongly. To this end, we examine the adsorption energies and geometries of K on seven low-index surfaces to determine the most preferred surface for K adsorption. A surprising finding from our calculations is that the bulk-terminated surface that binds K most strongly undergoes a surface reconstruction in the absence of any adsorbed species. The reconstructed surface binds K even more strongly than the bulk-terminated surface. We have examined the coadsorption of H or CO with K on this reconstructed surface to give some initial insight into the influence of K on reactant adsorption on this material.

7.2. Computational details

Our plane wave DFT calculations were performed with the Vienna *ab initio* simulation package (VASP)[42-45]. We employed the revised Perdew-Burke-Ernzerhof (rPBE) generalized gradient functional[46-47] along with the projector augmented wave (PAW)[48-49] method to describe ionic cores. A plane wave expansion with a cutoff of 400

eV was used for all calculations. Geometries were relaxed using a conjugate gradient algorithm until the forces on all unconstrained atoms were less than 0.03 eV/Å.

The β–Mo_2C phase has an orthorhombic crystal structure, with *a*=4.724 Å, *b*=6.004 Å, and *c*=5.199 Å[50]. The DFT-optimized orthorhombic lattice constants for β–Mo_2C phase (*a*=4.720 Å, *b*=6.072 Å, and *c*=5.268 Å) are in good agreement with the experimental values. As described previously, the most stable bulk structure of β–Mo_2C phase is an eclipsed configuration where half of the C atoms occupy half of the octahedral interstitial sites on one layer, and half of the C atoms occupy the neighboring upright position on the adjacent layer[39, 51]. This bulk structure is illustrated in Fig. 7.1. Calculations with the bulk structure confirmed that this material is metallic.

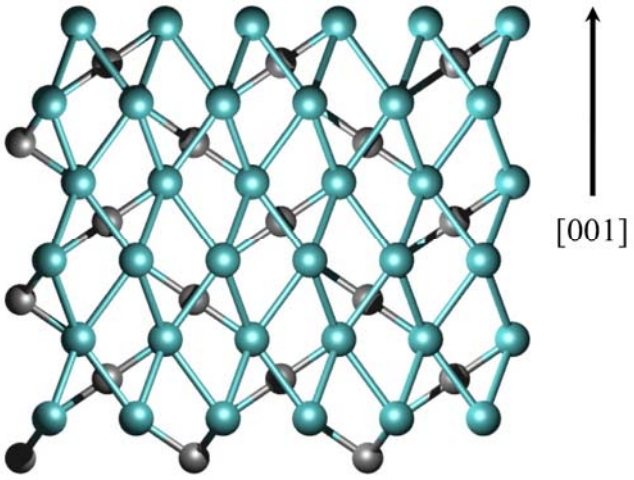

Figure 7.1: The most stable bulk structure of β–Mo_2C phase viewed along the [010] axis. Mo (C) atoms are shown as blue (gray) spheres.

We cleaved this structure along seven low Miller index planes, namely (001), (010), (100), (110), (101), (011), and (111), to construct surfaces. Each surface was represented by slabs 10-15 Å thick. All possible bulk terminations perpendicular to the surface normal to these planes were considered. The (001), (010), and (111) surfaces have both pure Mo and pure C terminations. The (100), (110), and (101) surfaces have mixed Mo/C terminations. The (011) surface has a pure Mo termination and a mixed

Mo/C termination. In all calculations, no atoms in the slab were constrained and a vacuum spacing of 14 Å was used normal to the surface.

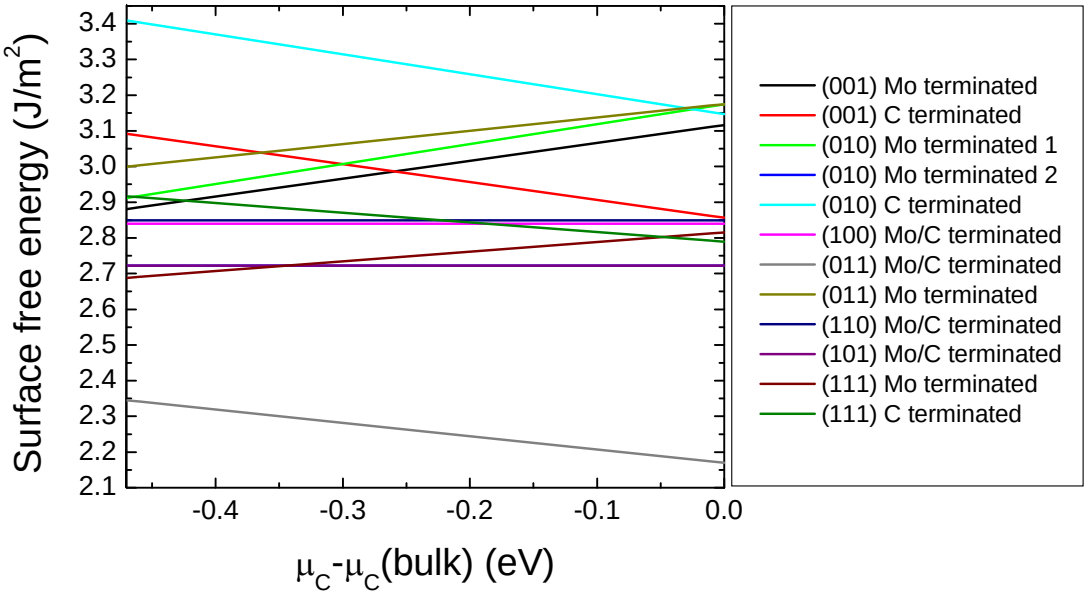

Figure 7.2: The surface free energies of seven low Miller index surfaces are plotted as a function of μ_c-μ_c(bulk). For each surface, the results for all possible terminations are shown.

In all of our calculations the surfaces were constructed as symmetric slabs. This implies that some of the surface slabs were non-stoichiometric. As a result, the surface energy, σ, is calculated by[39, 52-55].

$$\sigma = (E_{slab} - n_{Mo}\mu_{Mo} - n_C\mu_C) / 2A . \quad (7.1)$$

Here, E_{slab} is the total energy of the slab, A is the surface area of one side of the slab, μ_x is the chemical potential of species x, and n_y is the number of atoms of species y in the supercell. After some algebra using the relationships described by previous reports[39, 52-55], the surface energy can be expressed as a function of difference between the chemical potential for a C atom, μ_C, and the chemical potential in bulk phase of C, $\mu_C(bulk)$. If a

surface is stoichiometric within the symmetric slabs, Eq. (7.1) can be reduced to the usual expression for the surface energy[45].

$$\sigma = (E_{slab} - nE_{bulk}) / 2A , \quad (7.2)$$

where E_{bulk} is the bulk total energy per Mo_2C unit and n is the number of Mo_2C units in the slab. In earlier work, Shi *et al.* compared the surface energies of different terminations using Eq. (7.2), and then used the predictions from these calculations to compare the surface energies of a variety of low index surfaces.[39] This approach is potentially problematic because differing surface terminations should be compared using Eq. (7.1). In our work, we calculated the surface energy for each surface with each possible terminations using Eq. (7.1), as shown in Fig. 7.2. In Fig. 7.2, the C-terminated (010) surface has the highest surface free energy at almost all the ranges of μ_c-μ_c(bulk). The lowest surface free energy is the mixed Mo/C-terminated (011) surface, in agreement with Shi *et al.*'s calculations[39].

Calculations for adsorbed K on each surface were performed at various coverages to understand coverage effects as discussed later. A 6×6×1 Monkhorst-Pack *k*-point mesh was used for a (1×1) surface unit cell, which was sufficient to give well converged results. For calculations at lower coverages, the number of *k*-points in the Monkhorst-Pack meshes were appropriately reduced. Calculations for H and CO adsorption with or without coadsorbed K were performed using a (2×2) surface unit cell with a 3×3×1 Monkhorst-Pack *k*-point mesh. The geometries of gas phase species were optimized in a supercell of the same size as the surface calculations. When examining adsorption, molecules were placed on only one side of the slab. Dipole corrections were therefore applied in computing all of the energies reported below[56-57]. The adsorption energy, E_{ads}, of an atom or molecule was defined by

$$E_{ads} = \left(E_{surf} + E_{adsorbate}\right) - E_{total} , \quad (7.3)$$

where E_{total} is the total energy of the system containing the adsorbed species, E_{surf} is the total energy for the optimized bare surface, and $E_{adsorbate}$ is the total energy for the adsorbate in the gas phase. With this definition, positive adsorption energies correspond to energetically favored states.

7.3. Results and discussion

As can be seen from Fig. 7.2, the range of surface energies among the set of surfaces we examined is not large, with energies varying from 2.2-3.4 J/m^2. Once the surface energies are known, the equilibrium crystal shape (ECS) of the material can be predicted from the Wulff construction[58-61]. We used this approach to examine the ECS for a range of carbon chemical potentials. Figure 7.3 shows that resulting ECS at the upper and lower bounds for μ_C. Intermediate values of the μ_C give similar results. One immediate observation from this figure is that the (001) surface, which has been the focus of much earlier theoretical work, is not the dominant surface on Mo_2C crystals in terms of the surface area associated with this surface.

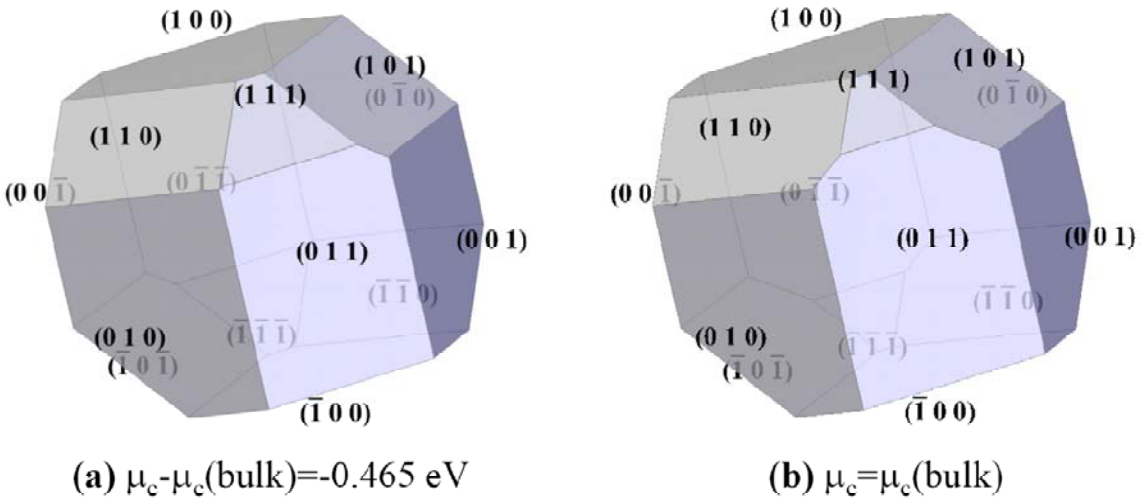

Figure 7.3: The predicted equilibrium crystal shapes of Mo_2C determined from the Wulff construction using the surface free energies at the lower and upper bound of μ_c-μ_c(bulk).

7.3.1. K adsorption β–Mo_2C surfaces

As described in the Introduction, we are interested in determining the location of adsorbed K in the limit of low K coverages on a catalyst particle. We have therefore examined K adsorption on the seven low Miller index surfaces mentioned in Sec. 2. For these calculations only the termination with the lowest surface energy among the terminations we examined on each surface was considered.

Figure 7.4 shows an example of the calculated K adsorption energy at six surface coverages on β–Mo_2C(001). Coverage is expressed in terms of the absorbate number density in $Å^{-2}$. In order to have confidence that a global minimum can be identified, large numbers of adsorption configurations must be examined for studying atomic or molecular adsorption[62-64]. To address this challenge, we examined a variety of initial configurations by dividing a (1×1) surface unit cell of the (001) surface into a 4×3 grid at intervals of ~1.6 Å. K is then positioned 3.3 Å above each grid point so that we have 12 initial configurations for adsorption on the surface. Each configuration was relaxed to find a local energy minimum for the adsorbed molecule. The structure with the most stable adsorption energy among the energy minima found in this way was used to perform lower coverage calculations. The adsorption energies shown in Fig. 7.4 are the result of these coverage dependent calculations.

Figure 7.4 shows that the adsorption energy of K is strongly dependent upon coverage. This is not surprising, as strong repulsive interactions induced by the dipole moment of adsorbed K are expected. Based on the steep work function changes upon the K adsorption, Bugyi *et al.* suggested that the K promoter donates charge to the surface upon adsorption on this kind of surface[29-30]. Our charge calculations by Bader analysis[65-67] at the highest coverage, 32.0 $Å^2$/atom, support the observation, showing that a charge of -0.9e is transferred into the surface from K. This charge transfer creates a dipole moment associated with an adsorbed K.

We can model the coverage dependent adsorption using a simple electrostatic method developed by Albano[68]. The coverage dependent adsorption energy is assumed to be entirely due to repulsive dipole-dipole interactions on the surface. This model has been successfully applied to several experiments including desorption of K from metal surfaces[68], desorption of K in the presence of coadsorbed O[68], molecular desorption of CH_3Cl from Pd(100)[69], and atomic I desorption from Ni surfaces[70]. The Albano model can be written as

$$E_{ad} = E_{ad}\big|_{N\to 0} - 1.602 \times \frac{9 \times \left(\mu\big|_{N\to 0}\right)^2 \times N^{3/2}}{\left(1 + 9 \times \alpha \times N^{3/2}\right)^2}. \qquad (7.4)$$

Here, E_{ad} is the adsorption energy (in eV), $E_{ad}\big|_{N\to 0}$ is the adsorption energy in the limit of zero coverage (in eV), $\mu\big|_{N\to 0}$ is the static dipole moment of the K-Mo_2C surface bond in the limit of zero coverage (in Debye), N is the surface coverage in atoms (in $Å^{-2}$), α is the constant polarizability of the adsorbed K (in $Å^3$), 9 is the geometric factor applicable to a hexagonal or square array of adsorbates, and 1.602 is the unit conversion factor. Fitting Eq. (7.3) to the data in Fig. 7.4 gives $E_{ad}\big|_{N\to 0}$, $\mu\big|_{N\to 0}$, and α values of 2.79 eV, 6.97 D, and 12.63 $Å^3$, respectively.

We used an approach similar to the one described above to calculate the coverage dependent adsorption energies of K for the other surfaces. For simplicity, we assumed that the polarizability of adsorbed K is independent of the surface orientation and equal to the value deduced above, 12.63 $Å^3$. With this assumption the Albano model includes only two parameters, which we fitted for each surface from computed adsorption energies at three distinct coverages. Table 7.1 summarizes $E_{ad}\big|_{N\to 0}$ and $\mu\big|_{N\to 0}$ for each surface. Among the seven surfaces, (001) has the highest adsorption energy and dipole moment. The (111) surface has a similar adsorption energy to the (001) surface, but the remaining surfaces we examined have adsorption energies that are from 0.26-0.78 eV lower. Our

evaluation of the ECS of β–Mo_2C showed that the surface area of (001) is expected to be considerably larger than (111) (see Fig. 7.3). On this basis, we selected the (001) surface for further calculations involving coadsorption of H or CO with K.

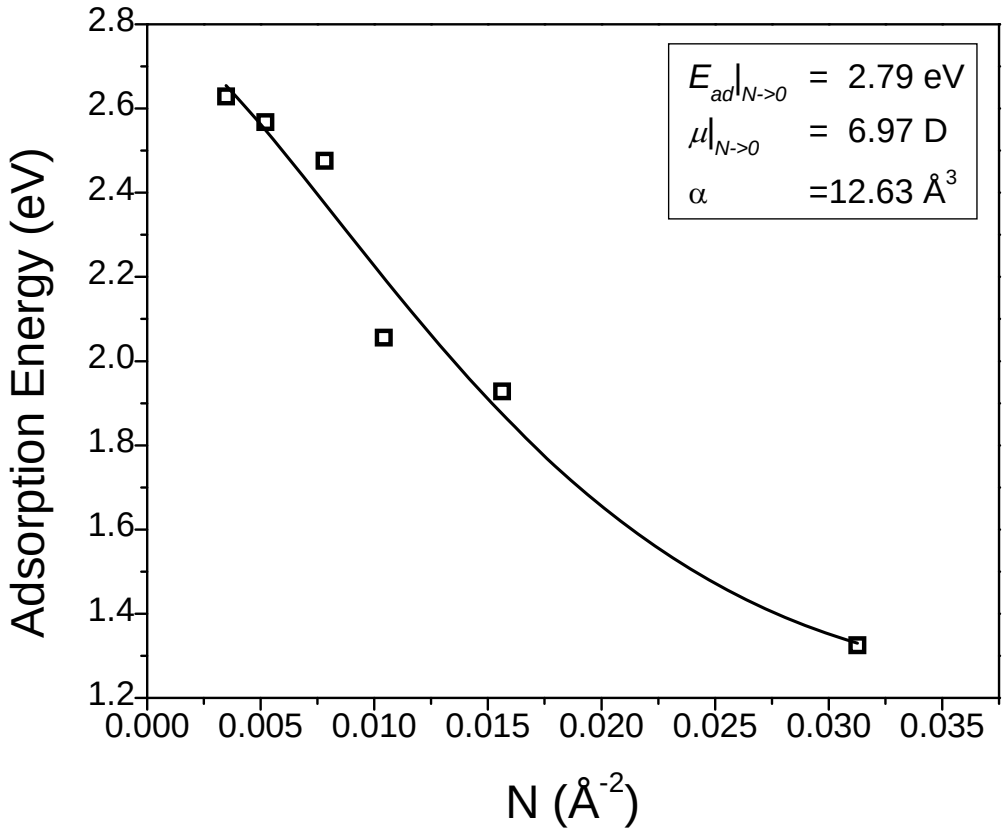

Figure 7.4: The adsorption energy of K as a function of coverage on Mo_2C(001). The solid curve shows a fit of the data to the Albano model[68].

Surface	(001)	(100)	(110)	(010)	(011)	(101)	(111)
$E_{ad}\|_{N\to 0}$ (eV)	2.79	2.53	2.16	1.92	2.39	2.07	2.77
$\mu\|_{N\to 0}$ (D)	6.97	6.63	6.32	5.24	5.88	5.22	6.38

Table 7.1: The adsorption energies and dipole moments of K in the limit of zero coverage for the seven surfaces obtained as described in the text.

7.3.2. K, H, and CO adsorption on bare unreconstructed and reconstructed β–Mo_2C (001) surfaces.

We noted above that most previous DFT calculations examining surfaces of β–Mo_2C used the (001) surface, even though later calculations by Shi *et al*. showed that the (011) surface has a markedly lower surface energy. Our analysis of K binding energies, however, suggests that it is quite appropriate to focus attention on the (001) surface if we are interested in low coverages of K on catalyst particles. While performing calculations with β–Mo_2C(001), however, we made the surprising observation that this surface can reconstruct, even in the absence of adsorbates. Figure 7.5 shows both unreconstructed and reconstructed bare (001) surfaces. The surface energy is lowered by 0.18 J/m^2 for any value of μ_c-μ_c(bulk) by this reconstruction. This structure was initially observed in calculations involving CO adsorption, but subsequent calculations confirmed that it can occur for the bare surface. During the reconstruction, C atoms move in a way that they form hexagons on the surface with adjacent C atoms separated ~3.5 Å. This observation implies that earlier calculations[20, 34-38] examining adsorption on β–Mo_2C(001) may not capture all features of these systems because they did not include the surface reconstruction.

The existence of a reconstruction for the (001) surface prompted us to consider whether surface reconstructions might also exist for some of the other surfaces we have considered. It is of course not possible to make any definitive statements about this possibility, but examination of the other surfaces shown in Fig. 7.2 based on coordination-based arguments did not suggest any obvious candidates for reconstruction.

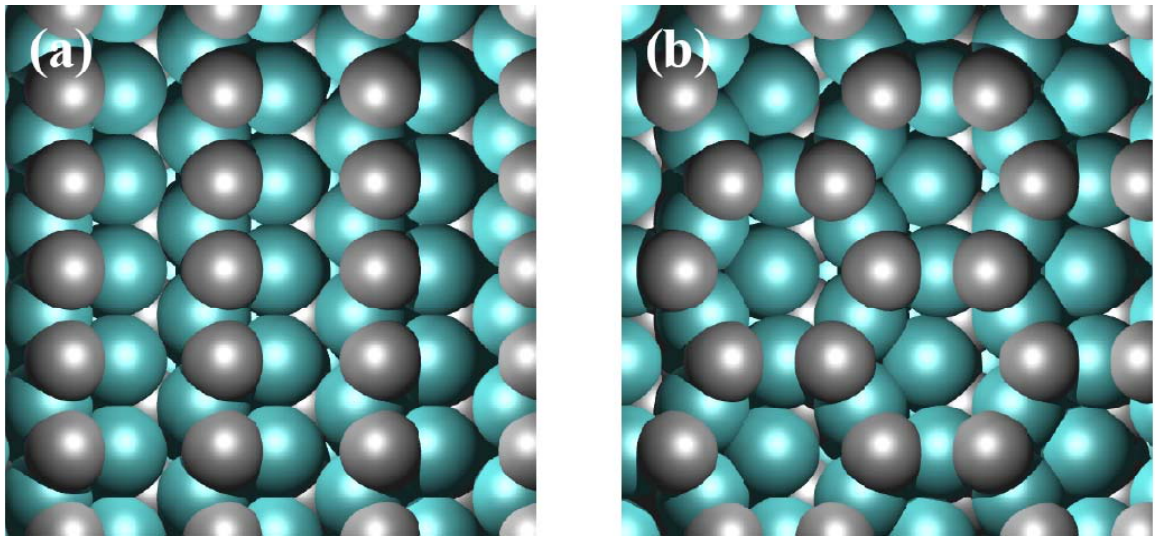

Figure 7.5: (a) Unreconstructed and (b) reconstructed bare (001) surface. Mo atoms are shown as green spheres and C atoms as gray spheres.

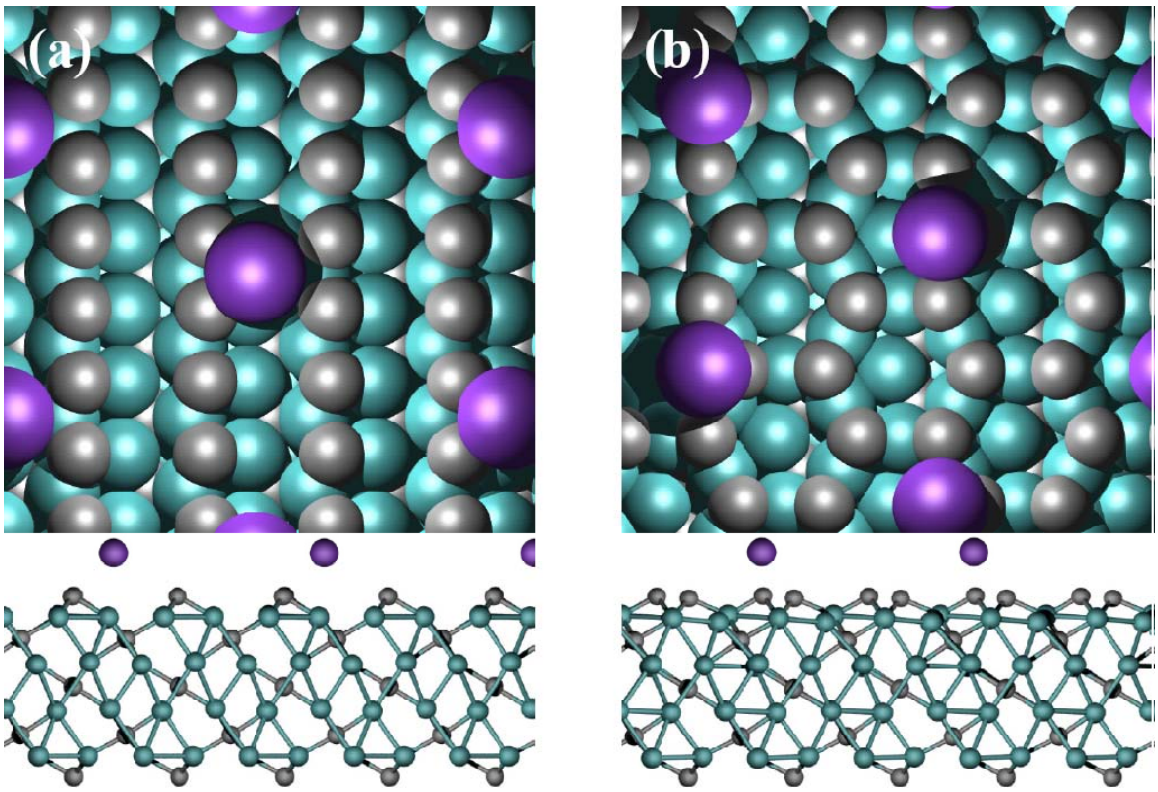

Figure 7.6: Top and side view of K adsorption on (a) unreconstructed and (b) reconstructed (001) surface. In addition to the atoms described in Fig. 7.5, K atoms are shown in purple.

Above, we argued that adsorption of K on the unreconstructed (001) surface is the most stable among the surfaces we considered. It is therefore important to compare K adsorption on the bulk terminated and reconstructed (001) surfaces. Possible adsorption sites on the reconstructed surface were determined as described above at a coverage of 32.0 $Å^2$/atom. The binding energy of K was then calculated in the most stable site on each surface with one K adsorbed in a (2×2) surface unit cell, which gives an area of 127.9 $Å^2$/atom. The results from these calculations are shown in Fig. 7.6. K binds on the unreconstructed (001) surface by coordinating with two C atoms and two Mo atoms. On the reconstructed surface, the adsorbed atom is coordinated with three C atoms and three Mo atoms. The adsorption energy of K on the unreconstructed (reconstructed) surface at this coverage is 2.48 eV (2.64 eV). That is, the reconstructed surface binds K more tightly than the unreconstructed surface and is therefore an appropriate surface to consider when examining the properties of K at low coverage on catalyst particles.

H adsorption on both the unreconstructed and reconstructed bare surfaces has also been examined. Initial configurations for both surfaces were constructed in a same as for K adsorption. The adsorption coverage of H we present here is 127.9 $Å^2$/atom with one H adsorbed in a (2×2) surface unit cell which is same as in the K adsorption. After all calculations, the most stable structures of H adsorption on both surfaces are found as shown in Fig. 7.7. H adsorption on each surface is preferred on the atop site of a C atom. For both cases, the bond length between C and H atoms is 1.10 Å, which is a typical C-H bond length. The adsorption energy of H on the reconstructed surface (1.02 eV) is 0.35 eV larger than on the unreconstructed surface (0.67 eV), indicating that this surface reconstruction would be strongly favored by the presence of adsorbed H. This adsorption energy for H is given relative to half of total energy of H_2 molecule in the gas phase.

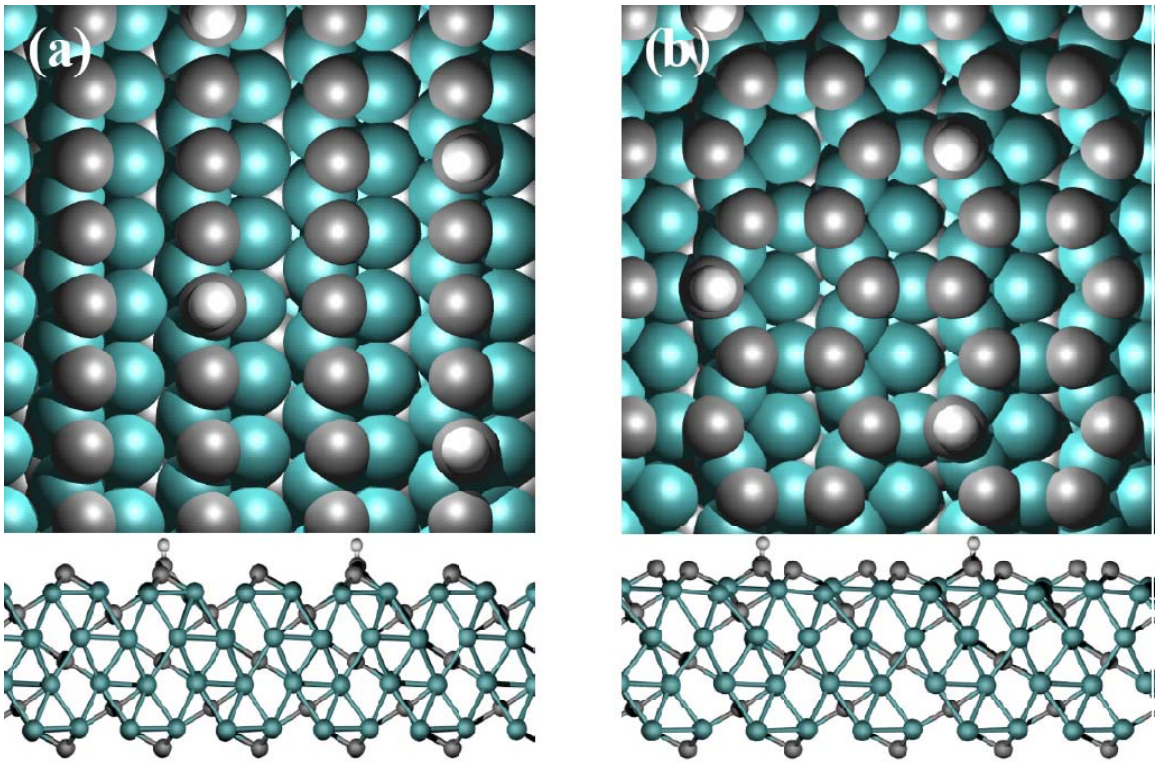

Figure 7.7: Top and side view of H adsorption on (a) unreconstructed and (b) reconstructed (001) surface. In addition to the atoms described in Fig. 7.5, H atoms are shown in white.

We also examined CO adsorption on the same surfaces. The same coverage as in the K or H adsorption was used for CO adsorption. Initial configurations were constructed in a same way as in the adsorption of K or H for both surfaces. It is known that CO vertically adsorbs onto this kind of surfaces where a C atom contacts the surface [34, 71], so we primarily considered this case. To make sure, however, one adsorption state with the O atom towards the surface was also examined. The CO adsorption structures in the most stable states for both surfaces are shown in Fig. 7.8. The structure with the O atom closer to the surface showed almost zero adsorption energy. As shown in Fig. 7.8, the CO adsorption on an atop site of C atom is energetically most favorable for each surface. The bond length between C in the molecule and C from the surface is 1.32 Å, which is similar to a typical C=C bond length. This is in good agreement with a recent in situ IR spectra study of CO adsorbed on fresh β–Mo_2C that observed the existence of

ketenylidene (C=C=O) species [71]. Ren *et al.* also demonstrated from their GGA-PBE DFT calculations that CO atop adsorption on the surface C atom forming C=C=O is energetically favored among CO adsorption states on C-terminated β–Mo_2C (001) [34]. We calculated the adsorption energy of CO on the unreconstructed (reconstructed) surface to be 1.65 eV (1.51 eV). For only this case, the adsorption on the reconstructed surface is less energetically favored to on the unreconstructed one. This energy difference however, is not sufficient to reverse the overall stability of the surface reconstruction at the CO coverages we examined.

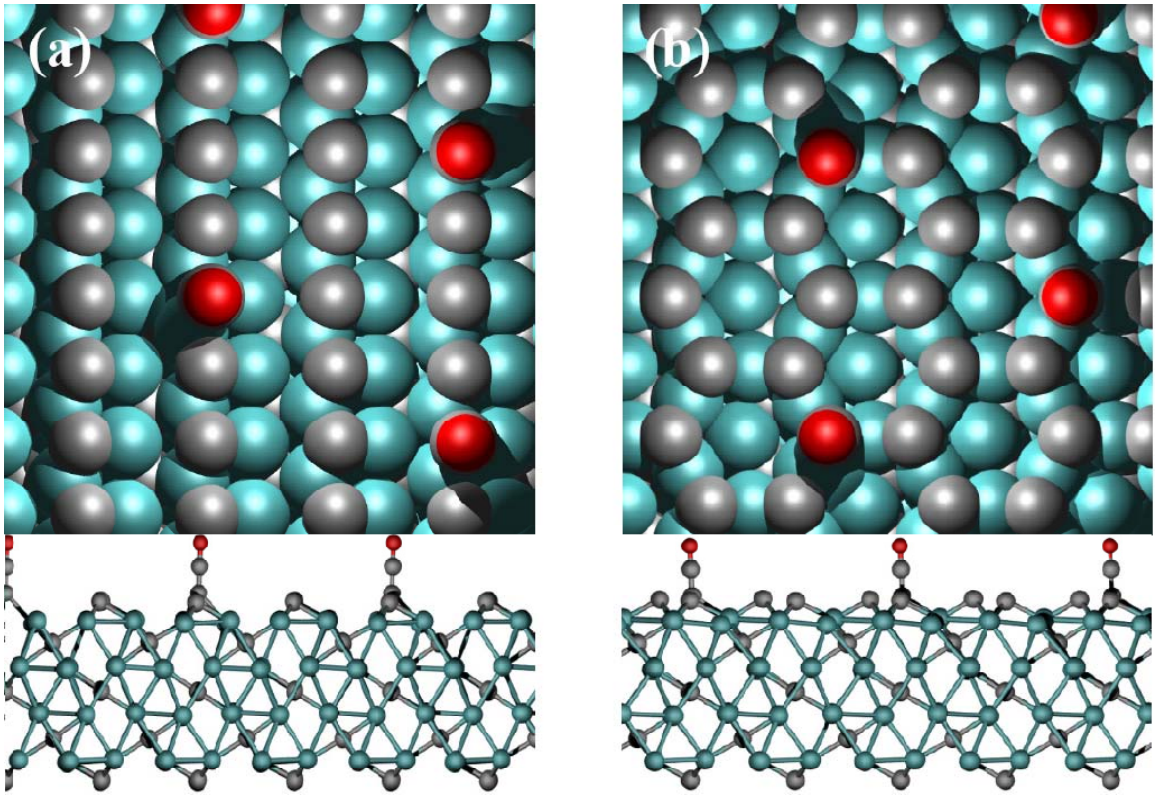

Figure 7.8: Top and side view of CO adsorption on (a) unreconstructed and (b) reconstructed (001) surface. In addition to the atoms described in Fig. 7.5, O atoms are shown in red.

7.3.3. H or CO coadsorption with K promoter on reconstructed β–Mo_2C (001) surfaces

Finally, we examined H/K and CO/K coadsorption on β–Mo_2C (001). Initial configurations were constructed with linear combinations of K and H or CO adsorbed structures in their most stable states. The most stable configurations for H and CO

coadsorbed with K are shown in Fig. 7.9. Their most stable adsorption structures are very similar in local geometry to the situation when the species are separately adsorbed. For H adsorption, we also considered configurations that involved formation of KH, since K is known to form a stable bulk hydride[72] These calculations indicated that formation of surface KH is not favored relative to the adsorption of H directly on the surface. The adsorption energy of H referenced to the energy of the optimized K adsorbed structure is 0.88 eV, which is 0.14 eV less than the adsorption energy of H on the non-promoted surface. For CO/K coadsorption, the bond length between C atom in the molecule and C atom on each surface is same as in CO single adsorption case. The adsorption energy of CO referenced to the energy of the optimized K adsorbed structure is 1.44 eV, which is reduced by 0.07 eV from CO adsorption on the bare surface. This initial examination of coadsorption with K atoms is not sufficient to draw conclusions about the overall effect of K on catalytic reactivity on this surface, but it should provide useful baseline data for future investigations of these issues.

7.4. Conclusion

In order to provide fundamental information on how the adsorption of K can lead to changes in the selectivity of catalytic reactions on Mo_2C catalysts, DFT calculations were performed to study the stability of seven low-index bare surfaces of β–Mo_2C and the adsorption of K on those surfaces. We used the Wulff construction to predict the equilibrium crystal shape of Mo_2C using surface energies calculated from DFT. Even though (011) surface has the lowest surface energy, we found that at low coverages, K atoms adsorb more strongly on the (001) surface.

During further investigation of the (001) surface, we observed a surface reconstruction that is favored for the bare surface in which the top layer of C atoms on the surface form hexagonal arrays. The adsorption of K and H was energetically favored on the reconstructed (001) surface, although CO was observed to bind more favorably to the

unreconstructed surface. Preliminary calculations of H or CO coadsorption with K on the (001) surface showed that each species remains to its most stable site on the bare surface, although the adsorption energy of H and CO is reduced upon coadsorption with K. Our results do not make direct predictions about the role of K promoters in the catalytic selectivity of β–Mo_2C surfaces, but by providing the first precise information about how K atoms bind on these surfaces they provide a useful foundation for future examinations of the interesting issue of catalytic selectivity.

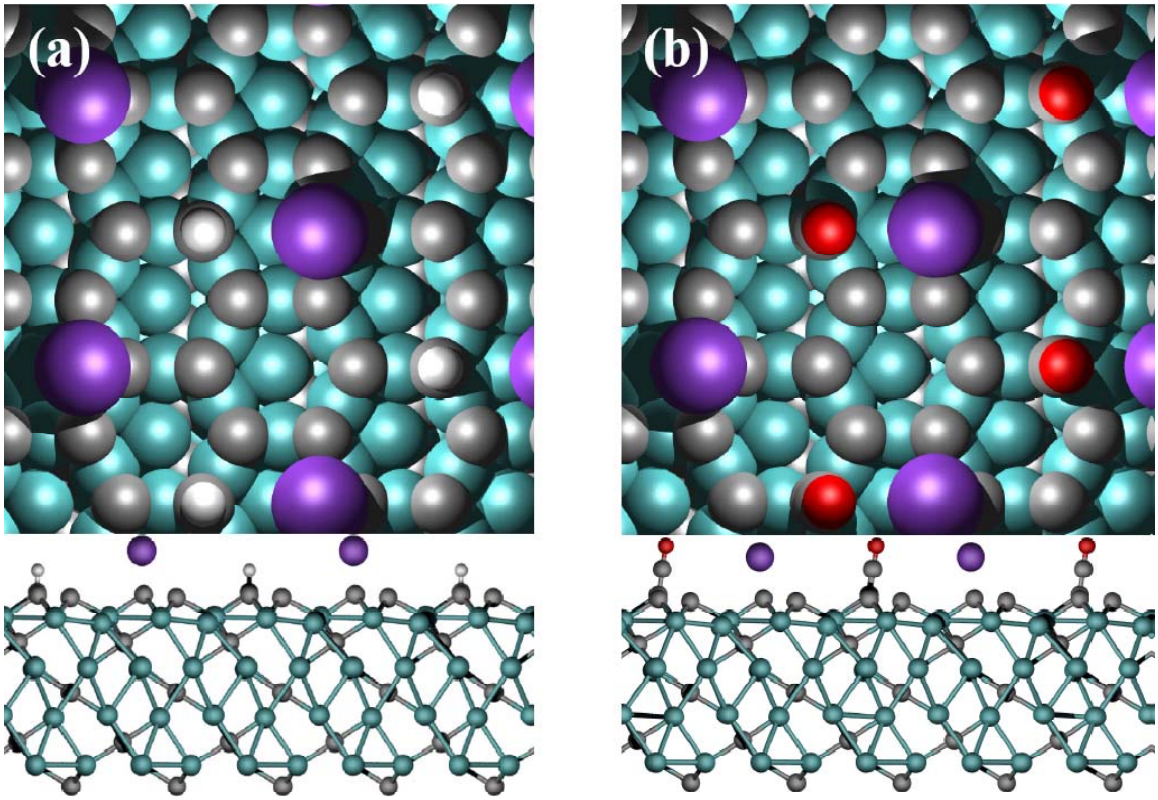

Figure 7.9: Top and side view of (a) H coadsorption and (b) CO coadsorption with K promoter on reconstructed (001) surface

References

(1) Liao, J. J.; Wilcox, R. C.; Zee, R. H., *Scripta. Metall. Mater.* **1990**, 24, 1647-1652.
(2) Hwu, H. H.; Chen, J. G., *Chem. Rev.* **2005**, 105, 185-212.
(3) Nelson, J. A.; Wagner, M. J., *Chem. Mater.* **2002**, 14, 4460-4463.
(4) Kojima, R.; Aika, K., *Appl. Catal. A-Gen.* **2001**, 219, 141-147.
(5) Patt, J.; Moon, D. J.; Phillips, C.; Thompson, L., *Catal. Lett.* **2000**, 65, 193-195.
(6) Ranhotra, G. S.; Bell, A. T.; Reimer, J. A., *J. Catal.* **1987**, 108, 40-49.
(7) Park, K. Y.; Seo, W. K.; Lee, J. S., *Catal. Lett.* **1991**, 11, 349-356.
(8) Lee, J. S.; Yeom, M. H.; Lee, D. S., *J. Mol. Catal.* **1990**, 62, L45-L51.
(9) Lee, J. S.; Yeom, M. H.; Park, K. Y.; Nam, I. S.; Chung, J. S.; Kim, Y. G.; Moon, S. H., *J. Catal.* **1991**, 128, 126-136.
(10) Schwartz, V.; da Silva, V. T.; Oyama, S. T., *J. Mol. Catal. A-Chem.* **2000**, 163, 251-268.
(11) Rodriguez, J. A.; Dvorak, J.; Jirsak, T., *Surf. Sci.* **2000**, 457, L413-L420.
(12) Ledoux, M. J.; Cuong, P. H.; Guille, J.; Dunlop, H., *J. Catal.* **1992**, 134, 383-398.
(13) Oyama, S. T., *Catal. Today* **1992**, 15, 179-200.
(14) Woo, H. C.; Park, K. Y.; Kim, Y. G.; Nam, I. S.; Chung, J. S.; Lee, J. S., *Appl. Catal.* **1991**, 75, 267-280.
(15) Hugosson, H. W.; Eriksson, O.; Nordstrom, L.; Jansson, U.; Fast, L.; Delin, A.; Wills, J. M.; Johansson, B., *J. Appl. Phys.* **1999**, 86, 3758-3767.
(16) Velikanova, T. Y.; Kublii, V. Z.; Khaenko, B. V., *Sov. Powder. Metall. Met. Ceram.* **1988**, 27, 891.
(17) Liu, P.; Rodriguez, J. A.; Hou, H.; Muckerman, J. T., *J. Chem. Phys.* **2003**, 118, 7737-7740.
(18) Liu, P.; Rodriguez, J. A., *J. Chem. Phys.* **2004**, 120, 5414-5423.
(19) Liu, P.; Rodriguez, J. A.; Asakura, T.; Gomes, J.; Nakamura, K., *J. Phys. Chem. B* **2005**, 109, 4575-4583.
(20) Ren, J.; Huo, C. F.; Wang, J. G.; Cao, Z.; Li, Y. W.; Jiao, H. J., *Surf. Sci.* **2006**, 600, 2329-2337.
(21) Ren, J.; Wang, J. G.; Huo, C. F.; Wen, X. D.; Cao, Z.; Yuan, S. P.; Li, Y. W.; Jiao, H. J., *Surf. Sci.* **2007**, 601, 1599-1607.
(22) *Powder Diffraction File, JCPDS International Center for Diffraction Data*. Pennsylvania, 2005.
(23) Piquemal, J.-Y.; Potvin, C.; Manoli, J.-M.; Djéga-Mariadassou, G., *Catal. Lett.* **2004**, 92, 189-195.
(24) Pielaszek, J.; Mierzwa, B.; Medjahdi, G.; Mareche, J. F.; Puricelli, S.; Celzard, A.; Furdin, G., *Appl. Catal. A-Gen.* **2005**, 296, 232-237.
(25) Liu, H. L.; Zhu, J. C.; Lai, Z. H.; Zhao, R. D.; He, D., *Scripta Mater.* **2009**, 60, 949-952.
(26) Kotarba, A.; Adamski, G.; Piskorz, W.; Sojka, Z.; Sayag, C.; Djega-Mariadassou, G., *J. Phys. Chem. B* **2004**, 108, 2885-2892.
(27) Xiang, M. L.; Li, D. B.; Xiao, H. C.; Zhang, J. L.; Li, W. H.; Zhong, B.; Sun, Y. H., *Catal. Today* **2008**, 131, 489-495.

(28) Xiang, M. L.; Li, D. B.; Li, W. H.; Zhong, B.; Sun, Y. H., *Fuel* **2006**, 85, 2662-2665.
(29) Bugyi, L.; Oszko, A.; Solymosi, F., *Surf. Sci.* **2000**, 461, 177-190.
(30) Bugyi, L.; Solymosi, F., *J. Phys. Chem. B* **2001**, 105, 4337-4342.
(31) King, D. A.; Woodruff, D. P., *The Chemical Physics of Solid Surfaces, Coadsorption, Promoters and Poisons*. Elsevier: Amsterdam, 1993; Vol. 6.
(32) Haider, M. A.; Gogate, M. R.; Davis, R. J., *J. Catal.* **2009**, 261, 9-16.
(33) Kitchin, J. R.; Norskov, J. K.; Barteau, M. A.; Chen, J. G., *Catal. Today* **2005**, 105, 66-73.
(34) Ren, J.; Huo, C. F.; Wang, J. G.; Li, Y. W.; Jiao, H. J., *Surf. Sci.* **2005**, 596, 212-221.
(35) Pistonesi, C.; Juan, A.; Farkas, A. P.; Solymosi, F., *Surf. Sci.* **2008**, 602, 2206-2211.
(36) Tominaga, H.; Nagai, M., *J. Phys. Chem. B* **2005**, 109, 20415-20423.
(37) Tominaga, H.; Nagai, M., *Appl. Catal. A-Gen.* **2007**, 328, 35-42.
(38) Tominaga, H.; Nagai, M., *Appl. Catal. A-Gen.* **2008**, 343, 95-103.
(39) Shi, X. R.; Wang, S. G.; Wang, H.; Deng, C. M.; Qin, Z. F.; Wang, J. G., *Surf. Sci.* **2009**, 603, 852-859.
(40) Linic, S.; Barteau, M. A., *J. Am. Chem. Soc.* **2004**, 126, 8086-8087.
(41) Liu, Z.-P.; Hu, P., *J. Am. Chem. Soc.* **2001**, 123, 12596-12604.
(42) Kresse, G.; Furthmuller, J., *Phys. Rev. B* **1996**, 54, 11169-11186.
(43) Kresse, G.; Hafner, J., *Phys. Rev. B* **1993**, 47, 558-561.
(44) Kresse, G.; Hafner, J., *J. Phys.: Condens. Matter* **1994**, 6, 8245-8257.
(45) Sholl, D. S.; Steckel, J. A., *Density functional theory : a practical introduction*. John Wiley & Sons, Inc.: Hoboken, NJ, 2009.
(46) Perdew, J. P.; Burke, K.; Ernzerhof, M., *Phys. Rev. Lett.* **1996**, 77, 3865-3868.
(47) Perdew, J. P.; Burke, K.; Ernzerhof, M., *Phys. Rev. Lett.* **1997**, 78, 1396-1396.
(48) Blöchl, P. E., *Phys. Rev. B* **1994**, 50, 17953.
(49) Kresse, G.; Joubert, D., *Phys. Rev. B* **1999**, 59, 1758-1775.
(50) Parthe, E.; Sadagopa, V., *Acta Crystallogr.* **1963**, 16, 202.
(51) Haines, J.; Leger, J. M.; Chateau, C.; Lowther, J. E., *J. Phys.-Condens. Mat.* **2001**, 13, 2447-2454.
(52) Siegel, D. J.; Hector, L. G.; Adams, J. B., *Surf. Sci.* **2002**, 498, 321-336.
(53) Rapcewicz, K.; Chen, B.; Yakobson, B.; Bernholc, J., *Phys. Rev. B* **1998**, 57, 7281-7291.
(54) Batyrev, I.; Alavi, A.; Finnis, M. W., *Faraday Discuss.* **1999**, 114, 33-43.
(55) Zhang, W.; Smith, J. R., *Phys. Rev. B* **2000**, 61, 16883-16889.
(56) Bengtsson, L., *Phys. Rev. B* **1999**, 59, 12301.
(57) Neugebauer, J.; Scheffler, M., *Phys. Rev. B* **1992**, 46, 16067.
(58) Wulff, G., *Z. Kryst. Mineral.* **1901**, 34, 449-530.
(59) Shi, H. Q.; Stampfl, C., *Phys. Rev. B* **2008**, 77, 094127.
(60) Soon, A.; Wong, L.; Delley, B.; Stampfl, C., *Phys. Rev. B* **2008**, 77, 125423.
(61) Kim, K. C.; Dai, B.; Johnson, J. K.; Sholl, D. S., *Nanotechnology* **2009**, 20, 204001.
(62) Šljivancanin, Ž.; Gothelf, K. V.; Hammer, B., *J. Am. Chem. Soc.* **2002**, 124, 14789-14794.

(63) Bhatia, B.; Sholl, D. S., *Angew. Chem. Int. Ed.* **2005**, 44, 7761-7764.
(64) Han, J. W.; Sholl, D. S., *Langmuir* **2009**, 25, 10737-10745.
(65) Henkelman, G.; Arnaldsson, A.; Jonsson, H., *Comp. Mater. Sci.* **2006**, 36, 354-360.
(66) Sanville, E.; Kenny, S. D.; Smith, R.; Henkelman, G., *J. Comput. Chem.* **2007**, 28, 899-908.
(67) Tang, W.; Sanville, E.; Henkelman, G., *J. Phys.-Condens. Mat.* **2009**, 21, 084204.
(68) Albano, E. V., *J. Chem. Phys.* **1986**, 85, 1044-1051.
(69) Berko, A.; Erley, W.; Sander, D., *J. Chem. Phys.* **1990**, 93, 8300-8305.
(70) Myli, K. B.; Grassian, V. H., *Langmuir* **1995**, 11, 849-852.
(71) Wu, W. C.; Wu, Z. L.; Liang, C. H.; Chen, X. W.; Ying, P. L.; Li, C., *J. Phys. Chem. B* **2003**, 107, 7088-7094.
(72) Kim, K. C.; Sholl, D. S., *J. Phys. Chem. C* **2010**, 114, 678-686.

Appendix 7.A: Coverage dependent adsorption energies of K for the six low Miller index surfaces

We assumed that the polarizability of adsorbed K is independent of the surface orientation and equal to the value deduced from K adsorption on (001), 12.63 $Å^3$. With this assumption the Albano model includes only two parameters (the adsorption energy in the limit of zero coverage and the static dipole moment of the K-Mo_2C surface bond in the limit of zero coverage), which we fitted for each surface from computed adsorption energies at three distinct coverages.

Figure 7.A.1: The adsorption energies of K at three distinct coverages on six Mo_2C surfaces as computed with DFT. The solid curves show fits of the data to the Albano model[68].

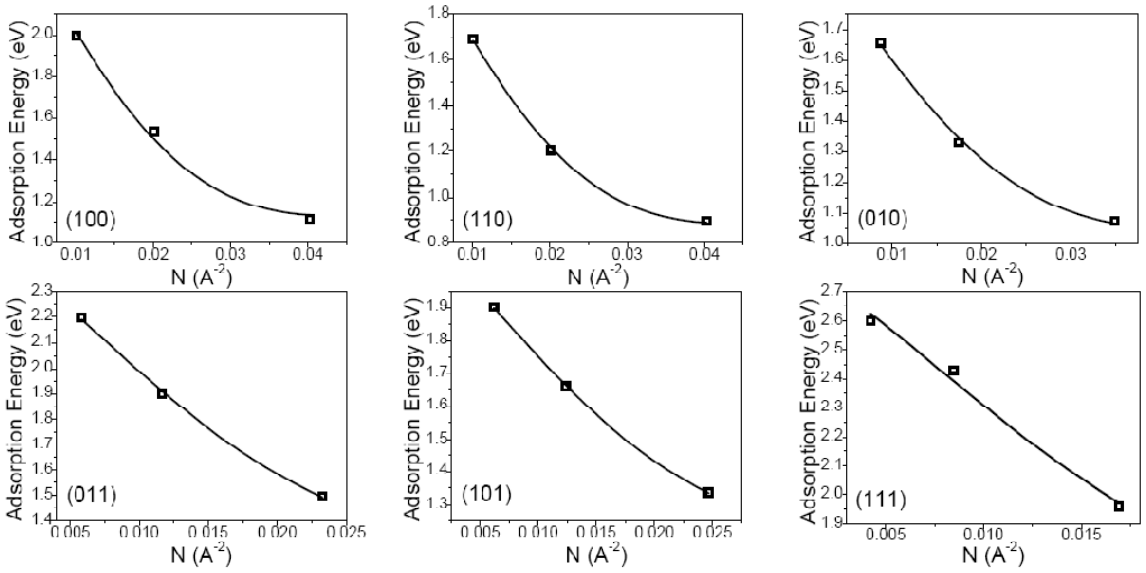

Appendix 7.B: Structural information for the optimized unreconstructed and reconstructed bare (001) surfaces

This appendix lists the coordinates for the most stable structures of unreconstructed and reconstructed bare (001) surfaces discussed in this Chapter. The coordinates for each surface are defined for a single supercell of a (2×2) surface unit cell with all coordinates in Å. A table defining unit cell vectors for supercell is also listed in Å.

Table 7.B.1: Unit cell vectors of supercell used for calculations in this Chapter. (in Å)

	x	y	z
a	10.536	6.072	0.000
b	0.000	12.143	0.000
c	0.000	0.000	22.296

Table 7.B.2: Coordinates for the optimized unreconstructed bare (001) surface. This configuration is shown in Fig. 7.5(a).

Atom	x	y	z	Atom	x	y	z	Atom	x	y	z
Mo	0.865	1.518	8.205	Mo	3.656	12.143	8.201	C	1.744	3.036	2.318
Mo	0.865	4.554	8.205	Mo	10.489	12.143	5.937	C	1.744	6.072	2.318
Mo	3.656	3.036	8.201	Mo	10.489	15.179	5.937	C	4.425	4.554	0.217
Mo	3.656	6.072	8.201	Mo	2.541	7.590	5.822	C	4.425	7.590	0.217
Mo	10.488	6.072	5.937	Mo	2.541	10.625	5.822	C	9.623	7.590	9.223
Mo	10.488	9.108	5.937	Mo	0.971	7.590	3.619	C	9.623	10.625	9.223
Mo	2.541	1.518	5.822	Mo	0.971	10.625	3.619	C	7.036	6.072	7.123
Mo	2.541	4.554	5.822	Mo	3.560	9.108	3.503	C	7.036	9.108	7.123
Mo	0.971	1.518	3.619	Mo	3.560	12.143	3.503	C	9.658	7.590	4.720
Mo	0.971	4.554	3.619	Mo	10.393	12.143	1.240	C	9.658	10.625	4.720
Mo	3.560	3.036	3.503	Mo	10.393	15.179	1.240	C	7.012	6.072	2.318
Mo	3.560	6.072	3.503	Mo	2.647	7.590	1.236	C	7.012	9.108	2.318
Mo	10.393	6.072	1.240	Mo	2.647	10.625	1.235	C	9.693	7.590	0.217
Mo	10.393	9.108	1.240	Mo	6.133	10.625	8.205	C	9.693	10.626	0.217
Mo	2.647	1.518	1.236	Mo	6.133	13.661	8.205	C	4.355	10.625	9.223
Mo	2.647	4.554	1.235	Mo	8.924	12.143	8.201	C	4.355	13.661	9.223
Mo	6.133	4.554	8.205	Mo	8.924	15.179	8.201	C	1.768	9.108	7.123
Mo	6.133	7.590	8.205	Mo	5.220	9.108	5.937	C	1.768	12.143	7.123
Mo	8.924	6.072	8.201	Mo	5.220	12.143	5.937	C	4.390	10.625	4.720
Mo	8.924	9.108	8.201	Mo	7.809	10.625	5.822	C	4.390	13.661	4.720
Mo	5.220	3.036	5.937	Mo	7.809	13.661	5.822	C	1.744	9.108	2.318
Mo	5.220	6.072	5.937	Mo	6.240	10.625	3.619	C	1.744	12.143	2.318
Mo	7.809	4.554	5.822	Mo	6.240	13.661	3.619	C	4.425	10.625	0.217
Mo	7.809	7.590	5.822	Mo	8.828	12.143	3.503	C	4.425	13.661	0.217
Mo	6.240	4.554	3.619	Mo	8.828	15.179	3.503	C	9.623	13.661	9.223
Mo	6.240	7.590	3.619	Mo	5.125	9.108	1.240	C	9.623	16.697	9.223
Mo	8.828	6.072	3.503	Mo	5.125	12.143	1.240	C	7.036	12.143	7.123
Mo	8.828	9.108	3.503	Mo	7.915	10.625	1.236	C	7.036	15.179	7.123
Mo	5.125	3.036	1.240	Mo	7.915	13.661	1.235	C	9.658	13.661	4.720

Mo	5.125	6.072	1.240	C	4.355	4.554	9.223	C	9.658	16.697	4.720
Mo	7.915	4.554	1.236	C	4.355	7.590	9.223	C	7.012	12.143	2.318
Mo	7.915	7.590	1.235	C	1.768	3.036	7.123	C	7.012	15.179	2.318
Mo	0.865	7.590	8.205	C	1.768	6.072	7.123	C	9.693	13.661	0.217
Mo	0.865	10.625	8.205	C	4.390	4.554	4.720	C	9.693	16.697	0.217
Mo	3.656	9.108	8.201	C	4.390	7.590	4.720				

Table 7.B.3: Coordinates for the optimized reconstructed bare (001) surface. This configuration is shown in Fig. 7.5(b).

Atom	x	y	z	Atom	x	y	z	Atom	x	y	z
Mo	0.810	1.518	8.114	Mo	3.774	12.112	8.366	C	1.878	3.035	2.376
Mo	1.190	4.554	8.420	Mo	0.105	6.095	5.958	C	1.878	6.072	2.376
Mo	3.774	3.067	8.366	Mo	0.106	9.084	5.958	C	4.557	4.554	0.284
Mo	3.774	6.040	8.366	Mo	2.777	7.590	5.975	C	4.553	7.590	0.276
Mo	0.106	12.167	5.958	Mo	2.685	10.625	5.887	C	8.163	7.590	9.461
Mo	0.105	3.012	5.958	Mo	1.100	7.590	3.673	C	9.786	10.625	9.324
Mo	2.777	13.661	5.975	Mo	1.117	10.625	3.685	C	7.206	6.079	7.190
Mo	2.685	4.554	5.887	Mo	3.695	9.106	3.551	C	7.206	9.100	7.189
Mo	1.100	1.518	3.673	Mo	3.695	12.145	3.551	C	9.783	7.589	4.778
Mo	1.117	4.554	3.685	Mo	10.534	12.142	1.299	C	9.819	10.625	4.763
Mo	3.695	3.034	3.551	Mo	10.534	15.180	1.299	C	7.146	6.072	2.376
Mo	3.695	6.074	3.551	Mo	2.790	7.590	1.306	C	7.146	9.108	2.377
Mo	10.534	6.070	1.299	Mo	2.779	10.625	1.299	C	9.825	7.590	0.284
Mo	10.534	9.109	1.299	Mo	6.078	10.625	8.114	C	9.820	10.625	0.276
Mo	2.790	13.661	1.306	Mo	6.458	13.661	8.420	C	2.895	10.625	9.461
Mo	2.779	4.554	1.299	Mo	9.042	12.175	8.366	C	4.518	13.661	9.324
Mo	6.077	4.554	8.114	Mo	9.042	15.148	8.366	C	1.938	9.115	7.189
Mo	6.458	7.590	8.420	Mo	5.374	9.131	5.958	C	1.938	12.136	7.189
Mo	9.042	6.103	8.366	Mo	5.374	12.119	5.958	C	4.514	10.625	4.777
Mo	9.042	9.076	8.366	Mo	8.044	10.625	5.974	C	4.551	13.661	4.763
Mo	5.374	15.203	5.958	Mo	7.953	13.661	5.888	C	1.878	9.107	2.376
Mo	5.374	6.048	5.958	Mo	6.368	10.625	3.674	C	1.878	12.144	2.376
Mo	8.045	16.697	5.975	Mo	6.385	13.661	3.685	C	4.557	10.625	0.284
Mo	7.953	7.589	5.888	Mo	8.963	12.142	3.551	C	4.553	13.661	0.276
Mo	6.368	4.554	3.673	Mo	8.963	15.181	3.551	C	8.163	13.661	9.461
Mo	6.385	7.590	3.685	Mo	5.266	9.106	1.300	C	9.786	16.697	9.324
Mo	8.963	6.070	3.551	Mo	5.266	12.144	1.300	C	7.206	12.151	7.189
Mo	8.963	9.109	3.551	Mo	8.058	10.625	1.307	C	7.206	15.172	7.190
Mo	5.266	3.035	1.300	Mo	8.048	13.661	1.299	C	9.783	13.661	4.778
Mo	5.266	6.073	1.300	C	2.895	4.554	9.460	C	9.819	16.697	4.763
Mo	8.058	16.697	1.307	C	4.518	7.590	9.324	C	7.146	12.143	2.377
Mo	8.048	7.590	1.299	C	1.938	3.043	7.189	C	7.146	15.179	2.376
Mo	0.810	7.589	8.114	C	1.938	6.064	7.189	C	9.825	13.661	0.284
Mo	1.190	10.625	8.419	C	4.514	4.554	4.777	C	9.820	16.697	0.276
Mo	3.774	9.139	8.366	C	4.551	7.590	4.763				

Appendix 7.C: Structural information for K adsorption in the most stable states on both the unreconstructed and reconstructed (001) surfaces

This appendix lists the coordinates for the most stable structures of K adsorption on both the unreconstructed and reconstructed (001) surfaces discussed in this Chapter. The coordinates for the adsorbate are defined for a single supercell of a (2×2) surface unit cell with all coordinates in Å. The shaded sections of the table give the coordinates of the adsorbate; all other coordinates define the portion of the surface atoms.

Table 7.C.1: Coordinates for the most stable K adsorbed on unreconstructed Mo_2C (001). This configuration is shown in Fig. 7.6(a).

Atom	x	y	z	Atom	x	y	z	Atom	x	y	z
K	6.430	9.107	11.402	Mo	3.664	9.107	8.269	C	4.408	7.587	4.717
Mo	0.874	1.514	8.208	Mo	3.675	12.123	8.233	C	1.760	3.036	2.317
Mo	0.874	4.558	8.208	Mo	10.509	12.144	5.941	C	1.761	6.072	2.317
Mo	3.679	3.036	8.196	Mo	10.509	15.179	5.945	C	4.438	4.553	0.211
Mo	3.675	6.092	8.233	Mo	2.563	7.588	5.823	C	4.443	7.589	0.211
Mo	10.509	6.071	5.941	Mo	2.563	10.627	5.824	C	9.626	7.593	9.242
Mo	10.511	9.108	5.936	Mo	0.992	7.589	3.620	C	9.627	10.622	9.243
Mo	2.557	1.518	5.826	Mo	0.992	10.626	3.620	C	7.062	6.064	7.105
Mo	2.557	4.554	5.826	Mo	3.580	9.108	3.498	C	7.065	9.108	7.084
Mo	0.991	1.518	3.620	Mo	3.579	12.144	3.497	C	9.681	7.588	4.717
Mo	0.991	4.553	3.620	Mo	10.412	12.145	1.232	C	9.681	10.627	4.717
Mo	3.577	3.036	3.498	Mo	10.412	15.179	1.229	C	7.029	6.071	2.313
Mo	3.579	6.071	3.497	Mo	2.664	7.590	1.233	C	7.028	9.108	2.312
Mo	10.412	6.070	1.232	Mo	2.664	10.625	1.233	C	9.712	7.589	0.212
Mo	10.411	9.108	1.235	Mo	6.158	10.622	8.167	C	9.712	10.626	0.212
Mo	2.661	13.662	1.231	Mo	6.153	13.652	8.200	C	4.435	10.612	9.273
Mo	2.661	4.554	1.231	Mo	8.939	12.147	8.210	C	4.359	13.654	9.226
Mo	6.153	4.563	8.200	Mo	8.940	15.179	8.204	C	1.800	9.108	7.117
Mo	6.158	7.593	8.167	Mo	5.225	9.108	5.937	C	1.794	12.143	7.128
Mo	8.939	6.069	8.210	Mo	5.232	12.150	5.935	C	4.408	10.628	4.717
Mo	8.928	9.108	8.218	Mo	7.828	10.634	5.802	C	4.405	13.663	4.715
Mo	5.236	3.036	5.934	Mo	7.828	13.669	5.817	C	1.761	9.108	2.318
Mo	5.232	6.065	5.935	Mo	6.258	10.626	3.617	C	1.761	12.143	2.317
Mo	7.828	4.546	5.817	Mo	6.258	13.661	3.616	C	4.443	10.626	0.211
Mo	7.828	7.581	5.802	Mo	8.849	12.148	3.499	C	4.438	13.662	0.211
Mo	6.258	4.554	3.616	Mo	8.850	15.179	3.498	C	9.649	13.660	9.228
Mo	6.258	7.589	3.617	Mo	5.139	9.108	1.235	C	9.648	16.698	9.228
Mo	8.849	6.067	3.499	Mo	5.140	12.145	1.234	C	7.062	12.151	7.105
Mo	8.848	9.108	3.498	Mo	7.935	10.625	1.232	C	7.050	15.179	7.129
Mo	5.141	3.036	1.235	Mo	7.932	13.661	1.232	C	9.680	13.663	4.721
Mo	5.140	6.070	1.234	C	4.359	4.561	9.226	C	9.680	16.695	4.721
Mo	7.932	16.697	1.232	C	4.435	7.603	9.273	C	7.029	12.144	2.313
Mo	7.935	7.590	1.233	C	1.786	3.036	7.137	C	7.030	15.179	2.315
Mo	0.892	7.592	8.207	C	1.794	6.072	7.127	C	9.708	13.662	0.209
Mo	0.892	10.623	8.208	C	4.405	4.552	4.715	C	9.708	16.697	0.209

Table 7.C.2: Coordinates for the most stable K adsorbed on reconstructed Mo_2C (001). This configuration is shown in Fig. 7.6(b).

Atom	x	y	z	Atom	x	y	z	Atom	x	y	z
K	8.139	10.625	11.663	Mo	3.778	9.140	8.391	C	4.558	7.586	4.776
Mo	0.813	1.514	8.122	Mo	3.778	12.110	8.391	C	1.888	3.035	2.392
Mo	1.203	4.554	8.432	Mo	0.117	6.095	5.968	C	1.888	6.073	2.392
Mo	3.778	3.063	8.384	Mo	0.113	9.086	5.974	C	4.569	4.554	0.297
Mo	3.778	6.045	8.384	Mo	2.786	7.591	5.992	C	4.561	7.589	0.286
Mo	0.113	12.165	5.974	Mo	2.697	10.625	5.904	C	8.175	7.622	9.493
Mo	0.117	3.013	5.968	Mo	1.107	7.591	3.688	C	9.796	10.625	9.356
Mo	2.786	13.660	5.992	Mo	1.126	10.626	3.700	C	7.212	6.080	7.217
Mo	2.691	4.554	5.900	Mo	3.701	9.105	3.565	C	7.213	9.101	7.188
Mo	1.107	1.517	3.688	Mo	3.701	12.146	3.565	C	9.789	7.588	4.792
Mo	1.129	4.554	3.700	Mo	0.010	6.069	1.311	C	9.829	10.626	4.773
Mo	3.705	3.036	3.568	Mo	0.007	9.110	1.313	C	7.155	6.070	2.390
Mo	3.705	6.072	3.568	Mo	2.801	7.589	1.323	C	7.154	9.107	2.387
Mo	0.007	12.141	1.313	Mo	2.792	10.626	1.316	C	9.840	7.590	0.295
Mo	0.010	3.038	1.311	Mo	6.063	10.626	8.101	C	9.831	10.626	0.286
Mo	2.801	13.662	1.323	Mo	6.463	13.645	8.436	C	2.890	10.625	9.487
Mo	2.792	4.554	1.316	Mo	9.041	12.168	8.367	C	4.531	13.664	9.349
Mo	6.077	4.554	8.130	Mo	9.041	15.145	8.393	C	1.947	9.115	7.205
Mo	6.463	7.606	8.435	Mo	5.382	9.127	5.963	C	1.947	12.136	7.205
Mo	9.041	6.106	8.393	Mo	5.382	12.124	5.963	C	4.520	10.626	4.787
Mo	9.041	9.083	8.367	Mo	8.053	10.625	5.980	C	4.558	13.665	4.776
Mo	5.385	15.200	5.976	Mo	7.961	13.667	5.900	C	1.885	9.107	2.390
Mo	5.385	6.051	5.976	Mo	6.376	10.626	3.685	C	1.885	12.144	2.390
Mo	8.059	16.697	6.005	Mo	6.394	13.663	3.697	C	4.569	10.626	0.294
Mo	7.961	7.584	5.900	Mo	8.971	12.143	3.564	C	4.561	13.662	0.286
Mo	6.378	4.554	3.692	Mo	8.971	15.183	3.567	C	8.175	13.629	9.493
Mo	6.394	7.589	3.697	Mo	5.276	9.105	1.309	C	9.784	16.697	9.349
Mo	8.971	6.069	3.567	Mo	5.276	12.146	1.309	C	7.213	12.150	7.188
Mo	8.971	9.108	3.564	Mo	8.069	10.626	1.320	C	7.212	15.171	7.217
Mo	5.276	15.178	1.313	Mo	8.062	13.662	1.315	C	9.789	13.663	4.792
Mo	5.276	6.073	1.313	C	2.897	4.554	9.479	C	9.827	16.697	4.779
Mo	8.069	16.697	1.322	C	4.531	7.587	9.349	C	7.154	12.144	2.387
Mo	8.062	7.589	1.315	C	1.945	3.041	7.203	C	7.155	15.181	2.390
Mo	0.813	7.594	8.122	C	1.945	6.066	7.203	C	9.840	13.661	0.295
Mo	1.194	10.625	8.435	C	4.524	4.554	4.798	C	9.829	16.697	0.286

Appendix 7.D: Structural information for H adsorption in the most stable states on both the unreconstructed and reconstructed (001) surface

Similar to Appendix 7.C but for H.

Table 7.D.1: Coordinates for the most stable H adsorbed on unreconstructed Mo_2C (001). This configuration is shown in Fig. 7.7(a).

Atom	x	y	z	Atom	x	y	z	Atom	x	y	z
H	9.752	10.651	10.674	Mo	3.667	9.144	8.211	C	4.413	7.613	4.708
Mo	0.902	1.532	8.242	Mo	3.673	12.118	8.198	C	1.818	3.051	2.349
Mo	0.713	4.568	8.080	Mo	-0.005	6.059	5.909	C	1.817	6.079	2.358
Mo	3.705	3.018	8.173	Mo	10.522	15.217	5.957	C	4.431	4.568	0.285
Mo	3.699	6.119	8.185	Mo	2.532	7.602	5.829	C	4.478	7.605	0.283
Mo	-0.010	12.126	5.957	Mo	2.636	10.637	5.918	C	9.597	7.650	9.166
Mo	-0.006	3.070	5.912	Mo	1.008	7.602	3.627	C	9.779	10.637	9.577
Mo	2.533	1.528	5.840	Mo	1.078	10.637	3.636	C	7.044	6.071	7.149
Mo	2.602	4.563	5.907	Mo	3.613	9.147	3.537	C	7.063	9.149	7.089
Mo	1.000	1.532	3.619	Mo	3.611	12.126	3.536	C	9.692	7.593	4.717
Mo	1.091	4.560	3.663	Mo	10.445	12.130	1.292	C	9.706	10.637	4.729
Mo	3.607	3.076	3.545	Mo	10.455	15.199	1.292	C	7.062	6.104	2.346
Mo	3.609	6.050	3.545	Mo	2.672	7.604	1.228	C	7.047	9.102	2.352
Mo	10.451	6.075	1.299	Mo	2.608	10.634	1.155	C	9.732	7.609	0.311
Mo	10.439	9.143	1.298	Mo	6.275	10.638	8.299	C	9.675	10.638	0.249
Mo	2.684	13.667	1.233	Mo	6.166	13.644	8.221	C	4.467	10.631	9.216
Mo	2.621	4.567	1.199	Mo	8.923	12.050	8.251	C	4.412	13.660	9.219
Mo	6.155	4.561	8.246	Mo	8.965	15.152	8.120	C	1.785	9.098	7.122
Mo	6.169	7.628	8.214	Mo	5.231	9.095	5.972	C	1.785	12.174	7.130
Mo	8.964	6.112	8.119	Mo	5.230	12.178	5.970	C	4.444	10.636	4.760
Mo	8.920	9.234	8.260	Mo	7.804	10.637	5.826	C	4.414	13.658	4.704
Mo	5.244	15.151	5.957	Mo	7.873	13.676	5.850	C	1.825	9.137	2.347
Mo	5.242	6.120	5.959	Mo	6.265	10.637	3.631	C	1.823	12.134	2.344
Mo	7.788	4.563	5.846	Mo	6.318	13.674	3.638	C	4.407	10.631	0.246
Mo	7.868	7.595	5.846	Mo	8.856	12.108	3.499	C	4.495	13.665	0.290
Mo	6.270	4.564	3.630	Mo	8.870	15.232	3.516	C	9.616	13.619	9.166
Mo	6.317	7.599	3.645	Mo	5.152	9.144	1.296	C	9.625	16.707	9.156
Mo	8.872	6.039	3.518	Mo	5.150	12.117	1.301	C	7.061	12.126	7.088
Mo	8.859	9.166	3.499	Mo	7.932	10.634	1.245	C	7.045	15.195	7.147
Mo	5.139	3.063	1.332	Mo	7.909	13.670	1.215	C	9.695	13.681	4.712
Mo	5.142	6.073	1.327	C	4.344	4.566	9.191	C	9.713	16.707	4.714
Mo	7.959	16.711	1.264	C	4.429	7.611	9.229	C	7.048	12.171	2.343
Mo	7.902	7.603	1.216	C	1.794	3.029	7.155	C	7.062	15.169	2.337
Mo	0.923	7.597	8.249	C	1.797	6.101	7.144	C	9.736	13.664	0.306
Mo	0.880	10.635	8.211	C	4.441	4.564	4.787	C	9.711	16.707	0.258

Table 7.D.2: Coordinates for the most stable H adsorbed on reconstructed Mo_2C (001). This configuration is shown in Fig. 7.7(b).

Atom	x	y	z	Atom	x	y	z	Atom	x	y	z
H	8.212	13.661	10.670	Mo	3.776	9.133	8.367	C	4.560	7.590	4.771
Mo	0.816	1.518	8.115	Mo	3.775	12.105	8.363	C	1.889	3.034	2.384
Mo	1.200	4.554	8.417	Mo	0.114	6.096	5.957	C	1.887	6.072	2.386
Mo	3.775	3.075	8.363	Mo	0.114	9.083	5.957	C	4.568	4.553	0.284
Mo	3.776	6.046	8.367	Mo	2.784	7.590	5.980	C	4.563	7.590	0.277
Mo	0.113	0.023	5.963	Mo	2.694	10.625	5.891	C	8.182	7.590	9.457
Mo	0.113	3.013	5.963	Mo	1.106	7.590	3.679	C	9.780	10.647	9.328
Mo	2.782	13.661	5.975	Mo	1.126	10.627	3.690	C	7.213	6.077	7.195
Mo	2.694	4.555	5.891	Mo	3.706	9.106	3.557	C	7.213	9.102	7.195
Mo	1.109	1.518	3.681	Mo	3.704	12.143	3.560	C	9.790	7.590	4.782
Mo	1.126	4.553	3.690	Mo	0.009	6.071	1.303	C	9.826	10.625	4.766
Mo	3.704	3.036	3.560	Mo	0.009	9.108	1.303	C	7.154	6.069	2.383
Mo	3.706	6.074	3.557	Mo	2.805	7.590	1.320	C	7.154	9.110	2.383
Mo	0.010	-0.001	1.302	Mo	2.793	10.624	1.309	C	9.834	7.590	0.287
Mo	0.010	3.037	1.302	Mo	6.081	10.630	8.118	C	9.835	10.625	0.279
Mo	2.798	13.661	1.313	Mo	6.424	13.661	8.427	C	2.900	10.626	9.459
Mo	2.793	4.555	1.309	Mo	9.053	12.157	8.370	C	4.566	13.661	9.313
Mo	6.080	4.549	8.118	Mo	9.053	15.166	8.370	C	1.941	9.111	7.194
Mo	6.461	7.590	8.417	Mo	5.384	9.129	5.963	C	1.944	12.137	7.191
Mo	9.040	6.105	8.364	Mo	5.382	12.125	5.971	C	4.525	10.627	4.789
Mo	9.040	9.074	8.364	Mo	8.060	10.630	5.991	C	4.559	13.661	4.768
Mo	5.382	15.198	5.971	Mo	7.957	13.661	5.885	C	1.887	9.107	2.385
Mo	5.384	6.050	5.963	Mo	6.376	10.627	3.677	C	1.889	12.145	2.384
Mo	8.060	16.692	5.991	Mo	6.393	13.661	3.689	C	4.568	10.626	0.284
Mo	7.961	7.590	5.888	Mo	8.969	12.141	3.552	C	4.560	13.661	0.278
Mo	6.376	4.552	3.677	Mo	8.969	15.182	3.552	C	8.184	13.661	9.571
Mo	6.392	7.590	3.687	Mo	5.278	9.107	1.299	C	9.780	16.675	9.328
Mo	8.971	6.069	3.555	Mo	5.275	12.145	1.300	C	7.214	12.154	7.197
Mo	8.971	9.110	3.555	Mo	8.070	10.625	1.311	C	7.215	15.169	7.197
Mo	5.275	3.034	1.300	Mo	8.060	13.661	1.304	C	9.786	13.661	4.779
Mo	5.278	6.073	1.299	C	2.900	4.554	9.459	C	9.826	16.697	4.766
Mo	8.070	16.698	1.311	C	4.533	7.590	9.328	C	7.153	12.142	2.378
Mo	8.063	7.590	1.307	C	1.944	3.042	7.191	C	7.153	15.180	2.378
Mo	0.812	7.590	8.117	C	1.941	6.068	7.194	C	9.835	13.661	0.286
Mo	1.200	10.625	8.417	C	4.525	4.553	4.789	C	9.835	16.698	0.279

Appendix 7.E: Structural information for CO adsorption in the most stable states on both the unreconstructed and reconstructed (001) surface

Similar to Appendix 7.C but for CO.

Table 7.E.1: Coordinates for the most stable H adsorbed on unreconstructed Mo_2C (001). This configuration is shown in Fig. 7.8(a).

Atom	x	y	z	Atom	x	y	z	Atom	x	y	z
C	9.733	16.697	0.233	Mo	0.916	7.582	8.219	C	4.445	4.554	4.745
O	9.865	10.625	12.143	Mo	0.937	10.625	8.222	C	4.447	7.595	4.749
				Mo	3.688	9.128	8.237	C	1.801	3.034	2.335
				Mo	3.688	12.122	8.237	C	1.801	6.074	2.335
Mo	0.916	1.526	8.219	Mo	0.006	6.069	5.934	C	4.479	4.554	0.226
Mo	0.774	4.554	8.143	Mo	0.002	9.112	5.950	C	4.485	7.591	0.230
Mo	3.709	3.011	8.231	Mo	2.589	7.584	5.829	C	9.620	7.639	9.210
Mo	3.709	6.096	8.231	Mo	2.615	10.625	5.847	C	9.725	10.626	9.654
Mo	0.002	12.139	5.950	Mo	1.029	7.591	3.635	C	7.096	6.070	7.154
Mo	0.006	3.039	5.934	Mo	1.030	10.625	3.633	C	7.125	9.109	7.122
Mo	2.589	1.523	5.830	Mo	3.620	9.110	3.521	C	9.714	7.583	4.719
Mo	2.602	4.554	5.848	Mo	3.620	12.141	3.521	C	9.715	10.625	4.718
Mo	1.029	1.516	3.635	Mo	10.450	12.142	1.255	C	7.061	6.074	2.330
Mo	1.037	4.554	3.640	Mo	10.456	15.183	1.250	C	7.062	9.105	2.327
Mo	3.623	3.035	3.519	Mo	2.709	7.589	1.254	C	9.753	7.590	0.235
Mo	3.623	6.072	3.519	Mo	2.701	10.625	1.248	C	9.746	10.626	0.230
Mo	10.456	6.068	1.250	Mo	6.255	10.625	8.233	C	9.785	10.625	10.970
Mo	10.450	9.109	1.255	Mo	6.203	13.648	8.223	C	4.475	10.625	9.229
Mo	2.709	13.662	1.254	Mo	8.970	12.060	8.256	C	4.443	13.649	9.236
Mo	2.708	4.554	1.259	Mo	8.994	15.172	8.191	C	1.814	9.100	7.120
Mo	6.171	4.554	8.224	Mo	5.284	9.112	5.968	C	1.814	12.151	7.120
Mo	6.203	7.603	8.223	Mo	5.284	12.139	5.968	C	4.453	10.625	4.744
Mo	8.994	6.079	8.191	Mo	7.870	10.625	5.820	C	4.447	13.656	4.749
Mo	8.970	9.191	8.256	Mo	7.882	13.669	5.837	C	1.805	9.111	2.333
Mo	5.275	15.180	5.963	Mo	6.288	10.625	3.627	C	1.805	12.140	2.333
Mo	5.275	6.071	5.963	Mo	6.294	13.661	3.633	C	4.481	10.625	0.225
Mo	7.857	4.554	5.839	Mo	8.881	12.143	3.505	C	4.485	13.660	0.230
Mo	7.882	7.582	5.837	Mo	8.880	15.187	3.508	C	9.620	13.612	9.210
Mo	6.286	4.554	3.628	Mo	5.176	9.111	1.253	C	9.693	16.697	9.219
Mo	6.294	7.590	3.633	Mo	5.176	12.140	1.253	C	7.125	12.142	7.122
Mo	8.880	6.064	3.508	Mo	7.971	10.625	1.246	C	7.096	15.181	7.154
Mo	8.881	9.108	3.505	Mo	7.969	13.662	1.247	C	9.714	13.668	4.719
Mo	5.176	3.037	1.252	C	4.370	4.554	9.234	C	9.710	16.697	4.729
Mo	5.176	6.070	1.252	C	4.444	7.602	9.236	C	7.062	12.146	2.327
Mo	7.966	16.697	1.248	C	1.823	3.041	7.155	C	7.061	15.177	2.330
Mo	7.969	7.589	1.247	C	1.823	6.067	7.155	C	9.753	13.661	0.235

Table 7.E.2: Coordinates for the most stable H adsorbed on reconstructed Mo_2C (001). This configuration is shown in Fig. 7.8(b).

Atom	x	y	z	Atom	x	y	z	Atom	x	y	z
C	8.285	13.661	10.957	Mo	0.830	7.590	8.122	C	4.524	4.550	4.784
O	8.342	13.660	12.126	Mo	1.206	10.630	8.411	C	4.555	7.590	4.765
				Mo	3.775	9.131	8.357	C	1.885	3.036	2.380
				Mo	3.775	12.106	8.352	C	1.882	6.074	2.384
Mo	0.818	1.518	8.110	Mo	0.103	6.096	5.974	C	4.563	4.551	0.280
Mo	1.206	4.549	8.411	Mo	0.103	9.083	5.974	C	4.559	7.590	0.272
Mo	3.775	3.074	8.352	Mo	2.785	7.590	5.974	C	8.188	7.590	9.444
Mo	3.775	6.048	8.357	Mo	2.689	10.623	5.881	C	9.786	10.646	9.316
Mo	0.113	12.169	5.956	Mo	1.104	7.590	3.674	C	7.208	6.076	7.186
Mo	0.113	3.011	5.956	Mo	1.119	10.627	3.686	C	7.208	9.103	7.186
Mo	2.775	13.661	5.961	Mo	3.703	9.108	3.550	C	9.786	7.590	4.776
Mo	2.689	4.556	5.881	Mo	3.699	12.141	3.555	C	9.823	10.625	4.763
Mo	1.107	1.518	3.676	Mo	0.006	6.074	1.296	C	7.150	6.068	2.376
Mo	1.119	4.552	3.686	Mo	0.006	9.105	1.296	C	7.150	9.111	2.376
Mo	3.699	3.038	3.555	Mo	2.804	7.590	1.317	C	9.833	7.590	0.281
Mo	3.703	6.071	3.550	Mo	2.790	10.621	1.306	C	9.835	10.627	0.274
Mo	0.007	12.141	1.296	Mo	6.082	10.629	8.117	C	2.907	10.625	9.450
Mo	0.007	3.038	1.296	Mo	6.404	13.661	8.424	C	4.556	13.661	9.307
Mo	2.797	13.661	1.310	Mo	9.053	12.128	8.344	C	1.938	9.110	7.193
Mo	2.790	4.558	1.306	Mo	9.053	15.194	8.344	C	1.943	12.138	7.183
Mo	6.082	4.550	8.117	Mo	5.382	9.128	5.956	C	4.524	10.629	4.784
Mo	6.459	7.590	8.407	Mo	5.372	12.124	5.973	C	4.553	13.661	4.764
Mo	9.035	6.106	8.352	Mo	8.062	10.635	5.994	C	1.882	9.105	2.384
Mo	9.035	9.073	8.352	Mo	7.950	13.661	5.876	C	1.885	12.143	2.380
Mo	5.372	15.199	5.973	Mo	6.374	10.627	3.669	C	4.563	10.629	0.280
Mo	5.382	6.051	5.956	Mo	6.389	13.661	3.692	C	4.557	13.661	0.275
Mo	8.062	16.687	5.994	Mo	8.964	12.144	3.554	C	8.212	13.661	9.632
Mo	7.956	7.590	5.879	Mo	8.964	15.178	3.554	C	9.787	16.677	9.316
Mo	6.374	4.553	3.669	Mo	5.276	9.108	1.292	C	7.200	12.157	7.192
Mo	6.382	7.590	3.676	Mo	5.274	12.145	1.296	C	7.200	15.166	7.192
Mo	8.968	6.070	3.548	Mo	8.069	10.627	1.308	C	9.788	13.661	4.786
Mo	8.968	9.109	3.548	Mo	8.055	13.661	1.303	C	9.823	16.697	4.763
Mo	5.274	15.178	1.296	C	2.907	4.554	9.450	C	7.150	12.142	2.377
Mo	5.276	6.072	1.292	C	4.537	7.590	9.320	C	7.150	15.181	2.377
Mo	8.069	16.696	1.308	C	1.943	3.042	7.183	C	9.823	13.661	0.281
Mo	8.064	7.590	1.302	C	1.938	6.069	7.193	C	9.835	16.695	0.274

Appendix 7.F: Structural information for H and CO coadsorption with K promoter in the most stable states on reconstructed (001) surface

Similar to Appendix 7.C but for H/K and H/CO coadsorption only on reconstructed (001) surface.

Table 7.F.1: Coordinates for the most stable H coadsorbed with K promoter on reconstructed Mo_2C (001). This configuration is shown in Fig. 7.9(a).

Atom	x	y	z	Atom	x	y	z	Atom	x	y	z
K	8.088	10.625	11.614	Mo	0.808	7.600	8.118	C	4.526	4.554	4.796
				Mo	1.150	10.625	8.438	C	4.557	7.586	4.773
H	2.912	10.625	10.689	Mo	3.785	9.124	8.392	C	1.890	3.033	2.392
				Mo	3.785	12.127	8.393	C	1.890	6.074	2.392
Mo	0.808	1.507	8.118	Mo	0.121	6.092	5.966	C	4.571	4.554	0.293
Mo	1.199	4.554	8.424	Mo	0.115	9.090	5.979	C	4.567	7.588	0.283
Mo	3.768	3.066	8.376	Mo	2.795	7.595	6.003	C	8.173	7.622	9.486
Mo	3.768	6.042	8.376	Mo	2.695	10.625	5.896	C	9.807	10.625	9.349
Mo	0.115	12.161	5.979	Mo	1.108	7.593	3.684	C	7.213	6.080	7.213
Mo	0.121	3.015	5.966	Mo	1.128	10.626	3.698	C	7.209	9.103	7.185
Mo	2.795	13.656	6.003	Mo	3.701	9.103	3.558	C	9.795	7.587	4.795
Mo	2.691	4.554	5.894	Mo	3.701	12.148	3.558	C	9.831	10.625	4.775
Mo	1.108	1.515	3.684	Mo	0.014	6.071	1.303	C	7.159	6.070	2.392
Mo	1.128	4.554	3.694	Mo	0.009	9.110	1.304	C	7.156	9.107	2.390
Mo	3.707	3.035	3.565	Mo	2.805	7.588	1.320	C	9.839	7.590	0.288
Mo	3.707	6.073	3.565	Mo	2.796	10.626	1.313	C	9.835	10.626	0.281
Mo	0.009	-0.002	1.304	Mo	6.058	10.625	8.097	C	4.519	13.644	9.346
Mo	0.014	3.037	1.303	Mo	6.465	13.643	8.427	C	1.951	9.119	7.208
Mo	2.805	13.663	1.320	Mo	9.036	12.162	8.360	C	1.951	12.132	7.208
Mo	2.799	4.554	1.315	Mo	9.036	15.136	8.387	C	4.518	10.626	4.781
Mo	6.080	4.554	8.125	Mo	5.383	9.128	5.956	C	4.557	13.665	4.773
Mo	6.465	7.608	8.427	Mo	5.383	12.123	5.956	C	1.885	9.107	2.385
Mo	9.036	6.115	8.387	Mo	8.054	10.625	5.978	C	1.885	12.144	2.385
Mo	9.036	9.089	8.360	Mo	7.965	13.668	5.897	C	4.571	10.626	0.289
Mo	5.387	15.200	5.975	Mo	6.376	10.626	3.682	C	4.567	13.663	0.283
Mo	5.387	6.051	5.975	Mo	6.396	13.664	3.695	C	8.173	13.629	9.486
Mo	8.059	16.697	5.998	Mo	8.977	12.143	3.561	C	9.825	16.697	9.332
Mo	7.965	7.583	5.897	Mo	8.974	15.181	3.566	C	7.209	12.148	7.185
Mo	6.380	4.554	3.693	Mo	5.279	9.106	1.305	C	7.213	15.171	7.213
Mo	6.396	7.588	3.695	Mo	5.279	12.145	1.305	C	9.795	13.664	4.795
Mo	8.974	6.070	3.566	Mo	8.077	10.626	1.326	C	9.827	16.697	4.775
Mo	8.977	9.108	3.561	Mo	8.066	13.661	1.317	C	7.156	12.144	2.390
Mo	5.281	3.034	1.309	C	2.913	4.554	9.470	C	7.159	15.181	2.392
Mo	5.281	6.073	1.309	C	4.519	7.607	9.346	C	9.839	13.661	0.288
Mo	8.070	16.697	1.322	C	1.944	3.040	7.204	C	9.830	16.697	0.281
Mo	8.066	7.591	1.317	C	1.944	6.067	7.204	C	2.894	10.625	9.590

Table 7.F.2: Coordinates for the most stable CO coadsorbed with K promoter on reconstructed Mo_2C (001). This configuration is shown in Fig. 7.9(b).

Atom	x	y	z	Atom	x	y	z	Atom	x	y	z
K	8.003	10.624	11.573	Mo	0.818	7.598	8.124	C	1.939	6.068	7.196
				Mo	1.135	10.626	8.438	C	4.517	4.554	4.791
C	3.108	10.625	10.968	Mo	3.794	9.096	8.365	C	4.552	7.586	4.771
O	3.280	10.625	12.134	Mo	3.794	12.155	8.366	C	1.881	3.031	2.386
Mo	0.818	1.509	8.124	Mo	0.117	6.092	5.961	C	1.881	6.076	2.386
Mo	1.203	4.554	8.417	Mo	0.105	9.089	5.985	C	4.566	4.554	0.290
Mo	3.767	3.065	8.361	Mo	2.797	7.601	6.008	C	4.565	7.590	0.282
Mo	3.767	6.043	8.361	Mo	2.687	10.626	5.889	C	8.188	7.619	9.473
Mo	0.105	12.162	5.985	Mo	1.104	7.591	3.679	C	9.813	10.625	9.342
Mo	0.117	3.015	5.961	Mo	1.121	10.626	3.706	C	7.211	6.079	7.205
Mo	2.797	13.650	6.008	Mo	3.692	9.107	3.562	C	7.207	9.106	7.185
Mo	2.681	4.554	5.885	Mo	3.692	12.144	3.562	C	9.792	7.584	4.793
Mo	1.104	1.516	3.679	Mo	0.006	6.073	1.299	C	9.826	10.626	4.770
Mo	1.115	4.554	3.684	Mo	0.002	9.109	1.304	C	7.151	6.071	2.390
Mo	3.700	3.035	3.559	Mo	2.799	7.590	1.318	C	7.147	9.109	2.391
Mo	3.700	6.073	3.559	Mo	2.784	10.626	1.314	C	9.830	7.586	0.285
Mo	0.002	-0.001	1.304	Mo	6.073	10.626	8.102	C	9.827	10.626	0.280
Mo	0.006	3.035	1.299	Mo	6.478	13.647	8.423	C	4.530	13.648	9.332
Mo	2.799	13.661	1.318	Mo	9.040	12.158	8.347	C	1.936	9.122	7.208
Mo	2.796	4.554	1.312	Mo	9.041	15.139	8.372	C	1.937	12.129	7.208
Mo	6.087	4.554	8.122	Mo	5.372	9.128	5.970	C	4.515	10.626	4.788
Mo	6.478	7.604	8.423	Mo	5.372	12.123	5.970	C	4.552	13.665	4.771
Mo	9.041	6.112	8.372	Mo	8.054	10.625	5.970	C	1.877	9.106	2.386
Mo	9.040	9.093	8.347	Mo	7.958	13.666	5.888	C	1.877	12.145	2.386
Mo	5.385	15.203	5.969	Mo	6.371	10.626	3.680	C	4.549	10.626	0.287
Mo	5.385	6.048	5.969	Mo	6.385	13.664	3.693	C	4.565	13.661	0.282
Mo	8.048	16.697	5.980	Mo	8.970	12.146	3.557	C	8.189	13.632	9.473
Mo	7.958	7.585	5.888	Mo	8.966	15.179	3.565	C	7.207	12.145	7.185
Mo	6.375	4.554	3.690	Mo	5.271	9.111	1.302	C	7.211	15.172	7.205
Mo	6.385	7.587	3.693	Mo	5.271	12.140	1.302	C	9.792	13.667	4.793
Mo	8.966	6.072	3.565	Mo	8.071	10.626	1.326	C	9.820	16.697	4.776
Mo	8.970	9.105	3.557	Mo	8.058	13.657	1.316	C	7.147	12.142	2.391
Mo	5.273	15.177	1.306	C	9.815	16.697	9.326	C	7.151	15.180	2.390
Mo	5.273	6.074	1.306	C	2.925	4.554	9.457	C	9.830	13.665	0.285
Mo	8.065	16.697	1.322	C	4.530	7.603	9.332	C	9.822	16.697	0.281
Mo	8.058	7.594	1.316	C	1.939	3.040	7.196	C	2.921	10.625	9.661

CHAPTER 8

CONCLUSIONS

This thesis has presented DFT calculations that have provided fundamental information on solid surfaces that retain chirality and the adsorption of chiral molecules on those surfaces. Our results have provided a qualitative and quantitative understanding of molecular geometries and energies upon adsorption onto these kind of surfaces, which cannot be easily probed experimentally.

In Chapters 3 and 4, our calculations examined the enantiospecificity of several amino acids on hydroxylated α-quartz surfaces, systems for which little quantitative information was available from experiments[1-2]. This work was initiated with the aim of complementing experiments by our collaborators. We were able, however, to quantify enantiospecific adsorption of amino acids on these surfaces prior to the experimental observations being complete. Our collaborators are currently obtaining their experimental results, and a future comparison between our calculations and these experiments is expected to lead to a more precise understanding of these fascinating systems. A chiral index proposed by Downs and Hazen has predicted that calcite would have the largest chirality among the mineral surfaces they examined[3]. Although Hazen *et al.* have demonstrated experimentally that chiral faces of the mineral calcite can discriminate between enantiomers of aspartic acid[4], theoretical calculations have not yet been used to probe the details of enantiospecific adsorption on this mineral's surfaces[5]. It would be therefore interesting to adapt the methods we have reported here to study calcite surfaces. Our results for quartz surfaces have described the configurations of amino acids in experiments under vacuum conditions, that is, in the absence of a solvent. This choice was made partly for computational convenience, but was also driven by the kinds of experiments being performed by our collaborators in ultra high vacuum. If the adsorption

of amino acids occurred in a solvent such as water, the enantiospecificity of amino acids on quartz surfaces might differ from the outcomes under vacuum conditions. Since considering solvent molecules with DFT calculations is expected to be computationally very expensive, efficient and careful approaches would be necessary if this problem was to be tackled. Neurock *et al.* have performed DFT calculations to study the effects of water solvent on metal surfaces for electrochemical applications[6-9]. These studies illustrate the complexity associated with considering solvent molecules within the computational demands of DFT calculations.

In Chapter 5, we screened transition metal pairs accessible to surface alloying of the kinked step that play a key role in surface chirality on metal surfaces on the basis of the thermodynamics of this kind of alloying[10]. A kinetic aspect of this alloying as compared with STM experiments was also investigated[11]. In this work, we focused on understanding what kinds of surface alloys are stable for highly stepped metal surfaces. Since primary long term goal of work in this field is to find the systems with pairs of chiral species and chiral surfaces that have large enantiospecificities, it would be interesting to examine if the alloys identified in our calculations lead to enhanced enantiospecificity on the surfaces. Utilizing the examples where enantiospecific adsorption on single metal surfaces has already been characterized would be a good starting point for work on this kind. For instance, since a large enantiospecificity of amino-(fluoro)methoxy adsorption on Cu(874) has been theoretically predicted[12], examining step decorated surfaces associated with this chiral Cu surface would be a useful initial approach to this topic.

In Chapter 6, our calculations were used to reconcile the previous disagreement between experiment and theory with regard to chemical speciation of glycine, a representative molecule among a class of chiral modifiers, on metal surfaces. Since glycine has a basic structure of amino acids, our results can be generally applied to more complicated amino acids on metal surfaces. This information will be helpful to create

understand and control chirally modified metal surfaces which use amino acids as chiral templates.

In addition to our main concentration in this thesis, molybdenum carbide catalysts, a promising material for a range of chemicals applications, has been examined. Our results for the surface stability of Mo_2C and adsorption of small molecules in the presence of K promoters on these surfaces provided fundamental insights into this material. A challenge for future theoretical work in this area will be to more directly connect the details of surface structure and properties with the selectivity of the relatively complex catalytic reactions that are of interest in most practical applications of this catalyst.

References

(1) Han, J. W.; James, J. N.; Sholl, D. S., *Surf. Sci.* **2008**, 602, 2478-2485.
(2) Han, J. W.; Sholl, D. S., *Langmuir* **2009**, 25, 10737-10745.
(3) Downs, R. T.; Hazen, R. M., *J. Mol. Cat. A: Chem.* **2004**, 216, 273-285.
(4) Hazen, R. M.; Filley, T. R.; Goodfriend, G. A., *Proc. Nat. Acad. Sci.* **2001**, 98, 5487-5490.
(5) Asthagiri, A.; Hazen, R. M., *Mol. Simulat.* **2007**, 33, 343-351.
(6) Taylor, C. D.; Neurock, M., *Curr. Opin. Solid State Mater. Sci.* **2005**, 9, 49-65.
(7) Taylor, C.; Kelly, R. G.; Neurock, M., *J. Electrochem. Soc.* **2006**, 153, E207-E214.
(8) Taylor, C. D.; Kelly, R. G.; Neurock, M., *J. Electrochem. Soc.* **2007**, 154, F217-F221.
(9) Taylor, C.; Kelly, R. G.; Neurock, M., *J. Electrochem. Soc.* **2007**, 154, F55-F64.
(10) Han, J. W.; Kitchin, J. R.; Sholl, D. S., *J. Chem. Phys.* **2009**, 130, 124710-8.
(11) Bellisario, D. O.; Han, J. W.; Tierney, H. L.; Baber, A. E.; Sholl, D. S.; Sykes, E. C. H., *J. Phys. Chem. C* **2009**, 113, 12863-12869.
(12) Bhatia, B.; Sholl, D. S., *Angew. Chem. Int. Ed.* **2005**, 44, 7761-7764.